

**MECHANISMS OF LOWER
GASTROINTESTINAL TOXICITY
CAUSED BY TYROSINE KINASE
INHIBITORS**

Thesis submitted in accordance with the requirements of the University of Liverpool
for the degree of Doctor in Philosophy

By Stephanie Ann French

December 2019

DECLARATION

I declare that this thesis has been composed solely by myself and that it has not been submitted, in whole or in part, in any previous applications for a degree. Except where stated otherwise by reference or acknowledgement, the work presented is entirely my own.



Stephanie Ann French

December 2019

This research was undertaken at the Department of Molecular and Clinical Pharmacology,
Institute of Translational Medicine, University of Liverpool

ACKNOWLEDGEMENTS

Thank you to my supervisors Prof Sir Munir Pirmohamed and Dr Andrea Davies for your support and guidance throughout my project. I am grateful for the time you have dedicated towards me and this project, as well as the laboratory training and emotional support.

Thank you to Dr Nick Harper and Dr Melanie Maerken for training in lentiviral transduction, and Dr Shankar Varadarajan for advice and guidance on experiments presented in chapter 4. Thank you to Dr Parveen Sharma and Dr Michael Cross for use of the Zeiss Axio Observer immunofluorescence microscope, and Jennifer Adcott at the Centre for Cell Imaging for the training on and use of the Zeiss 710 Confocal Microscope. In addition, a big thank you to the Department of Gastroenterology including Prof Mark Pritchard for welcoming me into his laboratories, Prof Barry Campbell and Dr Carrie Duckworth for their training and assistance with the enteroid work, from organoid set-up and subculture to experimentation. Also, thank you to Dr Jeff Barclay for use of the microinjection equipment used in the enteroid permeability studies and Alistair Jones and Dr Louise Thompson for training in this technique. Thanks to Dr Felix Ikuomola for the antibodies borrowed in pre-liminary experiments. Thank you to Dr Dan Carr, Dr Eunice Zang, Dr Ben Francis and Prof Andrea Jorgensen for their support in analysing and validating the GWAS data. In addition, thank you to the National Cancer Research Institute chronic myeloid leukaemia subgroup, particularly Prof Richard Clark, Prof Letizia Foroni and Dr Sandra Loaiza for providing patients samples, and Prof Stephen O'Brien at the SPIRIT2 trial office at Newcastle University for supplying clinical data.

Thank you to the Medical Research Council for funding this project, and the Liverpool Technology Directorate voucher scheme for the additional funding I received to perform work within the Centre for Cell Imaging.

Many thanks for the help and support I received from friends within the Wolfson Centre for Personalised Medicine and Gastroenterology Department, especially Louise, Melanie, George, Harvey and Carmen for the memories and laughs which helped keep me sane through the ups and downs. Thank you to Shan for your unwavering encouragement, support and love. I will endeavour to 'control my emotions and discipline my mind'. Thank you to my grandparents for their encouragement and faith in me. To my mum, thank you for your continual emotional support and friendship – I am so lucky to have such a great mum – and to my dad for teaching me the importance of taking on challenges and self-growth. I miss you every day.

ABSTRACT

Lower gastrointestinal (GI) toxicity – manifested as diarrhoea – often occurs in cancer patients undergoing treatment with tyrosine kinase inhibitors (TKIs). TKIs used for chronic myeloid leukaemia have a differential propensity to cause lower GI toxicity, with bosutinib having the highest incidence. Management strategies include treatment with non-specific anti-diarrhoea drugs, such as loperamide, which can be ineffective. The aim of this project was to use a human intestinal cell line model and a murine intestinal organoid (enteroid) model to investigate the mechanisms of TKI-induced diarrhoea, and to perform a genome-wide association study (GWAS) to identify genetic determinants of the adverse event.

Using human Caco-2 cells in a transwell set-up, we found the EGFR inhibitor gefitinib and the BCR-ABL inhibitors bosutinib, imatinib and dasatinib increased paracellular permeability to ions. These changes occurred at sub-apoptotic concentrations of 5 μ M, 50 μ M, 10 μ M and 10 μ M for bosutinib, imatinib, dasatinib and gefitinib, respectively. Bosutinib (25-100 μ M) and imatinib (100 μ M) also increased paracellular permeability to macromolecules but dasatinib and gefitinib (up to 100 μ M) had no effect. All four TKIs induced a decrease in cell viability in a concentration-dependent manner, as determined by MTT, CellTitre-Glo[®] and ToxiLight[™] assay, allowing us to postulate the involvement of cell death in TKI-induced barrier dysfunction. Only bosutinib, however, induced re-localization of several cell-cell junction proteins, specifically E-cadherin, ZO-1 and occludin, as investigated by immunofluorescence. Western blotting showed bosutinib also caused a concentration- and time- dependent decrease in levels of these tight junction (TJ) and adherens junction (AJ) proteins, while a transient decrease in *ZO-1* mRNA transcript level was detected by RTqPCR. Imatinib, however, had no effect on TJs and AJs at both the protein and mRNA level.

Specific pathways upstream of this bosutinib-induced TJ degradation were explored *in vitro* by investigating the mechanism leading to occludin degradation. Whilst an array of pathway inhibitors including oxidative stress and cell death inhibitors were unable to prevent bosutinib-induced occludin degradation, TIMP-2 downregulation was identified as a potential mechanism.

In the murine intestinal organoid model, increased paracellular permeability, determined by leakage of a fluorescently-labelled macromolecule from the enteroid lumen, was seen only with bosutinib (10 μ M). Cytotoxicity of bosutinib (10 μ M), dasatinib (0.1-10 μ M) and gefitinib (10 μ M) was confirmed in the enteroid model by the ToxiLight[™] assay. By contrast, imatinib up to 10 μ M had no effect on enteroid cell viability. Bosutinib-induced re-localization of TJ and AJ proteins were also seen; however, decreased protein levels were not observed.

The GWAS, performed on 145 dasatinib-treated chronic myeloid leukaemia (CML) patients (40 with diarrhoea) from the SPIRIT2 trial, found *PLXNC1*, a semaphorin receptor involved in controlling adherence and inflammation, to be significantly associated with the diarrhoea phenotype (odds ratio = 5.10, $p < 5 \times 10^{-8}$). *CCR3*, a chemokine receptor linked to celiac disease, was associated at the suggestive significance level (odds ratio = 3.37, $p < 1 \times 10^{-5}$). However, a replication cohort composed of a further 137 SPIRIT2 dasatinib-treated patients (33 with diarrhoea), failed to support these findings. This likely reflects the study limitations and mechanistic complexity of diarrhoea, rather than a lack of genetic involvement.

This work suggests decreased intestinal barrier integrity, potentially mediated by cell death and cell junction disruption, is important in the aetiology of TKI-induced diarrhoea. The GWAS suggests the involvement of inflammation in dasatinib-induced diarrhoea; however, further studies will be required to confirm or refute this hypothesis. Our study provides a foundation for further investigation into the mechanisms of TKI-induced diarrhoea.

PUBLICATIONS AND COMMUNICATIONS

Papers

Carr, D. F., Ayehunie, S., Davies, A., Duckworth, C. A., **French, S. A.** *et al.* (2017). "Towards Better Models and Mechanistic Biomarkers for Drug-Induced Gastrointestinal Injury." *Pharmacology and Therapeutics* 172:181–94

French, S., Davies, A., Pirmohamed, M. *et al.* "Tyrosine kinase inhibitors induce intestinal barrier dysfunction in a human cell line, mouse enteroid and mouse *in vivo* model". *In preparation.*

Abstracts

French, S., Davies, A., Pirmohamed, M. "Mechanisms of Chemotherapy-Induced Diarrhoea." International Society of Pharmacovigilance Annual Meeting 2017, Liverpool UK

French, S., Davies, A., Pirmohamed, M. "Using an Enteroid Model to Determine the Mechanisms of Bcr-Abl Inhibitor-Induced Diarrhoea." EMBO|EMBL Symposia Organoids 2018, Heidelberg Germany

French, S., Davies, A., Pirmohamed, M. "Mechanisms of Chemotherapy-Induced Diarrhoea." British Society of Gastroenterology Annual Meeting 2018, Liverpool UK

TABLE OF CONTENTS

Declaration.....	1
Acknowledgements.....	2
Abstract.....	3
Publications and communications	4
Table of contents	5
List of figures.....	10
List of tables.....	14
Abbreviations.....	16
Chapter 1: Introduction.....	21
1.1 The use of tyrosine kinase inhibitors in cancer treatment	22
1.1.1 Overview of tyrosine kinase inhibitors	22
1.1.2 Pharmacology of EGFR and BCR-ABL inhibitors.....	23
1.2 Gastrointestinal toxicity	31
1.2.1 Implications of lower gastrointestinal toxicity.....	33
1.2.2 The importance of understanding drug-induced gastrointestinal toxicity.....	34
1.3 Physiology of the gastrointestinal tract.....	35
1.3.1 Layers of the intestinal walls	35
1.3.2 The epithelial cell layer.....	37
1.3.3 The enteric nervous system.....	39
1.3.4 The enteroendocrine system.....	39
1.3.5 The enteric immune system	40
1.3.6 The muscular system.....	41
1.3.7 The gut microbiota	41
1.4 Mechanisms of chemotherapy-induced lower gastrointestinal toxicity.....	42
1.4.1 Secretion: the transcellular pathway.....	43
1.4.2 Intestinal barrier dysfunction: the paracellular pathway	46
1.4.3 Dysmotility	50
1.4.4 Inflammation and ER stress	50
1.5 Models for studying gastrointestinal toxicity	53
1.5.1 <i>In vivo</i> and <i>ex vivo</i> models.....	53
1.5.2 <i>In vitro</i> models.....	54
1.5.3 Models utilized in this project	59
1.6 Aims and objectives of this project	60

Chapter 2: Materials & Methods.....	61
2.1 Chemicals and drug compounds	62
2.2 Buffers and solutions.....	62
2.3 Cell line culture and experiments	63
2.3.1 Caco-2 cells.....	63
2.3.2 HEK293T/17 cells.....	64
2.3.3 Cell line subculture and maintenance	64
2.3.4 Short tandem repeat profiling.....	65
2.3.5 Cell permeability assay	65
2.3.6 Cell dissociation assay	66
2.3.7 Cell line cytotoxicity assays	67
2.3.8 Cell line Western blotting.....	68
2.3.9 Reverse transcription-quantitative polymerase chain reaction (RT-qPCR)....	71
2.3.10 Immunofluorescence.....	72
2.3.11 MMP array.....	73
2.3.12 Generation of Caco-2 cells stably expressing fluorescently labelled occludin and lifeact for time-lapse imaging	74
2.3.13 Enzyme-linked immunosorbent assay (ELISA)	81
2.4 Organoid culture and experiments.....	82
2.4.1 Organoid culture and maintenance.....	82
2.4.2 Organoid permeability assay	83
2.4.3 Organoid cytotoxicity assays	84
2.4.4 Organoid histology	85
2.4.5 Organoid Western blotting.....	88
2.4.6 Organoid swelling assay	88
2.5 Statistical analyses of cell line and organoid experiments	89
2.6 Genome-wide association study (GWAS)	89
2.6.1 Study design	89
2.6.2 DNA collection and extraction.....	91
2.6.3 Discovery cohort.....	91
2.6.4 Association analysis.....	92
2.6.5 Validation and replication of lead single nucleotide polymorphisms (SNPs) .	93
2.6.6 Replication cohort	96
Chapter 3: Investigating the mechanisms of tyrosine kinase inhibitor-induced diarrhoea using Caco-2 cells	97
3.1 Introduction	98

3.2	Results.....	100
3.2.1	Caco-2 cells form a fully differentiated monolayer of polarised enterocytes within 10 days	100
3.2.2	Apical bosutinib increases flux through the charge-selective permeation pathway in Caco-2 cells	102
3.2.3	Basolateral plasma concentrations of TKIs do not alter flux through the charge-selective permeation pathway in Caco-2 cells.....	104
3.2.4	Bosutinib increases flux through the size-selective permeation pathway in Caco-2 cells.....	105
3.2.5	Bosutinib is cytotoxic to Caco-2 cells.....	106
3.2.6	Bosutinib decreases cell-cell adhesion strength in Caco-2 cells	111
3.2.7	Bosutinib, dasatinib and gefitinib decrease protein levels of intercellular junction proteins in Caco-2 cells.....	113
3.2.8	Bosutinib alters levels of <i>TJP1</i> and <i>OCN</i> mRNA in Caco-2 cells	118
3.2.9	Bosutinib induces re-localization of junction proteins in Caco-2 cells	120
3.2.10	Bosutinib causes cytoskeletal rearrangement and cellular retractions in Caco-2 cells.....	124
3.2.11	Bosutinib induces re-localization of occludin when viewed using time-lapse microscopy	128
3.3	Summary of results	132
3.4	Discussion.....	132
3.4.1	Limitations and future work	137
Chapter 4: Investigating the pathways involved in bosutinib-induced intercellular junction disruption in Caco-2 cells		139
4.1	Introduction	140
4.2	Results.....	144
4.2.1	Bosutinib does not induce the release of TNF α	144
4.2.2	Bosutinib does not induce ER stress	146
4.2.3	Bosutinib-induced cytoskeletal rearrangement and cellular retractions do not involve MLCK	147
4.2.4	Bosutinib-induced cellular retractions do not involve Rho kinase activation	148
4.2.5	Bosutinib decreases occludin levels by protein degradation.....	149
4.2.6	Bosutinib-induced degradation of occludin does not involve the lysosomal or proteasomal pathway, but bosutinib-induced cellular retractions involve the proteasomal pathway.....	150
4.2.7	Bosutinib-induced occludin degradation and cellular retractions do not involve ROS signalling.....	153

4.2.8	Bosutinib-induced occludin degradation and cellular retractions do not involve cell death pathways	155
3.4.1	Bosutinib-induced cellular retractions, but not occludin degradation, is attenuated by MMP inhibitor GM6001	158
4.2.9	Bosutinib decreases levels of TIMP2	160
4.3	Summary of results	163
4.4	Discussion.....	163
4.2.10	Limitations and future work	168
Chapter 5: Investigating the mechanisms of tyrosine kinase inhibitor-induced diarrhoea using a mouse enteroid model.....		171
5.1	Introduction	172
5.2	Results.....	175
5.2.1	The BALB/c mouse enteroid model expresses relevant epithelial cell types.....	175
5.2.2	Bosutinib increases permeability in mouse enteroids	177
5.2.3	Bosutinib is cytotoxic to mouse enteroids.....	179
5.2.4	Bosutinib does not alter levels of intercellular junction proteins	186
5.2.5	Bosutinib induces the re-localization of occludin	187
5.2.6	Tyrosine kinase inhibitors do not induce enteroid swelling, an indicator of ion secretion.....	189
5.3	Summary of results	191
5.4	Discussion.....	191
5.4.1	Limitations and future work	196
Chapter 6: A genome-wide association study (GWAS) to identify genetic markers of dasatinib-induced diarrhoea		200
6.1	Introduction	201
6.2	Results.....	205
6.2.1	Patient characteristics	205
6.2.2	SNPs significantly associated with dasatinib-induced diarrhoea in the discovery cohort	206
6.2.3	Validation of imputed SNPs in the discovery cohort using PCR-based genotyping methods.....	214
6.2.4	Validation of SNPs in the replication cohort failed to confirm findings in the discovery cohort	216
6.3	Summary of results	217
6.3.1	Discussion.....	217
6.4	Limitations and future work	219
Chapter 7: Final Discussion		222

7.1	General discussion	223
7.2	Future studies and implications	226
	References	229
	Appendices	259

LIST OF FIGURES

Chapter 1: Introduction

- Figure 1.1. Structures of TKIs used in this project. p22
- Figure 1.2. Protein domains of BCR-ABL. p23
- Figure 1.3. Protein domains of EGFR. p26
- Figure 1.4. Anatomical layers of the intestines. p36
- Figure 1.5. Transport of ions across the intestinal epithelium. p45
- Figure 1.6. Proteins of tight junctions (TJs) and adherens junctions (AJs). p47
- Figure 1.7. Inflammatory responses leading to diarrhoea. p51

Chapter 2: Methods

- Figure 2.1. Schematic of transwell set-up used in permeability experiments. p66
- Figure 2.2. Schematic flow diagram for cloning of mCherry-Lifeact into pLJM1 P2A to generate pLJM1 P2A-L1. p75
- Figure 2.3. Schematic flow diagram for cloning of mEmerald-Occludin into pLJM1 P2A to generate pLJM1 P2A-O1. p76
- Figure 2.4. Flow chart of discovery and validation cohort used in dasatinib-induced diarrhoea GWAS. p90
- Figure 2.5. Annotated allelic discrimination plot for rs73718779 generated in SDS v2.2. p95

Chapter 3: Investigating the mechanisms of tyrosine kinase inhibitor-induced diarrhoea using Caco-2 cells

- Figure 3.1 Expression of intestinal alkaline phosphatase (ALPI) during Caco-2 cell differentiation. p101
- Figure 3.2. Decrease in paracellular permeability during Caco-2 cell differentiation. p101
- Figure 3.3. Effect of apical TKIs on the charge-selective permeation pathways. p103
- Figure 3.4. Effect of basolateral TKIs at C_{max} plasma concentrations on the charge-selective permeation pathway. p104
- Figure 3.5. Effect of TKIs on size-selective permeation pathway. p105
- Figure 3.6. Effect of TKIs on cell viability using MTT assay. p106
- Figure 3.7. Effect of TKIs on cell viability using CellTitre-Glo® assay. p107
- Figure 3.8. Effect of bosutinib on PARP cleavage. p108
- Figure 3.9. Effect of TKIs on nuclear fragmentation. p109
- Figure 3.10. Effect of TKIs on cell viability using ToxiLight™ assay. p110
- Figure 3.11. Effect of TKIs on cell-cell adhesion strength. p112
- Figure 3.12. Effect of bosutinib and imatinib on levels of tight junction and adherens junction proteins. p114

Figure 3.12. and 3.13. Effect of dasatinib and gefitinib on levels of tight junction and adherens junction proteins. p115

Figure 3.14. Effect of bosutinib and imatinib on levels of tight junction and adherens junction proteins over 24 h. p117

Figure 3.15. Effect of bosutinib and imatinib on tight junction and adherens junction mRNA levels over 24 h. p119

Figure 3.16. Effect of TKIs on localization of ZO-1. p121

Figure 3.17. Effect of TKIs on localization of E-cadherin. p122

Figure 3.18. Effect of TKIs on localization of occludin. p123

Figure 3.19. Effect of TKIs on protein levels of junction proteins determined by immunofluorescence. p124

Figure 3.20. Effect of TKIs on actin cytoskeleton. p125

Figure 3.21. Effect of TKIs on cell morphology. p126

Figure 3.22. Effect of TKIs on the formation of retraction fibres. p127

Figure 3.23. Gel electrophoresis of PCR amplification products. p128

Figure 3.24. Gel electrophoresis of products from colony screening. p129

Figure 3.25. Caco-2 cells transduced with lentivirus particles. p130

Figure 3.26. Effect of bosutinib on occludin re-localization determined by time-lapse imaging of Caco-2 cells stably expressing mEmerald-occludin (still images). p131-132

Figure 3.27. Effect of bosutinib on occludin re-localization determined by time-lapse imaging of Caco-2 cells stably expressing mEmerald-occludin (video) (see flashdrive).

Chapter 4: Investigating the pathways involved in bosutinib-induced intercellular junction disruption in Caco-2 cells

Figure 4.1. Simplification of the signalling pathways involved in increased paracellular permeability. p142

Figure 4.2. Effect of TKIs on TNF α release. p145

Figure 4.3. Effect of bosutinib and imatinib on levels of ER stress related proteins. p146

Figure 4.4. Effect of myosin light chain kinase (MLCK) inhibition on bosutinib-induced cytoskeletal rearrangement. p147

Figure 4.5. Effect of myosin light chain kinase (MLCK) inhibition on bosutinib-induced changes in cellular retractions. p148

Figure 4.6. Effect of Rho kinase inhibitor Y-27632 on bosutinib-induced changes in cellular retractions. p148

Figure 4.7. Assessment of the half-life of occludin protein using cycloheximide. p149

Figure 4.8. Effect of lysosomal inhibitor chloroquine and proteasomal inhibitor MG-132 on bosutinib-induced degradation of occludin. p150

Figure 4.9. Effect of lysosomal inhibitors bafilomycin and 3-methyladenine on bosutinib-induced degradation of occludin. p151

Figure 4.10. Effect lysosomal inhibitor chloroquine and proteasomal inhibitor MG-132 on bosutinib-induced in cellular retractions. p152

Figure 4.11. Effect of proteasomal inhibitor MG-132 on bosutinib-induced in cellular retractions. p152

Figure 4.12. Effect of ROS inhibitors on bosutinib-induced degradation of occludin. p153

Figure 4.13 Effect of high concentrations of ROS inhibitor deferoxamine on bosutinib-induced occludin degradation. p154

Figure 4.14. Effect of ROS inhibitors on bosutinib-induced cellular retractions. p155

Figure 4.15. Effect of cell death inhibitors on bosutinib-induced degradation of occludin. p156

Figure 4.16. Effect of cell death inhibitors on bosutinib-induced cellular retractions. p157

Figure 4.17. Effect of MMP inhibitor GM6001 on bosutinib-induced degradation of occludin. p158

Figure 4.18. Effect of high concentrations of MMP inhibitor GM6001 on bosutinib-induced occludin degradation. p159

Figure 4.19. Effect of MMP inhibitor GM6001 on bosutinib-induced cellular retractions. p160

Figure 4.20. Effect of bosutinib on protein levels of MMPs and TIMPs. p161

Figure 4.21. Effect of bosutinib on TIMP-2 protein levels. p162

Chapter 5: Investigating the mechanisms of tyrosine kinase inhibitor-induced diarrhoea using a mouse enteroid model

Figure 5.1. Schematic of an intestinal organoid. p173

Figure 5.2. Assessing the presence of epithelial cell types in a mouse enteroid model. p176

Figure 5.3. Enteroid lumen injected with FITC-dextran. p177

Figure 5.4. Effect of TKIs on paracellular permeability. p178

Figure 5.5. Effect of TKIs on cell viability determined by ToxiLight™ assay after 4 and 24 h. p179

Figure 5.6. Correlation between enteroid death determined by caspase-3 activation and enteroid circularity. p180

Figure 5.7. Effect of TKIs on cell viability determined by circularity after 4 h. p181

Figure 5.8. Effect of TKIs on cell viability determined by circularity after 24 h. p182

Figure 5.9. Correlation between enteroid death determined by ToxiLight™ assay and enteroid circularity. p183

Figure 5.10. Quantification of the number of apoptotic cells in bosutinib and imatinib treated enteroids using active caspase-3 staining. p184

Figure 5.11. Effect of bosutinib and imatinib on enteroid epithelium layer integrity. p185

Figure 5.12. Effect of bosutinib and imatinib on tight junction and adherens junction protein levels. p186

Figure 5.13. Effect of bosutinib and imatinib on localization of E-cadherin. p187

Figure 5.14. Effect of bosutinib and imatinib on localization of occludin. p188

Figure 5.15. Effect of bosutinib and imatinib on localization of ZO-1. p188

Figure 5.16. Effect of TKIs on enteroid swelling after 30 min. p189

Figure 5.17. Effect of gefitinib on enteroid swelling over 24 h. p190

Chapter 6: A genome-wide association study (GWAS) to identify genetic markers of dasatinib-induced diarrhoea

Figure 6.1. Genome-wide Manhattan plot showing SNPs linked to dasatinib-induced diarrhoea. p207

Figure 6.2. Regional association plots and recombination rates for chromosomal regions showing associations with dasatinib-induced diarrhoea at the genome-wide significance level. p208

Figure 6.3. Regional association plots and recombination rates for chromosomal regions showing associations with dasatinib-induced diarrhoea at the suggestive significance level. p210-212

Appendices

Figure A.1. Certificate of cell line authenticity for Caco-2 cells. p259

Figure A.2. Plasmid maps of mCherry-Lifeact-7 and mEmerald Occludin-C-14. p260

Figure A.3. Plasmid map of lentiviral transfer plasmid pLJM1 P2A. p261

Figure A.4. Plasmid maps of second-generation packaging plasmid psPAX2 and envelope plasmid pMD2.G. p262

Figure A.5. DNA sequence of mCherry-LifeAct within pLJM1 P2A-L1 plasmid. p263

Figure A.6. DNA sequence of mEmerald-occludin within pLJM1 P2A-O1 plasmid. p264-265

LIST OF TABLES

Chapter 1: Introduction

Table 1.1. Protein targets of clinically used EGFR and BCR-ABL inhibitors. p25

Table 1.2. Phases of chronic myeloid leukaemia. p27

Table 1.3. Definitions of grades 1 to 5 diarrhoea. p32

Table 1.4. Diarrhoea incidences, onset and duration of clinically used EGFR and BCR-ABL inhibitors. p33

Table 1.5. Alterations in TJ and AJ expression in lower GI toxicity. p49

Table 1.6 Cells amenable for use as *in vitro* lower gastrointestinal models to study toxicity. p56

Chapter 2: Methods

Table 2.1. Cell volumes used to give the same number of cells per surface area, between experiments using different plates. p64

Table 2.2. Components of SDS gels used for Western blotting. p69

Table 2.3. Primary antibodies (IgGs) used for Western blotting of Caco-2 cell and organoid protein lysates. p70

Table 2.4. Secondary antibodies (IgGs) used for Western blotting of Caco-2 cell and organoid protein lysates. p71

Table 2.5. Primary antibodies (IgGs) used for immunofluorescent staining of Caco-2 cell and organoids. p73

Table 2.6. PCR primers to generate plasmid inserts. p77

Table 2.7. Restriction enzymes used for digestion of insert DNA and lentiviral plasmid (pLJM1 P2A). p78

Table 2.8. Sequences of primers for PCR colony screening. p79

Table 2.9. Primary antibody details and dilutions used for organoid immunohistochemistry. p87

Table 2.10 Sequences of Taqman™ and KASP™ probes for the six SNPs in the imputation validation and replication study. p94

Chapter 6: A genome-wide association study (GWAS) to identify genetic markers of dasatinib-induced diarrhoea

Table 6.1. Summary of a literature search identifying SNPs significantly associated with chemotherapy-induced diarrhoea in candidate gene studies. p202-203

Table 6.2. Summary of a literature search identifying SNPs significantly associated with chemotherapy-induced diarrhoea in genome-wide association studies. p204

Table 6.3. Patient demographics of discovery and replication cohorts from SPIRIT2 trial. p206

Table 6.4. Index SNPs associated with dasatinib-induced diarrhoea at suggestive ($p < 1 \times 10^{-5}$) and genome-wide significance ($p < 5 \times 10^{-8}$) levels. p213

Table 6.5. Confirmation of imputation accuracy of the discovery cohort using Taqman™ or KASP™ genotyping. p215

Table 6.6. Assessment of selected associated SNPs in replication cohort. p216

ABBREVIATIONS

3-MA	3-Methyladenine
5-FU	5-Fluorouracil
ABCB1	ATP-binding cassette super-family B member 1 (also called MDR1)
ABCG2	ATP-binding cassette super-family G member 2 (also called BCRP)
ABL	Abelson murine leukaemia viral oncogene homolog 1
ADRs	Adverse drug reactions
AJs	Adherens junctions
APES	3-Aminopropyltriethoxysilane
AK	Adenylate kinase
ALPI	Alkaline phosphatase (Intestinal)
ANOVA	Analysis of variance
APES	3-Aminopropyltriethoxysilane
APS	Ammonium persulfate
ATCC	American type culture collection
ATP	Adenosine Triphosphate
AUC	Area under the curve
<i>B2M</i>	β -2-Microglobulin gene
BCA	Bicinchoninic acid
BCR (-ABL)	Breakpoint cluster region (- Abelson murine leukaemia viral oncogene homolog 1 fusion protein)
BCRP	Breast cancer resistance protein
BiP	Binding immunoglobulin protein
BMI	Body mass index
BSA	Bovine serum albumin
CaCC	Ca ²⁺ -dependent Cl ⁻ channels
CCR3	C-C chemokine receptor type 3
Cdc42	Cell division control protein 42 homolog
<i>CDH1</i>	Cadherin 1 (gene coding for E-cadherin)
cDNA	Complementary DNA
CEL	Chronic eosinophilic leukaemia
CFTR	Cystic fibrosis transmembrane regulator
CgA	Chromogranin A
CHOP	CCAAT-enhancer-protein homologous protein or C/EBP homologous
CHR	Complete haematological response

CI	Confidence intervals
c-KIT	Mast/Stem cell growth factor receptor
CML	Chronic myeloid leukaemia
CQ	Chloroquine
CYP	Cytochrome P450
DAB	3,3'-Diamino-benzidine
DAPI	4',6-Diamidino-2-Phenylindole
DCLK1	Double cortin Like Kinase 1
dH ₂ O	Distilled water
DMEM	Dulbecco's modified Eagle's medium
DMSO	Dimethylsulfoxide
DPP6	Dipeptidyl peptidase like 6
DPX	Distyrene, plasticizer, xylene
DSMZ	Deutsche Sammlung von Mikroorganismen und Zellkulturen (The Leibniz Institute DSMZ - German Collection of Microorganisms and Cell Cultures)
DSS	Dextran sodium sulphate
ECL	Enhanced chemiluminescence
EDTA	Ethylenediaminetetraacetic acid
EGF	Epidermal growth factor
EGFR	Epidermal growth factor receptor
ELISA	Enzyme-linked immunosorbent assay
ER	Endoplasmic reticulum
FAK	Focal adhesion kinase
FBS	Fetal bovine serum
FD-4	FITC (fluorescein isothiocyanate)-dextran (4kDa)
FITC	Fluorescein isothiocyanate
GFP	Green fluorescent protein
GI	Gastrointestinal
GIST	Gastrointestinal stromal tumours
GLP1/2	Glucagon like peptide 1/2
h	hours
H&E	Haematoxylin and eosin
HEPES	4-(2-Hydroxyethyl)-1-piperazineethanesulfonic acid
HRP	Horseradish peroxidase
HWE	Hardy-Weinberg Equilibrium
IBD	Inflammatory bowel disease

IBS	Irritable bowel syndrome
IBS-C	Irritable bowel syndrome (constipation predominant)
IBS-D	Irritable bowel syndrome (diarrhoea predominant)
IgA/G	Immunoglobulin A/G
IL	Interleukins
IM-54	2-(1H-Indol-3-yl)-3-pentylamino-maleimide
INF	Interferon
JNK	c-Jun N-terminal kinase
iPSC	Induced pluripotent stem cells
KCNQ5	Potassium (K+) voltage-gated channel subfamily KQT member 5
LD	Linkage disequilibrium
LDEV	Lactate dehydrogenase-elevating virus
Lgr5	Leucine-rich repeat-containing G-protein coupled receptor 5
MAF	Minor allele frequency
MAPK(KK)	Mitogen-activated protein kinase (kinase kinase)
MARVEL	Myelin and lymphocyte (MAL) and related proteins for vesicle trafficking and membrane link
MCR	Major cytogenetic response
MCT1/4	Monocarboxylate transporter 1/4
MDR1	Multidrug resistance protein 1 (also called ABCB1)
MG-132	Carbobenzoxy-L-leucyl-L-leucyl-L-leucinal
MLC	Myosin light chain
MLCK	Myosin light chain kinase
MTT	3-(4,5,-Dimethylthiazol-2-yl)-2,5-diphenyltetrazolium bromide
MUC2	Mucin 2
MYO16	Myosin XVI
MYT1L	Myelin transcription factor 1 like
NF-κB	Nuclear factor kappa B
NKCC1	Na-K-Cl cotransporter 1
NSCLC	Non-small cell lung cancer
OCLN	Occludin
OCT-1	Organic cation transporter 1 (also called SLC22A1)
PARP1	Poly [ADP-ribose] polymerase 1
PCR	Polymerase chain reaction
PBS	Phosphate buffered saline
PDGFR	Platelet-derived growth factor receptor

Ph+ ALL	Philadelphia chromosome positive acute lymphoblastic leukaemia
Ph+ CML	Philadelphia chromosome-positive chronic myeloid leukaemia
PI3K	Phosphoinositide 3-kinase
PIP2	Phosphatidylinositol 4,5-bisphosphate
PIP3	Phosphatidylinositol 3,4,5-triphosphate
PP2A	protein phosphatase 2A
PKC	protein kinase C
PLXNC1	Plexin C1
PYY	Polypeptide YY (tyrosine tyrosine)
Rac	Ras-related C3 botulinum toxin substrate 1
RhoA	Ras homolog family member A
RIPK1	Receptor-interacting serine/threonine-protein kinase 1
ROCK	Rho-associated protein kinase
Ser	Serine residue
SD	Standard deviation
SDS-PAGE	Sodium dodecyl sulfate- polyacrylamide gel electrophoresis
SEM	Standard error of the mean
SERPINB6	Serpin (serine protease inhibitors) family B member 6
SLC22A1	Solute carrier family 22 member 1 (also called OCT-1)
SMCTs	Sodium-dependent monocarboxylate transporters
SNP	Single nucleotide polymorphism
Src	Proto-oncogene c-Src
TBS-T	Tris-buffered saline with 0.1% Tween-20
TEER	Transepithelial electrical resistance
TEMED	Tetramethylethylenediamine
TFF3	Trefoil factor 3
TGF- α	Transforming growth factor α
Thr	Threonine residue
TIMP	Tissue inhibitor of metalloproteinases
TKI	Tyrosine kinase inhibitors
TJs	Tight junctions
<i>TJP1</i>	Tight junction protein 1 (gene coding for zonula occludens-1)
TNF	Tumour necrosis factor
TKI	Tyrosine kinase inhibitor
Tyr	Tyrosine residue
UPR	Unfold-protein response

UGT1A1	Uridine 5'-diphospho-glucuronosyltransferase (UDP)-glucuronosyltransferase 1-1
VEGFR	Vascular endothelial growth factor receptor
WTCCC	Wellcome Trust Case Control Consortium
ZO-1	Zonula occludens-1
Z-VAD-FMK	Cell permeable fluoromethyl ketone

CHAPTER 1: INTRODUCTION

1.1 The use of tyrosine kinase inhibitors in cancer treatment

1.1.1 Overview of tyrosine kinase inhibitors

Small molecule tyrosine kinase inhibitors (TKIs) are orally administered chemotherapeutic agents which provide greater targeting specificity than conventional cytotoxic chemotherapies (Keller *et al.*, 2009; Fullmer *et al.*, 2011; Shi *et al.*, 2013; Iqbal *et al.*, 2014). Whilst the latter act on rapidly dividing cells, targeted therapies – such as TKIs – act on the proteins of aberrantly expressed or mutated genes within specific cancerous cells. This discriminatory cytotoxicity of targeted chemotherapy should lead to fewer adverse drug reactions (ADRs) and higher treatment efficacy. As such TKIs have been an area of focus in novel chemotherapeutic drug development.

TKIs can be subdivided based on kinase targets. For example, breakpoint cluster region protein (BCR) - Abelson murine leukaemia viral oncogene homolog 1 (ABL) fusion protein (BCR-ABL) inhibitors such as imatinib (De Francia *et al.*, 2013), dasatinib (Wang *et al.*, 2013) and bosutinib (Pfizer, 2014; Brümendorf *et al.*, 2015) are frequently used for the treatment of Philadelphia chromosome-positive (Ph⁺) chronic myeloid leukaemia (CML) (Fig 1.1A-C). Some BCR-ABL inhibitors, such as imatinib and dasatinib, can also be used for the treatment of Ph⁺ acute lymphoblastic leukaemia (ALL) (Malagola *et al.*, 2016). By contrast, epidermal growth factor receptor (EGFR) inhibitors, such as gefitinib (Shi *et al.*, 2013), are commonly used for the treatment of non-small cell lung cancer (NSCLC) (Fig 1.1D).



Figure 1.1. Structures of TKIs used in this project. Chemical structures of BCR-ABL inhibitors bosutinib (A), imatinib (B) and dasatinib (C), and EGFR inhibitor gefitinib (D). Images produced in ChemDraw Professional version 19.0.1.28 (perkinelmer.com/uk/category/chemdraw) by S. French.

Other classes of TKIs include platelet-derived growth factor receptor (PDGFR) inhibitors (Papadopoulos *et al.*, 2018) and vascular endothelial growth factor receptor (VEGFR) inhibitors (Lacal *et al.*, 2018); however, the clinical relevance of PDGFR and VEGFR inhibition will not be discussed here. In general, however, it is important to note there is often overlap between the spectrum of kinases that are targeted by different drugs. For example, BCR-ABL inhibitors imatinib and dasatinib also target PDGFR (Kitagawa *et al.*, 2013).

1.1.2 Pharmacology of EGFR and BCR-ABL inhibitors

1.1.2.1 Primary pharmacodynamics (mode of action) of BCR-ABL inhibitors

BCR-ABL is formed as a result of a reciprocal translocation between chromosome 9 and chromosome 22 within hematopoietic stem cells (Sattler *et al.*, 2003; Cilloni *et al.*, 2012). Chromosome 9 contains Abelson murine leukaemia viral oncogene homolog 1 (*ABL*) - which encodes for a nuclear-cytoplasm shuttling tyrosine kinase involved in differentiation, cell division, stress signalling and adhesion; chromosome 22 harbours the less well-studied breakpoint cluster region protein (*BCR*) gene (Sattler *et al.*, 2003). Translocation of these two chromosomes creates a truncated chromosome 9 known as the Philadelphia (Ph) chromosome, harbouring the oncogenic BCR-ABL gene, and an elongated chromosome 22. Within the BCR-ABL fusion protein, ABL is constitutively active due to the juxtaposition of BCR (Fig 1.2) and retained within the cytoplasm (no longer shuttling between the cytoplasm and nucleus). The protein undergoes autophosphorylation activating an array of downstream signalling pathways involved in proliferation and survival including the Ras-Raf-MEK-ERK pathway, the JAK-STAT pathway and the PI3K/AKT pathway (Cilloni *et al.*, 2012). BCR-ABL inhibitors competitively block the adenosine triphosphate (ATP) binding site on the ABL domain (Fig 1.2). This prevents autophosphorylation of BCR-ABL attenuating the downstream pathways which would otherwise cause over-expansion and survival of haematopoietic cells associated with Ph+ CML and Ph+ ALL (Cilloni *et al.*, 2012).

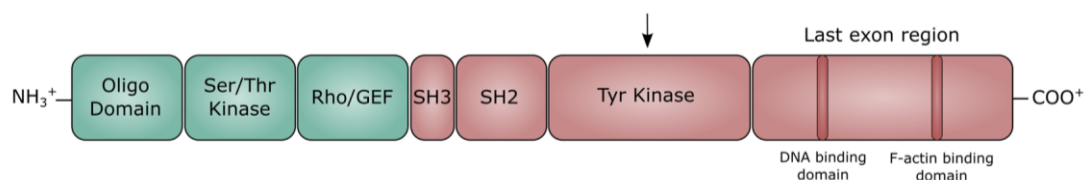


Figure 1.2. Protein domains of BCR-ABL. Green represents the BCR protein and pink represents the ABL protein within BCR-ABL. Abbreviations: Ser/Thr kinase, Serine/Threonine kinase; SH2/3, Src homology 2/3 domain; Tyr, Tyrosine. Arrow indicates the approximate binding site for BCR-ABL inhibitors within the ATP-binding pocket of the tyrosine kinase domain. Information on domains obtained from Cilloni *et al.* (2012). Diagram produced in the open-source vector graphics editor Inkscape version 0.92.4 (inkscape.org/release/inkscape-0.92.4) by S. French.

BCR-ABL inhibitors exhibit varied potencies towards BCR-ABL. *In vitro* inhibition activity assays against ABL are often used to determine BCR-ABL inhibition potency, and these studies have shown that bosutinib, imatinib and dasatinib inhibit c-ABL with half-minimal inhibitor concentrations (IC50s) of 0.5-1nM, 190-400nM and 0.8-9nM, respectively (Rix *et al.*, 2007, 2009; Pfizer, 2014).

Imatinib is a relatively selective BCR-ABL inhibitor; however, it also inhibits a handful of other tyrosine kinases at similar potencies. These kinases include Mast/Stem cell growth factor receptor (c-KIT) and PDGFR (Rix *et al.*, 2007) (Table 1.1). c-KIT is a cell surface tyrosine kinase that initiates an array of downstream pathways, including PI3K/AKT, MAPK and Src pathways, involved in survival, proliferation and stem cell maintenance (Li *et al.*, 2019). Gain-of-function c-KIT mutations can lead to GI stromal tumours (GIST) (70-85% of GISTs contain a mutation rendering c-KIT overactive (Li *et al.*, 2019)) and it is therefore unsurprising that imatinib is a first-line therapy against GISTs (Iqbal *et al.*, 2014).

Similarly to c-KIT, PDGFR is a cell-surface receptor tyrosine kinase involved in a diverse array of biological processes under both pathological and physiological conditions (Farooqi *et al.*, 2015). PDGFR influences PI3K/AKT, MAPK and Src family kinase signalling, controlling processes such as proliferation, survival, differentiation, migration and haematopoiesis (the formation of blood cells). PDGFR activation is especially important during early stages of growth and development where it is involved in organ and blood vessel formation. However, constitutively active PDGFR fusion proteins – which akin to BCR-ABL can be formed during chromosomal translocation – are involved in oncogenesis of blood cancers, including chronic eosinophilic leukaemia (CEL) (Appiah-Kubi *et al.*, 2017). Imatinib is currently approved for the treatment of PDGFR fusion protein-positive chronic eosinophilic leukaemia (CEL) (Iqbal *et al.*, 2014).

Similarly to imatinib, dasatinib also inhibits c-Kit and PDGFR (Rix *et al.*, 2007) (Table 1.1); however, dasatinib is not currently approved for the treatment of GISTs and PDGFR fusion protein-positive CEL. Bosutinib, by contrast, exhibits reduced activity against c-Kit and PDGFR, but like dasatinib, can inhibit the Src family kinases (Table 1.1) (Rix *et al.*, 2007, 2009; Kitagawa *et al.*, 2013).

Src family kinases – the eight mammalian members of which are Blk, Fgr, Fyn, Hck, Lck, Lyn, Src and Yes – are non-receptor intracellular oncogenic tyrosine kinases involved in cell growth, differentiation, migration and survival (Parsons *et al.*, 2004) as well as progression of Ph⁺ CML and Ph⁺ ALL (Li, 2008). BCR-ABL and Src family kinases directly interact causing

bilateral activation. BCR-ABL activates Src family kinases leading to initiation of the JAK-STAT and PI3K/AKT pathways involved in leukaemogenesis, whilst Src family kinases can phosphorylate residues on BCR-ABL involved in activation of MEK/ERK oncogenic signalling (Li, 2008). Through dual inhibition of both BCR-ABL and Src family kinases, dasatinib and bosutinib show increased efficacy and lowered rates of drug resistance (see 1.1.2.4 Efficacy and adverse drug reactions of BCR-ABL and EGFR TKIs) than more selective BCR-ABL inhibitors such as imatinib.

Table 1.1. Protein targets of clinically used BCR-ABL and EGFR inhibitors. The main inhibited kinases are shown in bold. A high selective entropy indicates a high level of off-target binding.			
Drug (references)	Cancer type (FDA-approved)	Selective entropy	Protein targets
Imatinib (Cohen <i>et al.</i> , 2012; Kitagawa <i>et al.</i> , 2013; Iqbal and Iqbal, 2014; Brümmendorf <i>et al.</i> , 2015; Malagola <i>et al.</i> , 2016)	Ph+ CML, Ph+ ALL, PDGFR fusion protein positive CEL, GIST	0.8	BCR-ABL , c-Kit, PDGFR
Dasatinib (Fullmer <i>et al.</i> , 2011; Kitagawa <i>et al.</i> , 2013; Malagola <i>et al.</i> , 2016)	Ph+ CML, Ph+ ALL	3.2	BCR-ABL , c-Kit, Ephrin receptors, MAPKs, PDGFR, Src family kinases including Src , TEC family kinases
Bosutinib (Keller <i>et al.</i> , 2009; Rix <i>et al.</i> , 2009; Pfizer, 2014)	Ph+ CML	3.1	BCR-ABL , Ephrin receptors, MAPKs, Src family kinases including Src , TEC family kinases
Gefitinib (Kitagawa <i>et al.</i> , 2013; Shi <i>et al.</i> , 2013)	NSCLC	0.5	EGFR , Ephrin receptors

Abbreviations: BCR-ABL, Breakpoint cluster region protein - Abelson murine leukaemia viral oncogene homolog 1 fusion protein; CEL, chronic eosinophilic leukaemia; c-Kit, Stem cell growth factor receptor Kit; EGFR, Epidermal growth factor receptor; GIST, Gastrointestinal stromal tumour; MAPKs, Mitogen-activated protein kinases; NSCLC, Non-small cell lung cancer; PDGFR, Platelet-derived growth factor receptor; Ph+ ALL, Philadelphia chromosome-positive acute lymphoblastic leukaemia; Ph+ CML, Philadelphia chromosome-positive chronic myeloid leukaemia; Src, Proto-oncogene c-Src.

However, bosutinib and dasatinib are promiscuous kinase inhibitors and this is reflected in their high selective entropy. Selective entropy is a single value indicator of drug off-target binding calculated using data from large pharmacological profiling experiments. Bosutinib,

imatinib and dasatinib have selective entropies of 3.1, 0.8 and 3.2, respectively (Uitdehaag *et al.*, 2014); therefore, whilst imatinib has few additional binding partners to those mentioned above, bosutinib and dasatinib interact with many other kinases. For both bosutinib and dasatinib these include mitogen-activated protein kinases (MAPKs), Ephrin receptors and TEC family kinases (Rix *et al.*, 2007, 2009; Kitagawa *et al.*, 2013; Pfizer, 2014).

The overlapping, but unique, target profiles of BCR-ABL inhibitors which impact multiple biological processes, such as immune regulation, cell communication and cell survival, are likely linked to drug efficacy and toxicity (see 1.1.2.4 Efficacy and adverse drug reactions of BCR-ABL and EGFR TKIs) (Rix *et al.*, 2007, 2009).

1.1.2.2 Primary pharmacodynamics (mode of action) of EGFR inhibitors

EGFR inhibitors function by a similar mechanism to BCR-ABL inhibitors through blocking the ATP binding site of their target protein. However, unlike BCR-ABL, *EGFR* – a proto-oncogene encoding a tyrosine kinase receptor located within the plasma membrane – is widely expressed in different cell types, thus limiting the selectivity of this therapy. Patients with NSCLC frequently have an activating mutation in the *EGFR* gene which leads to constitutive receptor activation and increased agonist sensitivity. This results in increased activation of downstream pathways – such as the Ras-Raf-MEK-ERK pathway, the PI3K/Akt pathway and the JAK-STAT pathway – leading to increased cell proliferation, angiogenesis and invasiveness (Lopes *et al.*, 2015). EGFR inhibitors prevent activation of downstream pathways by binding to the cytoplasmic face of the transmembrane receptor at the ATP-binding site (Fig 1.3, (Lopes *et al.*, 2015)). This prevents ligands, such as epidermal growth factor (EGF) and transforming growth factor α (TGF- α) from inducing EGFR autophosphorylation and hence restricting downstream activation of pro-survival and proliferation pathways (Lopes *et al.*, 2015). In this way, gefitinib can be used for the treatment of NSCLC harbouring *EGFR* activating mutations (Hida *et al.*, 2009).

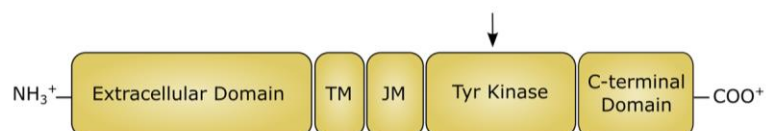


Figure 1.3. Protein domains of EGFR. Abbreviations: Tyr, Tyrosine; TM, Transmembrane domain; JM, Juxtamembrane domain. Arrow indicates the approximate binding site for EGFR inhibitors within the ATP-binding pocket of the tyrosine kinase domain. Information on domains obtained from Lopes *et al.* (2012). Diagram produced in Inkscape by S. French.

Gefitinib is a relatively selective EGFR inhibitor with at least 100-fold higher affinity towards EGFR (also called ErbB1) than the three other ErbB family members (ErbB2-4). This selectivity is reflected by its low selective entropy of 0.5 (Uitdehaag *et al.*, 2014). However, gefitinib does show inhibition activity towards several Ephrin receptors (Table 1.1), cell-surface tyrosine kinases involved in migration and proliferation partially through EGFR cross-talk (Kitagawa *et al.*, 2013). In NSCLC, Ephrin receptor genes are frequently mutated and over-expressed, contributing to pathogenesis and tumour progression (Mäki-Nevala *et al.*, 2013; Staquicini *et al.*, 2015). Therefore, Ephrin receptor ‘off-target’ binding by gefitinib may contribute to drug efficacy (Uitdehaag *et al.*, 2014).

1.1.2.3 Pharmacokinetics of BCR-ABL and EGFR TKIs

The small molecule TKIs used in this project – bosutinib, dasatinib, imatinib and gefitinib – are taken orally usually in the form of tablets or capsules at the doses recommended by the British National Formulary Edition 78 (www.bnf.nice.org.uk/drug). Imatinib, often used as first-line therapy, is given at a dose of 400mg once daily for subjects with chronic phase Ph+ CML (Brümmendorf *et al.*, 2015), and at a dose of 600mg for patients with accelerated phase or blast phase/crisis Ph+ CML (Cohen *et al.*, 2002) (see Table 1.2 for medical definition of the three phases of CML). Patients undergoing dasatinib treatment receive lower doses: 100mg once daily is recommended for subjects with chronic phase CML (Fullmer *et al.*, 2011) and 140mg for more advanced stages of CML. Imatinib and dasatinib can also be used for the treatment of Ph+ ALL at recommended doses of 600mg and 140mg daily, respectively (Malagola *et al.*, 2016). Bosutinib, currently not approved for the treatment of Ph+ ALL, is given to patients in chronic, accelerated and blast phases of Ph+ CML at a dose of 500mg once daily (Pfizer, 2014). Gefitinib, on the other hand, is an EGFR inhibitor given to subjects with NSCLC at a recommended dose of 250mg daily (Shi *et al.*, 2013).

Table 1.2. Phases of chronic myeloid leukaemia. Medical definitions of the three stages of CML taken from Cohen <i>et al.</i> , 2002. Blasts, sometimes also called leukaemic cells, are immature and abnormal white blood cells.	
Chronic phase	<15% blasts in peripheral blood and bone marrow No extramedullary involvement other than spleen or liver
Accelerated phase	15% - 30% blasts in peripheral blood and bone marrow
Blast phase/crisis	>30% blasts in in peripheral blood and bone marrow Extramedullary involvement other than spleen or liver

Bosutinib, given at 500mg daily, reaches a peak plasma concentration (C_{max}) of 101ng/mL (190nM) at day 1, and a steady state C_{max} of 200ng/mL (377nM) at day 15 (Pfizer, 2014). This is much lower than plasma concentrations seen during daily treatment with imatinib, 1058ng/mL-2596ng/mL (2.14-5.26 μ M) (Peng *et al.*, 2005; De Francia *et al.*, 2013), and gefitinib, 662ng/mL-1064ng/mL (1.5-2.4 μ M) (Nakamura *et al.*, 2010; Miura *et al.*, 2014). Dasatinib, on the other hand, reaches a steady state C_{max} of 54.6 ng/mL (100nM) and 79.7ng/mL (163nM) during the standard 100mg and 140mg once daily regime, respectively (Birch *et al.*, 2013; Wang *et al.*, 2013).

The time to achieve peak plasma concentrations (T_{max}) was on average 6 h in Ph+ CML patients treated with bosutinib, suggesting a moderately low absorption rate (Pfizer, 2014). This is similar to gefitinib, which has a T_{max} of 3-7 h (Peters *et al.*, 2014). Dasatinib and imatinib, however, are rapidly absorbed and a peak plasma concentration is achieved within 0.5-3 h (McCormack *et al.*, 2011) and 2-4 h (Cohen *et al.*, 2002) respectively.

The absolute bioavailability of bosutinib has been determined experimentally, by comparing dose exposure (area under the curve, AUC) after oral administration and intravenous administration in the same subjects, to be 33% (Pfizer, 2014; Abbas *et al.*, 2016). This reflects a relatively low systemic exposure and is similar to the bioavailability of dasatinib (29%) (McCormack *et al.*, 2011), but much lower than that of imatinib (98%) (Cohen *et al.*, 2002) and gefitinib (60%) (Peters *et al.*, 2014).

The TKIs investigated in this project have a large volume of distribution due to high distribution through most tissues and organs. Bosutinib has the highest apparent volume of distribution of >5000L, calculated by dividing total amount of drug in the body by the concentration in the plasma, after a single 500mg dose (Pfizer, 2014). Despite high distributions throughout the body, these TKIs are also highly bound to plasma proteins (~90%) (Cohen *et al.*, 2002; McCormack and Keam, 2011; Peters *et al.*, 2014; Abbas and Hsyu, 2016). The half-life of bosutinib in Ph+ CML patients is approximately 22 h (Pfizer, 2014), whilst the half-life of imatinib is 18 h (Cohen *et al.*, 2002), dasatinib is 5-6 h (McCormack *et al.*, 2011) and gefitinib is 48-72 h (Peters *et al.*, 2014).

Bosutinib, like most TKIs, undergoes intestinal and hepatic first pass metabolism through the action of cytochrome P450 (CYP) enzymes (Hussaarts *et al.*, 2019). Bosutinib, imatinib, dasatinib and gefitinib are all predominantly metabolised by CYP3A4, primarily within the liver (Cohen *et al.*, 2002; McCormack and Keam, 2011; Peters *et al.*, 2014; Pfizer, 2014). Bosutinib is metabolized to its inactivate components, oxydechlorinated bosutinib (M2) and

N-desmethylated bosutinib (M5) (Pfizer, 2014; Abbas *et al.*, 2016). Dasatinib is also metabolised to inactive components (McCormack *et al.*, 2011). Imatinib, by contrast, is metabolised to an *active* metabolite with similar potency to the parent drug as well as inactive metabolites by CYP3A4 (Cohen *et al.*, 2002).

The major excretory route for bosutinib and its metabolites is through the biliary system, and as a result these compounds leave the body primarily in the faeces. This route accounts for over 90% of excreted drug, and only 3% is excreted via urine (Pfizer, 2014; Abbas *et al.*, 2016). Imatinib, dasatinib and gefitinib are also excreted principally by the biliary system (Cohen *et al.*, 2002; McCormack and Keam, 2011; Peters *et al.*, 2014).

Drugs excreted in the bile can enter the GI tract and be reabsorbed back into circulation, thus prolonging the pharmacological action of the drug. This is known as enterohepatic recirculation (Hussaarts *et al.*, 2019). Bosutinib, imatinib, dasatinib and gefitinib are substrates of the transporters ABCB1 and ABCG2 (Peters *et al.*, 2014; Pfizer, 2014; Hussaarts *et al.*, 2019), known to be involved in drug efflux from intestinal cells and liver, suggesting these TKIs may undergo enterohepatic recirculation.

1.1.2.4 *Efficacy and adverse drug reactions of BCR-ABL and EGFR TKIs*

First-line therapy for CML is imatinib, a first generation drug (Cohen *et al.*, 2012). Imatinib is relatively efficacious in the treatment of chronic phase CML, the most common phase of CML upon initial diagnosis (see Table 1.2). Eighty eight percent of patients achieve a complete haematological response (CHR) (defined as a normal platelet count, normal white blood cell count and no enlargement of the spleen) and 49% achieve a major cytogenetic response (MCR) ($\leq 35\%$ cells are Ph+) (Cohen *et al.*, 2002). However, treatment of accelerated and blast phase CML with imatinib is less successful; only 28% and 4% of patients achieve a CHR, respectively (Cohen *et al.*, 2002). This non-response to treatment is known as intrinsic or primary resistance and is defined as “an inability to achieve a CHR at 3 months and MCR at 6 months” (Iqbal *et al.*, 2014).

In addition to intrinsic resistance, patients may lose imatinib sensitivity over time. This is known as acquired or secondary resistance and can occur through: accumulation of *BCR-ABL* mutations (that reduce the affinity of imatinib to bind in the ATP pocket), or over-expression of drug transporter genes or increased expression of *BCR-ABL* (Iqbal *et al.*, 2014). Secondary resistance is especially common for patients in the accelerated or blast phase of CML, and approximately 25% of CML patients develop resistance to the imatinib within 5 years (Abbas *et al.*, 2016).

Some patients cannot tolerate the adverse events associated with this drug. In a study involving 260 newly diagnosed CML patients treated with the standard 400mg dose of imatinib, 5% of patients were discontinued from the drug because of adverse events (Kantarjian *et al.*, 2010). Unsurprisingly the most common adverse drug reactions were haematological including neutropenia (low neutrophil count) (58%), thrombocytopenia (low platelet count) (62%) and anaemia (low haemoglobin levels) (84%). Non-haematological side effects included fluid retention (42%), predominantly superficial oedema (36%), nausea (20%), diarrhoea (17%), rash (17%) and musculoskeletal inflammation (17%) (Kantarjian *et al.*, 2010).

Dasatinib, a second-generation TKI, is effective in approximately half of Ph+ CML patients experiencing imatinib resistance. An MCR is achieved in 56% of chronic phase, 39% of acute phase and 25-50% of blast phase patients; whilst 86%, 47% and 28-42% achieve a CHR in the respective afore-mentioned phases (Fullmer *et al.*, 2011). However, dasatinib induces haematological side effects, including neutropenia, thrombocytopenia and anaemia, at slightly higher rates than imatinib (Kantarjian *et al.*, 2010). Dasatinib is also associated with an array of non-haematological adverse events including fluid retention (19%), predominantly pleural effusion (10-30%), diarrhoea (17-20%), headache (12%), rash (11%) and musculoskeletal pain (11%) (Kantarjian *et al.*, 2010; Fullmer *et al.*, 2011). Similarly to imatinib treatment, resistance and intolerance can lead to dasatinib treatment discontinuation and the requirement of alternative TKI treatment (Abbas *et al.*, 2016).

Bosutinib, a third-generation BCR-ABL inhibitor, is active against many mutated forms of *BCR-ABL* involved in imatinib and dasatinib resistance including Q252H, Y253F, D276G, E279K, M351T, F359V, L384M, H396P, H396R, and G398R (Pfizer, 2014; Abbas *et al.*, 2016). Seventy five percent of chronic phase Ph+ CML patients undergoing treatment with bosutinib as third-line therapy (i.e. resistant or intolerant to imatinib, and a second-line BCR-ABL inhibitor such as dasatinib) achieve a CHR whilst 50% achieve a MCR (Khoury *et al.*, 2012). However, patients with V299L and T315I mutations are highly resistant to bosutinib (Abbas *et al.*, 2016).

Haematological adverse events are less frequent during bosutinib treatment, 28-42% of patients experience thrombocytopenia, 25% experience anaemia, and neutropenia occurs in only 13% (Pfizer, 2014; Brümmendorf *et al.*, 2015). However, ~90% patients experience GI adverse events, including diarrhoea (70-90%), nausea (43%) and vomiting (38%). Patients also frequently experience rash (32%) and headache (18%); however, fewer patients

experience pleural effusion, cardiac toxicity or musculoskeletal toxicity than with imatinib and dasatinib treatment (Khoury *et al.*, 2012).

From these data it is clear that despite belonging to the same TKI inhibitor class of BCR-ABL inhibitors imatinib, dasatinib and bosutinib have distinct toxicity profiles (Keller *et al.*, 2009; Fullmer *et al.*, 2011; Cohen *et al.*, 2012).

Gefitinib, an EGFR inhibitor, was the first targeted drug to be approved for NSCLC treatment and can be used as first-, second- or third-line treatment (Hida *et al.*, 2009). Patients with specific *EGFR* mutations, including exon 19 deletions or L858R, have a much higher response rate (54-94%) to gefitinib relative to patients with wild-type *EGFR* (5-14%). Therefore, screening for these relevant *EGFR* mutations at diagnosis is undertaken to enable treatment stratification (Hida *et al.*, 2009; Shi *et al.*, 2013). Adverse events of gefitinib during standard treatment with 250mg daily include acne-like rash (49%), diarrhoea (28%), nausea (5%) and leukopenia (low leukocyte count) (5%) (Shi *et al.*, 2013).

1.2 Gastrointestinal toxicity

Chemotherapy, including targeted treatment, is well known for inducing a wide range of ADRs at high frequency. One of the most common adverse event during treatment with BCR-ABL and EGFR inhibitors is gastrointestinal (GI) toxicity, including diarrhoea, vomiting, nausea and abdominal pain (Keller *et al.*, 2009; Fullmer *et al.*, 2011; Cohen *et al.*, 2012; Shi *et al.*, 2013; Kantarjian *et al.*, 2014; Pfizer, 2014). GI bleeding, a less frequent GI toxicity, can occur during treatment with some forms of TKIs. Dasatinib (Fullmer *et al.*, 2011; Kmira, 2013) and imatinib (Sener *et al.*, 2019) induce this adverse event at a frequency of about 4-14% and 5-8% in CML patients, respectively. Several case reports have also shown dasatinib can induce acute and haemorrhagic colitis at low incidence (Erkut *et al.*, 2010; Kmira, 2013; Eskazan *et al.*, 2014). Bosutinib-induced GI bleeding, however, is rare with very few cases reported in the literature (Khoury *et al.*, 2012).

Diarrhoea, on the other hand, is especially problematic for patients undergoing treatment with bosutinib: approximately 80% of CML patients receiving this third generation BCR-ABL inhibitor develop diarrhoea (Kantarjian *et al.*, 2014; Brümmendorf *et al.*, 2015), 10% of which experience grade 3-4 diarrhoea (See Table 1.3 for definitions of diarrhoea grades). Other BCR-ABL inhibitors also frequently induce diarrhoea but at a lower rate of both high (3-4) and low (1-2) grade toxicities. For example, approximately 20% of dasatinib- and imatinib-treated

CML patients experience diarrhoea, and very few cases of grade 3-4 toxicities are reported ($\leq 3\%$) (Fullmer *et al.*, 2011; Cohen *et al.*, 2012) (See Table 1.4).

Table 1.3. Definitions of grades 1 to 5 diarrhoea. Diarrhoea grades as defined by the Common Terminology Criteria for Adverse Events (CTCAE) v 5.0, of the National Cancer Institute (www.ctep.cancer.gov/protocolDevelopment/electronic_applications/docs). Abbreviations: ADL, Activities of daily living. Instrumental ADL refer to preparing meals, shopping for groceries or clothes, using the telephone, managing money, etc. Self-care ADL refer to bathing, dressing and undressing, feeding self, using the toilet, taking medications, and not bedridden.

Grade 1	Increase of <4 stools per day over baseline; mild increase in ostomy output compared to baseline
Grade 2	Increase of 4-6 stools per day over baseline; moderate increase in ostomy output compared to baseline; limiting instrumental ADL
Grade 3	Increase of >6 stools per day over baseline; hospitalization indicated; severe increase in ostomy output compared to baseline; limiting self-care ADL
Grade 4	Life-threatening consequences; urgent intervention indicated
Grade 5	Death

The median time to event of bosutinib-induced diarrhoea in CML patients receiving the standard dose of 500mg per day is 3 days (Pfizer, 2014; Brümmendorf *et al.*, 2015). This is a relatively rapid onset compared to other TKIs; imatinib induces diarrhoea after a median of 43 days (Brümmendorf *et al.*, 2015) and the EGFR inhibitor erlotinib given to NSCLC patients has a median diarrhoea onset of 12-32 days (Rugo *et al.*, 2019). The time to event for diarrhoea induced by dasatinib and gefitinib (the EGFR inhibitor used in this project) is not reported in the literature.

Bosutinib-induced diarrhoea has a median duration of 1-3 days when patients receive antidiarrhoeal medication and undergo dose reduction or interruption as required (Pfizer, 2014; Brümmendorf *et al.*, 2015; Khoury *et al.*, 2018). CML patients undergoing treatment with imatinib, at 400mg daily, have a median diarrhoea duration of 5.5 days (Brümmendorf *et al.*, 2015). Whilst this time period is longer than that of bosutinib-induced diarrhoea, imatinib-induced diarrhoea is typically lower grade and lower incidence (Table 1.4). It is important to note that the median duration of an adverse event is defined as the “start to stop of event with no grade change (any change in grade represents a ‘new event’)” (Khoury *et al.*, 2018); therefore, the total time patients experienced diarrhoea, especially patients with high grade toxicity, will most likely have been higher than the numbers stated here.

Table 1.4. Diarrhoea incidences, onset and duration of clinically used EGFR and BCR-ABL inhibitors. *50% was seen in patients with GIST and was lower in patients with CML		
Drug (references)	Diarrhoea incidence, % (grade)	Diarrhoea onset and duration in days, median (range)
Imatinib (Kantarjian <i>et al.</i> , 2010; Cohen <i>et al.</i> , 2012; Brümmendorf <i>et al.</i> , 2015)	17-50* (all grades) 1-2 (grades 3-4)	Onset: 43 (range not reported) Duration: 5.5 (range not reported)
Dasatinib (Kantarjian <i>et al.</i> , 2010; Fullmer <i>et al.</i> , 2011)	17-20 (all grades) 3 (grades 3-4)	Onset: Not reported Duration: Not reported
Bosutinib (Keller <i>et al.</i> , 2009; Pfizer, 2014; Brümmendorf <i>et al.</i> , 2015)	70-90 (all grades) 10 (grade 3-4)	Onset: 3 (1-210) Duration: 1-3 (1-413)
Gefitinib (Shi <i>et al.</i> , 2013)	28 (all grades) 2 (grade 3-4)	Onset: Not reported Duration: Not reported

1.2.1 Implications of lower gastrointestinal toxicity

Chemotherapy-induced lower GI toxicity has negative consequences for patients. In addition to negatively impacting patient quality of life, this toxicity can be dose-limiting requiring dose reduction or interruption, resulting in decreased treatment efficacy. Moreover, patient compliance in taking oral medication can decrease if the patient experiences GI adverse events, thus further decreasing drug efficacy. In some cases, the treatment is discontinued, as has been seen in patients treated with both BCR-ABL and EGFR inhibitors (Messersmith *et al.*, 2004; Czito *et al.*, 2006; Kantarjian *et al.*, 2014; Brümmendorf *et al.*, 2015). This is especially problematic for patients undergoing bosutinib treatment, as diarrhoea leads to bosutinib discontinuation, dose interruption and reduction in 1-3%, 14% and 5-6% of patients with diarrhoea, respectively (Cortes *et al.*, 2010; Kantarjian *et al.*, 2014). Moreover, bosutinib is a third-generation inhibitor given to patients with resistance or intolerance to other BCR-ABL inhibitors such as imatinib and dasatinib; therefore, bosutinib withdrawal can have serious clinical implications, due to a lack of alternative treatments for the patient.

Patients with grade 3 or 4 diarrhoea – approximately 1 in 10 bosutinib treated patients (Kantarjian *et al.*, 2014) – frequently require hospitalization. The economic cost and required beds associated with treating this adverse reaction, strain the already tight budget of the

NHS. Furthermore, additional diarrhoea-associated complications can develop, such as hypokalemia (Agarwal *et al.*, 1994). Medications used to treat diarrhoea, such as loperamide (a μ -opioid receptor agonist which slows gut transit), do not target the mechanism of chemotherapy-induced toxicity. Consequently, anti-diarrhoeal treatment can be insufficient for high grade toxicity (Cortes *et al.*, 2010), and the increased probability of complications may not be abrogated. Moreover, anti-diarrhoeal medications have adverse effects themselves: loperamide can induce nausea, vomiting, presyncope and abdominal pain (Markland *et al.*, 2015).

Chemotherapy-induced lower GI toxicity also has a negative impact within the pharmaceutical industry, at both the pre- and post-marketing stages. It is a bottleneck in the pharmaceutical research and development pipeline contributing to drug attrition (Cook *et al.*, 2014). GI toxicity is the second most common cause of drug withdrawal from phase I clinical trials, and the prevailing cause in phase III (Redfern *et al.*, 2010). This has a huge negative economic impact on drug development due to the high investment required to perform clinical trials.

1.2.2 The importance of understanding drug-induced gastrointestinal toxicity

By understanding the mechanisms of GI toxicity, we can make progress to abrogate the related issues discussed above. For example a greater understanding at the molecular and cellular level would allow more reliable *in vitro* pre-clinical predictions of GI toxicity, which is currently hindered by the species differences in sensitivity to GI toxicity (Olson *et al.*, 2000). The development of better *in vitro* models, akin to hERG screening in cardiotoxicity (Cook *et al.*, 2014), could allow high throughput analysis of chemical compounds for gut toxicity instead of the currently laborious process of histopathology. To our knowledge there is no literature documenting the use of *in vitro* gut models as accurate screening tools (Carr *et al.*, 2017).

A more comprehensive understanding of the mechanism would also encourage targeted pharmacogenomic studies to identify alleles associated with this toxicity. Candidate gene studies have already identified genetic variants associated with chemotherapy-induced diarrhoea. For example, patients with UDP-glucuronosyltransferase 1-1*28 (*UGT1A1**28) have a greater risk of developing intestinal toxicity after administration of irinotecan (Iyer *et al.*, 2002), whilst rs7699188 and rs2231142 – single-nucleotide polymorphisms (SNPs) within ATP-binding cassette sub-family G member 2 (*ABCG2*) – are associated with gefitinib-induced diarrhoea (Cusatis *et al.*, 2006; Lemos *et al.*, 2011). This research aids personalised medicine

by enabling stratification of patients at risk of grade 3 and 4 diarrhoea. Whilst, pharmacogenomic testing for GI adverse events is not widespread (Carr *et al.*, 2017), The Pharmaceuticals and Medical Devices Agency in Japan recommends pre-emptive testing for *UGT1A1*6* and *UGT1A1*28* before treatment with irinotecan (Etienne-Grimaldi *et al.*, 2015) to identify patients requiring dose reduction or alternative medication, due to high risk of high grade ADRs including diarrhoea.

1.3 Physiology of the gastrointestinal tract

To understand the potential pathomechanistic basis of TKI-induced lower GI toxicity, it is necessary to first review the functioning of the lower GI system under normal conditions. The main roles of the GI system are digestion, absorption and elimination. The small intestine – which is comprised of the duodenum, jejunum and ileum (from proximal to distal) – are involved in digestion as well as water, nutrient and vitamin absorption. The large intestine, which can be subdivided into four major sections – the caecum, colon (ascending, transverse, descending and sigmoid colon), rectum and anus – function to absorb remaining water, electrolytes and nutrients from indigestible material and eliminate waste. Uptake of short-chain fatty acids produced by bacterial fermentation of dietary fibres, and vitamins synthesized by bacteria, such as B vitamins, also occurs within the large intestine (Keshav *et al.*, 2013).

1.3.1 Layers of the intestinal walls

The anatomical layers and structure of the small and large intestinal walls are very similar (Keshav *et al.*, 2013). Both are comprised of the serosa/aventitia, the muscularis externa, the submucosa and the mucosa, all of which are discussed in further detail below. See Fig 1.4 for a schematic of the layers of the intestines.

The outermost layer of organs within the peritoneal cavity, including the duodenal bulb, ileum, jejunum, transverse colon and sigmoidal colon, is the serosa. This double membrane of mesothelial cells and connective tissue lines the body cavity and organs. Mesothelial cells secrete serous fluid, which functions to decrease friction between organs during muscle contraction. The outermost layer of organs outside the peritoneal cavity, specifically the duodenum, the ascending colon and descending colon, is the adventitia; a loose connective tissue which anchors organs to the body cavity.

The outermost layer is bound to the muscularis externa, which contains a longitudinal and circular muscle layer as well as the myenteric plexus, the main GI nerve supply which controls

gut motility. The muscularis externa enable the peristalsis contractions responsible for gut transit. However, it is interesting to note that within the large intestine, three separate bands of longitudinal muscle fibres (together called the taenia coli) are also present *outside* the serosa which undergo tonic contractions to produce the haustra (segmented pouches) unique to the large intestine.

Above the muscularis externa is the submucosa, which also contains a neural network (the submucosal plexus) and connects the muscular layer to the inner most layer, termed the mucosa. Within the mucosa, the outer-most layer is a thin muscle layer which enables local mucosal movement termed the muscularis mucosae. Above the muscularis mucosae is the lamina propria. Comprised of loose connective tissue, this immune and stromal cell-rich layer contains vascular tissue which supplies the outer epithelium lining with nutrients, and lymphoid tissue involved in immune regulation (Keshav *et al.*, 2013).

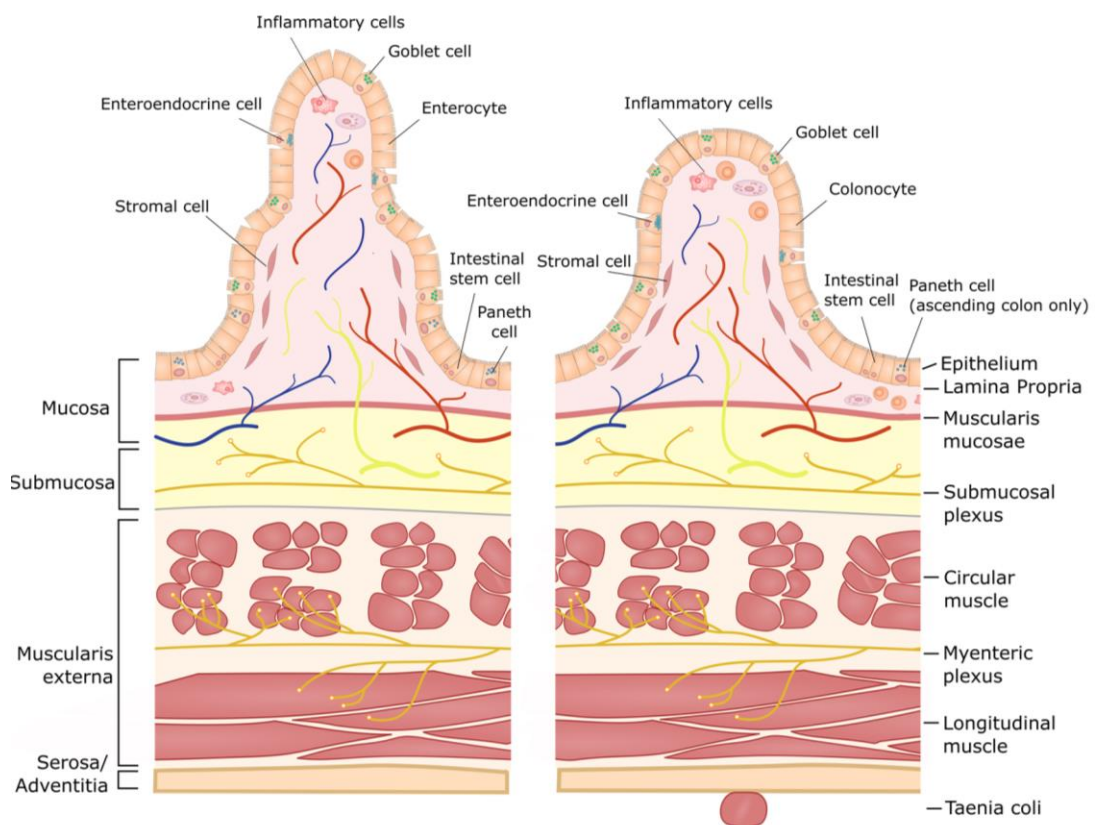


Figure 1.4. Anatomical layers of the small and large intestines. Schematic of the structure of the small (left) and large (right) intestinal layers, and the cell types of the intestinal epithelial layer. Blue and red lines represent blood vessels, whilst yellow lines represent lymphatic vessels. Information on anatomical layers and cell types obtained from Keshav *et al.* (2013) and Peterson *et al.* (2014), respectively. Diagram produced in Inkscape by S. French.

Within the lamina propria, there are regional differences which reflect functioning. For example, the duodenum, which is the first segment of the small intestine, contains Brunner's glands to produce alkaline secretions to neutralize stomach acid; the ileum contain lymphoid nodules called Peyer's patches which are involved in immune regulation and surveillance; and the jejunum contains neither Peyer's patches nor Brunner's glands (Keshav *et al.*, 2013). Surface mucus-secreting cells and specialised goblet cells within the epithelium, which secrete mucus onto the luminal side of the outermost epithelial layer, are also often present. This outer lining is a single-cell epithelial barrier which, in the small intestine is folded to form villi and crypts, and crypts only in the colon.

1.3.2 The epithelial cell layer

Within both the small and large intestines, the inner-most epithelial layer forms a selective barrier to prevent penetration of luminal contents containing toxins, microorganisms and certain antigens into the lamina propria, whilst enabling absorption of nutrients (Peterson *et al.*, 2014). This layer contains many different specialized cells (Fig 1.4) including enterocytes, goblet cells, enteroendocrine cells and Paneth cells, each with different (although sometimes overlapping) roles, formed from undifferentiated stem cells which reside at the crypt base.

1.3.2.1 Intestinal stem cells

Stem cells such as Leucine-rich repeat-containing G-protein coupled receptor 5 (Lgr5)-positive stem cells, differentiate into the cell types of intestinal epithelial layer as they migrate up along the villus axis and, in the majority of cases, are shed from the tip (Barker *et al.*, 2008). Shedding occurs at a rapid rate with the majority of epithelial cells being renewed approximately every four days. This high cell turnover rate accounts for the high sensitivity of the lower GI tract to toxicity during treatment with non-targeted chemotherapies such as irinotecan and 5-fluorouracil (5-FU), which target dividing cells rather than proteins specific to cancer growth and survival (Wardill *et al.*, 2013).

1.3.2.2 Enterocytes

Enterocytes, the most abundant cell type formed from small intestinal stem cells, are involved in absorption and secretion in the small intestines. The major absorptive cell type present in the colon, however, is the columnar colonocyte. The microvilli present on both cell types provide an increased surface area for their function. Recent studies have shown these cells also have an important role in immune defence such as the production of anti-microbial peptides (Peterson *et al.*, 2014).

1.3.2.3 *Enteroendocrine cells*

The less frequent but equally widespread enteroendocrine cells are mainly involved in the normal functioning of the GI tract by controlling processes such as bile secretion, enzyme release and satiety (Gunawardene *et al.*, 2011). They can be subdivided based on their hormone and peptide secretion. For example, enterochromaffin (EC) cells – which can also act as neuroendocrine cells – release the inflammatory mediators serotonin and histamine; whilst I-cells in the proximal small intestine secrete cholecystokinin to control satiety and inhibit gastric emptying. Other enteroendocrine cells in the intestines are D-, S-, K-, L- and N-cells, and each has a unique intestinal distribution and secretory peptide profile (Gunawardene *et al.*, 2011).

1.3.2.4 *Paneth cells*

Another major intestinal cell class is the Paneth cell. These innate immune cells, present in the small intestine and in low number in the ascending colon, are responsible for the release of anti-microbial peptides, such as the enzyme lysozyme and defensins, in response to bacterial activation of their toll-like receptors (Peterson *et al.*, 2014). Being located within close proximity to the intestinal stem cells, they also secrete factors that aid stem cell maintenance. They differ from the other principle cells of the intestines due to their migration downwards to the crypt base, as opposed to upwards towards the villus tip. Consequently, these Paneth cells have a longer cellular half-life than those destined for the villus.

1.3.2.5 *Goblet cells*

The final major cell type of the intestines, the goblet cell, also has a protective function, secreting mucus glycoproteins called mucins which form a protective barrier against bacteria. Within both the small and large intestine, the major mucus component secreted by goblet cells is mucin 2 (MUC2); a glycosylated gel-forming mucin which has high capacity to bind water (Johansson *et al.*, 2011). Within the small intestine, the combination of mucins, water, electrolytes and other components such as antibacterial proteins and IgAs, forms a single discontinuous mucus layer which limits bacterial contact with the epithelium. However, within the colon, a continuous double mucus layer is present. The dense inner layer prevents bacterial penetration, whilst the loose outer layer provides a habitat, and nutrients, for commensal bacteria. Goblet cells also secrete trefoil peptides such as trefoil factor 3 (TFF3) which stimulate epithelial repair following injury, and increases structural integrity of the mucus barrier (Peterson *et al.*, 2014).

1.3.3 The enteric nervous system

The digestive system is highly complex containing an enteric muscular system, nervous system, immune system, endocrine system and microbiota.

There are approximately 100 million neurons, specifically afferent neurones, interneurons and efferent neurones, in the gut which form the enteric nervous system (Grundy *et al.*, 2012). Alone they form complete neuronal circuits – exemplified by neuronal responses in isolated gut tissue – and can therefore be thought of as an independent branch of the autonomic nervous system. This neuronal topology enables local coordination of physiological gut functions, with neurones in the myenteric plexus controlling gut motility and those in the submucosal plexus aiding secretion, immune regulation and vaso-constriction/dilation (Grundy *et al.*, 2012).

In addition to functioning independently, the enteric nervous system is linked to the central nervous system via parasympathetic and sympathetic pathways. Vagal and spinal afferent fibres extend into the lamina propria allowing detection of stimuli in the mucosal layer. This allows cranial control of gut functions such as secretion, motility and immune responses so intestinal functions can be modulated depending on the needs of the entire organism. This autonomic innervation, more commonly known as the gut-brain axis, also allows intestinal signalling to the brain stem for GI perception, such as detection of visceral discomfort and nausea (Grundy *et al.*, 2012).

1.3.4 The enteroendocrine system

The enteroendocrine system is composed of the aforementioned enteroendocrine cells, which modulate an array of homeostatic functions through release of signalling molecules and hormones in response to changes in luminal contents. These hormones and peptides, secreted across the basolateral membrane, can act on nerves, nearby cells (paracrine signalling), or be released into the bloodstream (Latorre *et al.*, 2016).

The enteroendocrine system has a key role in controlling gut motility, through interactions with the enteric nervous system. For example, serotonin (5-hydroxytryptamine, 5-HT) released from enterochromaffin cells (and serotonergic neurons) can induce the peristaltic reflex and segmentation through activation of motor neurones. The enteroendocrine system also regulates the enteric immune system, through paracrine secretions which effect nearby immune cells. Moreover, enteroendocrine cells can control digestion and satiety, through release of peptides and molecules which control these processes. For example, glucagon like

peptide-1 and 2 (GLP1 and GLP2) and polypeptide YY (PYY), which are released from L cells in response to carbohydrate and fats, promote satiety and food aversion, delay gut motility to increase time for nutrient absorption and aid regulation of postprandial glucose levels (Latorre *et al.*, 2016).

The enteric nervous system is intertwined with the enteroendocrine (hormonal) system and the interaction between these two systems is often referred to as the enteric neuroendocrine system (Keshav *et al.*, 2013). The secretion of hormones from enteroendocrine cells can stimulate chemoreceptors on afferent nerves which extend into the lamina propria, and release of neurotransmitters from secretomotor neurones can activate enteroendocrine cells. This results in an overlapping signalling network with many complex feedback loops. A good example of this complexity is signalling initiated by serotonin. 5-HT is present in both enteroendocrine (enterochromaffin) cells and serotonergic neurones and can act as both an endocrine hormone and a neurotransmitter, regulating an array of functions including GI motility, inflammation, secretion and vasodilation (Mawe *et al.*, 2013)..

1.3.5 The enteric immune system

The enteric immune system is located mainly in the mucosa and can be divided into the innate (non-specific) and adaptive immune system (Keshav *et al.*, 2013). The physical barriers (such as mucin secreted by goblet cells) and chemical barriers (including detergent bile acid) as well as Paneth cells, mast cells, eosinophils, neutrophils, macrophages and dendritic cells comprise the innate immune system. The more complex adaptive immune system is composed of gut lymphocytes (B and T cells), which are distinct from blood lymphocytes, and are present in the lamina propria and aggregated lymphoid nodules.

Within the small intestine, specifically the ileum, Peyer's patches are present – aggregated lymphoid nodules overlaid with a specialized follicle-associated epithelium, which contain a reduced number of goblet cell and enterocytes (Miller *et al.*, 2007). Microfold (M)-cells make up 5-10% of the follicle-associated epithelium in humans. These cells contain basolateral membrane invaginations in which antigen-presenting cells, such as dendritic cells, reside. M-cells sample and transcytose luminal antigens and microorganisms from the GI lumen, presenting them to the underlying immune cells. These activated immune cells migrate to nearby lymphoid nodules where they initiate the production and expansion of plasma cells, which release secretory IgAs. Equivalent structures to Peyer's patches are present in the large intestine, termed caecal patches in the ileocaecal valve and colonic patches in the colon and rectum (Mowat *et al.*, 2014).

Under normal physiological conditions, the immune system acts to identify and counter pathogens; however, over-activity of the immune response can result in inflammation which may lead to diarrhoea (see 1.4.4 Inflammation and ER stress).

1.3.6 The muscular system

The two main intestinal muscular layers are comprised of smooth muscle subunits connected by gap junctions which allow electrical impulses to travel between cells during contraction (Grundy *et al.*, 2012; Spencer *et al.*, 2016). Contraction does not require external input as gut pacemaker cells, called the interstitial cells of Cajal, generate slow wave potentials which spread across the muscle. Contraction and relaxation of longitudinal and circular muscles generate two types of intestinal motility: a) peristalsis, which functions to propel gut contents along the intestines; and b) segmentation, which allows mixing of the luminal contents with intestinal secretions (Keshav *et al.*, 2013). These processes are modulated extrinsically by the central nervous system and intrinsically by the enteric nervous, enteroendocrine and immune systems. For example, excitatory enteric motor neurones, which originate from the myenteric plexus and innervate the circular and longitudinal muscle layers, initiate contraction by releasing acetylcholine and tachykinins such as substance P and neurokinin A. Inhibitory motor neurones oppose the action of excitatory neurones, and induce relaxation, through release of several neurotransmitters including nitric oxide and vasoactive intestinal polypeptide. Distension induced by food passing along the intestine leads to caudad relaxation in front of the bolus of food and orad contraction behind, aiding propulsion along the GI tract towards the distal end (Grundy *et al.*, 2012). Drugs which result in increased intestinal motility, through modulation of the aforementioned processes can lead to diarrhoea (See 1.4.3 Dysmotility).

1.3.7 The gut microbiota

The intestines contains an estimated 10^{13-14} mutualistic bacteria (Johansson *et al.*, 2011; Jandhyala *et al.*, 2015). With a few exceptions, the number of bacteria increases along the intestinal tract from approximately 500/ml in the stomach, 10^5 /ml in the proximal small intestine to 10^{9-12} /ml in the colon (Mowat *et al.*, 2014). The majority of species are obligate anaerobes, however, aerobic species are present in the upper small intestine, and a total of 500-1000 different intestinal bacterial species exist. The four major phyla of these species are *Bacteroidetes*, *Firmicutes*, *Proteobacteria* and *Actinobacteria*, with the former two representing 90% of the intestinal microbiome (Rinninella *et al.*, 2019).

This mutualistic microbiome is vital for the physiological functioning of the gut. It has an immunomodulatory role – for example, through regulating chemokine and IgA production and affecting gut-associated lymphoid tissue development – and helps exclude pathogenic bacteria (Jandhyala *et al.*, 2015). It also has a role in gut barrier maintenance, such as preserving tight junctions (TJs) during stress-induced damage (see section 1.4.2 Intestinal barrier dysfunction: the paracellular pathway). In addition, the microbiota is important in nutrient and xenobiotic metabolism. Bacteria use glycans present in mucus, and indigestible polysaccharides in food, as an energy source to produce vitamins (such as B vitamins and vitamin K) and short-chain fatty acids. Short-chain fatty acids, such as acetate and butyrate, can be taken up by the host, enabling partial recovery of energy used in mucus layer production (Johansson *et al.*, 2011).

Diarrhoea induced by cytotoxic chemotherapy-induced such as 5-FU and irinotecan is associated with marked changes in the intestinal microbiota in patients (Stringer *et al.*, 2013) and *in vivo* (Stringer *et al.*, 2007, 2009). For example, patients with chemotherapy-induced diarrhoea (chemotherapy regimes were capecitabine, cisplatin/5-FU, FOLFOX, 5-FU/folinic acid, carboplatin and gemcitabine) show decreased faecal *Firmicutes* (including *Lactobacillus* spp. and *Enterococcus* spp), *Bacteroidetes* (specifically *Bacteroides* spp.) and *Actinobacteria* (specifically *Bifidobacterium* spp.). It is likely that alterations in the microbiota contribute to the pathogenesis of diarrhoea; changes in the intestinal microbiome can result in immune dysfunction and increased stress responses (Jandhyala *et al.*, 2015). However, due to the lack of *in vitro* models incorporating the gut microbiome (Carr *et al.*, 2017), the specific mechanistic role of the gut microbiota in chemotherapy-induced diarrhoea remains poorly understood and as such was not investigated during this project.

1.4 Mechanisms of chemotherapy-induced lower gastrointestinal toxicity

Despite the wealth of research performed on a handful of drugs (primarily irinotecan, 5-FU and methotrexate) (Bowen *et al.*, 2007; Logan, 2008; Logan *et al.*, 2008, 2009; Melo *et al.*, 2008; Hamada *et al.*, 2010, 2013; Youmba *et al.*, 2012; Nakao *et al.*, 2012; Beutheu *et al.*, 2013; Sakai *et al.*, 2013; Soares *et al.*, 2013; Song *et al.*, 2013; Stringer *et al.*, 2013; Lima-Júnior *et al.*, 2014), a detailed mechanistic understanding of chemotherapy-induced lower GI toxicity is lacking for most chemotherapeutic agents. Fortunately, a detailed understanding of the GI tract, basic mechanistic knowledge of lower GI disorders (such as ulcerative colitis, Crohn's disease and irritable bowel syndrome), and previous studies of chemotherapy-

induced diarrhoea, enable us to hypothesize the potential processes involved in TKI-induced diarrhoea. These processes include secretion, intestinal barrier dysfunction, increased motility and inflammation. These processes are connected from a molecular level to a systems level, and this high level of overlap means lower GI toxicity is frequently multifactorial (Keshav *et al.*, 2013). However, for simplicity they will be discussed separately below. It is important to note that the examples of chemotherapy-induced diarrhoea mechanisms may be specific to the drug of interest and cannot be extrapolated to all forms of chemotherapy.

1.4.1 Secretion: the transcellular pathway

Until the late 1960s, the intestines were believed to have a purely digestive and absorptive role but cholera enterotoxin studies in the early 1970s showed the intestinal epithelium was capable of actively secreting electrolytes (Field *et al.*, 1972), a process later found to have functional importance. Under normal conditions, this secretion is tightly regulated by the transcellular pathway to allow fluid balance.

The transcellular pathway involves movement of ions between the lumen and underlying tissue through intestinal cells via channels, active transporters and co-transporters in both the apical and basolateral membranes (Field, 2003). The transcellular pathway varies spatially along the length of the intestine and along the crypt-villus axis, with secretion dominating in the undifferentiated crypt bases and nutrient absorption dominating as cells move up the crypts and differentiate. The main ions secreted via this pathway are chloride ions (Cl^-) and hydrogen carbonate ions (HCO_3^-), whilst sodium ions (Na^+) are more important in coupled uptake of sugars and amino acids (Keshav and Bailey, 2013) (Fig 1.5).

Cl^- secretion occurs through Cl^- channels such as the ATP-gated cystic fibrosis transmembrane regulator (CFTR), Ca^{2+} -dependent Cl^- channels (CaCC) and voltage-gated Cl^- channels (Matos *et al.*, 2007) (Fig 1.5C). Cl^- secretion is predominant in undifferentiated crypt cells, and functions to protect the stem cell niche by “flushing” crypts of potential toxins. Consistent with this, Na-K-Cl cotransporter 1 (NKCC1), a symporter involved in basolateral uptake of Cl^- , and CFTR are downregulated during differentiation (Barrett, 2018).

HCO_3^- secretion, in contrast to Cl^- secretion, has recently been shown to occur at similar levels in undifferentiated and differentiated intestinal cells, using an intestinal organoid model (see section 1.5.2.2. From 2-dimensional to 3-dimensional cultures) (Barrett, 2018). However, higher levels of the HCO_3^- producing enzyme, carbonic anhydrase, and the $\text{Cl}^-/\text{HCO}_3^-$

antiporters down regulated in adenoma (DRA), are seen in differentiated cells. HCO_3^- secretion does not occur by facilitated diffusion through channels as with Cl^- secretion but by co-transport via $\text{Cl}^-/\text{HCO}_3^-$ antiporters, such as the aforementioned DRA (Seidler, 2013) (Fig 1.5C). HCO_3^- levels are high in the proximal small intestine in order to neutralize stomach acid.

Sodium-glucose transport is prevalent in enterocytes, which are located in the villus region of the small intestine. Monosaccharides, glucose and galactose, enter cells across the brush border through symport with Na^+ through sodium/glucose co-transporter 1 (SGLT1), also known as solute carrier family 5 member 1 (SLC5A1), which is only expressed in mature enterocytes (Dyer *et al.*, 2002; Wright *et al.*, 2011). This uphill accumulation of hexoses at the brush border is followed by downhill transport of monosaccharides across the basolateral membrane into the bloodstream. Colonocytes, however, are predominantly involved in the transportation and metabolism of short-chain fatty acids (Kiela *et al.*, 2009; Dalile *et al.*, 2019) (Fig 1.5A). Short-chain fatty acids are transported across the apical membrane by H^+ -coupled and Na^+ -coupled transporters, monocarboxylate transporter 1 (MCT1) and sodium-dependent monocarboxylate transporters (SMCTs), respectively. Short-chain fatty acids not metabolized by colonocytes, pass across the basolateral membrane – for example through monocarboxylate transporter 4 (MCT4) – enter portal circulation and are oxidised by hepatocytes (Fig 1.5B).

Secretory diarrhoea occurs during excess net movement of ions into the intestinal lumen due to decreased absorption and/or increased secretion. The resulting decrease in luminal water, which can also occur due to nutrient malabsorption, causes water to flow by osmosis through the paracellular pathway (see section 1.4.2 Intestinal barrier dysfunction: the paracellular pathway) into the gut lumen, secondary to the flow of ions – a process known as ‘solute-solvent drag’ (Hammel *et al.*, 2005). This is seen in inflammatory bowel disease (IBD) (Gareau *et al.*, 2013), infectious diarrhoeas such as that induced by cholera (Field *et al.*, 1972), and during treatment of rats with irinotecan (Sakai *et al.*, 1997).

Excess Cl^- secretion has also been implicated in EGFR inhibitor-induced diarrhoea (Van Seville *et al.*, 2015), as several lines of evidence suggest epidermal growth factor (EGF) has a role in inhibiting Cl^- secretion. EGFR agonists EGF and TGF- α can inhibit secretagogue (such as carbachol or thapsigargin)-induced Cl^- transport in T84 human colonic epithelial cells (Uribe *et al.*, 1996; Chow *et al.*, 2007; McCole *et al.*, 2007), and EGF can inhibit carbachol-induced Cl^- secretion in mouse colon (McCole *et al.*, 2007).

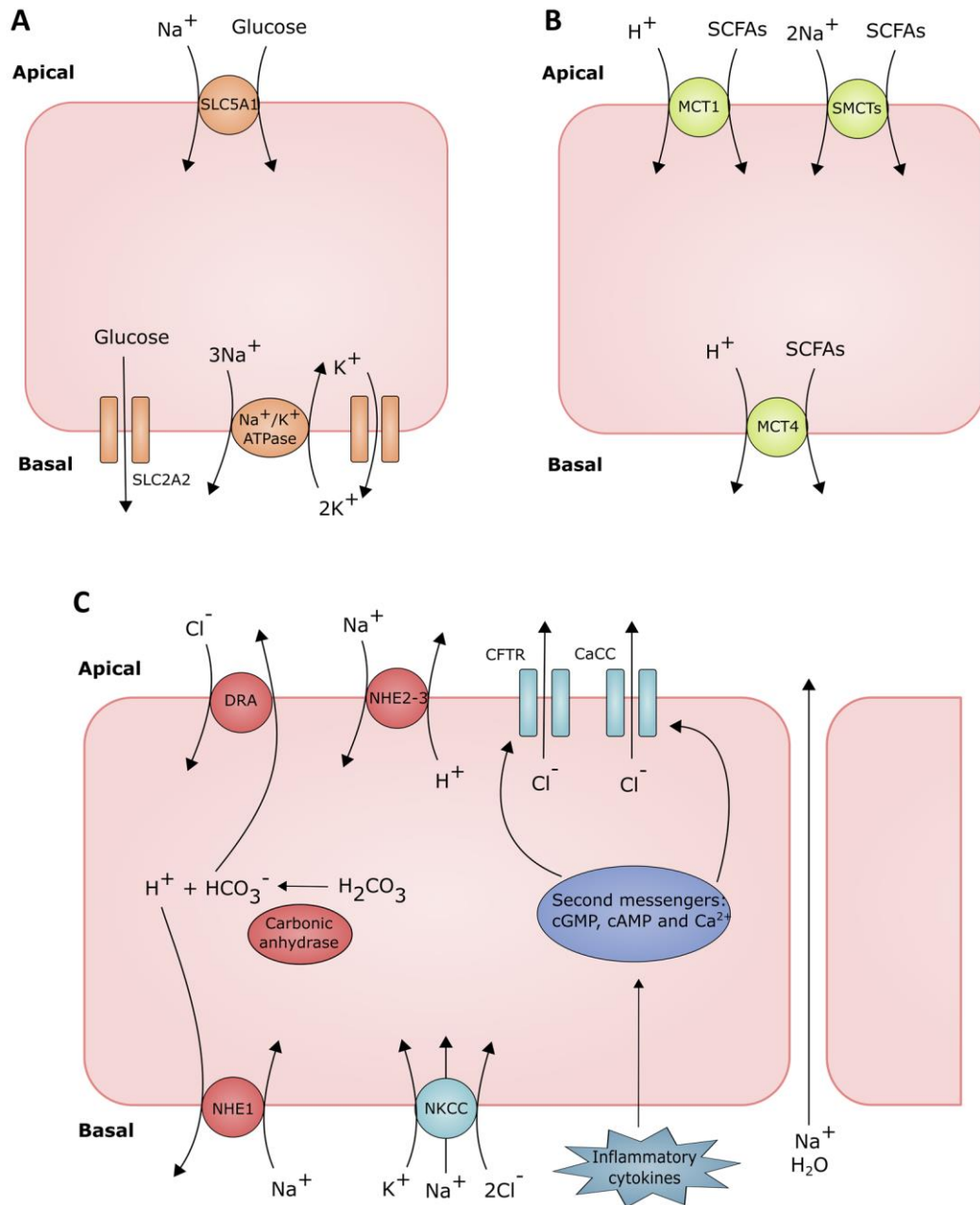


Figure 1.5. Transport of ions across the intestinal epithelium. Schematic of the transport processes involved in monosaccharide uptake in enterocytes (A, orange), short chain fatty acid uptake in colonocytes (B, yellow) and ion secretion in undifferentiated crypt cells (C). Secretion of HCO_3^- is shown in red, however, HCO_3^- secretion can also occur in differentiated enterocytes, and Cl^- secretion is shown in blue. Secondary messenger levels, controlled by an array of pathways including the inflammatory response, are involved in controlling transporter activity. Abbreviations: CaCC, Ca^{2+} -dependent Cl^- channels, CFTR, cystic fibrosis transmembrane regulator; DRA, down-regulated in adenoma; MCT1/4, monocarboxylate transporter 1/4; NHE1-3, sodium proton exchanger 1-3; NKCC, sodium-potassium-chloride cotransporter; SCFAs, short-chain fatty acids; SLC5A1, solute carrier family 5 member 1; SLC2A2, solute carrier family 2 member 2; SMCTs, sodium-coupled monocarboxylate transporter. Diagram produced in Inkscape by S. French.

Src is also involved in controlling chloride secretion. Interferon gamma (IFN- γ)-induced and H₂O₂-induced inhibition of Cl⁻ transport in human colon epithelial cells is mediated by Src (Uribe *et al.*, 2002; Chappell *et al.*, 2008) implying Src inhibition by bosutinib and dasatinib could lead to increased Cl⁻ secretion. However, unlike with EGFR inhibitors (Van Sebille *et al.*, 2015), Cl⁻ secretion has not been put forward as a mechanistic hypothesis for diarrhoea induced by Src inhibitors.

1.4.2 Intestinal barrier dysfunction: the paracellular pathway

The paracellular pathway also has a highly important role in regulating the passage of ions and fluids into the lumen; however, it differs from the transcellular pathway in that substances move between neighbouring cells (through the intercellular space rather than transcellularly). This movement is controlled by junctional complexes, or more specifically tight junctions (TJs) and adherens junctions (AJs), which interconnect cells of the epithelial layer. Each junction is a dynamic conglomerate of transmembrane and cytosolic proteins linked internally to the actin cytoskeleton and externally to junctional complexes on adjacent cells (Fig 1.6, Zihni *et al.*, 2016).

TJs are situated on the apical side of the cell and are believed to have a more prominent role in regulating paracellular permeability and barrier function than AJs. The main transmembrane components of TJs are the tetraspan claudin family proteins (which is made up of 24 isoforms) and MARVEL domain proteins (consisting of occludin, MARVELD3 and tricellulin) (Zihni *et al.*, 2016). Unlike MARVEL domain proteins, most claudins are similar to traditional ion channels and have anion or cation selectivity, depending on the claudin isoform. However, some, such as claudin-1, have sealing properties which prevent the passage of ions. These paracellular TJ channels control the 'pore' pathway; a pathway regulating the flow of ions and small molecules. The second pathway, the 'leak' pathway – which augments paracellular movement of macromolecules – is controlled by MARVEL domain proteins (Liang *et al.*, 2014). The less well studied more basally-located AJs, which contain a single-pass transmembrane glycoprotein, E-cadherin, are involved in initiation of intercellular contact and TJ assembly (Zihni *et al.*, 2016).

Transmembrane proteins in TJs and AJs bind to adaptor proteins which link to the cytoskeleton and enable bilateral signalling to and from the TJ complexes. E-cadherin binds to adaptor proteins of the catenin class: the three dominant forms are p120-catenin, α -catenin and β -catenin. However, the most common adaptor protein is zonula occludens 1 (ZO-1), which is present in both TJs and AJs (Stevenson *et al.*, 1986). ZO-1 and other adaptor

proteins modulate an array of cellular processes such as differentiation and initiation of the stress response, through transcriptional and post-transcriptional regulation. Conversely, adaptor proteins enable information to be transmitted from intracellular compartments to TJs and AJs allowing cellular control of permeability and cell adhesion (Zihni *et al.*, 2016).

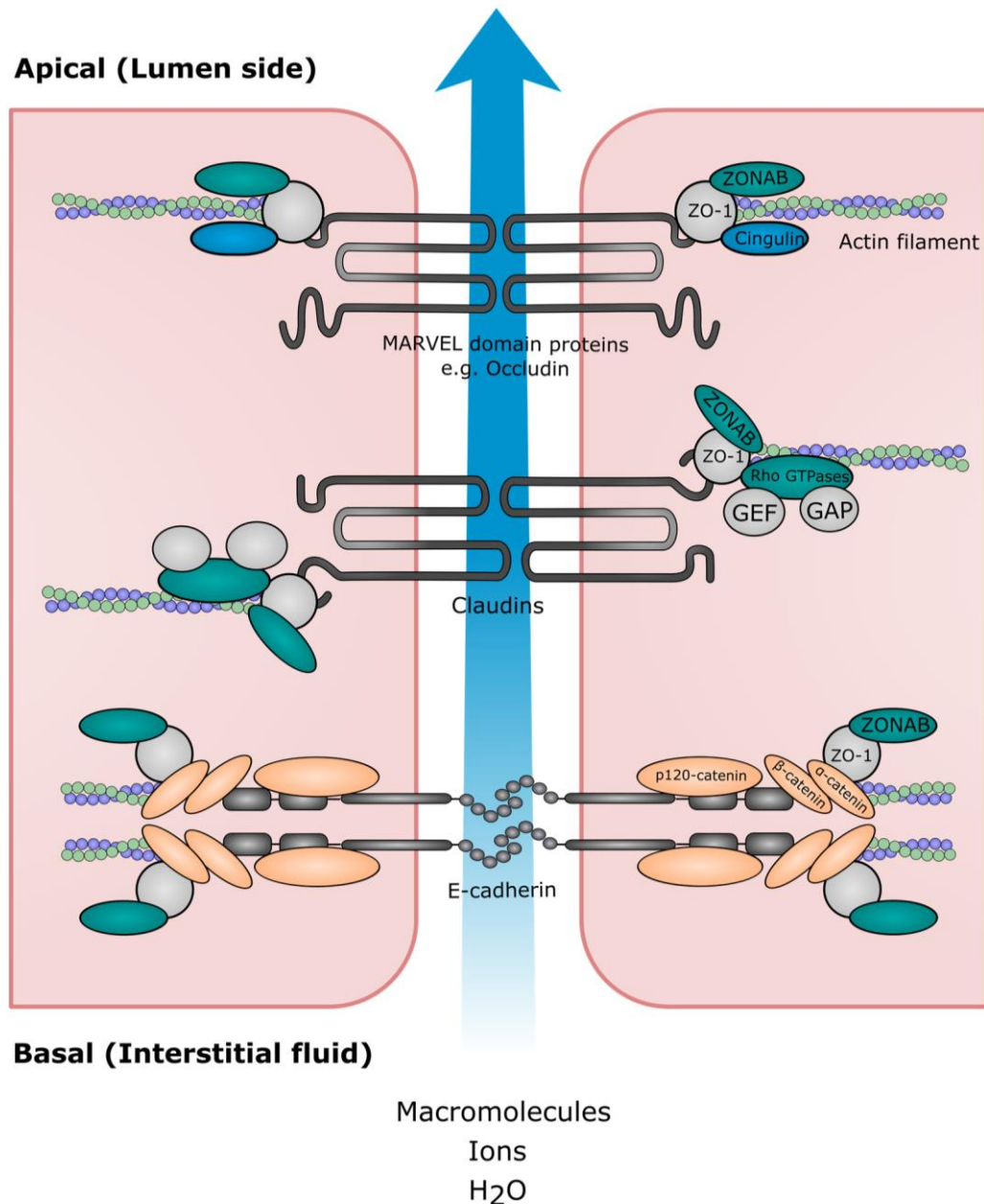


Figure 1.6. Proteins of tight junctions (TJs) and adherens junctions (AJs). Simplified schematic of the interconnected cytosolic and transmembrane proteins found at TJs and AJs. Abbreviations: GAP, GTPase-activating protein; GEF, guanine nucleotide exchange factor; MARVEL, myelin and lymphocyte (MAL) and related proteins for vesicle trafficking and membrane link; ZO-1, zonula occludens 1; ZONAB, ZO-1-associated nucleic acid binding protein. Diagram produced in Inkscape by S. French

Despite the comprehensive protein ultrastructure of TJs and AJs, detailed knowledge of the pathophysiological regulation of these junctions during disruption is lacking, partly due to the vast array of proteins within TJ and AJ complexes (Adachi *et al.*, 2006; Zihni *et al.*, 2016). However, TJ and AJ dysregulation is a well-documented process in the pathogenesis of diarrhoea.

When these junction proteins are disrupted, intestinal permeability increases and hydrostatic pressure from blood vessels and the lymphatic system forces fluids into the lumen resulting in diarrhoea (Field, 2003). This decreased barrier integrity can also lead to bacterial translocation further exacerbating the diarrhoea adverse event, as reported *in vivo* during methotrexate treatment (Song *et al.*, 2006).

TJ and AJ dysregulation has been shown to be induced by both conventional chemotherapy – such as the topoisomerase inhibitor irinotecan (Nakao *et al.*, 2012), the anti-folate drug methotrexate (Hamada *et al.*, 2010, 2013; Youmba *et al.*, 2012; Beutheu *et al.*, 2013) – and targeted chemotherapy such as EGFR inhibitors (Fan *et al.*, 2014) (Table 1.5). Caco-2 cells and rats treated with methotrexate showed decreased occludin and ZO-1 expression and redistribution of these proteins away from the plasma membrane, which is consistent with increased permeability through the ‘leak’ pathway (Hamada *et al.*, 2010; Youmba *et al.*, 2012; Beutheu *et al.*, 2013). Beutheu *et al.* also showed methotrexate can increase permeation through the ‘pore’ pathway in Caco-2 cells. This decrease in intestinal resistance also occurs in rats treated with irinotecan (Nakao *et al.*, 2012). Similar findings have also been shown for 5-FU which decreases the number of intercellular junctions and levels of AJ proteins in human colorectal cancer cell lines and mice (Song *et al.*, 2013; Buhrmann *et al.*, 2015; Tao *et al.*, 2015). The EGFR inhibitor erlotinib reduces junction protein levels and increases paracellular permeability in rat IEC-6 cells and mice (Fan *et al.*, 2014). TJ and AJ degradation during gefitinib treatment has also been shown in IEC-6 cells, but changes in permeability and translatability into a rodent model has not been assessed (Hong *et al.*, 2014). Finally, an increase in intestinal permeability is seen in patients treated with gefitinib (Melichar, Dvořák, *et al.*, 2010), 5-FU (Daniele *et al.*, 2001) and high-dose methotrexate (Meng *et al.*, 2016). However, these studies did not assess TJs and AJs. Overall, these data suggest increased flux through both the ‘pore’ and ‘leak’ pathways, partially due to TJ degradation and decreased barrier integrity, may be a common process likely involved in the pathogenesis of certain forms of chemotherapy-induced diarrhoea.

Table 1.5. Alterations in TJ and AJ expression in lower GI toxicity. *In vitro* and *in vivo* studies showing alterations in protein levels of TJ and AJ proteins due to chemotherapy treatment. Only studies on rodent models or intestinal-derived cell lines are reported. Upwards, downwards and sideways arrows indicate an increase, decrease or no change in expression level, respectively. N/A denotes an area where no studies have been reported. NS denotes a non-significant change

Chemotherapy	Tight junction proteins		Adherens junction proteins		Present in tight junction and adherens junctions
	Claudins	Occludin	E-cadherin	Catenins	Zona occludens-1
Irinotecan (<i>Topoisomerase I inhibitor</i>)	↓ Claudin-1 in rat jejunum and colon (Nakao <i>et al.</i> , 2012)	↓ Rat jejunum and colon ^{NS} (Nakao <i>et al.</i> , 2012)	N/A	N/A	➔ Rat jejunum and colon (Nakao <i>et al.</i> , 2012)
Methotrexate (<i>Dihydrofolate reductase inhibitor</i>)	↓ Claudin-1 in rat jejunum (Youmba <i>et al.</i> , 2012) ➔ Claudin-1 in human Caco-2 (Youmba <i>et al.</i> , 2012) ↑ Claudin-2 in rat small intestine (Hamada <i>et al.</i> , 2013)	↓ Rat jejunum (Youmba <i>et al.</i> , 2012) ↓ Human Caco-2 (Youmba <i>et al.</i> , 2012) ↓ Rat small intestine (Hamada <i>et al.</i> , 2013)	N/A	N/A	➔ Rat jejunum (Youmba <i>et al.</i> , 2012) ↓ Human Caco-2 cell line (Youmba <i>et al.</i> , 2012; Beutheu <i>et al.</i> , 2013)
5-FU (<i>Thymidylate synthase inhibitor</i>)	↓ Claudin-1 in mouse small intestine (Song <i>et al.</i> , 2013) ↑ Claudin-2 in human HCT116 cell line (Buhrmann <i>et al.</i> , 2015)	↓ Mouse small intestine (Song <i>et al.</i> , 2013)	↓ Human HCT116 cell line (Buhrmann <i>et al.</i> , 2015)	↓ β-catenin in colorectal tumour mouse model (Tao <i>et al.</i> , 2015)	➔ Mouse small intestine (Song <i>et al.</i> , 2013)
Erlotinib (<i>EGFR inhibitor</i>)	N/A	N/A	↓ Rat intestinal tissue (Fan <i>et al.</i> , 2014) ↓ Rat IEC-6 cell line (Fan <i>et al.</i> , 2014)	N/A	➔ Rat IEC-6 cell line (Fan <i>et al.</i> , 2014)
Gefitinib (<i>EGFR inhibitor</i>)	N/A	N/A	↓ Rat IEC-6 cell line (Hong <i>et al.</i> , 2014)	N/A	↓ Rat IEC-6 cell line (Hong <i>et al.</i> , 2014)

1.4.3 Dysmotility

Dysmotility including increased intestinal transit, which can occur as a result of altered activity of the enteric or central neural pathways or enteroendocrine signalling (Mawe *et al.*, 2013; Spencer *et al.*, 2016), is another mechanism which can cause diarrhoea (McQuade *et al.*, 2016). Increased motility reduces the time for water reabsorption from luminal contents to occur.

However, few studies have assessed the effect of chemotherapy on intestinal motility, potentially due to the lack of *in vitro* models. However, *ex vivo* experiments on rodent models have shown that 5-FU and irinotecan increase GI transit suggesting a role of dysmotility in certain forms of chemotherapy-induced diarrhoea (Soares *et al.*, 2008; Lima-Júnior *et al.*, 2014). 5-FU-treated mice displayed an exacerbation in carbachol-induced contractions of dissected duodenum smooth muscle (Soares *et al.*, 2008), whilst irinotecan-treated mice exhibit increased sensitivity to acetylcholine-induced duodenal segment contractions *ex vivo* (Lima-Júnior *et al.*, 2014). It has been suggested that irinotecan decreases intestinal transit time through modulation of acetylcholine signalling and the potassium voltage-gated channel subfamily KQT member 5 (KCNQ5) (Takahashi *et al.*, 2014). Diarrhoea predominant IBS (IBS-D) patients also display a rapid colon transit relative to healthy patients further confirming the pathogenic role of dysmotility in diarrhoea (Chey *et al.*, 2001).

1.4.4 Inflammation and ER stress

The generalised mechanism of cytotoxic chemotherapy-induced GI mucositis and high grade diarrhoea is believed to involve apoptosis and inflammation (Sonis *et al.*, 2004). The hypothesized 5-stage mechanism involves: 1) initiation by a cytotoxic agent causing an increase in reactive oxygen species (ROS); 2) ROS-induced cell death and gene upregulation including increased production of pro-inflammatory cytokines; 3) positive feedback leading to signal amplification damaging submucosa and basal epithelium; 4) inflammatory cell infiltration and bacterial colonisation; and 5) healing (Sonis *et al.*, 2004). This inflammatory cascade often causes shortening of villi and damages crypt architecture, thus reducing the surface area for reabsorption, decreasing mucosal integrity and causing excess mucous secretion. Aberrant cell death also contributes to inflammatory damage and reduces intestinal barrier integrity. Overall, this results in malabsorption of water and electrolytes leading to diarrhoea (Fig 1.7).

In line with this hypothesis, many diarrhoea-inducing chemotherapeutic agents have been shown to increase the expression of intestinal inflammatory cytokines *in vivo*. Treatment of

dark Agouti rats with irinotecan to induce mild to moderate diarrhoea results in increased intestinal tissue levels of nuclear factor kappa B (Nf-kb), tumour necrosis factor (Tnf), interleukin Il-1 β and Il-6 (Logan *et al.*, 2008). In Swiss mice, a cytokine production inhibitor diminished irinotecan-induced diarrhoea (Melo *et al.*, 2008), attenuated intestinal cytokine (Tnf- α and Il-1 β) upregulation and decreased histopathological damage (inflammatory cell infiltration, shortened villi and loss of crypt architecture). A similar finding was seen in *Il-18*^{-/-} mice (Lima-Júnior *et al.*, 2014). 5-FU has also been shown to induce inflammatory cytokine release of Tnf- α , Il- β , Il-6, Il-17a and Il-22, and cause histopathological damage in rodent models (Sakai *et al.*, 2013; Soares *et al.*, 2013).

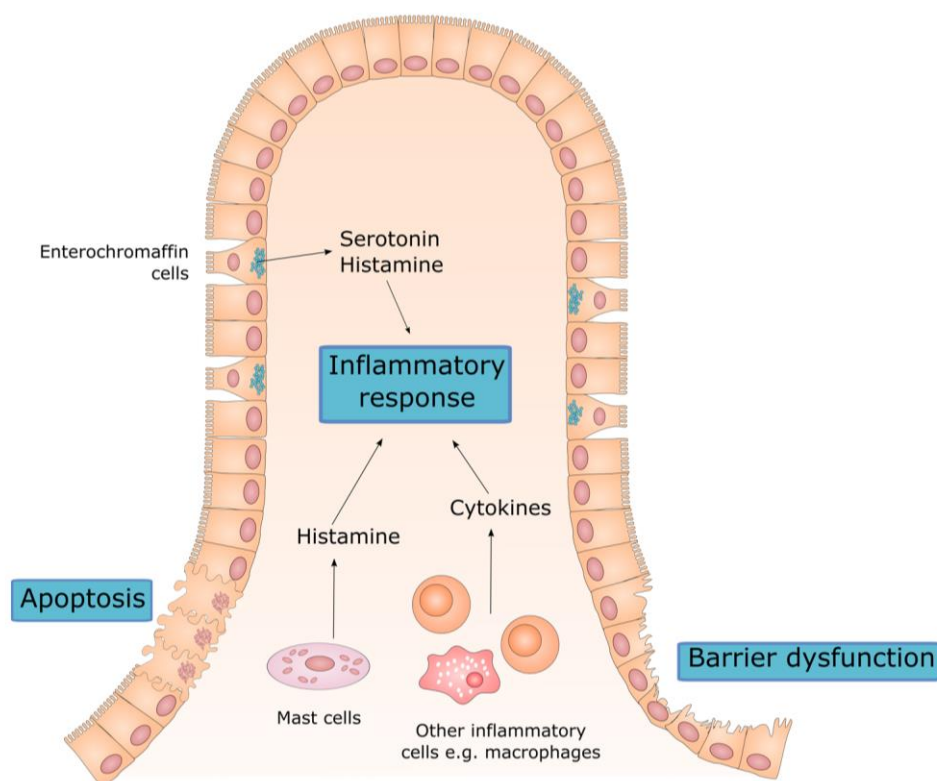


Figure 1.7. Inflammatory responses leading to diarrhoea. Simplified schematic of the key processes involved in inflammatory diarrhoea. Information for diagram obtained from Sonis *et al.* (2004). Diagram produced in Inkscape by S. French.

However, very few studies have assessed the effect of chemotherapy on inflammation in the context of chemotherapy-induced diarrhoea in humans. One study showed patients with chemotherapy-induced diarrhoea – including that induced by capecitabine, cisplatin and 5-FU – have increased (although not significant) blood serum levels of TNF- α post-treatment (Stringer *et al.*, 2013). Chemotherapy (type not stated) has also been shown to induce

intestinal apoptosis and crypt/villi damage in patients undergoing treatment (Keefe *et al.*, 2000).

Whilst an inflammatory response leading to damage and atrophy of the mucosa is highly plausible for cytotoxic chemotherapy, certain diarrhoea-inducing targeted therapies, such as the EGFR inhibitor lapatinib (Moy *et al.*, 2007), show no histological signs of intestinal epithelial damage (Van Sebille *et al.*, 2015). Lapatinib induces diarrhoea at a frequency of approximately 40% in patients with breast cancer, however it rarely causes high grade diarrhoea (Moy *et al.*, 2007). These data allow us to hypothesize that certain TKIs may induce low grade diarrhoea by a mechanism separate to inflammation, or a mechanism which involves a low level of localised acute inflammation insufficient to induce visible mucosal damage.

By contrast, certain EGFR inhibitors have been shown to induce endoplasmic reticulum (ER) stress which can contribute to GI inflammation (Fan *et al.*, 2014; Hong *et al.*, 2014). ER stress under normal physiological conditions is prevented by the unfolded-protein response (UPR) (Shkoda *et al.*, 2007; Kaser *et al.*, 2008). The UPR is a signalling cascade responsible for maintaining correct protein-folding (Cao, 2015); through refolding or degradation of misfolded proteins in the ER. Under environmental perturbations, the UPR machinery can become over-loaded and misfolded proteins accumulate in the ER resulting in the initiation of the ER stress signalling pathway, which can induce cell death and inflammation (Hetz, 2012). Intestinal epithelial cells have high rates of protein synthesis making them particularly sensitive to ER stress-induced damage (Cao, 2015).

Studies have shown dysregulation of the UPR pathway impairs intestinal epithelial barrier function. Polymorphisms in UPR genes are linked with IBD (Barrett *et al.*, 2008; McGovern *et al.*, 2010), ER stress markers are upregulated in IBD (Hu *et al.*, 2007; Shkoda *et al.*, 2007), and knock-out studies in mice with dextran sodium sulphate (DSS)-induced colitis demonstrate a causal role of ER stress in its pathogenesis (Bertolotti *et al.*, 2001; Kaser *et al.*, 2008). ER stress has also been directly implicated in drug-induced disruption of intestinal barrier integrity. Knock down of C/EBP Homologous Protein (CHOP), a master regulator of ER stress, in IEC-6 cells (a rat intestinal epithelial cell line) attenuates erlotinib-induced decrease in E-cadherin levels, increase in IL-6 secretion and apoptosis (Fan *et al.*, 2014). In addition, markers of ER stress, such as CHOP, are upregulated by diarrhoea-inducing chemotherapies including gefitinib (Hong *et al.*, 2014) and erlotinib (Fan *et al.*, 2014) in IEC-6 cells.

As stated previously, diarrhoeal mechanisms are highly interconnected, and inflammation is a good example of this interconnectivity. Pro-inflammatory cytokines – such as IL-1 β (Al-Sadi *et al.*, 2008), TNF- α (Ma *et al.*, 2004) and IFN γ (Bruewer *et al.*, 2003) – can disrupt tight junction integrity through downregulation and relocalisation of TJ proteins including ZO-1 in colorectal cancer cell lines, resulting in increased paracellular permeability and further disrupting intestinal integrity. Moreover, inflammation can increase sensitivity to dysmotility. *Il18*^{-/-} mice, or mice treated with an IL-18 inhibitor, show decreased sensitivity to irinotecan-induced duodenal contractility (Lima-Júnior *et al.*, 2014).

1.5 Models for studying gastrointestinal toxicity

1.5.1 *In vivo* and *ex vivo* models

Animal models are widely used in safety pharmacology as predictive models for human GI toxicity, and they can also be used to further mechanistic understanding. The majority of pathomechanistic research on chemotherapy-induced intestinal injury has been carried out on rodent models, mainly focussing on alterations in intestinal absorption, permeability and motility (Mao *et al.*, 1996; Southcott *et al.*, 2008; Nariya *et al.*, 2009; Dong *et al.*, 2014; Maioli *et al.*, 2014; Forsgård *et al.*, 2016; Carr *et al.*, 2017).

Relative to other forms of toxicity, GI toxicity shows high concordance (of around 80%) between animal studies and humans for an array of pharmaceuticals including anti-cancer agents (Greaves *et al.*, 2004). This suggests animal models have good translatability and observations made in animal studies may be applicable to humans.

1.5.1.1 *Rodent models*

Rodent models can be used to assess for indications of GI toxicity and this is often performed via the faecal pellet method (Marks *et al.*, 2013). Intestinal motility can be assessed by oral administration of solid transport markers (e.g. charcoal/barium sulphate) (Carr *et al.*, 2017) or *ex vivo* by measuring contractility of intestinal segments (Soares *et al.*, 2008; Lima-Júnior *et al.*, 2014). Changes in intestinal permeability can be assessed by oral administration of markers which can then be detected in the plasma (e.g. fluorescein isothiocyanate (FITC)-dextran (Dong *et al.*, 2014)) or urine (e.g. lactulose (Southcott *et al.*, 2008)). The lactulose-mannitol test is a common test which measures both changes in intestinal permeability and absorption. Changes in permeability can also be assessed *ex vivo*, for example, by measuring transmural resistance using an Ussing chamber (Dong *et al.*, 2014) or using the *in vitro* everted sac model to study FITC-dextran permeation (Maeda *et al.*, 2010). More standard

techniques such as immunohistochemistry, immunoblotting and PCR can also be carried out on intestinal tissue.

Mice (such as C57BL/6, BALB/c and Swiss mice) are generally considered a good model for GI toxicity, particularly involving intestinal inflammation, because their intestinal development, microbiome and immune response is comparable to that of humans (Jiminez *et al.*, 2015). Furthermore, genetically modified mice, such as knock-out mice, are readily available which aids mechanistic studies by enabling the roles of specific genes to be explored.

These factors – along with their small body size, short gestation period and relatively low husbandry costs – explain why mice are the most commonly used animal model in GI research. However, only relatively small tissue samples can be harvested from mice, and therefore rats are often used as an alternative model if tissue mass is a limiting factor in performing informative experiments.

Unlike mice, rat strains are often outbred – such as Wistar and Sprague-Dawley rats – leading to greater inter-experimental variability (Jiminez *et al.*, 2015), and fewer strains of genetically modified rats are available, further limiting the use of this model. However, an array of research into the mechanism of chemotherapy-induced diarrhoea has been carried out in rats, by studying permeability and histopathological changes (Mao *et al.*, 1996; Song *et al.*, 2006; Southcott *et al.*, 2008; Nariya *et al.*, 2009; Maeda *et al.*, 2010).

1.5.1.2 Non-rodent animal models

Pigs are a commonly used alternative to rodents due to similar intestinal physiology and morphology to humans (Jiminez *et al.*, 2015). However, their large size and much longer gestation period means studies on this species are much less frequent. Rabbits, guinea pigs, dogs, monkeys and the non-mammalian zebrafish model have also been studied, but to a lesser degree (Greaves *et al.*, 2004). It is not surprising that the majority of animals chosen for studying human intestinal toxicity and diseases have a monogastric anatomical structure akin to that in humans.

1.5.2 In vitro models

Very few *in vitro* GI models have been developed with the primary focus of toxicity. Current models are mainly utilized for oral drug absorption predictions (Antunes *et al.*, 2013; Li *et al.*, 2013; Huang *et al.*, 2014) and to increase understanding at a physiological (Sung *et al.*, 2011) and developmental level (Kim *et al.*, 2005; Spence *et al.*, 2011; Feng *et al.*, 2013; McCracken

et al., 2014). However, currently available models – detailed below – may be adapted for studying toxicity.

1.5.2.1 Cell types

Cells utilized for *in vitro* research can be broadly divided into primary cells and cell lines, and the latter subdivided into cancer cell lines and non-tumour-derived immortalized cell lines (Carr *et al.*, 2017). GI research has utilized an array of intestinal cell types, including enterocytes, intestinal stem cells, goblet cells and enterochromaffin cells (de Bruïne *et al.*, 1992; Sato *et al.*, 2009; Vázquez *et al.*, 2013). Embryonic and induced-pluripotent stem cells (iPSC) have also been employed, which can be differentiated into many of the cell types in the intestinal epithelial lining, each of which have their merits and constraints (Table 1.6).

Primary cells are derived directly from human or animal tissue and maintained *in vitro* as suspension cells, an explant culture or a monolayer. Primary cells have high physiological relevance due to genotypic and phenotypic similarity to *in vivo* cells, and therefore research performed on human primary cells has a higher probability of translatability to patients (Kauffman *et al.*, 2013). In addition, primary cells can be used to generate models genotypically linked to patients facilitating personalised medicine and aiding comprehension of toxicity stratification (Dekkers *et al.*, 2013). However, primary cells are infrequently used in preliminary research. This is partly due to difficulty in obtaining samples used to isolate epithelial cells, especially that of human primary intestinal tissue. Whilst, human primary cells are commercially available (Kauffman *et al.*, 2013), they are expensive, technically challenging to maintain (due to cell dedifferentiation, and an increased sensitivity to cell contamination) and have a limited life-span *in vitro* (Kaeffer, 2002).

Cell lines however are easily accessible, can be maintained to a high passage and are more durable. As the name suggests, cancer cell lines are derived from tumours. Non-tumour-derived immortalized cell lines are derived from healthy cells and induced to propagate indefinitely by transformation using viral oncogenes (Carr *et al.*, 2017). The homogeneous nature of single cell lines can be advantageous in terms of data reproducibility but – along with aneuploidy, DNA mutations and altered expression profiles in cancer cell lines (Hilgendorf *et al.*, 2007; Moon *et al.*, 2013; Vaessen *et al.*, 2017) – underlie the low translatability when modelling healthy tissue. Non-tumour-derived immortalized cell lines, however, exhibit greater similarity to primary cells but still display some cancer-like properties to allow continued growth. The majority of available intestinal non-tumour-derived cell lines and cancer cell lines are used to model enterocytes (Hu *et al.*, 2004;

Kauffman *et al.*, 2013; Carr *et al.*, 2017). Most intestinal non-tumour-derived cell lines are of epithelial origin (e.g. IEC-6 and FHs74Int cells) and the majority of intestinal cancer cell lines are from carcinomas (cancer developed from epithelial cells; e.g. HT29, and, the most commonly used, Caco-2) (Carr *et al.*, 2017). However, cell lines which model other cell types are also available such as those which model goblet cells (e.g. HT29-MTX cells) (Vázquez *et al.*, 2013) and enterochromaffin cells (e.g. NCI-H716) (de Bruïne *et al.*, 1992).

Table 1.6 Cells amenable for use as <i>in vitro</i> lower gastrointestinal models to study toxicity. Table detailing the merits and constraints of different cell types used in <i>in vitro</i> research.		
CELL TYPE	MERITS	CONSTRAINTS
<p>Cancer cell lines</p> <p>Colorectal adenocarcinoma cell lines (e.g. human Caco-2, HT-29, T84 (Kauffman <i>et al.</i>, 2013))</p> <p>Non-tumour-derived immortalised cell lines</p> <p>Intestinal epithelium-derived cells (e.g. rat IEC-6 (Hong <i>et al.</i>, 2014))</p>	<p>Easily accessible</p> <p>Can be maintained to a high passage</p> <p>Spontaneously differentiate</p>	<p>Long differentiation time period</p> <p>Unable to form gut-like geometries <i>de novo</i></p> <p>Poor translatability compared to primary cells</p> <p>Single cell type</p> <p>Unamenable to organoid generation</p>
<p>Primary intestinal epithelial cells (IEC)</p> <p>IECs isolated from patient samples or animal models (Kauffman <i>et al.</i>, 2013)</p>	<p>Greater biological relevance than cell lines</p> <p>Models can be genotypically linked to patients</p> <p>Formerly differentiated</p>	<p>Finite lifespan <i>in vitro</i></p> <p>Difficulty obtaining human primary intestinal epithelial cells</p> <p>Variability between subjects</p> <p>Unamenable to organoid generation</p>
<p>Induced pluripotent stem cell (iPSC)</p> <p>Patient-specific somatic cells can be reprogrammed to embryonic-like cells which are further manipulated forming induced intestinal models. iPSC lines are also available (Kauffman <i>et al.</i>, 2013)</p>	<p>Models can be genotypically linked to patients</p> <p>Potential to differentiate into many cell types</p> <p>Amenable to organoid generation</p>	<p>Organoids from iPSCs are a poor model of <i>adult</i> intestines.</p> <p>Organoids from iPSCs have slow formation</p>
<p>Embryonic stem cell (ESC)</p> <p>Primary ESCs can be collected from embryos and ESC lines are commercially available (Yamada <i>et al.</i>, 2002)</p>	<p>Mice embryonic stem cells grow rapidly</p> <p>Potential to differentiate into many cell types</p> <p>Amenable to organoid generation</p>	<p>Organoids from ESCs are a poor model of <i>adult</i> intestines</p>
<p>Intestinal stem cells</p> <p>Lgr5+ stem cells of the intestinal crypt can be extracted from rodents and patients (Sato <i>et al.</i>, 2009)</p>	<p>Models can be genotypically linked to patients</p> <p>Potential to differentiate into many cell types</p> <p>Amenable to organoid generation</p>	<p>Human adult intestinal stem cells grow slowly</p> <p>Difficulty obtaining human intestinal stem cells</p>

It is possible to culture two or more cell types together – a technique called co-culturing – to increase physiological relevance through increased cellular heterogeneity. Crosstalk between cells can aid in the generation of differentiated phenotypes. For example co-culturing HT29-MTX cells with intestinal epithelial cells enables a physiologically-relevant mucus layer to be amalgamated into the model (Vázquez *et al.*, 2013).

1.5.2.2 From 2-dimensional to 3-dimensional cultures

The simplest model of the intestines is that of a basic monolayer where adherent intestinal cells are cultured until they reach 100% confluency. Upon reaching confluency, cells undergo contact-dependent differentiation forming distinctive apical and basal cellular aspects (Kauffman *et al.*, 2013). Commonly utilised cells for this include Caco-2 (Seth *et al.*, 2004) and IEC-6 cells (Hong *et al.*, 2014).

Transwell models (2.3.5 Cell permeability assay, Fig 2.1) are slightly more complex than basic monolayers as they model both the environment above and below the intestinal epithelial layer (Kauffman *et al.*, 2013). Cells are seeded onto a porous membrane of a suspended insert by addition to the upper (apical) compartment of a transwell plate, which models the lumen. The cells form a monolayer imitating the intestinal lining and the transwell set-up permits access to the basolateral chamber – which represents the lamina propria (environment underlying the intestinal epithelial lining). In this way, transwells are good models for studying changes in permeability even when employed with cancer cell lines. They are amenable for use with cell lines such as Caco-2 cells (Carrasco-Pozo *et al.*, 2013; Fan *et al.*, 2014; Tong *et al.*, 2014), human primary intestinal epithelial cells (Kauffman *et al.*, 2013), human iPSC-derived intestinal cells (Kauffman *et al.*, 2013), and co-cultures (Pusch *et al.*, 2011; Antunes *et al.*, 2013; Li *et al.*, 2013). However, human primary intestinal epithelial cells and iPSC-derived intestinal cells have much greater paracellular permeability than *in vivo* limiting the translatability and physiological relevance of this model (Kauffman *et al.*, 2013).

The main use of transwells is predicting absorption of orally administered drugs (Artursson *et al.*, 2001; Pusch *et al.*, 2011; Antunes *et al.*, 2013; Li *et al.*, 2013; Moon *et al.*, 2013). However, increase in intestinal permeability – such as that measured by decreased transepithelial electrical resistance (TEER) or increased permeation of an apically administered macromolecule to the basolateral chamber – can be measured using a transwell (Beutheu *et al.*, 2013; Fan *et al.*, 2014). Increased paracellular permeability is an indicator of compromised barrier function, which can be the result of inflammation, cell death and/or cell junction disruption. Transwell models have been employed previously to

assess chemotherapy-induced changes in intestinal permeability (Fan *et al.*, 2014) exemplifying how this model is amenable for research at a mechanistic level.

With a few exceptions utilizing either co-culturing (Li *et al.*, 2013) or micro-scaffolds (Yu *et al.*, 2012), most transwell models lack 3-dimensional structures such as crypts. Scaffolds, which can be generated by 3D printing (Lee *et al.*, 2005), moulding (Wang *et al.*, 2009; Sung *et al.*, 2011) and bio-reactors (Yu *et al.*, 2014), manipulate the cellular micro-environment enabling generation of 3-dimensional models. Whilst these models exhibit greater physiologically relevant topology, they are still limited by lack of cell type heterogeneity; a problem being overcome by progressive research on organoids.

Organoids are organotypic cultures – often described as mini organs – derived from cells or organ explants (Fatehullah *et al.*, 2016). Intestinal organoids (called enteroids) form an enclosed ‘lumen’ with several intestinal crypts and villus-like projections (without the requirement of a micro-scaffold). Highly reminiscent of the *in vivo* structure, these enteroids contain all the major cell types of the intestinal epithelial layer including enterocytes, goblet cells, Paneth cells, enteroendocrine cells and Lgr5⁺-stem cells (Sato *et al.*, 2009). In this regard organoids represent an important bridge between *in vitro* and *in vivo* studies increasing translatability. Thus far enteroids have been developed from: 1) rodent (Yamada *et al.*, 2002) and human (Finkbeiner *et al.*, 2015) embryonic stem cell lines; 2) rodent (Sato *et al.*, 2009; Moon *et al.*, 2013), human (Sato *et al.*, 2011) and pig (Khalil *et al.*, 2016) intestinal stem cells; 3) rodent (Ueda *et al.*, 2010) and human (Spence *et al.*, 2011; Ayehunie *et al.*, 2013) iPSCs; and 4) rodent (Sato *et al.*, 2009) and human (Jung *et al.*, 2011) whole crypt preparations. The application of organoids in research so far have included determining efficacy and pharmacokinetic parameters of chemotherapeutic agents (Imura *et al.*, 2010), again with few experiments focussing on toxicity. However, assays have been developed to measure cell death (Grabinger *et al.*, 2014), chloride secretion (Dekkers *et al.*, 2013) and permeability (Leslie *et al.*, 2015) that can be utilized for mechanistic studies.

Another relatively new model is the ‘humans-on-a-chip’ micro-device which is the only *in vitro* model out of those discussed to take on a systems biology approach. In this model, cells (Imura *et al.*, 2010) or tissue slices (van Midwoud *et al.*, 2010) from different organs are compartmentalised and subjected to specific microenvironments that mimic dynamic *in vivo* conditions. For example, these micro-devices can incorporate fluid flow that mimics peristalsis. Applications of ‘humans-on-a-chip’ micro-devices with a microintestine component include determining pharmacokinetic parameters (Imura *et al.*, 2010; van

Midwood *et al.*, 2010) and ascertaining cytotoxicity of chemotherapeutics (Imura *et al.*, 2010). In this regard, the microintestine component is typically utilized to determine absorptive properties rather than focusing on the intestines as a target of toxicity.

1.5.3 Models utilized in this project

Preliminary research will be carried out on differentiated Caco-2 cell monolayers, a human colorectal adenocarcinoma cell line. This cell line is readily available in our laboratory and is routinely used in non-clinical studies by pharmaceutical companies. Several drug transporters – including those involved in import (OCT-1/SLC22A1) and export (ABCB1/MDR1 and ABCG2/BCRP) of BCR-ABL inhibitors (bosutinib, imatinib and dasatinib) and EGFR inhibitor (gefitinib) – are expressed at a similar level between Caco-2 cells and the human jejunum (Hilgendorf *et al.*, 2007; Brück *et al.*, 2017; Vaessen *et al.*, 2017).

Caco-2 cells model the intestinal epithelium; however, this model lacks an immune, nerve and muscular component; therefore, this project will mainly focus on diarrhoeal mechanisms involving the intestinal lining: changes in trans- and para-cellular permeability (due to cell death and/or cell-cell junction disruption). The main focus will be on the latter mechanism as it has been shown that chemotherapy TKIs, specifically nilotinib, erlotinib and gefitinib, induce barrier dysfunction in rat intestinal epithelial IEC-6 cells (Fan *et al.*, 2014; Hong *et al.*, 2014).

When employed in transwells, the Caco-2 model is recognised by the Food and Drug Administration (FDA) as a good model for determining absorptive ability, metabolism and efflux of drugs (Hu *et al.*, 2004). Although this project will not assess any of these pharmacokinetic parameters, it is not an unreasonable assumption – given the interconnectivity of intestinal absorption, permeability and barrier function – that Caco-2 transwell models represent a good model for studying intestinal permeability.

Where positive findings are observed in Caco-2 cells, similar experiments will be performed on an enteroid model developed from the proximal small intestine of BALB/c mice, as differentiated Caco-2 cells more closely resemble the small intestine than the colon (Hidalgo *et al.*, 1989). These enteroids will be developed from whole crypt preparations to enable relatively quick enteroid propagation (Sato *et al.*, 2009). As stated above, enteroids form a physiologically relevant 3D structure and have been shown to contain all the major cell types of the intestinal epithelium (Sato *et al.*, 2009) and in this regard, can be used to determine the translatability of results. Human enteroids would represent a more clinically relevant and

translatable model, however this is beyond the remit of this project due to lack of access to patient samples.

1.6 Aims and objectives of this project

This research project aims to investigate the mechanism of TKI-induced diarrhoea by performing *in vitro* assays on an intestinal epithelial cell model (Caco-2 cells) and an organoid model (BALB/c mouse enteroids). We also aim to determine genetic variants associated with dasatinib-induced diarrhoea through a genome-wide association study (GWAS). The primary focus of research will be on bosutinib as this TKI induces diarrhoea, a marker of lower GI toxicity, at higher incidence than other TKIs.

The sequential objectives are outlined below:

- 1. To determine the effect of TKIs on intestinal barrier integrity and cell viability in Caco-2 cells**
 - a. To assess the effect of TKIs on intestinal barrier integrity by measuring: 1) changes in paracellular permeability in a transwell set-up; and 2) changes in protein levels, gene expression and localization of TJ and AJ proteins
 - b. To perform cytotoxicity assays with TKIs

- 2. To determine the mechanism of TKI-induced changes in permeability in Caco-2 cells**
 - a. To assess the ability of TKIs to induce ER stress and cytokine release
 - b. To determine signalling pathways involved in barrier dysfunction through use of pathway inhibitor drugs

- 3. To assess the translatability of findings from the Caco-2 model to a mouse enteroid model**
 - a. To perform barrier integrity (see aim 1) and cytotoxicity studies on enteroids

- 4. To identify genetic variants associated with dasatinib-induced diarrhoea**
 - a. To undertake a genome-wide association study (GWAS) on dasatinib-treated CML patients to identify SNPs associated with dasatinib-induced diarrhoea

CHAPTER 2: MATERIALS & METHODS

2.1 Chemicals and drug compounds

Bosutinib was kindly provided by Pfizer (Surrey, UK) and used in chapter 1. Bosutinib used in subsequent chapters was obtained from Tocris (Abingdon, UK). Imatinib was kindly provided by Novartis (Surrey, UK); dasatinib from Tocris; and gefitinib from Sigma-Aldrich (Gillingham, UK). Drug stocks of 50mM were prepared by solubilising in DMSO and aliquots were stored at -20 °C.

Tunicamycin, chloroquine, MG-132, bafilomycin, 3-MA, N-acetyl cysteine, necrostatin-1, IM-54, ferrostatin and z-vad-fmk were kindly provided by Dr. Shankar Varadarajan, University of Liverpool. GM6001 was kindly donated by Dr Mark Morgan, University of Liverpool. Cycloheximide and deferoxamine were purchased from Abcam (Cambridge, UK), ML-7 from Tocris and Y-27632 from Stem Cell Technologies (Cambridge, UK). 3-MA was solubilised in nuclease-free H₂O. All other compounds were solubilised in DMSO.

2.2 Buffers and solutions

Tris-buffered Saline (TBS)

1.21g Tris-base (0.1M)
8.77g NaCl (0.15M)
1L of distilled water (dH₂O)
pH adjusted to 7.6

Tris-buffered Saline-Tween (TBS-T)

As above with 1mL Tween-20 (0.1% (v/v))

Sodium Dodecyl Sulphate Polyacrylamide Gel Electrophoresis (SDS-PAGE) Running Buffer

11.4g Glycine (0.152M)
3.0g Tris-base (25mM)
1g Sodium dodecyl sulfate (3.47mM)
1L of dH₂O

Western blot Transfer Buffer

11.4g Glycine (0.152M)
3.03g Tris-base (25mM)
200mL of methanol (20%)
800mL of dH₂O

N-2-hydroxyethyl-piperazine-N'-2-ethanesulfonic acid (HEPES)-Buffered Saline

7.95g NaCl (136mM)

372.8mg KCl (5mM)

47.7mg Na₂HPO₄ (336μM)

1.00g Glucose (5.6mM)

2.38g HEPES (10mM)

1L dH₂O

pH adjusted to 7.4

Tris-Acetate-EDTA (TAE) Buffer

484mg Tris(hydroxymethyl)aminomethane (4μM)

114μl Acetic acid (2mM)

38mg EGTA (1mM)

100mL dH₂O

Lysogeny (LB) Broth

10g Tryptone

5g Yeast extract

5g NaCl (85mM)

1L ddH₂O

2.3 Cell line culture and experiments

Caco-2 cells and HEK293T/17 cells were obtained from the American Type Culture Collection (ATCC) (Middlesex, UK).

2.3.1 Caco-2 cells

The Caco-2 cell line (ATCC® HTB-37™) is a human colorectal cancer cell line developed from a colorectal adenocarcinoma of a 72-year old Caucasian male. In their undifferentiated state Caco-2 cells resemble immature colonic epithelial cells (Sambuy *et al.*, 2005). However, Caco-2 cells spontaneously differentiate into enterocytes with a foetal-like small intestinal phenotype upon reaching confluency. Loss of the colonic phenotype, along with secretion of the small bowel marker α₁-antitrypsin, is seen at day 6 (3-4 days post-confluency). However, intestinal alkaline phosphatase (ALPI), an enterocyte differentiation marker, becomes elevated later at 13-21 after seeding (Engle *et al.*, 1998), and the standard time period for full differentiation into enterocytes is 21 days (18-19 days post-confluency) (Lea, 2015).

2.3.2 HEK293T/17 cells

The HEK293 cell line is derived from human embryonic kidney epithelial cells. HEK293T/17 cells (ATCC® CRL-11268) are highly transfectable derivatives of HEK293 cells and were used for lentivirus generation in this project (see 2.3.12 Generation of Caco-2 cells stably expressing fluor-labelled occludin and lifeact for time-lapse imaging). Subculture and maintenance of this cell line was identical to that of Caco-2 cells.

2.3.3 Cell line subculture and maintenance

Caco-2 and HEK293T/17 cells were maintained in Thermo Scientific™ Nunc™ EasYFlask™ T75 and T75 Cell Culture Flasks, respectively, in high glucose Dulbecco's Modified Eagle's Medium (DMEM) supplemented with heat-inactivated foetal bovine serum (FBS) (10% v/v final conc.) and L-glutamine (2mM final conc.), all purchased from Thermo Fisher Scientific, Loughborough, UK. Cells were incubated at 37°C under a humidified atmosphere of 5% CO₂ and growth media replaced on alternate days. Cells were maintained up to a passage of 30 and sub-cultured upon reaching ~80% confluency. For passaging, growth media was removed, and cells were washed with phosphate buffered saline (PBS), pH 7.3, at 37°C, detached with 0.25% (v/v) trypsin-ethylenediaminetetraacetic acid (EDTA) solution (Sigma-Aldrich) and split 1:4. Caco-2 cells for experimental work were seeded at the densities stated in Table 2.1, to give a consistent cell number per surface area of 1.34×10^5 cells/cm². Cells were fed on alternate days for a minimum of 10 days, unless otherwise stated.

Plate type	Well surface area (cm²)	Concentration (cells/mL)	Volume (μl)
12-well Transwell (clear polyester membrane, 12mm, 0.4μm pore size) (Corning)	1.12	3×10^5	500
Nunclon™ Delta Surface 24-well plate (Thermo Fisher Scientific)	2	3×10^5	893
Nunclon™ Delta Surface 96-well plate (Thermo Fisher Scientific)	0.32	3×10^5	143
Nunc™ Lab-Tek™ II Chamber Slide™ System (4-well) (Thermo Fisher Scientific)	1.7	3×10^5	756
CELLview™ 4-compartment culture dish with glass bottom (Greiner Bio-One, Gloucestershire, UK)	1.9	3×10^5	848

2.3.4 Short tandem repeat profiling

DNA from Caco-2 cells (3×10^6 cells) was extracted using DNeasy Blood & Tissue Kit (QIAGEN, Manchester, UK) according to the manufacturer's protocol. Cells were brought into suspension by passaging (see 2.3.3 Cell line subculture and maintenance). In brief, cells were spun down at 300g for 3 min, supernatant discarded and washed once with PBS (200 μ l). Ethanol (200 μ l) was added to cells and the mixture pipetted into a DNeasy Mini spin column in a collection tube. Samples were centrifuged at 6000g for 1 min and flow-through discarded. Column was washed with AW1 buffer (500 μ l) and spun at 6000g for 1 min, then with AW2 buffer (500 μ l) and spun at 20,000g for 3 min. Spin columns were transferred to new collection tubes, AE buffer (200 μ l) was added to spin column membranes and columns incubated at room temperature for 1 min. DNA was eluted by spinning at 6000g for 1 min. DNA was analysed at the Cell Line Authentication Facility, University of Liverpool. Authentication was undertaken by Mrs Patricia Gerard using the GenePrint[®] 10 (Promega, Southampton, UK) authentication method. The Leibniz Institute DSMZ, German Collection of Microorganisms and Cell Cultures (DSMZ), and ATCC databases were used for comparison. Cells were confirmed to be Caco-2 cells (see Appendices, Fig A.1).

2.3.5 Cell permeability assay

Cells were seeded into 11 wells of a 12-well transwell plate (see Table 2.1) with 0.5ml and 1.5ml growth media in apical and basal compartments, respectively, and cultured for up to 14 days as described in 2.3.3. A diagram of the transwell setup can be visualized in Fig 2.1. Media without cells was added to the final well to determine the basal resistance of the polyester membrane and maximum FITC-dextran (4kDa) (FD-4) flux.

Prior to drug dosing cells were washed twice with phenol red-free DMEM. Phenol red-free DMEM containing 2mg/ml FD-4 (0.5ml) was added to the apical compartment and test drugs were either added to the apical or basal compartment. Electrical resistance measurements were obtained using 'chop-stick' electrodes with the Millicell ERS-2 Epithelial Volt-ohm Meter (Millipore (UK) Ltd., Watford, UK). Electrical resistance values (Ω) were converted to a transepithelial electrical resistance (TEER) value by subtracting basal resistance (measurement from well without cells) and multiplying by the surface area of the monolayer. Aliquots of DMEM (50 μ l) were removed from the basal chamber for up to 24 h and transferred to a black 96-well plate. Fluorescence was measured using the Beckman Coulter DTX 880 Multimode detector (excitation 485nm; emission 535nm). A 1 in 2 serial dilution of

FD-4 (2mg/ml) was used to generate a standard curve to convert fluorescence to FD-4 concentrations through interpolation.

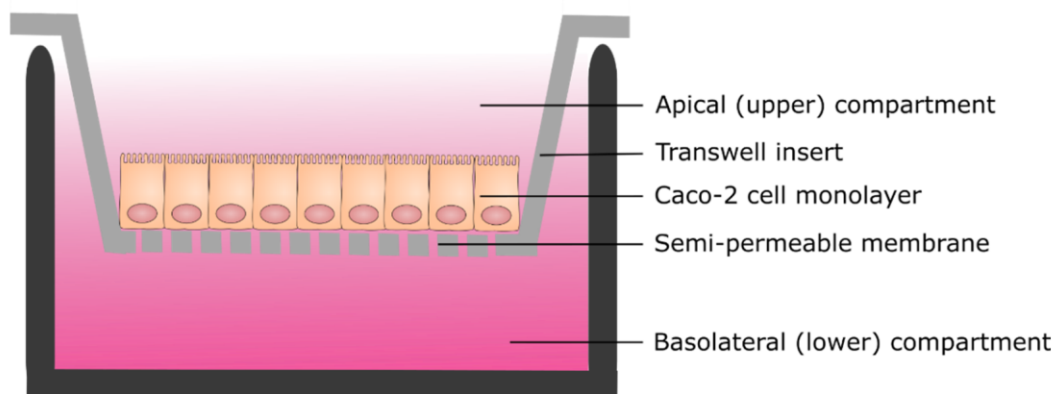


Figure 2.1. Schematic of transwell set-up used in permeability experiments. Diagram shows a cross section through one of the wells in a transwell plate. The epithelial cell layer is modelled by the Caco-2 cell monolayer. The apical (upper) compartments models the intestinal lumen whilst the basolateral (lower) compartment models the lamina propria, the space underneath the epithelial cell layer. The semi-permeable membrane enables macromolecules, such as FITC-dextran, or ions to flow across the monolayer, whilst providing sufficient support for Caco-2 cells to grow and differentiate. Drugs can be added to the apical or basolateral compartment to model local or systemic exposure, respectively. The transwell setup permits access to the both the apical and basolateral compartments, such that ‘chop-stick’ electrodes can be placed in both compartments to measure resistance across the monolayer. Moreover, after addition of a labelled macromolecule to the apical compartment, aliquots of basolateral compartment media can be obtained to determine levels of macromolecules in the basolateral compartment, in order to assess macromolecular flux across the monolayer.

2.3.6 Cell dissociation assay

Differentiated monolayers of Caco-2 cells in 24-well plates were drug treated with a range of concentrations for up to 24 h. As described by Nagafuchi *et al.* (1994), cells were then washed with PBS once and incubated with HEPES-buffered saline containing either 0.01% (v/v) trypsin and 1mM CaCl₂ (T_c treatment) or 0.01% (v/v) trypsin and 1mM EGTA (T_e treatment) for 2 h at 37°C. EGTA treatment completely disperses cells to enable determination of the total number of cells per well. Cells were dissociated through pipetting up and down 15 times using a p1000 tip and 100µl aliquots transferred (in triplicate) into a 96-well plate for imaging. One image per well was taken using light microscopy at x4 magnification. The number of cell clumps per well was determined using a pipeline set up on the cell image analysis software, CellProfiler (Carpenter *et al.*, 2006). After automatic detection of cell clumps the ‘raw’ (original) and ‘object’ (processed through CellProfiler) images were exported and compared manually to confirm accuracy of the automatic detection of cell clumps. Data are presented

as N_{TC} (the total number of clumps after T_c treatment) divided by N_{TE} (the total number of 'clumps' after T_e treatment. NB T_e treatment completely separates the cells so each 'clump' is a single cell). Cells with weakened cell-cell adhesion strength will have greater dispersion upon pipetting thus creating more (smaller) clumps and a higher N_{TC} value; therefore N_{TC}/N_{TE} is the extent of cell dissociation normalized to the total cell number, and is inversely proportional to cell-cell adhesion strength.

2.3.7 Cell line cytotoxicity assays

The cytotoxicity of TKIs was determined using three separate 96-well format assays: 3-(4,5-dimethylthiazol-2-yl)-2,5-diphenyltetrazolium bromide (MTT) assay (Sigma-Aldrich); CellTiter-Glo[®] luminescent assay (Promega, Southampton, UK); and ToxiLight[™] luminescent assay (Lonza, Verviers, Belgium), as described below. Differentiated monolayers of Caco-2 cells in 96-well plates were dosed with 100 μ l drugged media and appropriate controls for up to 24 h. Three technical repeats and at least three biological repeats were performed for all assays. Viability was determined relative to no treatment control after subtraction of a background reading without cells. Plates were read on the Beckman Coulter DTX 880 Multimode detector.

2.3.7.1 MTT assay

The MTT assay was used to assess NAD(P)H-dependent cellular oxidoreductase enzyme activity which can indicate the number of viable cells in a semi-quantitative manner. Thiazolyl Blue Tetrazolium Bromide in PBS (5mg/ml, 10 μ l) was added to cells in 100 μ l drugged media and incubated for 3 h at 37°C in the dark. Purple formazan crystals, generated through NAD(P)H-dependent oxidoreductase activity, were dissolved by a 15 min incubation with 100 μ l MTT Solubilization Solution (90% (v/v) Isopropanol, 10% (v/v) Triton X-100, 0.1N HCl). Absorbance was measured at 570nm.

2.3.7.2 CellTiter-Glo[®] assay

The CellTiter-Glo[®] assay was used to determine cellular ATP levels, which indicates the presence of metabolically active cells, and therefore can be used to determine cell viability. CellTiter-Glo[®] reagent (100 μ l) was added to the cells and incubated at room temperature for 2 min with gentle agitation. Samples were transferred to a white 96-well plate and luminescence was measured for 1 second per well.

2.3.7.3 *ToxiLight™ assay*

The ToxiLight™ Non-Destructive Cytotoxicity Bio Assay Kit was used to measure adenylate kinase (AK) release from cells; a marker of cell death. AK detection reagent was reconstituted in 10ml assay buffer and allowed to equilibrate to room temperature for 15 min prior to use. After drug treatment, ToxiLight™ 100% lysis reagent (50µl) was added to three untreated wells and tris acetate (50µl), a non-cytotoxic buffer, was added to all remaining wells (a required volume correction to ensure volumes in control and TKI-treated wells were equal to those with lysis buffer) and incubated for 15 min. Twenty microlitres of solution from each well were transferred to a white 96-well plate, 100µl AK detection reagent added and luminescence read after a 5 min incubation at room temperature. Viability was calculated as the inverse of cell death (AK release), relative to 100% lysis.

2.3.8 Cell line Western blotting

2.3.8.1 *Preparation of protein lysates*

Differentiated monolayers of Caco-2 cells in 24-well plates, were drug dosed (1-50µM) for up to 24 h. After washing cells twice with ice cold PBS, proteins were lysed with RIPA buffer (Sigma-Aldrich) containing 1% (v/v) Calbiochem protease inhibitor cocktail III (Merck Millipore, Watford, UK,) and stored at -20°C.

Protein determination was performed using the DC™ Protein Assay (Bio-Rad, Watford, UK). A 5-point bovine serum albumin (BSA) standard curve (0.2-1.5mg/ml) was prepared in RIPA buffer. Caco-2 protein lysate samples and standard curve samples (5µl), reagent A (25µl) and reagent B (200µl) were added to a clear 96-well plate. After 15 min incubation at room temperature absorbance was measured at 595nm on the Beckman Coulter DTX 880 Multimode detector. Protein samples were adjusted to equal concentrations using RIPA buffer. Stock 4x Laemmli buffer (Bio-Rad) containing 20% (v/v) β-mercaptoethanol was added and samples were then denatured at 95°C for 5 min prior to gel loading.

2.3.8.2 *SDS-PAGE and membrane transfer*

Whole cell lysates (15ng) and Kaleidoscope protein ladder (8µl) (Bio Rad) were loaded into a gel that comprised a 3% acrylamide (v/v) stacking and 8% acrylamide (v/v) resolving gel, prepared as described in Table 2.2.

Proteins were separated by sodium dodecyl sulphate-polyacrylamide gel electrophoresis (SDS-PAGE) at 30mA per gel, constant Amps, for 1h in SDS-PAGE running buffer (see 2.2 Buffers and Solutions). Proteins were then electrophoretically transferred onto a methanol-

soaked Immobilon-P Polyvinylidene Difluoride Transfer Membrane (Merck Millipore) at 200mA per gel, constant Amps, in Western blot transfer buffer for 1 h.

Gel	3% acrylamide (v/v) stacking gel	8% acrylamide (v/v) resolving gel
dH ₂ O	3.20ml	4.73ml
ProtoGel stacking buffer (Geneflow)	1.25ml	-
ProtoGel resolving buffer (Geneflow)	-	2.50ml
ProtoGel acrylamide to bisacrylamide stabilized solution (Geneflow)	500µl	2.67ml
10% (w/v) Sodium dodecyl sulfate (SDS)	50µl	100µl
10% (w/v) Ammonium persulfate (APS)	25µl	50µl
Tetramethyl-ethylene-diamine (TEMED)	7.5µl	15µl

2.3.8.3 Antibody incubations and membrane visualization

Membranes were blocked in 10% (w/v) non-fat milk in TBS-T for 1 h prior to incubation with primary antibodies in 5% (w/v) non-fat milk in TBS-T or TBS-T, as indicated in Table 2.3, at 4°C overnight with constant agitation. The membrane was washed with constant agitation in TBS-T at room temperature (6 x 5 min washes). Membranes were incubated with the appropriate horseradish peroxidase (HRP)-coupled secondary antibody in 5% (w/v) non-fat milk in TBS-T (Table 2.4) for 1 h at room temperature with constant agitation then washed as before. Membranes were visualised with the Pierce™ enhanced chemiluminescence (ECL) Western Blotting Substrate (Thermo Fisher Scientific) on the Bio-Rad ChemiDoc™ Touch Imaging System. Densitometry was performed using ImageJ software (Schneider *et al.*, 2012), and levels of the protein of interest normalised to the β-actin loading control.

Table 2.3. Primary antibodies (IgGs) used for Western blotting of Caco-2 cell and organoid protein lysates. Primary antibodies (immunoglobulins, IgG) were diluted in 5% (w/v) non-fat milk in TBS-T. Molecular weight is given as the predicted band location given by the manufacturer. Unless otherwise stated in 'Target', antibody was suitable for both human Caco-2 and mouse enteroid work.

Target	Manufacturer and Catalogue number	Host	Titre of primary IgG	Titre of secondary IgG	Molecular weight (kDa)
Intestinal Alkaline Phosphatase (ALPI)	Novus Biologicals (Abingdon, UK); H00000248-M03	Mouse	1:500	1:10,000	70, monomeric 140, dimeric
β -actin	Santa Cruz Biotechnology (Insight Biotechnology Ltd., Middlesex, UK); sc-47778	Mouse	1:1,000	1:5,000	42
Binding immunoglobulin protein (BiP)	Abcam (Cambridge, UK); ab21685	Rabbit	1:1,000	1:10,000	78
CCAAT-enhancer-protein homologous protein (CHOP)	Abcam (Cambridge, UK); ab11419	Mouse	1:1,000	1:2,000	29
E-cadherin	Cell Signaling Technology (London, UK); 14472	Mouse	1:1,000	1:10,000	135
Human Occludin	Abcam (Cambridge, UK); ab167161	Rabbit	1:10,000	1:10,000	65
Mouse Occludin	Novus Biologicals (Abingdon, UK); NBP1-87402	Rabbit	1:1,000	1:10,000	65
Poly[ADP-ribose]polymerase 1 (PARP1)	Cell Signaling Technology (London, UK); 9542	Rabbit	1:1,000	1:5,000	116, full length 89, cleaved
Tissue inhibitor of metalloproteinases 2 (TIMP-2)	Cell Signaling Technology (London, UK); 5738	Rabbit	1:1,000	1:5,000	22
Zonula occludens 1 (ZO-1)	Thermo Fisher Scientific (Loughborough, UK); 61-7300	Rabbit	1:1,000	1:10,000	195

Target	Manufacturer and Catalogue number	Catalogue number	Host	Conjugation
Mouse	Cell Signaling Technology (London, UK)	7076S	Horse	Horseradish peroxidase
Rabbit	Cell Signaling Technology (London, UK)	7074S	Goat	Horseradish peroxidase

2.3.9 Reverse transcription-quantitative polymerase chain reaction (RT-qPCR)

Differentiated Caco-2 cell monolayers in 24-well plates were drug treated (25 μ M) for up to 24 h. RNA was extracted using the ReliaPrep™ RNA Cell Miniprep System (Promega) following the manufacturer's protocol. Cells were washed twice in ice cold PBS and lysed in 250 μ l BL + TG buffer with pipetting. Isopropanol (85 μ l) was added to the lysates, mixed, and then transferred to a mini-column in a collection tube. Samples were centrifuged at 14,000g for 30 sec and the liquid flow-through discarded between washes. RNA wash solution (500 μ l) was added to the column and spun at 14,000g for 30 sec. DNase I incubation mix was applied directly to the spin column membrane and incubated for 15 min at room temperature. Column wash solution (200 μ l) was then added and spun at 14,000g for 15 sec. RNA wash solution (500 μ l) was added and spun at 14,000g for 30 sec. The mini-column membrane was washed again with RNA wash solution (300 μ l) then centrifuged at 14,000g for 2 min. RNA was eluted using nuclease-free H₂O (30 μ l), by addition to column membrane then spinning at 14,000g. RNA was stored at -80°C. RNA purity and quantity was determined using the Thermo Scientific Nanodrop 8000 spectrophotometer. RNA samples with a 260nm/280nm \geq 2 were used for reverse transcription to generate complimentary DNA (cDNA).

Reverse transcription was performed using the High Capacity cDNA Reverse Transcription Kit (Thermo Fisher Scientific). Reverse Transcription Master Mix contained 10x RT Buffer (2 μ l), 25x dNTP Mix (0.8 μ l), 10x RT Random Primers (2 μ l), MultiScribe™ Reverse Transcriptase (1 μ l) and nuclease-free H₂O (9.2 μ l) per reaction. This master mix (15 μ l) was added to purified RNA samples (20ng/ μ l, 5 μ l) in a 96-well reaction plate. Reverse transcription was performed in an Applied Biosystems Veriti 96 Well Thermal Cycler at 25°C for 10 min, 37°C for 120 min then 85°C for 5 min.

Purity, quality and concentration of cDNA samples was determined using the Nanodrop 8000. Samples were adjusted to 80ng/ μ l in nuclease-free H₂O and gene expression determined by

TaqMan[®] assay (Applied Biosystems, Paisley, UK). PCR reaction mix was prepared using 20x TaqMan[®] Gene Expression Assay (1 μ l), 2x TaqMan[®] Gene Expression Master Mix (10 μ l) and nuclease-free H₂O (5 μ l) per reaction. PCR reaction mix (16 μ l) was added to cDNA (4 μ l) or no-template controls (nuclease-free H₂O only, 4 μ l) in a 384-well PCR plate in triplicate. TaqMan[®] Gene Expression Assays were *CDH1* (E-cadherin) (Hs01023894_m1), *TJP1* (Zonula occludens-1/ZO-1) (Hs01551861_m1), *OCLN* (occludin) (Hs00170162_m1) and *B2M* (beta-2-microglobulin) (Hs99999907_m1). Samples were amplified using the following cycling conditions: - a) 2 min at 20°C; b) denaturation at 95°C for 10 min; and c) 40 cycles of 15 sec at 95°C (denaturation) and 1 min at 60°C (primer annealing and extension), using the Applied Biosystems 7900HT Fast Real-Time PCR System. $\Delta\Delta$ Ct and RQ values were determined using RQ Manager and results normalised to the *B2M* housekeeping gene.

2.3.10 Immunofluorescence

Differentiated Caco-2 cell monolayers were grown on Nunc[®] Lab-Tek[®] 4-well Chamber Slides[™]. Cells were then dosed with drugs (25 μ M) or vehicle control for up to 24 h. After washing twice with ice cold PBS, cells were fixed with 4% (v/v) paraformaldehyde in PBS for 30 min at 4°C. Cells were washed 3 times with ice cold PBS before addition of permeabilization buffer (0.2% (v/v) Tween-20, 0.5% (v/v) Triton X-100, in PBS) for 30 min at 4°C. Blocking was then performed for a minimum of 1 h at room temperature with 1x blocking buffer (Blocker[™] BSA (10%) in PBS (Thermo Fisher Scientific) diluted to a 1% (v/v) working solution in PBS).

After blocking, cells were incubated with the appropriate primary antibody in 1x blocking buffer (Table 2.5). Incubation was performed overnight at 4°C. Cells were then washed three times using ice cold PBS at 10 min intervals on an orbital shaker and subsequently incubated with the corresponding secondary antibody – Goat anti-mouse Alexa Fluor[®]594 (ThermoFisher Scientific, A-11012) or Goat anti-rabbit Alexa Fluor[®]488 (ThermoFisher Scientific, A-11008) – at a 1:1000 dilution in 1x blocking buffer for 1 h. In preliminary experiments, secondary antibody only was added to one of the four chambers to assess any off-target binding of the secondary antibody. Minimal off-target binding was observed. Cells were washed again at 10 min intervals using cold PBS then 1:1000 Phalloidin-iFluor 594 Reagent CytoPainter (Abcam, ab176757) in 1x blocking buffer added for 20 min; again followed by two washing steps. Walls of the chamber slide were removed and one drop of 4',6-Diamidino-2-Phenylindole (DAPI)-containing VECTASHEILD (Vector Laboratories Ltd., Peterborough, UK) was added per well. Slides were then sealed using a coverslip and z-stack

images collected on a Zeiss Axio Observer.Z1 fitted with ApoTome 2. Levels of target proteins were semi-quantitatively determined by measuring mean fluorescence intensity in ImageJ (Schneider *et al.*, 2012).

Table 2.5. Primary antibodies (IgGs) used for immunofluorescent staining of Caco-2 cell and organoids. Primary antibodies were diluted in 1x blocking buffer. Unless otherwise stated in 'Target', antibody was suitable for both human Caco-2 and mouse enteroid work.			
Target	Manufacturer and Catalogue number	Host	Titre of primary IgG
E-cadherin	Cell Signaling Technology (London, UK); 14472	Mouse	1:50
Human Occludin	Abcam (Cambridge, UK); ab31721	Rabbit	1:500
Mouse Occludin	Novus Biologicals (Abingdon, UK); NBP1-87402	Rabbit	1:50
Zonula occludens 1 (ZO-1)	Thermo Fisher Scientific (Loughborough, UK); 61-7300	Rabbit	1:50

2.3.11 MMP array

Total protein levels of MMP1, 2, 3, 8, 9, 10 and 13, and TIMP1, 2 and 4 were determined by the Human MMP Antibody Array (Abcam, ab134004) following the manufacturer's protocol. In brief, cell lysates were collected using 2x Cell Lysis Buffer diluted to a 1x solution in dH₂O containing 1% (v/v) protease inhibitor cocktail. Cell growth media was also harvested. Protein lysate concentrations were determined using the Pierce™ bicinchoninic acid (BCA) Protein Assay Kit (Thermo Fisher Scientific) according to the manufacturer's protocol. BSA calibration standards (see 2.3.8 Western blotting) and lysates (25µl) were loaded into a clear 96-well plate and 200µl of a working reagent consisting a 50:1 ratio of Reagent A:B were added and incubated for 30 min at 37°C. Absorbance was read at 562nm using the Beckman Coulter DTX 880 Multimode detector.

Array membranes were placed printed side up into the 8-well tray and blocked with 2 ml 1x Blocking Buffer at room temperature for 30 min with agitation. Both media and cell samples were spun at 18,000g for 10 min to pellet out cellular debris. Cell samples were then diluted to 250µg/ml in 1x Blocking Buffer. Either 1 ml of media or protein sample was incubated with the array membranes overnight at 4°C, with agitation. Membranes were transferred to a clean container and washed with 20 ml of 1x Wash Buffer I for 30 min, with agitation. Membranes were returned to the 8-well tray and washed with 2 ml of 1x Wash Buffer I for 5 min, 3 times. Membranes were then washed twice with 1x Wash Buffer II for 5 min.

Membranes were incubated with 1 ml of 1x Biotin-Conjugated Anti-Cytokines overnight at 4°C, with agitation. Membranes were washed using the three wash steps above and 2 ml of 1x HRP-Conjugated Streptavidin was applied and incubated for 2 h at room temperature, with agitation. Membranes were washed, again as described above. Membranes were incubated with 250µl Detection Buffer C combined with 250µl Detection Buffer D for 2 min at room temperature and membranes then imaged using the Bio-Rad ChemiDoc™ Touch Imaging System. Protein levels were determined using ImageJ software and normalized to the average reading of the positive controls on the membrane.

2.3.12 Generation of Caco-2 cells stably expressing fluorescently labelled occludin and lifeact for time-lapse imaging

2.3.12.1 Overview of experimental strategy

The following plasmid work and lentiviral production was performed with the assistance of Dr Nicolas Harper in the Department of Molecular and Clinical Cancer Medicine at the University of Liverpool. A second generation lentiviral system, which is replication incompetent and lacks virulence genes, was used for enhanced safety (Zufferey *et al.*, 1997).

Plasmids containing fluorescently labelled genes of interest: mCherry-Lifeact-7 and Occludin-C-14 were purchased from Addgene (#54491 and #54211, respectively). The fluorescently labelled genes of interest were amplified by polymerase chain reaction (PCR) and ligated into a lentiviral transfer plasmid (pLJM1 P2A), donated by Dr Nicolas Harper (Fig 2.2 and 2.3). After transformation of bacteria with the modified pLJM1 P2A plasmid, positive colonies were identified by PCR, expanded overnight and plasmids extracted by Mini-prep. Next, lentiviral particles were generated by transfection of HEK-293T cells with the newly generated lentiviral transfer plasmid, the packaging psPAX2 plasmid (Addgene, #12260) and the envelope pMD2.G plasmid (Addgene, #12259). Lentiviral particles were then used to transduce Caco-2 cells and cells were imaged using time-lapse fluorescence microscopy. For complete plasmid maps see Appendices Fig A.2-4.

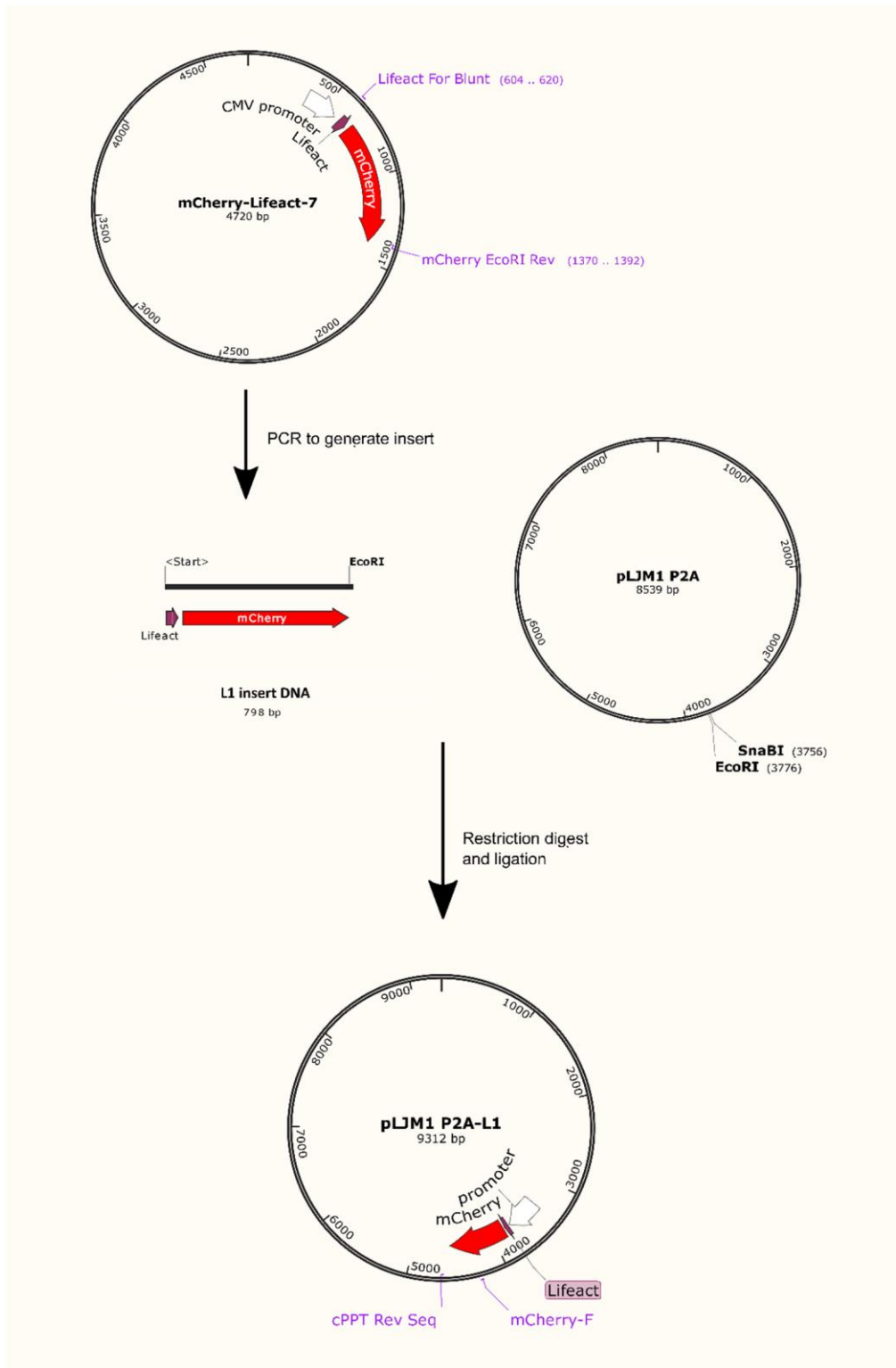


Figure 2.2. Schematic flow diagram for cloning of mCherry-Lifeact into pLJM1 P2A to generate pLJM1 P2A-L1. Simplified schematic of steps involved in the generation of the lentiviral transfer plasmid containing the fluorescently-labelled gene of interest. Plasmids maps were generated using SnapGene software (GSL Biotech, Chicago, USA). Primers are shown in purple and restriction enzymes in bold black. Many plasmid features have been removed for the simplicity of this schematic. For complete plasmid maps see Appendices, Fig A.2 and A.3.

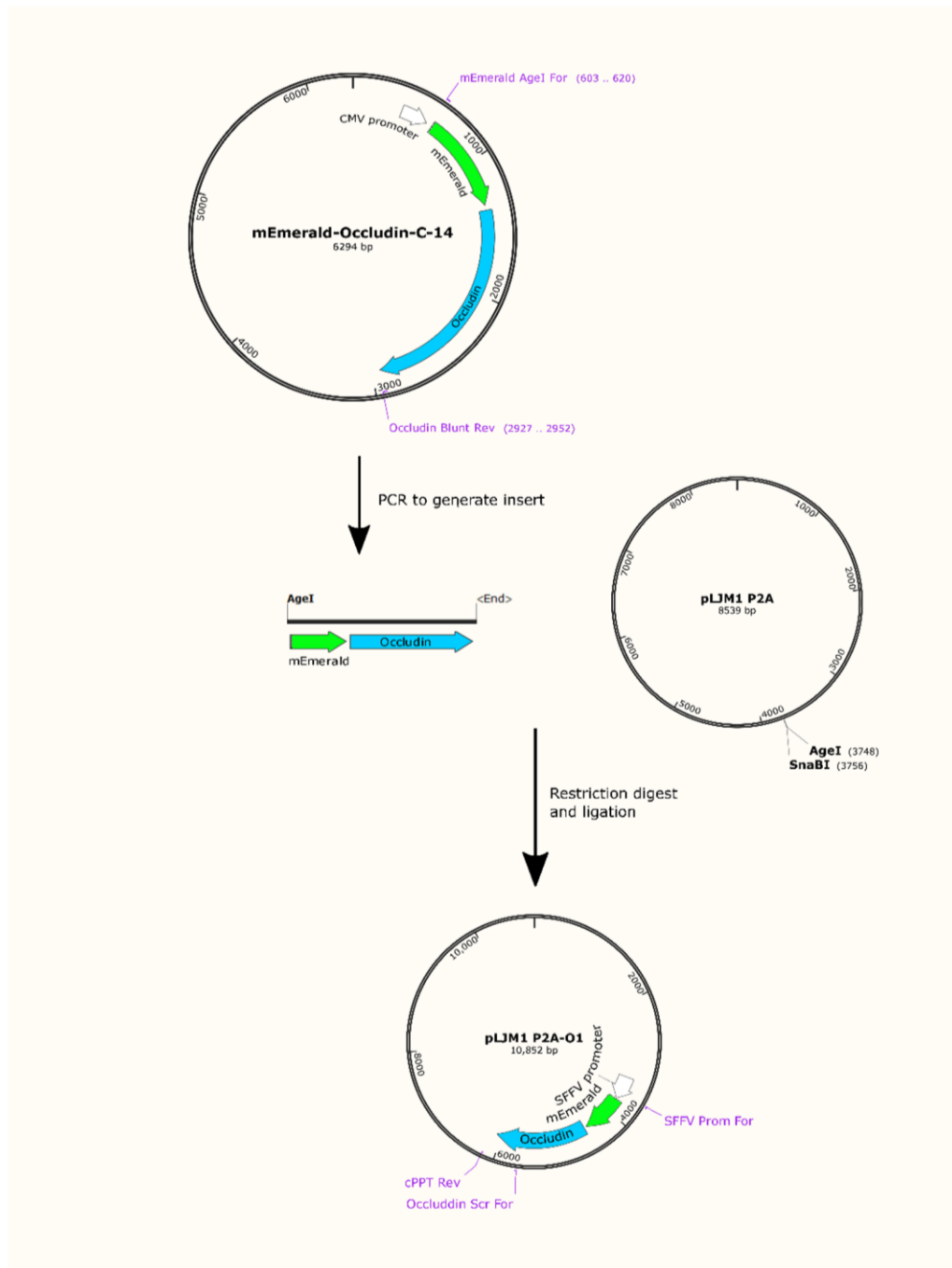


Figure 2.3. Schematic flow diagram for cloning of mEmerald-Occludin into pLJM1 P2A to generate pLJM1 P2A-O1. Simplified schematic of steps involved in the generation of the lentiviral transfer plasmid containing the fluorescently-labelled gene of interest. Plasmids maps were generated using SnapGene software (GSL Biotech, Chicago, USA). Primers are shown in purple and restriction enzymes in bold black. Many plasmid features have been removed for the simplicity of this schematic. For complete plasmid maps see Appendices, Fig A.2 and A.3.

2.3.12.2 Polymerase chain reaction (PCR) to generate plasmid inserts

A 50µl PCR reaction containing 1µl plasmid template (25ng/µl), 10µl Q5 reaction buffer (#B90275; New England Biolabs, Hitchin, UK), 1µl deoxynucleotide (dNTPs) solution mix (10mM) (New England Biolabs), 5µl forward and reverse primers (10µM) (Integrated DNA Technologies) (Table 2.6), 0.5µl Q5 High-fidelity DNA polymerase (New England Biolabs, #M04915) and 32.5µl nuclease-free H₂O, was performed in duplicate. Thermocycling was performed using the SimpliAmp Thermal cycler (Life Technologies) with the following cycling conditions: a) initial denaturation at 95°C for 2 min; b) 35 cycles of: 30 sec at 95°C (denaturation), 30 sec at 58°C (primer annealing) and 2 min at 68°C (extension); and c) final extension at 68°C for 10 min.

Template plasmid	Primer name	Primer sequence (5' - 3')	Name of insert DNA	Size of PCR product (bp)
mCherry-Lifeact-7 plasmid (Addgene, 54491)	Forward: Lifeact For Blunt	GCCACCATGGGCGT GGC	L1	798
	Reverse: mCherry EcoRI Rev	CCGGAATTCTTACT TGTACAGCTCGTCC ATGC		
mEmerald-Occludin-C-14 (Addgene, 54211)	Forward: mEmerald AgeI For	CGCTACCGGTCGCC ACCA	O1	2353
	Reverse: Occludin Blunt Rev	GCGGTACCCTATGT TTTCTGTCTATC		

2.3.12.3 DNA electrophoresis

To confirm the successful generation of PCR products, PCR samples were separated in ethidium bromide-stained TAE-buffered agarose gels (1.5% (w/v) or 0.75% (w/v) UltraPure™ Agarose (Invitrogen), 0.8µl ethidium bromide in 100ml TAE buffer, see 2.2 Buffers and Solutions) at 135V for 20 min before the DNA was visualized under UV light.

2.3.12.4 PCR clean-up

After amplification of plasmid inserts, PCR clean-up was undertaken using the Wizard® SV Gel and PCR clean-up system (Promega) following the manufacturer's protocol. In brief, membrane binding solution (200µl) was added to a spin column in a collection tube prior to the addition of PCR product. Columns were spun at 16,000g for 60 sec and flow-through discarded. Columns were washed twice with wash buffer (750µl then 500µl) and spun at 16,000g for 60 sec. Flow-through was discarded and samples were spun for an additional 5

min at 16,000g. To elute DNA, nuclease-free H₂O (40µl for PCR product, 25µl for DNA digest product) was added to the spin column membrane and incubated at 42°C for 3 min, then spun at 16,000g for 5 min. DNA was then quantified by Nanodrop.

2.3.12.5 Restriction enzyme digestion

Restriction enzyme digestion was undertaken using 8µl 10x CutSmart buffer (New England Biolabs, B7204S), 1µl restriction enzyme(s) (New England Biolabs, Table 2.7) and 70µl insert DNA (100ng/µl) or 15µl plasmid DNA (50ng/µl) in nuclease-free H₂O, to give a final volume of 80µl. Products were digested for 1 h or 2 h at 37°C for insert DNA and plasmid DNA, respectively.

Insert DNA digest		Plasmid digest	
Insert DNA	Restriction enzyme	Plasmid	Restriction enzymes
L1	EcoRI	pLJM1 P2A	EcoRI and SnaBI
O1	AgeI	pLJM1 P2A	AgeI and SnaBI

2.3.12.6 Ligation of lentiviral plasmid and inserts

Restriction enzyme digestion products, as generated above, were purified using PCR clean-up (see 2.3.12.4 PCR clean-up) before ligation. DNA concentration and quality were again assessed by Nanodrop. Ligation was performed in a 10µl reaction volume containing: 1µl 10x T4 DNA ligase buffer (New England Biolabs, B0202S), 0.5µl T4 DNA ligase (New England Biolabs, M0202S), 1µl plasmid (50ng/µl) and 4µl insert DNA (100ng/µl) in nuclease-free H₂O made up to 10µl final volume. The ligation reaction mix was incubated overnight at 4°C to generate plasmids pLJM1 P2A-L1 and pLJM1 P2A-O1. The ligation reaction was halted by incubation at 65°C for 10 min before being cooled on ice.

2.3.12.7 Bacterial transformation

Fifty microlitres NEB® Stable competent *E.coli* (New England Biolabs) was added to 5µl of the incubated ligation mixture containing PLJM1 P2A-L1 and PLJM1 P2A-O1, vortexed and incubated on ice for 30 min. Bacteria were transformed by heat shock at 42°C for 1 min then placed on ice for 2 min. Three hundred and fifty microliters of Super Optimal Broth medium (2% (w/v) tryptone, 0.5% (w/v) yeast extract, 10mM NaCl, 2.5mM KCl, 10mM MgCl₂, 10mM MgSO₄ in dH₂O) containing 1% (w/v) glucose) was added to the bacteria and incubated

for 1 h 30 min with shaking at 37°C. Bacteria were streaked onto LB agar plates containing 100mg/ml carbenicillin (Sigma-Aldrich) and incubated at 37°C overnight.

2.3.12.8 PCR colony screening

Bacterial colonies were picked and screened for the presence of lentiviral plasmids containing the gene of interest (PLJM1 P2A-L1 and PLJM1 P2A-O1). Picked bacteria were added to a 15µl reaction containing 7.5µl OneTaq Quick Load x2 Master Mix with Standard Buffer (New England Biolabs, M04865), 1.5µl of each forward and reverse screening primers (Table 2.8) and 6µl nuclease-free H₂O. PCR was performed using the following cycling conditions: a) initial denaturation for 2 min at 95°C; b) 25 cycles of: 30 sec at 95°C (denaturation), 30 sec at 58°C (primer annealing) and 30 sec at 68°C (extension); and c) final extension for 10 min at 68°C. The presence of the desired PCR product was determined by agarose gel electrophoresis (see 2.3.12.3 DNA electrophoresis) and positively identified colonies were further incubated overnight in 5ml LB broth (see 2.2 Buffers and solutions) containing 100mg/ml carbenicillin with shaking at 37°C.

Table 2.8 Sequences of primers for PCR colony screening. Primers were ordered from Integrated DNA Technologies. Expected size of PCR product is given in base pairs (bp). Starred primers were also used for DNA sequencing.			
Plasmid	Primer	Primer sequence (5' - 3')	Size of PCR product (bp)
pLJM1 P2A-L1	Forward: mCherry-F	CCCCGTAATGCAGAAGAAGA	401
	Reverse: cPPT Rev*	CTATTATGTCTACTATTCTTTCC	
pLJM1 P2A-O1	Forward: Occludin Scr For	CTGCAAAGGGAAGAGCAGG	531
	Reverse: cPPT Rev*	CTATTATGTCTACTATTCTTTCC	

2.3.12.9 Isolation of plasmid DNA

Plasmid DNA was isolated from bacteria using the QIAprep spin mini-prep kit following the manufacturer's protocol. In brief, bacterial cultures were centrifuged at 6,200g for 3 min and the bacterial pellet resuspended in P1 buffer (250µl). P2 buffer (250µl) and N3 buffer (350µl) were added with mixing by inversion. The mixture was centrifuged at 16,000g for 10 min and the supernatant transferred to a QIAprep spin column. The column was spun at 16,000g for 30 sec and flow-through discarded. The column was washed with PB buffer (500µl) and spun at 16,000g for 30 sec, then PE buffer (750µl) and spun at 16,000g for 30 sec. Residual wash buffer was removed by centrifugation at 16,000g for 1 min. DNA was eluted by adding

nuclease-free H₂O (50µl) directly to the column membrane and incubation for 1 min followed by 1 min centrifugation at 16,000g.

2.3.12.10 DNA sequencing

Plasmids pLJM1 P2A-L1 (colony 5) and pLJM1 P2A-O1 (colony 15) were sequenced using the Sanger sequencing service provided by Source BioScience (Nottingham, UK). pLJM1 P2A-L1 was sequenced using cPPT Rev (Table 2.8), whilst pLJM1 P2A-O1 was sequenced using cPPT Rev (Table 2.8) and SFFV Prom For (TTTGAATTAACCAATCAGCCTGC) primers. Sequence analysis was undertaken in SnapGene (GSL Biotech, Chicago, USA) and sequences can be found in the Appendices, Fig A.5 and A.6.

2.3.12.11 Lentivirus production

Production of second generation lentiviral particles requires three plasmids: a) an envelope plasmid, in this case pMD2.G (Addgene, #12259), which codes for the viral fusion protein vesicular stomatitis virus glycoprotein protein (VSV-G), enabling virus to bind to and enter host cells; b) a packaging plasmid, in this case psPAX2 (Addgene, #12260), containing *HIV-1 gag* (which codes for structural virion proteins), *HIV-1 pol* (which codes for the enzymes involved in virus DNA replication and integration), *HIV-1 rev* (involved in post-transcriptional regulation) and *HIV-1 tat* (involved in transcriptional regulation); and c) the transfer plasmid, which contains the transgene of interest flanked by long terminal repeats necessary for packaging, reverse transcription and integration (Zufferey *et al.*, 1997).

HEK293T cells (10ml, 4 x 10⁵ cells/ml) were seeded into 100mm cell culture dishes and allowed to adhere overnight. psPAX2 (2µg), pMD2.G plasmid (2µg) and pLJM1 P2A-L1 or pLJM1 P2A-O1 (6µg) were diluted in NaCl (300µl, 150mM). Polyethylenimine (20µl, 1mg/ml) was also diluted in NaCl (300µl, 150mM). Both mixtures were combined, vortexed and left at room temperature for 15 min, before being added dropwise to the plated HEK293T cells, and incubated overnight under standard cell culture conditions. Growth media was replaced the next day, and cells cultured for 3 days. The virus-containing growth media was harvested, spun at 300g for 5 min, and the supernatant aliquoted and stored at -80°C. Due to time constraints, the viral titre was not determined.

2.3.12.12 Transduction

Caco-2 cells were plated at 2 x 10⁵ cells/well into 12-well plates and transduced the following day with a mixture containing either pLJM1 P2A-L1 virus or pLJM1 P2A-O1 virus (undetermined titre) and polybrene (final concentration 8µg/ml). Two volumes of virus were used (50µl and 100µl) in an attempt to determine optimal virus volume for transduction.

Plates were immediately spun at 300-400g for 1 h, to enhance viral infection, and incubated under standard cell culture conditions overnight. The following day media was replaced, and upon reaching ~80% confluency cells were harvested and expanded in culture for use in subsequent experiments. Due to time constraints, single cell clones of transfected cells were not generated after transduction so a heterogeneous mix of transduced Caco-2 cells were used for imaging.

2.3.12.13 Time-lapse Imaging of transduced cells

The following time-lapse microscopy work was performed with the assistance and training from Prof Violaine See, Dr Marco Marcello and Dr Jennifer Adcott in the Centre for Cell Imaging at the University of Liverpool. This work was part funded by the University's Technology Directorate voucher scheme.

Virus-transduced Caco-2 cells were seeded into 4-compartment Cellview™ culture dishes (Greiner Bio-One International) at the concentration stated in Table 2.1. Cells formed differentiated monolayers after 10 days and were treated with vehicle control or 25µM bosutinib. Live imaging was undertaken using a Zeiss 710 Confocal Microscope with excitation at 488nm and detection between 492-551nm in order to detect mEmerald. mCherry was not imaged to the presence of artefacts (explained in more detail below). Z-stack images were taken every 5 min for up to 5 h during which cells were incubated in a humidified atmosphere at 37°C with 5% (v/v) CO₂. Maximum intensity projection .TIFF files were generated using Fiji software (Schindelin *et al.*, 2012) and the descriptor-based series registration (2d/3d+t) plugin was used to remove stage jitter. Animations were generated in .GIF format with a 70 millisecond delay between each image (.TIFF file) i.e. at approximately x4000 the original speed.

2.3.13 Enzyme-linked immunosorbent assay (ELISA)

Differentiated Caco-2 cell monolayers in 24-well plates were dosed with vehicle and TKIs (25µM) for 24 h. Media was harvested and stored at -80°C. Levels of TNF-α were determined by Human TNF-alpha DuoSet ELISA (R&D Systems, Abingdon, UK). Capture antibody was diluted to a stock solution of 480µg/ml in PBS, detection antibody to 3µg/ml in PBS and protein standards to 135ng/ml in reagent diluent (R&D Systems).

Capture antibody (4µg/ml in PBS) (100µl per well) was added to a High Binding 96-well plate (Greiner Bio-One, Gloucestershire, UK). The plate was sealed and incubated overnight at room temperature with agitation. Wells were washed with wash buffer (300µl) 3 times by

inversion. Plates were blocked with reagent diluent (300µl) for 1 h 30 min at room temperature, with agitation. Wells were washed 3 times with wash buffer (400µl) by inversion. Standards (100µl, 0pg/ml - 1000pg/ml TNF-α protein standards in DMEM) and test media samples (100µl) were added, and the plate covered with an adhesive strip and incubated overnight at 4°C with agitation. Wells were washed 5 times with wash buffer (300µl) by inversion. Detection antibody was added (100µl, 50ng/ml in reagent diluent) and incubated for 2 h at room temperature with agitation. Wells were washed 3 times with wash buffer (300µl) by inversion. One hundred microlitres of diluted streptavidin-HRP (1 in 40 in reagent diluent) was added and incubated in the dark for 20 min at room temperature. Wells were washed 3 times with wash buffer (300µl) by inversion. One hundred microlitres of Substrate Solution (SIGMAFAST™ OPD tablets in 20ml dH₂O) was added and incubated in the dark for 20 min. Stop solution (50ul, 2M H₂SO₄) was added and the plate gently rocked before reading at 492nm (with a background reading at 570nm) using a Tecan Sunrise plate reader.

2.4 Organoid culture and experiments

2.4.1 Organoid culture and maintenance

2.4.1.1 Mice

Male BALB/c mice (aged 8-12 weeks) were purchased from Charles Rivers Laboratories (Margate, UK), and housed in specific pathogen-free conditions under a 12:12 hours light-dark cycle, at the University of Liverpool. Animals were given standard chow (Special Diet Services, Essex, UK) and water *ad libitum*. Schedule 1 culling was performed by cervical dislocation. All procedures were performed under UK Home Office licences. Prof Mark Pritchard, University of Liverpool, was the project licence holder (project licence number 40/3392).

2.4.1.2 Isolating murine small intestinal crypts to generate organoids

The proximal region of BALB/c male mouse small intestines was removed and contents flushed out with ice cold PBS. The intestines were cut longitudinally then into 1cm lengths, transferred to a universal tube and shaken with ice-cold PBS until no debris was present. The tissues were suspended in ice cold chelation buffer (2mM EDTA in PBS) for 30 min at 4°C with constant agitation. Tissues were transferred to ice-cold shaking buffer (43.3mM sucrose, 59.4mM sorbitol in PBS) and vigorously shaken by hand until crypts were released into solution. The crypt solution was filtered through a Falcon® 70µM cell strainer allowing only the crypts to pass through the membrane. Crypts were spun at 200g for 10 min at 4°C. The crypt pellet was resuspended in ice-cold phenol red-free and lactose dehydrogenase

elevating virus (LDEV)-free Matrigel Basement Membrane Matrix (Scientific Laboratory Supplies Limited, Nottingham, UK) containing 500ng/ml Epidermal Growth Factor (EGF), 1000ng/ml Noggin and 5000ng/ml R-spondin (R&D Systems, Abingdon, UK) at a concentration of approximately 10 crypts/ μ l. Crypt-containing Matrigel (50 μ l per well) was pipetted directly into a pre-warmed 24-well plate and incubated at 37°C for 10 to 20 min to polymerise the Matrigel. The Matrigel dome was overlaid with 450 μ l 1:1 phenol red-free DMEM/Nutrient Mixture F-12 Ham (Thermo Fisher Scientific) with 25mM HEPES buffer, 4.5mM L-glutamine (Life Technologies), 100 μ g/ml Primocin (InvivoGen, Toulouse, France), 1% (v/v) 100x N-2 supplement (Life Technologies) and 2% (v/v) 50x B-27TM supplement (Life Technologies). Complete media supplemented with 50ng/ml EGF, 100ng/ml Noggin and 500ng/ml R-spondin was replaced every 4 days.

2.4.1.3 Organoid subculture and maintenance

Organoids were split 1 in 4 once a week. The Matrigel domes were washed once with 500 μ l PBS and resuspended by pipetting up and down (with a P1000 pipette) with 500 μ l ice-cold PBS. The Matrigel/organoid solution was passed through an insulin syringe (27G needle), 10ml ice-cold PBS added to further dilute Matrigel, and the solution spun at 200g for 6 min at 4°C. The supernatant was removed, and the organoid pellet resuspended in ice cold Matrigel containing growth factors and plated out as described above. For experiments, organoids were seeded into 48-well plates using 20 μ l Matrigel per well overlaid with 200 μ l media containing growth factors. Organoids were maintained at 37°C under a humidified atmosphere of 5% CO₂.

All experiments were performed 3 to 5 days after sub-culturing. Organoids were washed once with PBS and test drugs added to media (as described above) without growth factors.

2.4.2 Organoid permeability assay

The permeability assay was adapted from a previously established assay, developed by Leslie *et al.* (Leslie *et al.*, 2015). Optimization of this assay for use at the Gastroenterology Department, University of Liverpool, was undertaken by Dr Louise Thompson. Organoids were grown in Matrigel domes on UV-sterilised 13mm coverslips in 48-well plates. Coverslips containing organoids were transferred onto a microscope slide and placed on the microscope stage of the microinjection system (Nikon Eclipse Ti-s fitted with an Eppendorf micromanipulator 5171, an Eppendorf FemtoJet express and a Jun-air compressor). Micropipettes were made from borosilicate glass capillaries with 1mm and 0.58mm external and internal diameter, respectively (Harvard Apparatus, Edenbridge, UK), using a Zeitz DMZ

Universal electrode puller with the following settings: Heat, 400; Preliminary pull, O30; Distance threshold for elongation, O22; AD, 120. FD-4 (10mg/ml in PBS) was loaded into a micropipette, using a p10 pipette tip. FD-4 was injected into organoid lumens using the microinjection system (injection and compensation capillary pressures of $P_i = 1400\text{hPa}$ and $P_c = 30\text{hPa}$, respectively). Three to six organoids were injected per treatment. After injection, organoids were washed twice with PBS, returned to media and allowed to stabilise for 3 h 30 min under standard organoid culture conditions, to allow the epithelial layer to re-seal and dye leakage to reach a steady low-level state (Dr L. Thompson, personal communication).

Images of injected organoids were captured at x10 magnification before (0 h) drug dosing using bright field and fluorescence microscopy on the microinjection system. Organoid growth media was dosed with vehicle, test drug or positive control (2mM EGTA) and further images captured for up to 4 h, with organoids being returned to dosed media and placed in incubator after image acquisition. Images were analysed using ImageJ (Schneider *et al.*, 2012) by drawing around the bright field organoid image and using this outline to determine the pixel intensity retained within the borders of the fluorescent image. The pixel intensity is directly proportional to the fluorescence intensity and therefore can be used to determine the levels of FD-4 retained within the organoid lumen in a semi-quantitative manner. The large variation in organoid size resulted in variable volumes of FD-4 being injected into the lumen; therefore, changes in pixel intensity were normalised to the starting value (time zero; 0 h) of each individual organoid.

2.4.3 Organoid cytotoxicity assays

2.4.3.1 ToxiLight™ assay

The ToxiLight™ Non-destructive Cytotoxicity BioAssay Kit (Lonza) was used to measure AK release from organoids, a marker of cell death, as described above (2.3.7.3 ToxiLight™ assay). Growth media was removed and organoids were overlaid with 300µl media containing test drugs (0.1µM – 10µM) for up to 24 h. Twenty microlitres of drugged media was transferred to a white 96-well plate and 100µl of AK detection reagent added and incubated at room temperature for 5 min. Background luminescence of the media was also tested using 20µl of drug-free media. Luminescence was read for 1 sec at 22°C using the Beckman Coulter DTX 880 Multimode detector.

Prior to drug dosing images of each well of the culture plate were obtained at x1 magnification using a Zeiss Stemi-2000C stereomicroscope. Using ImageJ (Schneider *et al.*, 2012) organoids were drawn around using the freehand draw tool and total area of the well

occupied by organoids was calculated. AK release was calculated by subtraction of the background luminescence and normalised to the organoid area per well.

2.4.3.2 *Circularity assay*

The circularity assay was developed by Dr Carrie Duckworth at the University of Liverpool as a method to measure enteroid cell death in a semi-quantitative manner (Jones *et al.*, 2019). Jones *et al.* showed increased circularity (i.e. organoids becoming rounder, e.g. due to loss of crypt architecture) positively correlated with caspase-3 cleavage, a marker of apoptosis, in male C57BL/6 mouse enteroids dosed with 100ng/ml TNF- α for up to 24 h (chapter 5, Fig 5.6). We therefore wished to use this assay to determine cell death in our TKI-treated male BALB/c mouse enteroids. In this assay, light microscopy images of organoids at x20 magnification were obtained before and after dosing using the Zeiss Axiovert 25 microscope. Organoids were drawn around with the freehand tool in ImageJ (Schneider *et al.*, 2012) to measure their circularity score pre- and post- dosing. Circularity score varied between organoids, due to differing sizes and number of crypts, therefore changes in circularity were calculated as a percentage relative to the circularity measurements at time zero (0 h).

2.4.4 Organoid histology

2.4.4.1 *Generating slides for staining*

3-aminopropyltriethoxysilane (APES) coating was applied to slides to improve tissue adhesion. APES-coated slides were generated by placing SuperFrost Microscope slides in 2% (v/v) APES in acetone for 2 min then acetone for 2 min. Slides were then washed for 2 min in dH₂O, three times, and dried in a 37°C incubator.

2.4.4.2 *Organoid fixing, embedding and sectioning*

Organoids were dosed with 10 μ M bosutinib, imatinib or vehicle for 4 h. Media was removed, and organoids were washed twice with PBS. The Matrigel dome was solubilised in 400 μ l Cell Recovery Solution (Corning, Amsterdam, The Netherlands) for 40 min on ice. All following pipetting steps were performed using P1000 tips with the ends cut off to increase the tip aperture, in order to reduce organoid damage and conserve organoid structure. The organoids were resuspended by gentle pipetting, and 4% (v/v) paraformaldehyde in PBS (400 μ l) was added and incubated for 30 min at room temperature. Organoids were pelleted by centrifugation at 200g for 2 min and the supernatant discarded. The organoid pellet was gently resuspended in 100 μ l liquefied HistoGel™ Specimen Processing Gel (ThermoFisher Scientific). Liquefaction was achieved by microwave-heating the HistoGel™ for up to 15 sec. The HistoGel™ suspended organoids were pipetted onto a cooling plate and allowed to

solidify before being transferred to a Histosette II histology cassette (Simport Scientific, Quebec, Canada), and stored in 70% (v/v) ethanol for a minimum of 2 h. HistoGel™-fixed samples were dehydrated through a series of alcohols: a) 90% (v/v) ethanol for 2 h; b) 100% (v/v) ethanol for 30 min; c) 100% (v/v) ethanol for 30 min; and d) 100% (v/v) ethanol for 1 h 30 min. Cassettes were transferred to xylene overnight and immersed in fresh xylenes for 5 min the following day. This latter xylene immersion step was then repeated twice to ensure complete removal of ethanol. Cassettes were transferred to liquified paraffin wax pre-heated to 60°C for 2 h, then a second container of liquified paraffin wax at 60°C for 3 h. Samples were then embedded in paraffin wax in Simport Scientific Disposable Base Molds using the ThermoFisher Scientific Histocentre 3 Tissue Embedder. Four micron sections were cut using a LEICA RM2255 microtome, placed onto APES-coated microscope slides (see 2.4.4.1) and dried at 37°C.

2.4.4.3 Organoid immunofluorescence

Sections were deparaffinised by two 5 min incubations in xylene and hydrated through a series of alcohols as follows: a) 100% (v/v) ethanol for 1 min; b) 100% (v/v) ethanol for 1 min; c) 90% (v/v) ethanol for 1 min; and d) 70% (v/v) ethanol for 1 min. Sections were fully hydrated in dH₂O for 1 min and permeabilized in 0.2% (v/v) Triton X-100 in PBS, for 20 min. Sections were washed three times in PBS for 5 min with agitation and blocked using Blocker™ BSA (10%) in PBS (ThermoFisher Scientific) diluted to a 1% working solution in PBS for 1 h. Sections were incubated with primary antibody in PBS overnight at 4°C (Table 2.5, 2.3.10 Immunofluorescence). Sections were washed for 10 min with agitation in PBS, three times, prior to a 1 h incubation with appropriate secondary antibody – goat anti-mouse Alexa Fluor®488 (ThermoFisher Scientific, A-11001) or goat anti-rabbit Alexa Fluor®488 (ThermoFisher Scientific, A-11008) – diluted 1 in 200 in PSB. Sections were washed for 10 min in PBS, three times. Sections were mounted with DAPI-containing VECTASHEILD (Vector Laboratories). Images were obtained by fluorescence microscopy using a Zeiss Axio Observer.Z1 fitted with ApoTome 2.

2.4.4.4 Organoid immunohistochemistry

Sections were deparaffinised by two immersions in fresh xylene for 5 min. Sections were hydrated in a series of decreasing alcohols as follows: a) 100% (v/v) ethanol for 5 min; b) 3% (v/v) H₂O₂ in methanol for 10 min; c) 100% (v/v) ethanol for 1 min; d) 90% (v/v) ethanol for 1 min; and e) 70% (v/v) ethanol for 1 min. Sections were then placed in dH₂O for 1 min. Antigen retrieval was performed by submerging sections in 10mM citrate buffer (2.94g/l sodium citrate di hydrate in dH₂O, pH 6) in a cling-film covered container and microwaved at 800W

for 10 min; any evaporated citrate buffer was replenished and the sections microwaved for a further 10 min. Slides were cooled for 10 min under running tap water, then permeabilized with 0.2% (v/v) Triton X-100 in PBS for 5 min. Sections were washed twice for 5 min in TBS-T with constant agitation. Sections were drawn around using a PAP pen (Abcam) to create a hydrophobic barrier to retain and localize solutions on the section. Sections were blocked with 2.5% normal horse serum (Vector Laboratories) for 30 min in a humidified chamber at room temperature. Primary antibody diluted in 2.5% normal horse serum (Table 2.9) was added to the sections and incubated in a humidified chamber for 2 h. The sections were washed three times for 5 min in TBS-T. Sections were incubated for 30 min in a humidified chamber at room temperature with the appropriate secondary antibody, ImmPRESS HRP reagent kit peroxidase anti-rabbit IgG (made in horse) or anti-goat Ig (made in horse) (Vector Laboratories). Sections were washed three times for 5 min in TBS-T. The 3,3'-diaminobenzidine (DAB) mixture was prepared by mixing one DAB tablet and one urea tablet (Sigma-Aldrich) in 5 ml dH₂O. DAB solution was applied to the sections and incubated in a humidified chamber, protected from light, for 6 min. Slides were washed in dH₂O for 5 min with agitation. Sections were counterstained with haematoxylin and dehydrated through a series of increasing alcohols as follows: a) 70% (v/v) ethanol for 1 min; b) 90% (v/v) ethanol for 1 min; c) 100% (v/v) ethanol for 1 min, followed by another 1 min step in fresh 100% (v/v) ethanol; and d) xylene for 5 min, twice (with the second step being in fresh xylene). Slides were mounted with distyrene-plasticiser-xylene (DPX) mountant (Sigma-Aldrich).

Target	Manufacturer and Catalogue number	Host	Dilution of primary IgG
Active caspase-3	R&D systems (Abingdon, UK); AF835	Rabbit	1:2000
Chromogranin A (CgA)	Abcam (Cambridge, UK); ab15160	Rabbit	1:800
Doublecortin like kinase 1 (DCLK1)	Abcam (Cambridge, UK); ab31704	Rabbit	1:500
Lysozyme (Lyz)	Agilent Dako (Santa Clara, California); A0099	Rabbit	1:3500
Trefoil factor 3 (TFF3)	Santa Cruz Biotechnology (Insight Biotechnology Ltd., Middlesex, UK); sc-18272	Goat	1:500

2.4.4.5 *Haematoxylin and eosin staining*

Sections were deparaffinised by two 5 min incubations in xylene and hydrated through a series of alcohols as follows: a) 100% (v/v) ethanol for 1 min; b) 100% (v/v) ethanol for 1 min; c) 90% (v/v) ethanol for 1 min; and d) 70% (v/v) ethanol for 1 min. Sections were fully hydrated in dH₂O for 5 min. Sections were stained with haematoxylin for 3 min and run under tap water for 10 min, before staining with eosin for 3 min 30 sec. Excess eosin was removed by dipping in dH₂O and samples dehydrated through a series of alcohols: a) 70% (v/v) ethanol for 15 sec, b) 90% (v/v) ethanol for 15 sec, c) 100% (v/v) ethanol for 15 sec, d) 100% ethanol for 15 sec, followed by incubation in xylene for 10 min. Slides were mounted with DPX mountant.

2.4.5 Organoid Western blotting

2.4.5.1 *Preparation of protein lysates*

Organoids were dosed with 10µM bosutinib, 10µM imatinib or vehicle for 4 h. Organoids were washed twice with PBS (500µl), and extracted from the Matrigel by incubation with 400µl Cell Recovery Solution (Corning) for 40 min on ice. Organoids were resuspended by pipetting, 10ml ice cold PBS was added to further dilute Matrigel, and the suspension spun at 200g for 6 min at 4°C. Supernatant was discarded and the organoid pellet solubilised in 50µl RIPA buffer (Sigma-Aldrich) containing 1% (v/v) protease inhibitor cocktail III (Merck Millipore). Protein levels were determined using the DC™ Protein Assay (Bio-Rad) as described previously in 2.3.8. Western blotting protocol was undertaken as described previously (see 2.3.8.1 Preparation of protein lysates). Antibodies used are described in Tables 2.3 and 2.4 (2.3.8.3 Antibody incubations and membrane visualisation).

2.4.6 Organoid swelling assay

The swelling assay was developed by Dekkers *et al.* (2013) as a method to assess CFTR activity, in a semi-quantitative manner, in patients with cystic fibrosis to potentially predict patient responses to CFTR restoring drugs. Dekkers *et al.* found that addition of forskolin, a compound which activates chloride secretion through the CFTR channel, increased luminal and total organoid surface area in C57BL/6 mice small intestinal organoids and human rectal organoids, due to an increase in luminal fluid content. We therefore adapted this assay, to determine whether TKIs induced secretion in our organoid model. Static images of organoids at x20 magnification were obtained using a Zeiss Axiovert 25 microscope, before and after drug dosing (10µM) for 30 min. Organoids were drawn around using the freehand tool in ImageJ (Schneider *et al.*, 2012) to measure changes in area (i.e. swelling), indicative of

secretion. Due to the variability in organoid size, changes in area of each organoid were normalized to the organoid area at time zero.

2.5 Statistical analyses of cell line and organoid experiments

All data are expressed as the mean \pm standard error of the mean (SEM) of at least three independent experiments, unless otherwise stated. Statistical analyses were performed in Prism 6 (Version 6.01; GraphPad Software Inc, California, USA). The unpaired two-tailed Student's t-test was used on data sets that consisted of two sample groups. Those consisting of more than two sample groups were analysed by one-way analysis of variance (ANOVA), and where significance was reached, a Dunnett's post-test was performed. Correlations between two variables were assessed by Spearman's rank correlation coefficient. Area under the curve (AUC) was compared for cell and organoid permeability experiments, to decrease multiple comparisons and therefore the probability of false positives. N represents the number of biological repeats and, where appropriate, n refers to the number of organoids sampled (chapter 5) or number of technical repeats (chapter 3 and 4) per biological repeat. The statistical significance threshold was set at 0.05 in all analyses.

2.6 Genome-wide association study (GWAS)

2.6.1 Study design

The SPIRIT2 trial is a UK-based phase 3 prospective randomised trial to compare the clinical efficacy of daily oral dasatinib (100mg) and imatinib (400mg) for the treatment of CML, with a 5-year event free survival follow-up (www.clinicaltrials.gov; study identifier: NCT01460693). Ethical permission for the original study was obtained from the London Research Ethics Committee, UK (REC ref# 07/H718/90). Written informed consent was obtained prior to patient inclusion. Patient information on age, gender and body mass index (BMI) was collected. GI adverse events, including occurrence of diarrhoea and grade, were logged according to the Common Terminology Criteria for Adverse Events (CTCAE) system, of the National Cancer Institute (www.ctep.cancer.gov/protocolDevelopment/electronic_applications/docs) Clinical information was kindly supplied by Prof Stephen O'Brien, Centre for Life, Newcastle University. Patient samples were a gift from the CML subgroup of the UK National Cancer Research Institute, and staff at the SPIRIT2 biobank (Prof Letizia Foroni and Prof Sandra Loaiza, Hammersmith Hospital campus, Imperial College London) kindly supplied these samples. In addition, Prof Richard E Clark, permitted access to these samples. The study was conducted in accordance with the declaration of Helsinki.

Genotyping had already been undertaken on some dasatinib-treated patients from the SPIRIT2 trial to perform a genome-wide association study (GWAS) to identify SNPs associated with dasatinib-induced pleural effusion, which occurs in about a third of patients (Fullmer *et al.*, 2011), in a previous study (Drs Ana Rodriguez, Benjamin Francis, Eunice Zhang and Andrea Davies, University of Liverpool, unpublished data). Imatinib patients were not genotyped, as the pleural effusion adverse event is rare with this treatment (Cohen *et al.*, 2002). In this study, we aim to use adverse event information from the SPIRIT2 trial and genotype information from the study on dasatinib-induced pleural effusion to identify genetic variants associated with dasatinib-induced diarrhoea.

2.6.1.1 Patient cohort

A total of 814 CML patients were recruited to the SPIRIT2 trial, 407 of which were recruited to the dasatinib arm, and assigned to the discovery cohort or replication cohort. Patients with high DNA concentrations to allow genome-wide screening were assigned to the discovery cohort. After removal of patients for which samples were not obtained or DNA extraction failed (51) or patient consent not obtained (9), 347 patients remained: 181 within the discovery cohort and 166 within the replication cohort (Fig 2.4). No power calculation was performed to determine the required patient sample size for this study.

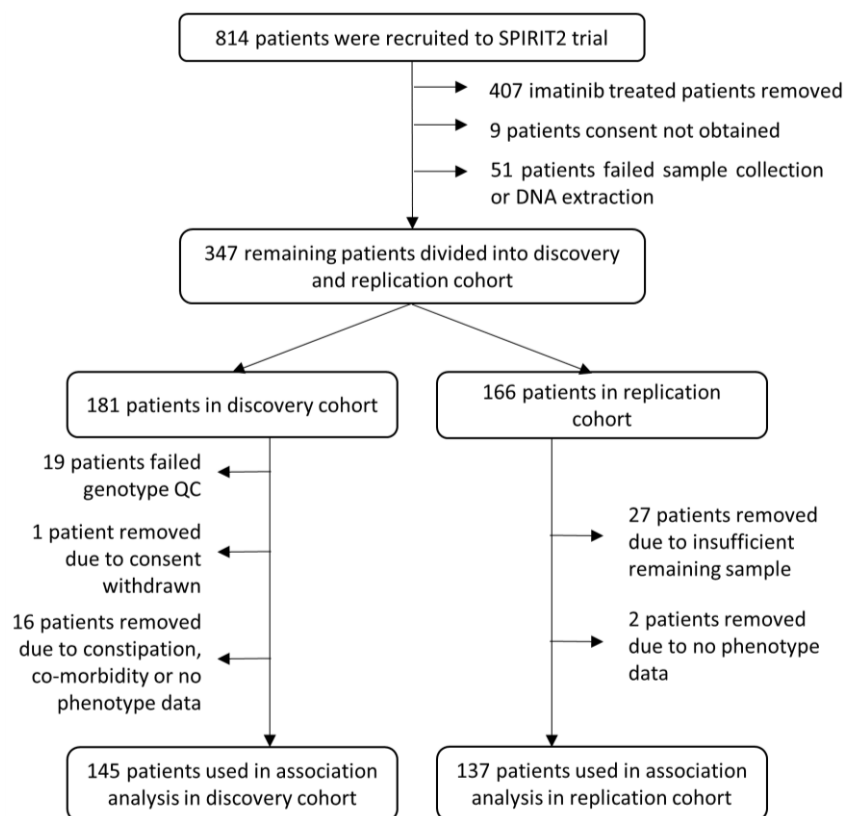


Figure 2.4. Flow chart of discovery and validation cohort used in dasatinib-induced diarrhoea GWAS.

2.6.2 DNA collection and extraction

DNA was extracted from patient bio-banked peripheral blood mononuclear cells using the AllPrep DNA/RNA Mini Kit (Qiagen®, Manchester, UK) according to the manufacturer's protocol. This was performed by Dr Andrea Davies and Ms Gemma Jones at the University of Liverpool.

2.6.3 Discovery cohort

2.6.3.1 *Genome-wide genotyping*

The purity of DNA (ratio of absorbance at 260nm and 280nm i.e. A260/A280) was assessed using the ThermoFisher Scientific NanoDrop™ 8000 UV-Vis Spectrophotometer and only samples with A260/A280 ratio 1.7-2.1 were included in downstream genotyping. The amount of double-stranded DNA was measured using the Quant-iT PicoGreen dsDNA Assay Kit (ThermoFisher Scientific). DNA was diluted to 50ng/μl in nuclease-free H₂O for genome-wide genotyping. This was performed by Dr Andrea Davies, at the University of Liverpool.

One hundred and eighty-one samples were genotyped using the Infinium™ OmniExpressExome-8 v1.4 chip (Illumina, Cambridge, UK) at the Oxford Genomic Centre, Wellcome Trust Centre for Human Genetics, Oxford University, UK. This was coordinated by Dr Eunice Zhang, at the University of Liverpool.

2.6.3.2 *Data quality control*

Genotype quality control was undertaken at both the individual sample level and the SNP level. This analysis was performed with binary .bim/.bed/.fam files using PLINK v1.07 (www.cog-genomics.org/plink2) (Purcell *et al.*, 2007). R v3.1.1. software (www.r-project.org) was used to generate QC plots. Data quality control analyses were undertaken with the help of Dr Benjamin Francis, in the Biostatistics Department at the University of Liverpool.

2.6.3.3 *Data quality control per individual*

Individuals with more than 3% of their genotyping data missing were removed from the analyses (n=3). Individuals with discrepancies between their reported gender and the predicted gender using X chromosome heterozygosity (whereby individuals with X chromosome heterozygosity >0.8 and <0.2 are assigned a genotypic gender of male and female, respectively) were also removed (n=0). Individuals with an unassigned genotypic gender or missing reported gender were removed (n=0). Identity-by-descent (relatedness, PI_HAT) – the average number of non-autosomal independent SNPs that each pair of individuals share – was calculated by pruning 50kb data regions and correlating the SNPs

within these regions. No kinship was detected between any sample pairs by identity by descent. Heterozygosity rate was calculated in an attempt to detect potential DNA contamination or inbreeding. Whilst 2 individuals fell outside of the ± 2 standard deviation (SD) margins of heterozygosity rate, these individuals were not removed due to their close proximity to the ± 2 SD cut-off point. Samples were merged with the HapMap Yoruba, Han Chinese, Japanese and Caucasian dataset, and principal component analysis was used to identify ethnic outliers. Non-Caucasian individuals were removed from the study (n=16). After quality control streamlining, the data set consisted of 161 patients.

2.6.3.4 Data quality control per SNP

A SNP call rate <95% can indicate inaccurate genotyping, therefore these SNPs were removed (n=66,225). SNPs with a minor allele frequency <1% were removed (n=266,747). Nineteen SNPs deviating from the Hardy-Weinberg Equilibrium (HWE) ($p < 1 \times 10^{-5}$) were also removed, leaving 617,980 SNPs that passed quality control.

2.6.3.5 Imputation

The Wellcome Trust Case Control Consortium (WTCCC) subjects of Caucasian ancestry were merged with our SPIRIT2 patient set to increase imputation accuracy. Haplotype backbone data was created based on genotype data using the SHAPEIT2 v2.r644 software package (Delaneau *et al.*, 2013). Imputation was performed using IMPUTE2 v2.3.0 (Howie *et al.*, 2009) with the 1000 Genomes March 2012 release. Imputed SNPs with a minor allele frequency <1%, INFO score (estimation of imputation accuracy) <0.4 and HWE p-value < 1×10^{-5} were excluded. After post-imputation quality control, genotype information on 9,080,496 SNPs remained for analysis. Caucasian WTCCC subjects were then removed and not used in subsequent analyses. Imputation was undertaken by Dr Benjamin Francis.

2.6.4 Association analysis

Patients were grouped based on diarrhoea phenotype into controls and cases: diarrhoea absent (grade 0) and diarrhoea present (grades 1-4), respectively. Sixteen patients had constipation, missing diarrhoea phenotype information or co-morbidity, and were therefore not used in the association analysis, thus leaving 145 patients to take forward to subsequent analyses (Fig 2.4).

Imputed genotypes were analysed in dosage format using the frequentist additive model in SNPtest (Burton *et al.*, 2007). The qqman package in R v.3.1.1. (www.cran.r-project.org) was used to generate the Manhattan plot. LocusZoom (Pruim *et al.*, 2010) was used to generate

regional association plots of SNPs which reached suggestive significance ($p < 1 \times 10^{-5}$) or genome-wide significance ($p < 5 \times 10^{-8}$). Statistical analysis was undertaken in SNPtest. Association analysis was performed with the help of Dr Benjamin Francis, and data interpretation was achieved with the assistance of Dr Eunice Zhang.

2.6.5 Validation and replication of lead single nucleotide polymorphisms (SNPs)

Lead SNPs identified from the discovery cohort with $p < 1 \times 10^{-5}$ were assessed. Singleton SNPs, those without any correlated SNPs, were not considered for validation or replication, due to the high probability of a false-positive association. Among correlated SNPs (with $r^2 > 0.2$), only the SNP with the most significant p-value, within each linkage-disequilibrium block, was taken forward for validation and replication.

Genotyping was undertaken using either TaqMan™ (Applied Biosystems) or KASP™ (LGC Biosearch Technologies, Hoddesdon, UK) SNP assays on the Applied Biosystems 7900HT Fast Real-Time PCR System. Among the six SNPs selected for validation and replication, two were inventoried TaqMan™ SNP Genotyping assays (rs35636998 and rs9559427); 2 were successfully custom designed TaqMan™ SNP Genotyping assays (using the online tool: www.thermofisher.com/order/custom-genomic-products/tools/gene-expression/) (rs12424256 and rs73718779); and 2 failed custom design and were redesigned using KASP™ technology (using the online tool: www.biosearchtech.com/products/pcr-kits-and-reagents/genotyping-assays/kasp-genotyping-chemistry) (rs6975293 and rs6760938). Probe details are listed in Table 2.10.

Genotypes predicted by imputation were then compared to genotypes assigned by TaqMan™ or KASP™ genotyping to calculate 'concordance with imputation' as a percentage. Adherence to HWE was calculated in an attempt to assess genotyping accuracy. Logistic regression assuming an additive mode of inheritance was performed in PLINK v1.07 on binary .bim/.bed/.fam files containing genotype information in order to calculate allelic odds ratios and P-values of associations.

Table 2.10 Sequences of Taqman™ and KASP™ probes for the six SNPs in the imputation validation and replication study. SNPs of interest are shown in square brackets (bold text). Polymorphisms (other than the SNP of interest) within the context sequence of KASP assays are indicated in accordance with IUPAC codes.			
SNP	Assay Type	Context Sequence (5' - 3')	Design Strand (forward or reverse)
rs12424256	Taqman™ (Custom)	CTATATTGCCAGGCTGGTCTCAAA[C/T]T CCTGACCTCAGGTGATCTGCCTGC	Reverse
rs9559427	Taqman™ (Inventoried)	TGTAAAGGTTTGTATACAGGTAAC[C/T] ACGTGTCATAGAGGTTTGTGTACA	Reverse
rs35636998	Taqman™ (Inventoried)	GCCACTGTGCCAGGCCAGATTTTG[A/G] CAAGTTTTAAAAGTGCCAGATTAA	Reverse
rs6975293	Taqman™ (Custom)	CTCTGGGTCTTATATCAGTGTCTGTTCTCTG GGACCAGCACTGKCCCCATATGG[C/G]TA CCACTGGGACGTGTAGTTGACCTCTGAYG TGCACRGCAGATGCACGGACAGKCAGGG	Forward
rs6760938	KASP™ (Custom)	ATGCACCTKCATGTCAATGGGGCTGGAGT AAGGCTCCCACGCTGCTGTCTTCCCCAYA[C/T]CCTGACAGCTGAGTGTGGGGACAA AAGTGTGCCCTTCCCTCCAGTGGCCAACA CRTGGTCT	Forward
rs73718779	KASP™ (Custom)	AGTTTGAGCATTTTCATTATCACTT[C/T]G CAATAATGCATAAACACTGAACAA	Reverse

2.6.5.1 TaqMan™ genotyping

Genomic DNA (40ng), including 10% repeats as quality control, and negative control (nuclease-free dH₂O) were loaded into 384-well optical plates and dried overnight. DNA was amplified in a 5µL reaction mix containing 2.5µL 2x Genotyping Master Mix (Applied Biosystems, 4371355), 0.125µL 40x TaqMan™ SNP Genotyping assay and 2.375µL nuclease-free H₂O. The plate was pre-read using the Applied Biosystems 7900HT Fast Real-Time PCR System to identify background fluorescence. Thermo-cycling was carried out with an initial activation step at 95°C for 10 min, followed by 40 cycles of 95°C for 15 sec (denaturation) and 60°C for 90 sec (primer annealing and extension). A post-read was performed after thermo-cycling and allelic discrimination was undertaken using SDS v2.2 (Applied Biosystems, Paisley, UK). An example allelic discrimination plot can be viewed in Fig 2.5.

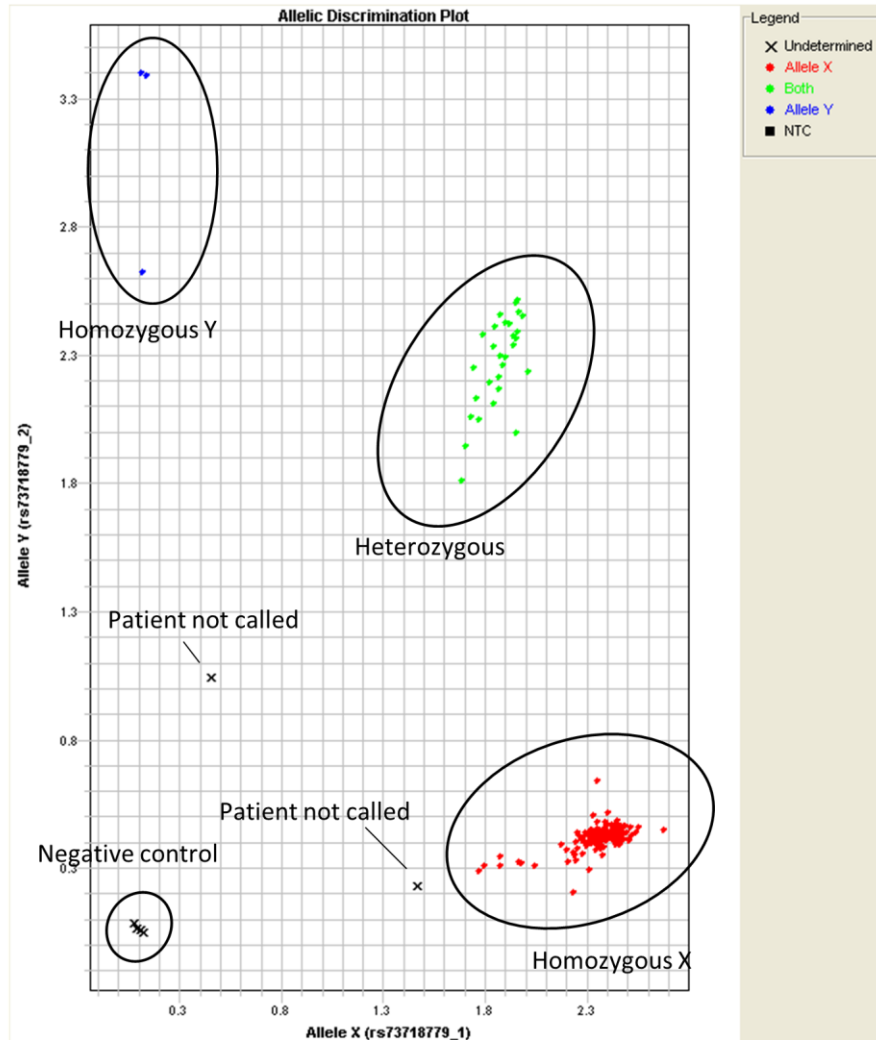


Figure 2.5. Annotated allelic discrimination plot for rs73718779 generated in SDS v2.2. Samples automatically called as homozygous X, heterozygous and homozygous Y are shown as red, green and blue circles respectively. Samples which were not called, including negative controls, are shown as black crosses.

2.6.5.2 KASP™ genotyping

Genomic DNA (40ng) and negative control (nuclease-free dH₂O) was loaded into 384-well optical plates, again including 10% repeats as quality control, and dried overnight. DNA was amplified in a 5µL reaction containing 2.5µL KASP v4.0 2x Master Mix (LGC, KBS-1016-021), 0.07µL primer and 2.43µL nuclease-free H₂O. Thermo-cycling was performed using the 61-55°C and 68-62°C touchdown protocols for rs6975293 and rs6760938, respectively, on the Applied Biosystems 7900HT Fast Real-Time PCR System. Cycling conditions were as follows: 1) a *Taq* enzyme activation step of 94°C for 15 min; 2) 10 touchdown cycles: 20 sec at 94°C then 60 sec at 61°C (rs6975293) or 68°C (rs6760938) with the 60 sec step decreasing by 0.6°C each cycle; 3) 26 cycles: 20 sec at 94°C then 60 sec at 55°C (rs6975293) or 62°C (rs6760938);

and 4) 30°C for 60 sec. The plate was read after thermo-cycling and allelic discrimination was carried out using SDS v2.2 (Applied Biosystems). An example allelic discrimination plot can be viewed in Fig 2.5.

2.6.6 Replication cohort

A potential 166 dasatinib-treated patients were available for the replication cohort (inclusion criteria described above). However, insufficient DNA remained to genotype 27 patients and adverse event information was not available for 2 patients, thus leaving a total of 137 patients to be taken forward into the replication cohort (Fig 2.4). DNA extraction and TaqMan™ or KASP™ genotyping was performed as above. DNA concentrations were determined using a ThermoFisher Scientific Nanodrop 8000 UV-VIS Spectrophotometer. As with the analysis of PCR-based genotype data in the discovery cohort, HWE was calculated, and logistic regression assuming an additive mode of inheritance was performed in PLINK v1.07 to determine allelic odds ratios and P-values for associations.

**CHAPTER 3: INVESTIGATING THE
MECHANISMS OF TYROSINE
KINASE INHIBITOR-INDUCED
DIARRHOEA USING CACO-2
CELLS**

3.1 Introduction

Within the gut, intestinal permeability is tightly regulated to allow the passage of nutrients into the circulation while preventing the translocation of bacteria and food antigens. Epithelial junctional complexes connect neighbouring cells of the epithelial layer and control paracellular permeability (Zihni *et al.*, 2016). They act as a 'gate' to facilitate the passive flow of ions and molecules through the paracellular space, and therefore also control water flow between the intestinal lumen and underlying tissue (Zihni *et al.*, 2016). Consequently, increased paracellular permeability due to epithelial junction disruption can lead to diarrhoea.

It is therefore not surprising that decreased levels and altered distribution of junctional complex proteins is seen in diarrhoea-dominant irritable bowel syndrome (IBS-D) (Bertiaux-Vanda *et al.*, 2011; Wilcz-Villega *et al.*, 2014) and inflammatory bowel disease (IBD) (Prasad *et al.*, 2005; Oshima *et al.*, 2008; Arijs *et al.*, 2011; Poritz *et al.*, 2011; Das *et al.*, 2012; Soletti *et al.*, 2013; Zhang *et al.*, 2015). For example, decreased levels and altered distribution of the junction proteins occludin (Bertiaux-Vanda *et al.*, 2011) and ZO-1 (Wilcz-Villega *et al.*, 2014) are seen in patients with IBS-D. Moreover, patients with Crohn's disease and ulcerative colitis frequently have decreased levels of occludin (Poritz *et al.*, 2011), ZO-1 (Das *et al.*, 2012) and E-cadherin (Arijs *et al.*, 2011; Zhang *et al.*, 2015). Epithelial junction disruption has also been implicated in chemotherapy-induced diarrhoea through the use of cell line and rodent models (Hamada *et al.*, 2010, 2013; Youmba *et al.*, 2012; Nakao *et al.*, 2012; Beutheu *et al.*, 2013; Song *et al.*, 2013; Fan *et al.*, 2014; Hong *et al.*, 2014; Buhrmann *et al.*, 2015; Refaat *et al.*, 2015; Tao *et al.*, 2015), and in patient studies, where increased intestinal permeability is seen in individuals treated with chemotherapy agents such as methotrexate (Meng *et al.*, 2016) and 5-fluorouracil (5-FU) (Daniele *et al.*, 2001). See Table 1.5 (1.4.2 Intestinal barrier dysfunction: the paracellular pathway) for a summary of studies showing alterations in TJ and AJ protein levels during chemotherapy.

There are two major categories of epithelial junctional complexes: tight junctions (TJs) (also known as zonula occludens) and the adherens junctions (AJs) (Zihni *et al.*, 2016). Whilst AJs have some control over paracellular permeability (Greenspon *et al.*, 2011), the main role of these junctions is in initiation, maintenance and maturation of cell-to-cell contacts. Formation of AJs leads to rapid assembly of the more apically located TJs, which have a more prominent role in regulating paracellular flux.

Paracellular permeability can be divided into two independent pathways: the charge-selective 'pore' permeation pathway and the size-selection 'leak' permeation pathway which controls flux of substances based on their charge and size, respectively (Zihni *et al.*, 2016).

The size-selective pathway allows the diffusion of larger solutes and macromolecules $\leq 60\text{\AA}$ in size (Buschmann *et al.*, 2013). Changes in this pathway can be determined by measuring diffusion of a tracer molecule – for example a fluorescently-labelled polysaccharide such as FITC-dextran – across a membrane/monolayer *in vitro*, *ex vivo* or *in vivo* (Zihni *et al.*, 2016). Occludin, a transmembrane protein in TJ complexes, is thought to be highly important in controlling macromolecular flux (Buschmann *et al.*, 2013), but the mechanistic basis of macromolecular diffusion is far from elucidated (Zihni *et al.*, 2016).

Passage through the charge-selective pathway is controlled by claudins, transmembrane proteins in TJ complexes which enables flux of ions up to $\sim 4.5\text{\AA}$ (Watson *et al.*, 2001). Claudins assemble into ion-selective channels (Krug *et al.*, 2012) which can be grouped according to their selectivity into: a) cation-selective claudins, e.g. claudin 2; b) anion-selective claudins, e.g. claudin 17 (Krug *et al.*, 2014); and c) sealing claudins which restrict ion transport, e.g. claudin 1 (Zihni *et al.*, 2016). The charge-selective pathway is believed to be controlled by channel opening, endocytosis, as well as transcriptional and post-transcriptional regulation of claudins. Alterations in claudin levels are seen in IBS-D (Bertiaux-Vanda *et al.*, 2011), ulcerative colitis (Prasad *et al.*, 2005; Oshima *et al.*, 2008; Poritz *et al.*, 2011; Das *et al.*, 2012) and Crohn's disease (Prasad *et al.*, 2005; Poritz *et al.*, 2011) and rodent models treated with the cytotoxic chemotherapeutic agents irinotecan, methotrexate and 5-FU (Nakao *et al.*, 2012; Youmba *et al.*, 2012; Hamada *et al.*, 2013; Song *et al.*, 2013; Buhrmann *et al.*, 2015). Changes in this pathway can be assessed by measuring electrical resistance (also known as transepithelial electrical resistance, TEER) across a membrane or monolayer (Furuse *et al.*, 2001).

Both the size-selective and the charge-selective pathways have been linked to chemotherapy-induced diarrhoea *in vitro* (Beutheu *et al.*, 2013; Fan *et al.*, 2014). For example, use of rat IEC-6 intestinal cell monolayers has shown erlotinib can increase permeability via the size-selective pathway (Fan *et al.*, 2014), whilst treatment of human Caco-2 adenocarcinoma epithelial cells with methotrexate can alter FITC-dextran flux and TEER (Youmba *et al.*, 2012; Beutheu *et al.*, 2013).

In this chapter, we have tested the hypothesis that the BCR-ABL inhibitors bosutinib, imatinib and dasatinib, and the EGFR inhibitor gefitinib, increase paracellular permeability and disrupt

cell junctions of intestinal epithelial cells *in vitro*. The aims of the chapter were to use the human Caco2 intestinal epithelium cell model to:

1. Evaluate the effect of bosutinib, imatinib, dasatinib and gefitinib on paracellular permeability (via both the 'pore' pathway and the 'leak' pathway) and cell-cell adhesion
2. Compare the cytotoxicity of bosutinib, imatinib, dasatinib and gefitinib
3. Determine the ability of bosutinib, imatinib, dasatinib and gefitinib to alter protein levels, mRNA levels and localization of TJ and AJ proteins, focussing on occludin, E-cadherin and ZO-1
4. Analyse changes in the cytoskeleton after addition of bosutinib, imatinib, dasatinib and gefitinib

3.2 Results

3.2.1 Caco-2 cells form a fully differentiated monolayer of polarised enterocytes within 10 days

Caco-2 cells were deemed an adequate model due to their human intestinal origin and frequent use in academic and pharmaceutical research (Carr *et al.*, 2017). They are undifferentiated cells (Engle *et al.*, 1998), and therefore preliminary experiments were required to determine the time period necessary for sufficient differentiation into mature polarised enterocytes with distinct apical and basal aspects. Accumulation of intestinal alkaline phosphatase (ALPI), a well-documented enterocyte differentiation marker (Hinnebusch *et al.*, 2004), was used to determine differentiation progression. Western blot analysis showed both dimeric (~140 kDa) and monomeric ALPI (~70 kDa) increased with time (Fig 3.1; One-way ANOVA, $p < 0.05$). Monomeric ALPI levels were significantly increased at days 10 and 13 relative to day 1 (Fig 3.1B; Dunnett's test, $p < 0.05$), whereas dimeric ALPI levels were only significantly increased at day 13 (Fig 3.1C; Dunnett's test, $p < 0.05$). Levels of both monomeric and dimeric ALPI appeared to plateau around 10 days after seeding.

The presence of a confluent cell monolayer after 10 days was further determined by using TEER. TEER was measured daily, for up to 15 days of growth (Fig 3.2). TEER increased with time and was significantly higher than day 1 from day 5 onwards (Fig 3.2; Dunnett's test, $p < 0.05$), excluding days 6, 7 and 12 – presumably due to a lower number of TEER readings taken on these days. TEER appeared to plateau at around day 10 – consistent with plateauing

levels of ALPI. Caco-2 monolayers used in subsequent experiments were therefore allowed to differentiate for 10-14 days prior to drug treatment.

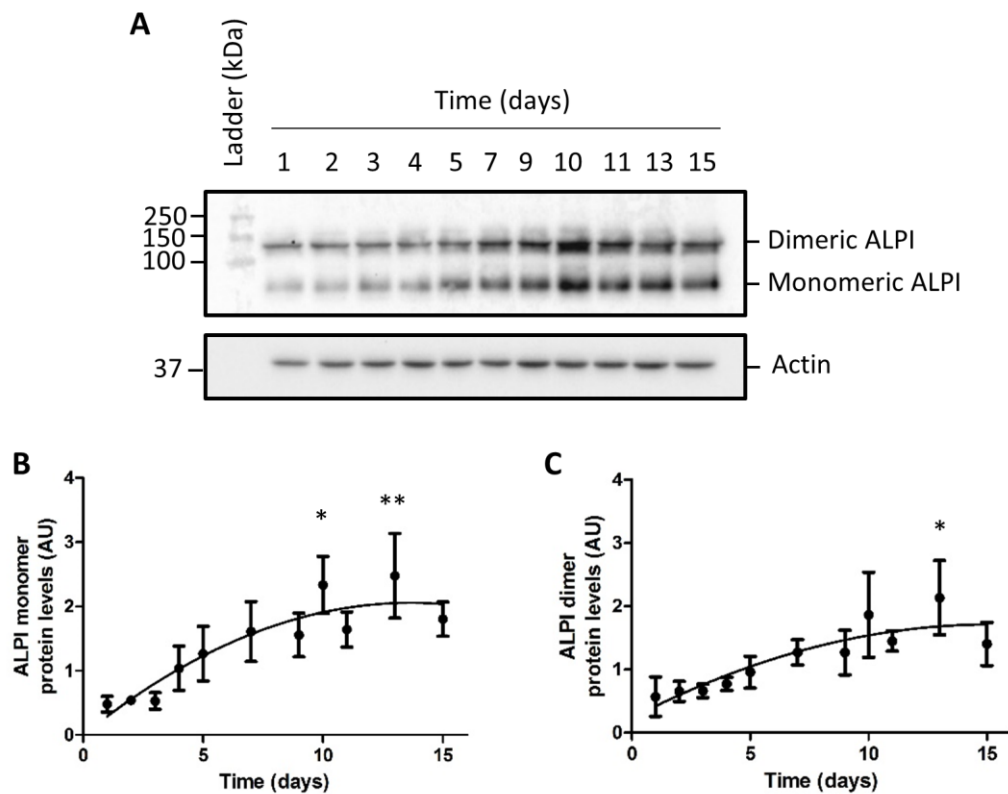


Figure 3.1 Expression of intestinal alkaline phosphatase (ALPI) during Caco-2 cell differentiation. Caco-2 cells were grown to a monolayer and allowed to differentiate for up to 15 days. The expression of monomeric ALPI (B) and dimeric ALPI (C) was analysed by Western blot (A). * $p < 0.05$, ** $p < 0.01$ versus day 1, One-way ANOVA followed by Dunnett's test, mean \pm SEM, N=3.

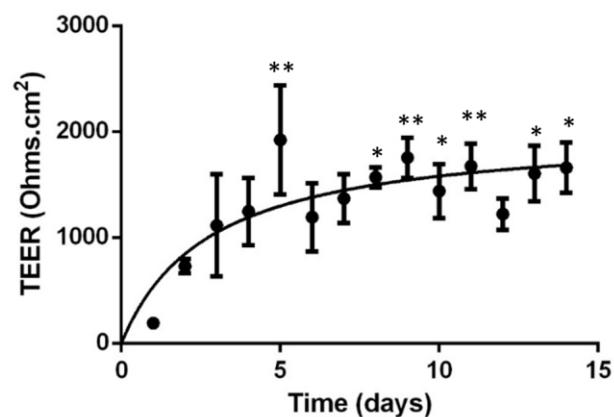


Figure 3.2. Decrease in paracellular permeability during Caco-2 cell differentiation. Caco-2 cells were seeded onto transwell membranes. Transepithelial electrical resistance (TEER) was measured each day from day 2 up to day 15. * $P < 0.05$, ** $P < 0.01$ versus day 2, One-way ANOVA followed by Dunnett's test, mean \pm SEM, N=3-4.

3.2.2 Apical bosutinib increases flux through the charge-selective permeation pathway in Caco-2 cells

Increased paracellular permeability via the 'pore' pathway has been implicated in TKI-induced diarrhoea (Fan *et al.*, 2014); therefore, changes in ion flux across Caco-2 monolayers after TKI addition were studied by measuring transepithelial electrical resistance (TEER).

TKIs were administered to the apical aspect to mimic oral administration, i.e. gut luminal exposure, to ensure experiments were as physiologically relevant as possible. All TKIs tested caused a time- and dose-dependent decrease in TEER (Fig 3.3). Bosutinib caused the most marked decrease in TEER at the 24 h time point out of all the TKIs tested (Fig 3.3A). TEER decreased by ~70%, ~40%, ~30% and 0% after 24 h treatment with 10 μ M bosutinib, dasatinib, gefitinib and imatinib, respectively. Bosutinib also induced the most rapid drop in TEER with values decreasing as early as 15 minutes after addition of the drug.

To statistically analyse data, area under the curve was calculated for each concentration. Bosutinib (Fig 3.3A; Dunnett's test, $p < 0.001$), gefitinib (Fig 3.3E; Dunnett's test, $p < 0.01$) and dasatinib (Fig 3.3D; Dunnett's test, $p < 0.05$) significantly decreased TEER at 10 μ M; however, imatinib did not significantly decrease TEER until a concentration of 50 μ M was reached (Fig 3.3C; Dunnett's test, $p < 0.01$).

To determine the minimum bosutinib concentration capable of decreasing TEER, TEER was assessed using concentrations below 10 μ M. The reported C_{max} plasma concentrations in Ph+ leukaemia patients during treatment with 500mg bosutinib daily at day 1, 150nM, and day 15, 400nM, were also included (Pfizer, 2014; European Medicines Agency, 2018). However, the steady state trough plasma concentration in patients receiving this same dose regime, 120nM, was not included (Mita *et al.*, 2018). Five micromolar bosutinib significantly decreased TEER (Fig 3.3B; Dunnett's test, $p < 0.01$) but lower concentrations, including plasma concentrations found in patients, had no significant effect.

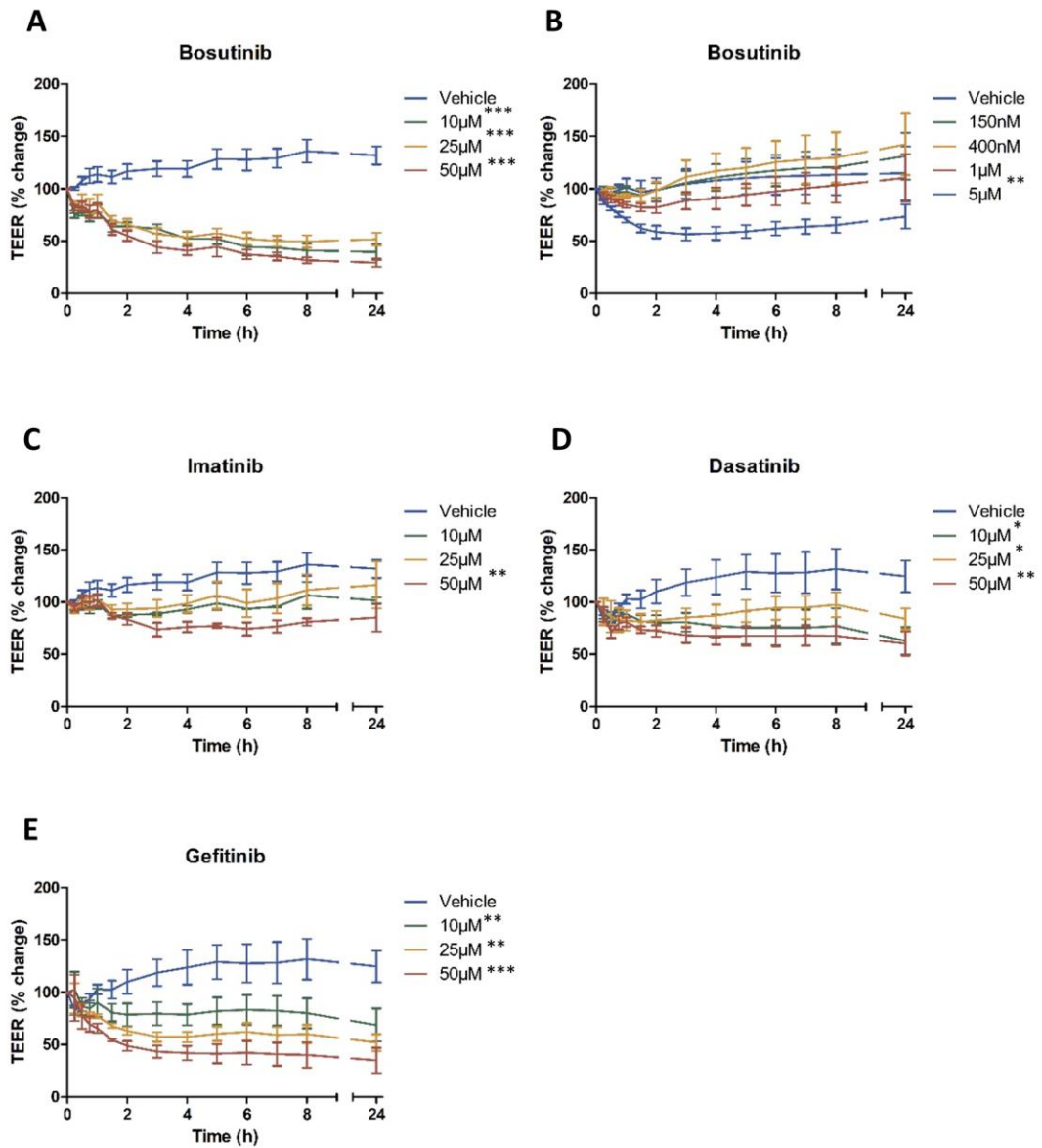


Figure 3.3. Effect of apical TKIs on the charge-selective permeation pathways. Caco-2 cells were seeded into transwell plates. After 10-14 days, bosutinib (A, B), imatinib (C), dasatinib (D) or gefitinib (E) was added to the apical compartment and transepithelial resistance (TEER) across the monolayer was measured using chopstick electrodes as described in methods. Data are presented relative to the starting value (time zero). * $p < 0.05$, ** $p < 0.01$, *** $p < 0.001$ of area under the curve of treated versus vehicle, One-way ANOVA followed by Dunnett's test, mean \pm SEM, N=3-4.

3.2.3 Basolateral plasma concentrations of TKIs do not alter flux through the charge-selective permeation pathway in Caco-2 cells

To gain an understanding of the effects of systemic TKIs (TKIs in the plasma after absorption) on permeability, changes in TEER were assessed after administering C_{max} plasma concentrations of TKIs to the basolateral compartment: 400nM bosutinib (Pfizer, 2014), 3 μ M imatinib (De Francia *et al.*, 2013), 150nM dasatinib (Wang *et al.*, 2013) and 1.5 μ M gefitinib (Miura *et al.*, 2014). No significant changes in TEER were seen over the 24 h period studied (Fig 3.4; t-test, $p>0.05$). Gefitinib induced a slight decrease in TEER although this did not achieve significance (Fig 3.4D; t-test, $p>0.05$).

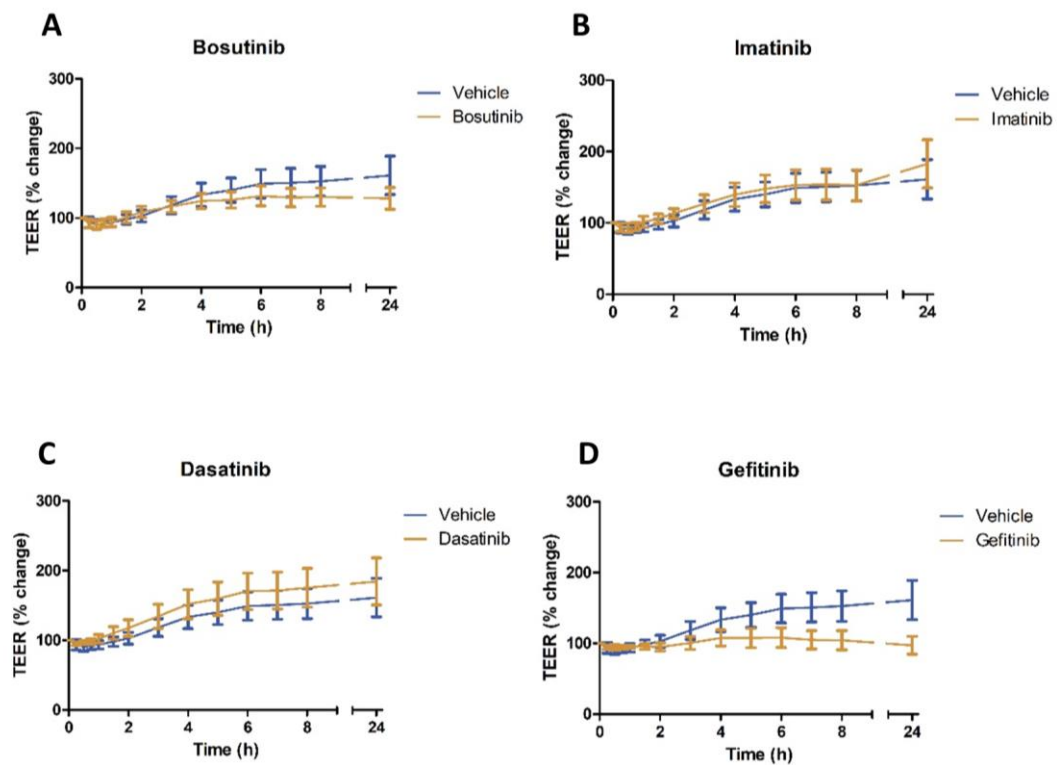


Figure 3.4. Effect of basolateral TKIs at C_{max} plasma concentrations on the charge-selective permeation pathway. Caco-2 cells were seeded onto transwell membranes. After 10-14 days, 400nM bosutinib (A), 3 μ M imatinib (B), 150nM dasatinib (C) or 1.5 μ M gefitinib (D) was administered to the basolateral compartment and transepithelial resistance (TEER) across the monolayer was measured. Data are presented relative to the starting value (time zero). Area under the curve of treated versus vehicle control was not significant for bosutinib, imatinib, dasatinib and gefitinib, t-test, mean \pm SEM, N=3-4.

3.2.4 Bosutinib increases flux through the size-selective permeation pathway in Caco-2 cells

As the 'leak' pathway may be involved in TKI-induced diarrhoea (Fan *et al.*, 2014), alterations in the size-selective permeation pathway were assessed by measuring the flux of a fluorescently labelled polysaccharide 4kDa FITC-dextran (FD-4) across the monolayer. FD-4 (2mg/ml) was administered to the apical compartment in combination with TKIs (up to 100 μ M), and accumulation of FD-4 in the basal compartment was measured. An increase in para-cellular permeability results in increased basal accumulation of FD-4. Bosutinib increased basal FD-4 accumulation in a time- and dose-dependent manner that reached significance at 25 μ M (Fig 3.5A; One-way ANOVA, $p < 0.01$). However, area under the curve analysis found gefitinib and dasatinib did not significantly increase FD-4 accumulation even at 100 μ M (Fig 3.5C, D; One-way ANOVA, $p > 0.05$). Imatinib (100 μ M) significantly increased flux through the 'leak' pathway, but the concentration of basal FD-4 accumulation was much lower than that induced by 100 μ M bosutinib (~600 μ g/mL and ~150 μ g/mL for bosutinib and imatinib, respectively). These data show that bosutinib consistently induces the greatest and most rapid increase in permeability to all the other TKIs tested.

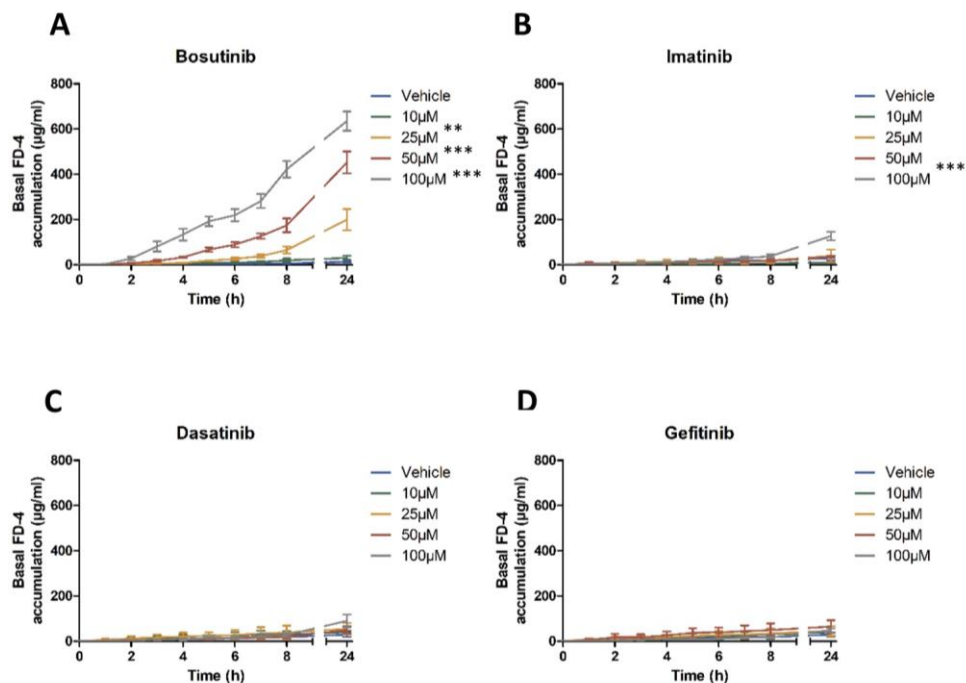


Figure 3.5. Effect of TKIs on size-selective permeation pathway. Caco-2 cells were seeded onto transwell membranes. After 10-14 days, 4kDa FITC-dextran (2mg/mL, FD-4) and a concentration range of bosutinib (A), imatinib (B), dasatinib (C) and gefitinib (D) were added to the apical compartment. DMEM (50 μ L) were collected from the basal compartment for up to 24h and fluorescence intensity measured. ** $p < 0.01$, *** $p < 0.001$ of area under the curve of treated versus vehicle, One-way ANOVA followed by Dunnett's test, mean \pm SEM, N=5-8.

3.2.5 Bosutinib is cytotoxic to Caco-2 cells

To assess whether the observed increases in permeability were a consequence of drug-induced cell death, Caco-2 cell viability was determined after TKI treatment for 24 h using MTT assay (Fig 3.6) and CellTitreGlo® assays (Fig 3.7).

MTT assays showed bosutinib, imatinib, dasatinib and gefitinib all significantly increased and then decreased viability with increasing drug concentrations (Fig 3.6; One-way ANOVA, $p < 0.05$). Bosutinib appeared to be the most cytotoxic, with viability decreasing from 50 μM after a 24 h incubation, whilst imatinib, dasatinib and gefitinib did not decrease viability until a concentration of 250 μM was reached (Fig 3.6; Dunnett's test, $p < 0.05$). Significant increases in viability were seen at 50 μM imatinib, 100 μM dasatinib and 50-100 μM gefitinib (Fig 3.6B-D; Dunnett's test, $p < 0.05$). No significant increases in viability were seen after bosutinib treatment for 24 h at any concentration, but 3 h treatment of 25 μM bosutinib significantly increased cell viability (Fig 3.6A; Dunnett's test, $p < 0.05$).

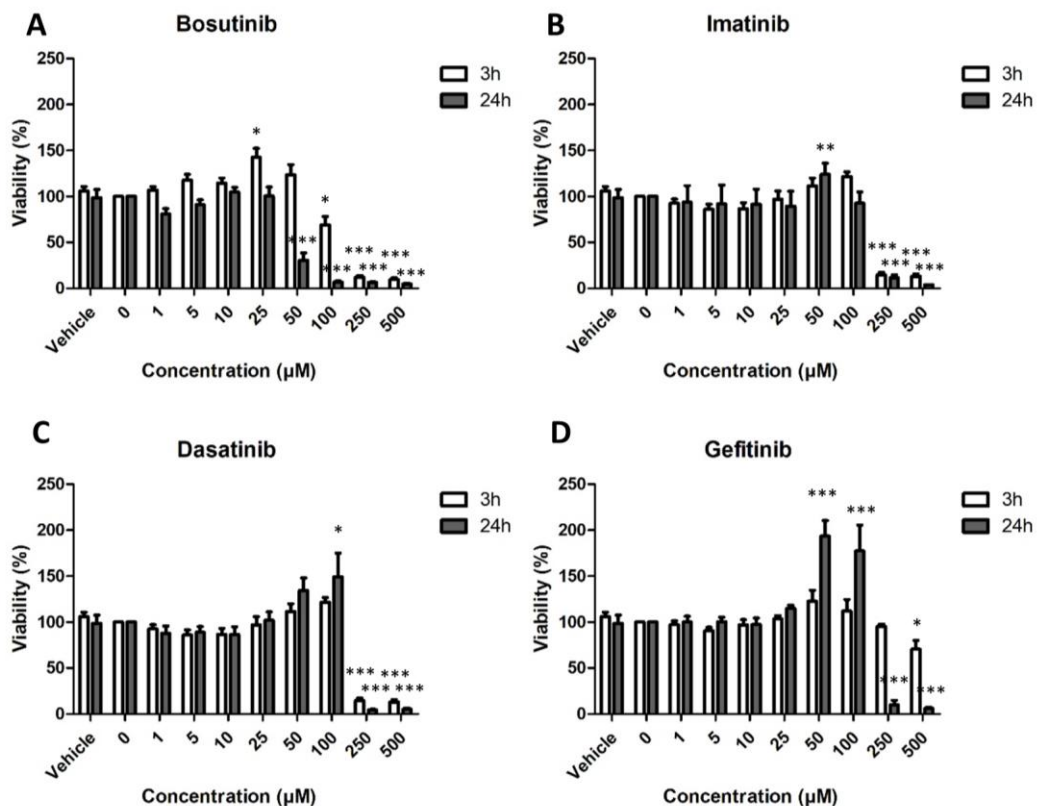


Figure 3.6. Effect of TKIs on cell viability using MTT assay. Caco-2 cells were treated with up to 500 μM bosutinib (A), imatinib (B), dasatinib (C) or gefitinib (D) for 3h and 24h. The percentage of viable cells remaining was then determined using MTT assay which measures NADH-dependent oxidoreductase enzyme activity. Data are representation as the percentage change relative to 0 μM . * $p < 0.05$, ** $p < 0.01$, *** $p < 0.001$ versus vehicle, One-way ANOVA followed by Dunnett's test, mean \pm SEM, N=3-5, n=3.

CellTiterGlo® assays demonstrated a more gradual and dose-dependent decrease in viability compared to the MTT assay, which showed a marked drop-off in viability above a certain threshold. Consistent with MTT results, bosutinib and gefitinib significantly decreased cell viability at 50µM and 250µM, respectively, after 24 h treatment (Fig 3.7A, D; Dunnett’s test, $p < 0.05$). However, significant levels of cell death were induced at lower concentrations than observed when using the MTT assay for imatinib and dasatinib (Fig 3.7B, C; Dunnett’s test, $p < 0.05$). Again, bosutinib and imatinib induced an apparent increase in viability at low concentrations, but this effect was not significant and less prominent than that seen with MTT assays.

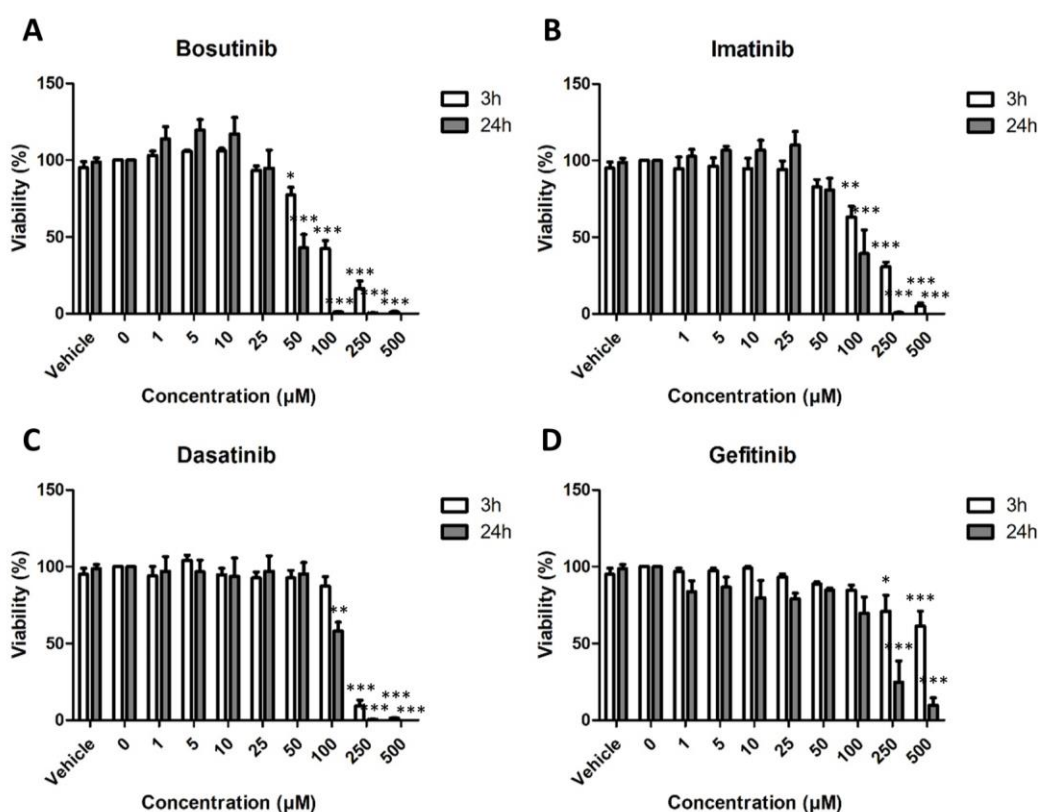


Figure 3.7. Effect of TKIs on cell viability using CellTiter-Glo® assay. Caco-2 cells were treated with up to 500µM bosutinib (A), imatinib (B), dasatinib (C) or gefitinib (D) for 3h and 24h. The percentage of viable cells remaining was then determined using CellTiter-Glo® luminescent cell viability assay which measures ATP levels. Data are representation as the percentage change relative to 0µM. * $p < 0.05$, ** $p < 0.01$, *** $p < 0.001$ versus vehicle, One-way ANOVA followed by Dunnett’s test, mean \pm SEM, N=3-5, n=3.

Due to the increases in cell viability seen at low concentrations, we attempted to determine whether MTT and CellTiterGlo® assays over-estimate viability. Cell death was further assessed by a number of different methods including poly(ADP-ribose) polymerase (PARP) cleavage by Western blotting, nuclear fragmentation as determined by 4',6-diamidino-2-phenylindole (DAPI) staining, and cell membrane degradation by ToxiLight™ assay.

PARP is involved in DNA repair during environmental stress (Sato *et al.*, 1992) and PARP cleavage is a marker of apoptosis (Oliver *et al.*, 1998). In a 3 h dose-response with bosutinib, PARP was cleaved to produce an 89kDa band indicative of apoptosis (Boulares *et al.*, 1999) at 25 μ M and 50 μ M (Fig 3.8A); however an increase in the ratio of cleaved PARP to full length PARP was only significant at 50 μ M (Fig 3.8B; Dunnett's test, $p < 0.05$). Following treatment with 25 μ M bosutinib over a 24 h time course, an 89kDa PARP cleavage fragment was detected from 3 h onwards (Fig 3.8C, D; Dunnett's test, $p < 0.001$). It is important to note that the low ratios of cleaved PARP : full length PARP seen at 16 h are probably due to a flaw in the experimental set-up — cells used for the 16 h time point were treated 8 h after 'time zero', for convenience of cell harvesting — rather than a true reflection of decreased cell death at 16 h.

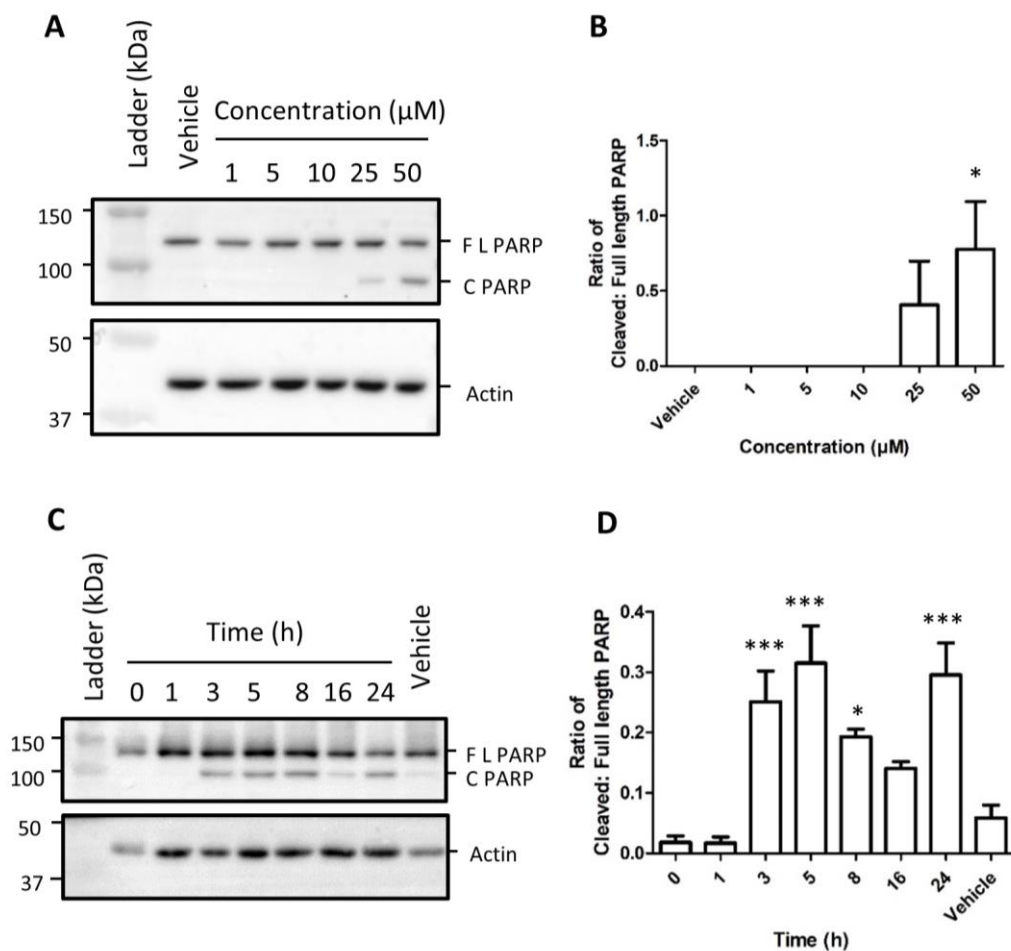


Figure 3.8. Effect of bosutinib on PARP cleavage. Caco-2 cells were incubated with 1-50 μ M bosutinib for 3 h (A-B) or 25 μ M bosutinib for up to 24h (C-D). The expression of cleaved PARP (C PARP) and full length PARP (F L PARP) was analysed by Western blot and results shown as a ratio of cleaved PARP : Full length PARP. Actin was used as a loading control. Representative blots (A,C). * $p < 0.05$, *** $p < 0.001$ versus vehicle, One-way ANOVA followed by Dunnett's test, mean \pm SEM (B, D), N=3.

Nuclear fragmentation was assessed after 3h treatment with 25 μ M TKIs (Fig 3.9A-E). Bosutinib treatment alone induced a significant increase in the percentage of cells (~6%) undergoing nuclear fragmentation (Fig 3.9F; Dunnett's test, $p < 0.001$).

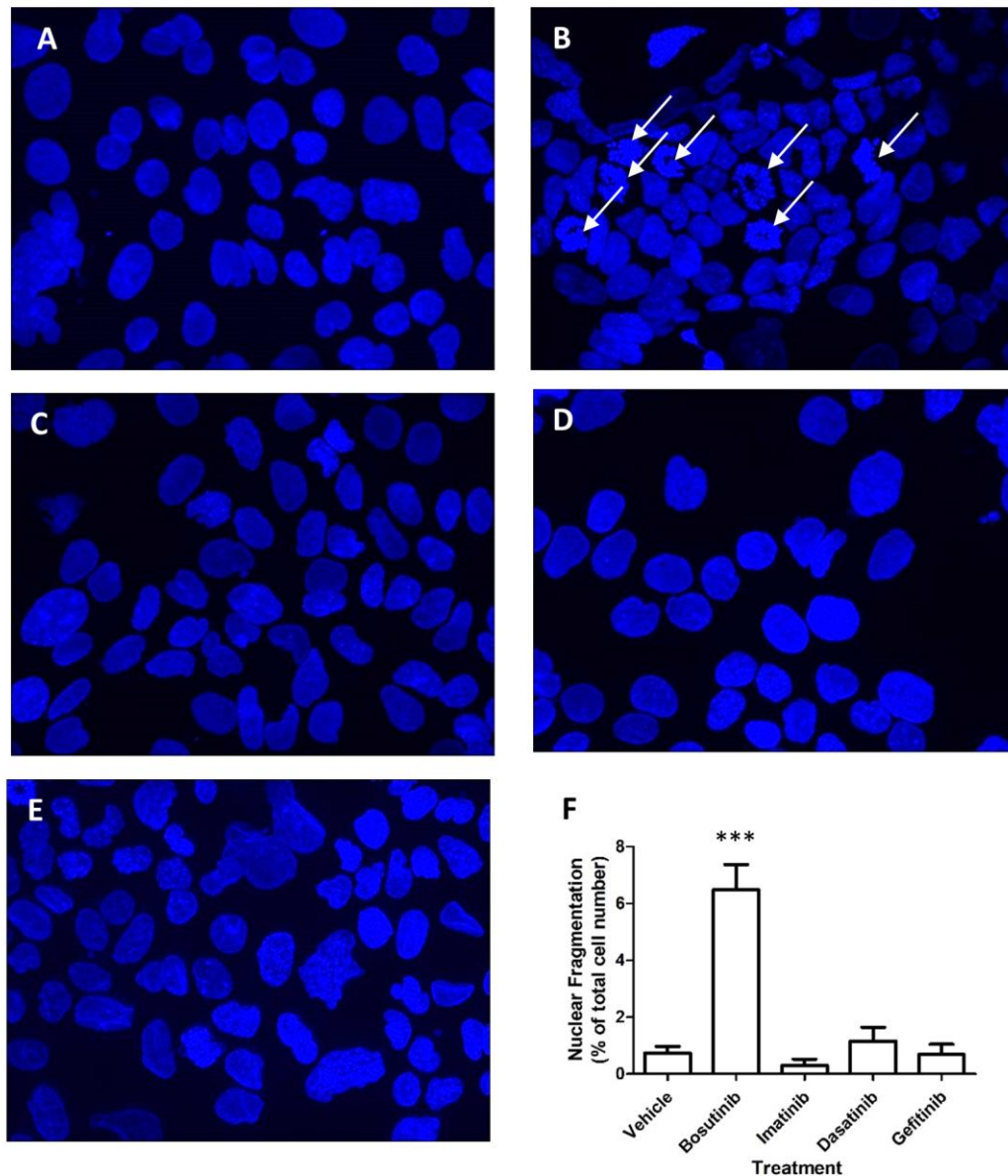


Figure 3.9. Effect of TKIs on nuclear fragmentation. Caco-2 cells were incubated with vehicle (A) or 25 μ M bosutinib (B), imatinib (C), dasatinib (D) and gefitinib (E) for 3 h, stained with DAPI and viewed at x40 magnification. Images are representative of 3 independent experiments (A-E). Number of fragmented nuclei (white arrows) were counted in ImageJ and calculated as a percentage of the total nuclei number (F). *** $p < 0.001$ versus vehicle, One-way ANOVA followed by Dunnett's test, mean \pm SEM, N=3, n (fields of view) = 3. Slides were not blinded before analysis.

ToxiLight™ assay, a non-destructive cell death assay which measures the release of cell membrane impermeable adenylate kinase into the growth media, was used to assess the end-point of cell death. Caco-2 cells were treated with a range of concentrations of bosutinib, imatinib, dasatinib and gefitinib up to 100µM. Concentrations of 50µM-100µM bosutinib, 100µM dasatinib and 25-100µM gefitinib caused a significant decrease in cell viability (Fig 3.10A, C, D; Dunnett's test, $p < 0.05$), but imatinib did not induce cell death (Fig 3.10B; One-way ANOVA, $p > 0.05$).

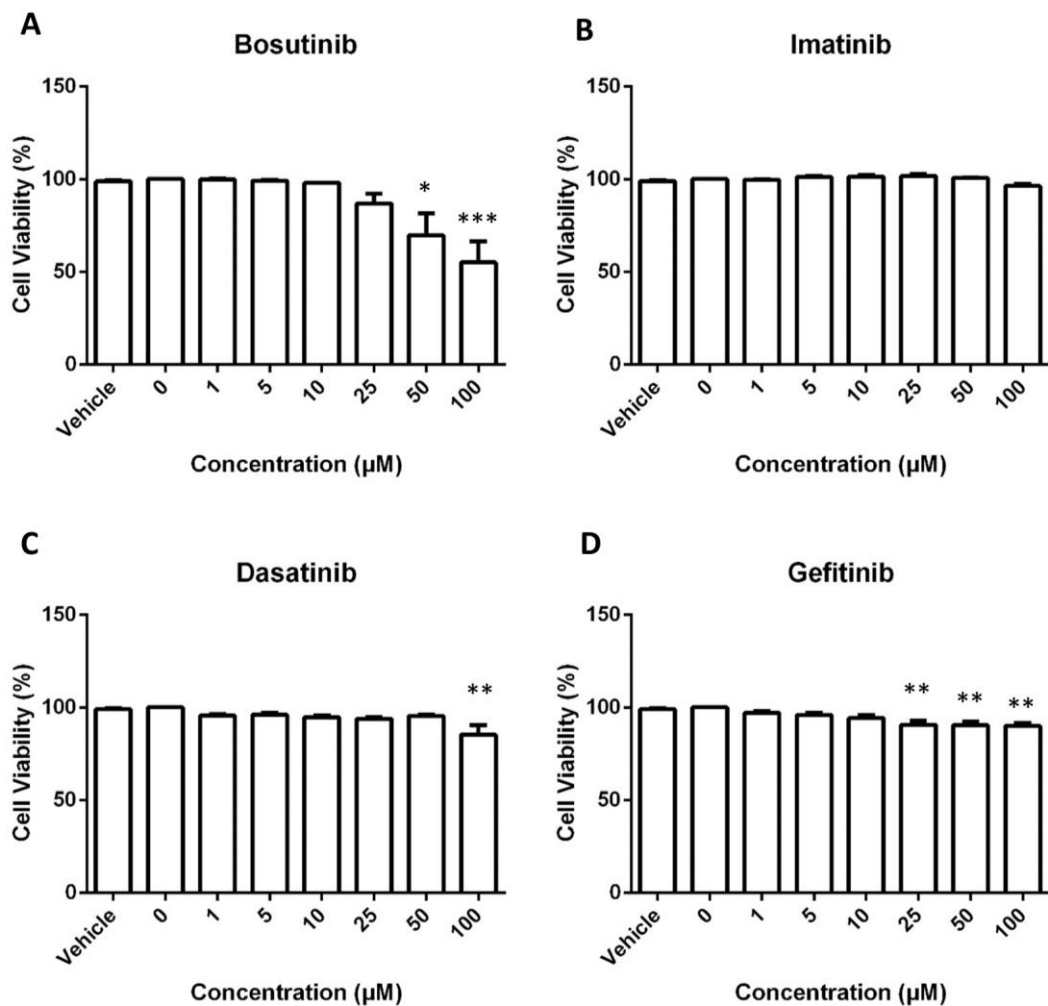


Figure 3.10. Effect of TKIs on cell viability using ToxiLight™ assay. Caco-2 cells were treated with up to 100µM bosutinib (A), imatinib (B), dasatinib (C) or gefitinib (D) for 24h. The percentage of viable cells remaining was then determined using ToxiLight™ luminescent cell viability assay. Data are represented as the percentage change relative to 0µM. * $p < 0.05$, ** $p < 0.01$, *** $p < 0.001$ versus vehicle, One-way ANOVA followed by Dunnett's test, mean \pm SEM, N=3-4, n=3.

3.2.6 Bosutinib decreases cell-cell adhesion strength in Caco-2 cells

Increased paracellular permeability suggests decreased intercellular junctional integrity, and therefore a simple cell-cell adhesion strength assay (Takeichi, 1977) was performed with Caco-2 cells after 24 h TKI treatment (0.1 μ M – 10 μ M). In this assay, cells were dispersed by pipetting either in the absence or presence of EGTA, after the addition of TKI. Cell dissociation index was calculated by dividing the number of cell clumps in the absence of EGTA (N_{TC}) by the number of clumps when EGTA was present (N_{TE}). EGTA causes all the cells to completely dissociate and thus N_{TE} is equal to the total cell number. Monolayers with weaker cell-cell adhesions will be more sensitive to cellular dispersal resulting in a greater number of clumps (higher N_{TC}); therefore, cell dissociation index is inversely proportional to cell-cell adhesion strength. Sub-apoptotic concentrations of TKIs were tested as cell death would naturally weaken cell-cell adhesion leading to false positive data.

Cell dissociation index was significantly increased by bosutinib (1 μ M and 10 μ M) and dasatinib (10 μ M) (Fig 3.11 A, C; Dunnett's test, $p < 0.05$). Imatinib and gefitinib (10 μ M), however, did not cause a decrease in cell-cell adhesion strength (Fig 3.11B, D; Dunnett's test, $p > 0.05$). Consistent with permeability data (Fig 3.3A, 1.5A), bosutinib demonstrated the most significant increase in cell dissociation index.

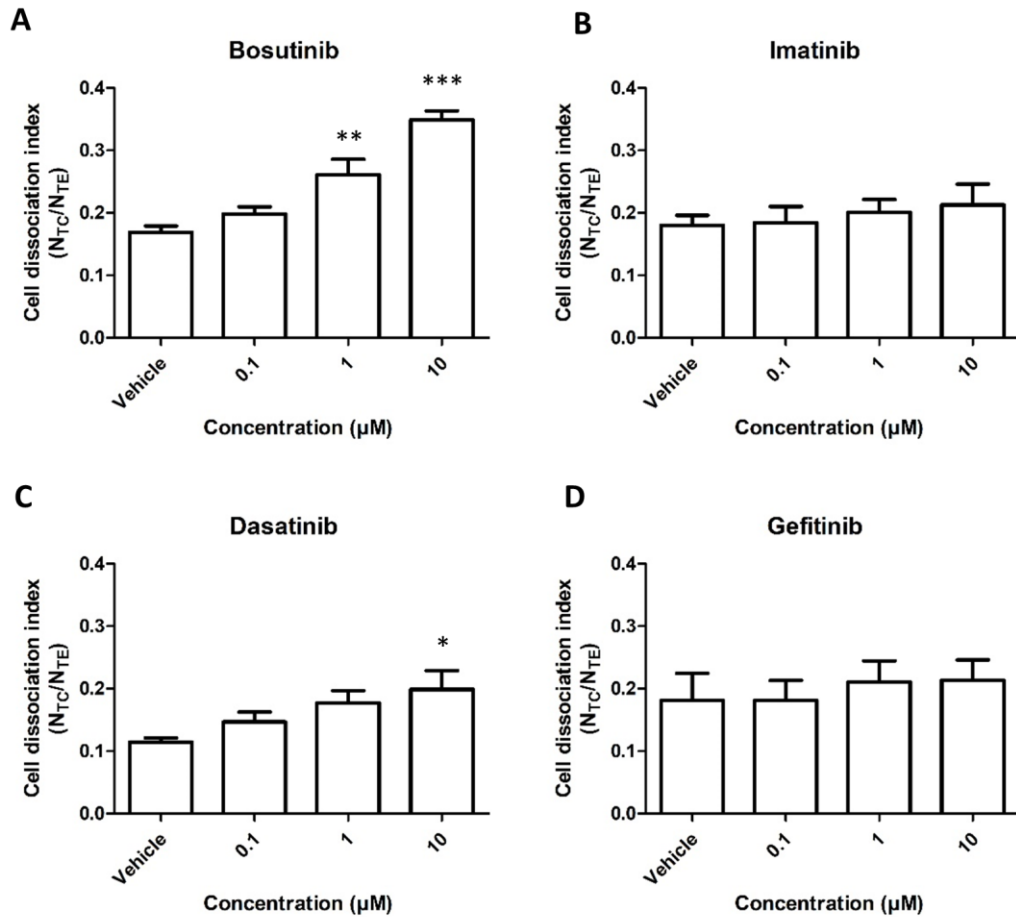


Figure 3.11. Effect of TKIs on cell-cell adhesion strength. Caco-2 cells were dosed with up to 10µM bosutinib (A), imatinib (B), dasatinib (C) and gefitinib (D) for 24 h with or without EGTA, then dispersed by pipetting. The cell dissociation index, which is inversely proportional to cell-cell adhesion strength, was calculated by dividing the number of clumped cells in the presence of calcium (i.e. absence of EGTA, N_{TC}) by the number of clumped cells in the presence of EGTA which is equivalent to the total cell number (N_{TE}). *p<0.05, **p<0.01, ***p<0.001 versus vehicle, One-way ANOVA followed by Dunnett's test, mean ± SEM, N=3, n=3.

3.2.7 Bosutinib, dasatinib and gefitinib decrease protein levels of intercellular junction proteins in Caco-2 cells

To determine the mechanistic basis of TKI-induced increase in paracellular permeability in Caco-2 cells, changes in the levels of intercellular junction proteins – ZO-1, E-cadherin and occludin – were investigated. E-cadherin is found in AJs, whilst occludin is present in TJs, and ZO-1 is a cytosolic protein present in both AJs and TJs. It has previously been shown that erlotinib, an EGFR TKI, decreases levels of E-cadherin at both the mRNA and protein level in rat intestinal epithelial cells (IEC-6) (Fan *et al.*, 2014), whilst gefitinib has also been shown to decrease expression of both E-cadherin and ZO-1 in IEC-6 cells (Hong *et al.*, 2014).

Caco-2 cells were dosed for 3 h with up to 100 μ M TKIs and protein levels of ZO-1, E-cadherin and occludin were analysed by Western blotting and normalised to β -actin. Bosutinib at 50 μ M after 3 h treatment significantly decreased E-cadherin and occludin (Fig 3.12A, E, G; Dunnett's test, $p < 0.05$) by ~25% and ~75%, respectively. Bosutinib-induced decreases in ZO-1 protein levels approached significance (Fig 3.12A, C; One-way ANOVA, $p < 0.1$). Twenty-five micromolar bosutinib also induced a significant decrease in occludin (Fig 3.12A, G; Dunnett's test, $p < 0.05$), while levels of E-cadherin and ZO-1 remained unaltered at this concentration.

ZO-1 and E-cadherin protein levels were not affected by imatinib or dasatinib (Fig 3.12B, D, F; Fig 3.13 A, C, E; One-way ANOVA, $p > 0.05$); however, dasatinib (100 μ M) significantly decreased occludin levels by ~50% (Fig 3.13A, G; Dunnett's test, $p < 0.01$). Imatinib at concentrations up to 100 μ M had no effect on occludin levels (Fig 3.12B, H; One-way ANOVA, $p > 0.05$).

One hundred micromolar gefitinib significantly decreased E-cadherin and occludin levels by about 20%, and 85%, respectively (Fig 3.13B, F, H; Dunnett's test, $p < 0.05$). Gefitinib also induced a dose-dependent reduction in ZO-1; however this decrease was not significant (Fig 3.13D; One-way ANOVA, $p > 0.05$).

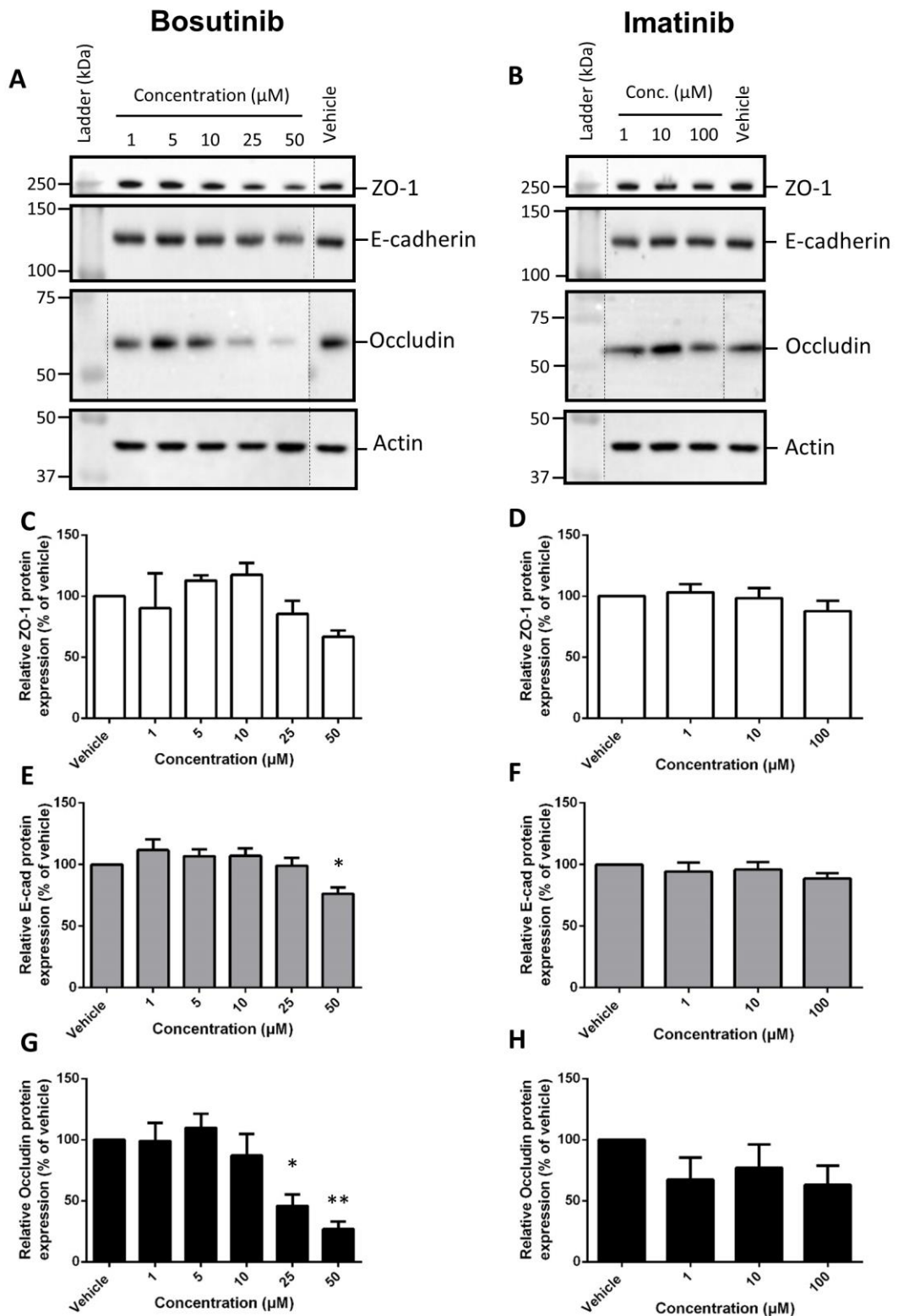


Figure 3.12. Effect of bosutinib and imatinib on levels of tight junction and adherens junction proteins. Caco-2 cells were treated with bosutinib (A, C, E, G) or imatinib (B, D, F, H) for 3 h. Expression of ZO-1 (C, D), E-cadherin (E, F) and occludin (G, H) was analysed by Western blot and normalized to actin. Data are represented as the percentage change relative to vehicle. Dotted lines represent where membranes have been cropped from the same blot. * $p < 0.05$, ** $p < 0.01$ versus vehicle, One-way ANOVA followed by Dunnett's test, mean \pm SEM, $N = 4$.

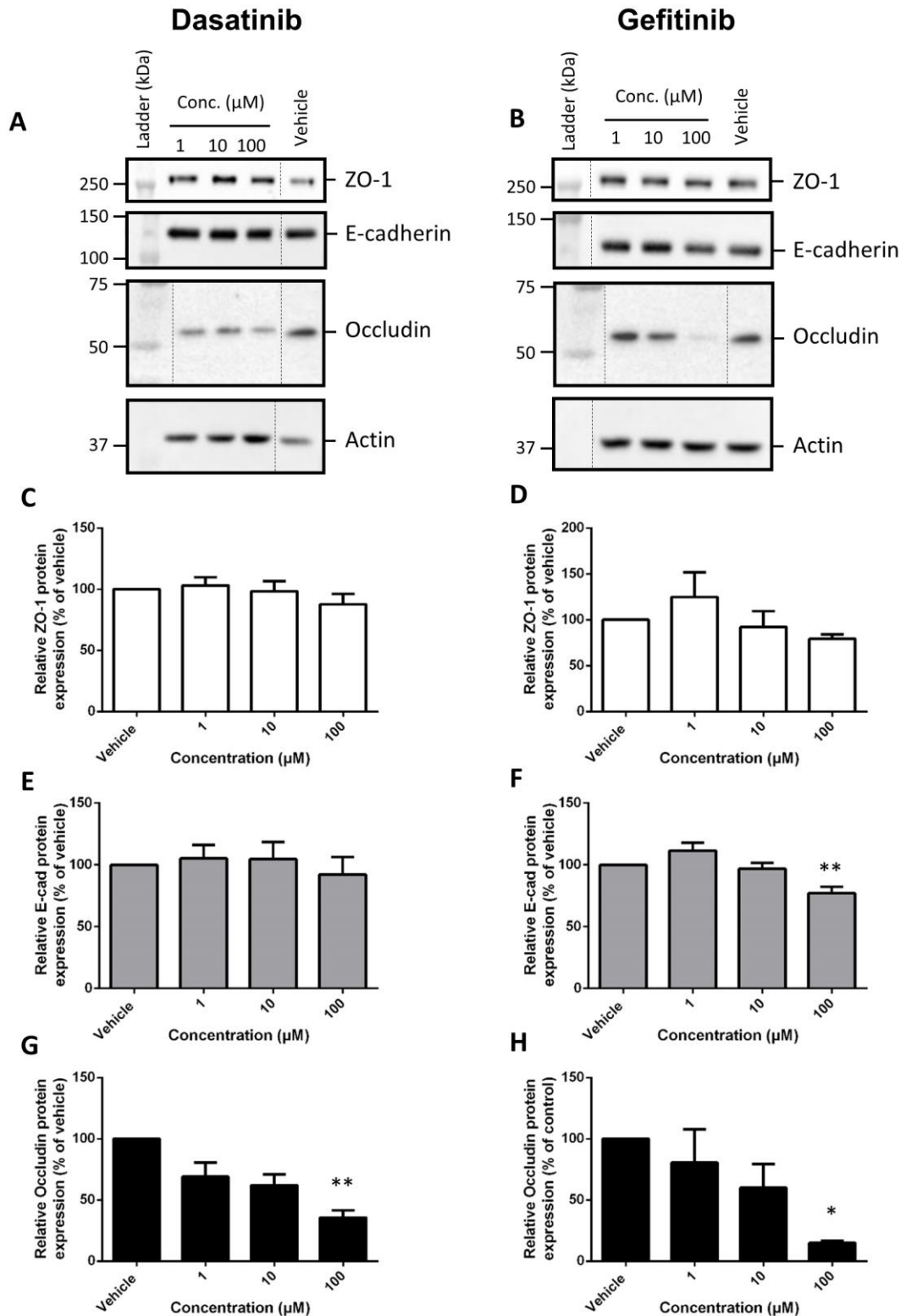


Figure 3.13. Effect of dasatinib and gefitinib on levels of tight junction and adherens junction proteins. Caco-2 cells were treated with dasatinib (A, C, E, G) or gefitinib (B, D, F, H) for 3 h. Expression of ZO-1 (C, D), E-cadherin (E, F) and occludin (G, H) was analysed by Western blot and normalized to actin. Data are represented as the percentage change relative to vehicle. Dotted lines represent where membranes have been cropped from the same blot. * $p < 0.05$, ** $p < 0.01$ versus vehicle, One-way ANOVA followed by Dunnett's test, mean \pm SEM, $N = 4$.

Changes in levels of E-cadherin, ZO-1 and occludin over a 24 h time course after addition of 25 μ M bosutinib or imatinib were also assessed by Western blotting. Bosutinib caused a time-dependent decrease in E-cadherin and ZO-1 protein levels to about 70% and 60%, respectively, by 24 h (Fig 3.14A, C, E; One-way ANOVA, $p < 0.05$). Bosutinib also significantly decreased levels of occludin (Fig 3.14A, G; One-way ANOVA, $p < 0.05$). A possible explanation for the discrepancy in protein expression at 16 h is explained above (see 3.2.5 Bosutinib is cytotoxic to Caco-2 cells). Imatinib (25 μ M) treatment however did not modulate ZO-1 or E-cadherin protein levels (Fig 3.14B, D, F; One-way ANOVA, $p > 0.05$). Surprisingly occludin levels were increased by imatinib (25 μ M) over time; however, this increase was not significant (Fig 3.14H; One-way ANOVA, $p > 0.05$).

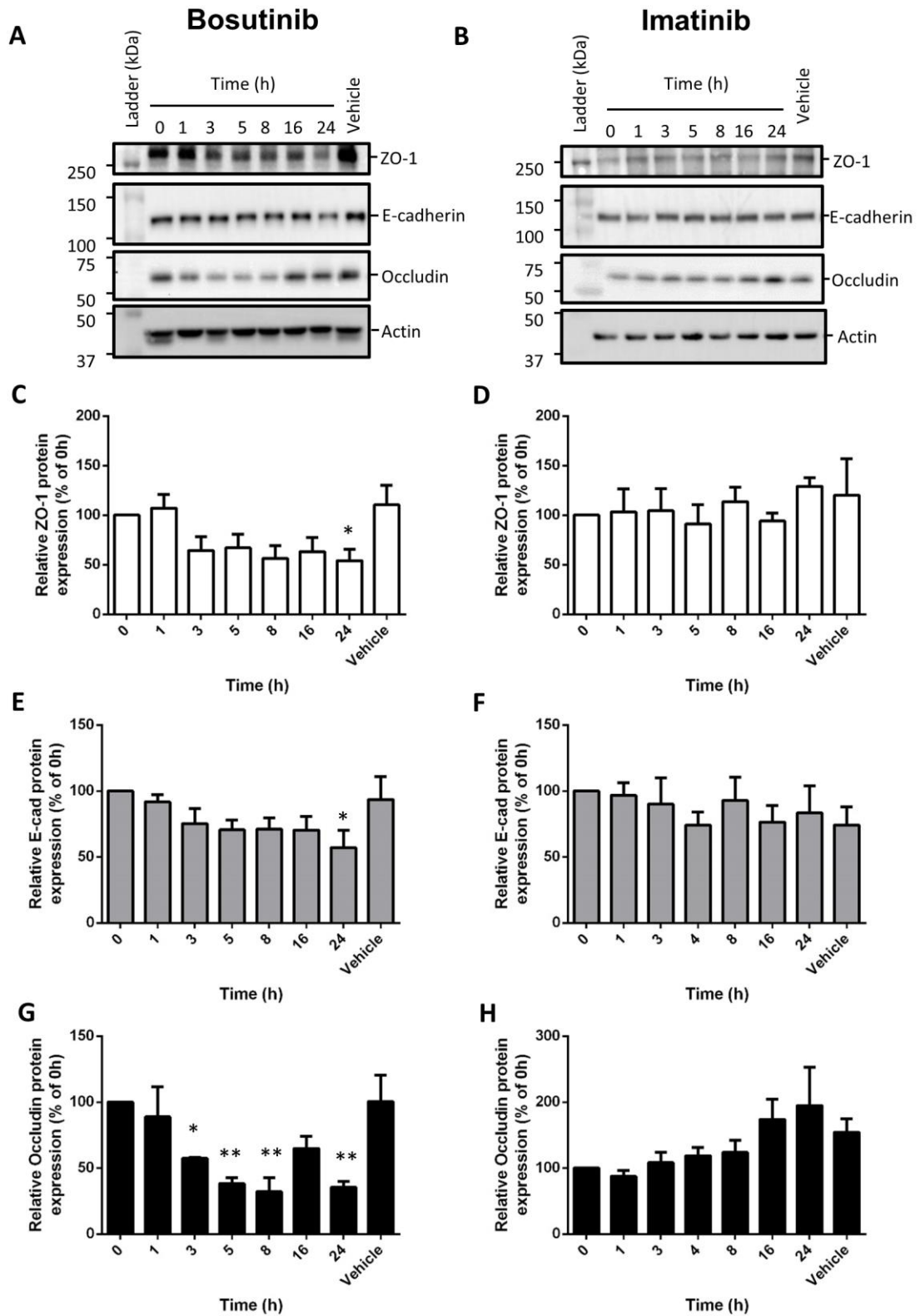


Figure 3.14. Effect of bosutinib and imatinib on levels of tight junction and adherens junction proteins over 24 h. Caco-2 cells were incubated with 25 μ M bosutinib (A, C, E, G), imatinib (B, D, F, H) for up to 24 h. The expression of ZO-1 (C, D), E-cadherin (E, F) and occludin (G, H) was analysed by Western blot and normalized to actin. Data are represented as the percentage change relative to 0h time point. * p <0.05, ** p <0.01 versus vehicle, One-way ANOVA followed by Dunnett's test, mean \pm SEM, N=4.

3.2.8 Bosutinib alters levels of *TJP1* and *OCLN* mRNA in Caco-2 cells

CDH1 (E-cadherin), *TJP1* (ZO-1) and *OCLN* (occludin) gene expression was then determined over a 24 h period after treatment with bosutinib or imatinib (25 μ M). Neither bosutinib (Fig 3.15C; One-way ANOVA, $p>0.05$) nor imatinib (Fig 3.15D; One-way ANOVA, $p>0.05$) caused a significant change in *CDH1* mRNA levels. Bosutinib, however, induced a significant transient decrease in *TJP1* mRNA levels at 5 h and 8 h (Fig 3.15A; Dunnett's test, $p<0.05$). The mRNA expression data for imatinib are consistent with Western blotting data confirming imatinib does not alter levels of ZO-1, E-cadherin or Occludin. Bosutinib increased mRNA levels of *OCLN* (Fig 3.15E, One-way ANOVA, $p<0.05$) with this increase becoming significant by 16 h treatment (Fig 3.15E, Dunnett's test, $p<0.05$). A similar trend was seen with imatinib but this was not significant (Fig 3.15F, One-way ANOVA, $p>0.05$).

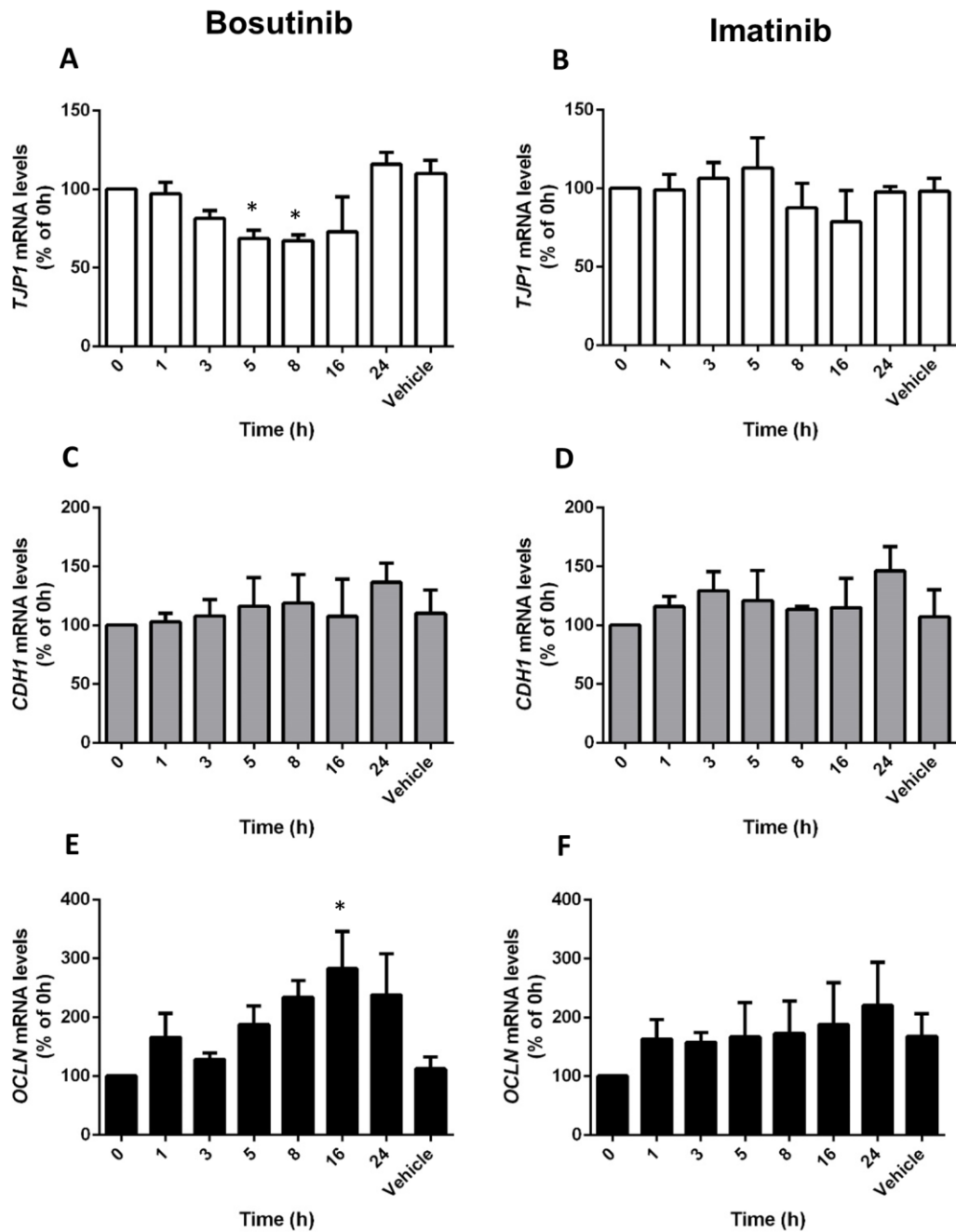


Figure 3.15. Effect of bosutinib and imatinib on tight junction and adherens junction mRNA levels over 24 h. Caco-2 cells were incubated with vehicle for 24h or 25 μ M bosutinib (A-C), imatinib (D-F) for up to 24h. The mRNA levels of *TJP1* (ZO-1), *CDH1* (E-cadherin) and *OCLN* (Occludin) was analysed by RTqPCR and normalized to housekeeping gene *B2M*. Data are represented as the percentage change relative to 0h time point. * $p < 0.05$ versus vehicle, One-way ANOVA followed by Dunnett's test, mean \pm SEM, N=4, n=4.

3.2.9 Bosutinib induces re-localization of junction proteins in Caco-2 cells

In addition to altered epithelial junction protein levels, re-localization of these proteins is often associated with increased permeability (Samak *et al.*, 2014, 2015). Immunofluorescence was used to assess potential redistribution of ZO-1, E-cadherin and occludin. Analysis of images using ImageJ confirmed changes in protein levels after 3 h TKI (25 μ M) treatment.

Bosutinib induced re-localization of ZO-1 away from the plasma membrane, with more diffuse staining being seen at the cell-cell contacts relative to imatinib, dasatinib, gefitinib and vehicle treated cells (Fig 3.16, 2a). Imatinib, dasatinib and gefitinib showed no difference from the vehicle (Fig 3.16, 3-5a). Raw integrated density analysis showed none of the TKIs induced changes in ZO-1 protein levels at 25 μ M after 3 h incubation (Fig 3.19A; One-way ANOVA, $p>0.05$), which is consistent with Western blotting data (Fig 3.12A, C, B, D; Fig 3. 13A, C, B, D).

Bosutinib caused E-cadherin to aggregate within the cytoplasm and re-localize away from the plasma membrane (Fig 3.17, 2a). Similar patterns were observed with the other TKIs tested, but to a lesser extent. Total levels of E-cadherin, as determined by raw integrated density, only decreased upon treatment with bosutinib (Fig 3.19B; Dunnett's test, $p<0.05$). However, it is important to note that the marked decrease in E-cadherin shown in Fig 3.17 (2a) was not observed consistently across the entire Caco-2 monolayer.

Bosutinib, dasatinib and gefitinib appeared to decrease levels of occludin present at the cell-cell contacts and, as with E-cadherin, the protein formed punctate structures within the cytoplasm (Fig 3.18). Occludin protein expression levels analysed by raw integrated density were consistent with Western blot data (Fig 3.12A, G, B, H; Fig 3.13A, G, B, H) demonstrating bosutinib, dasatinib and gefitinib (Fig 3.19C; Dunnett's test, $p<0.05$), but not imatinib (Fig 3.19C; Dunnett's test, $p>0.05$), significantly decreased levels of occludin.

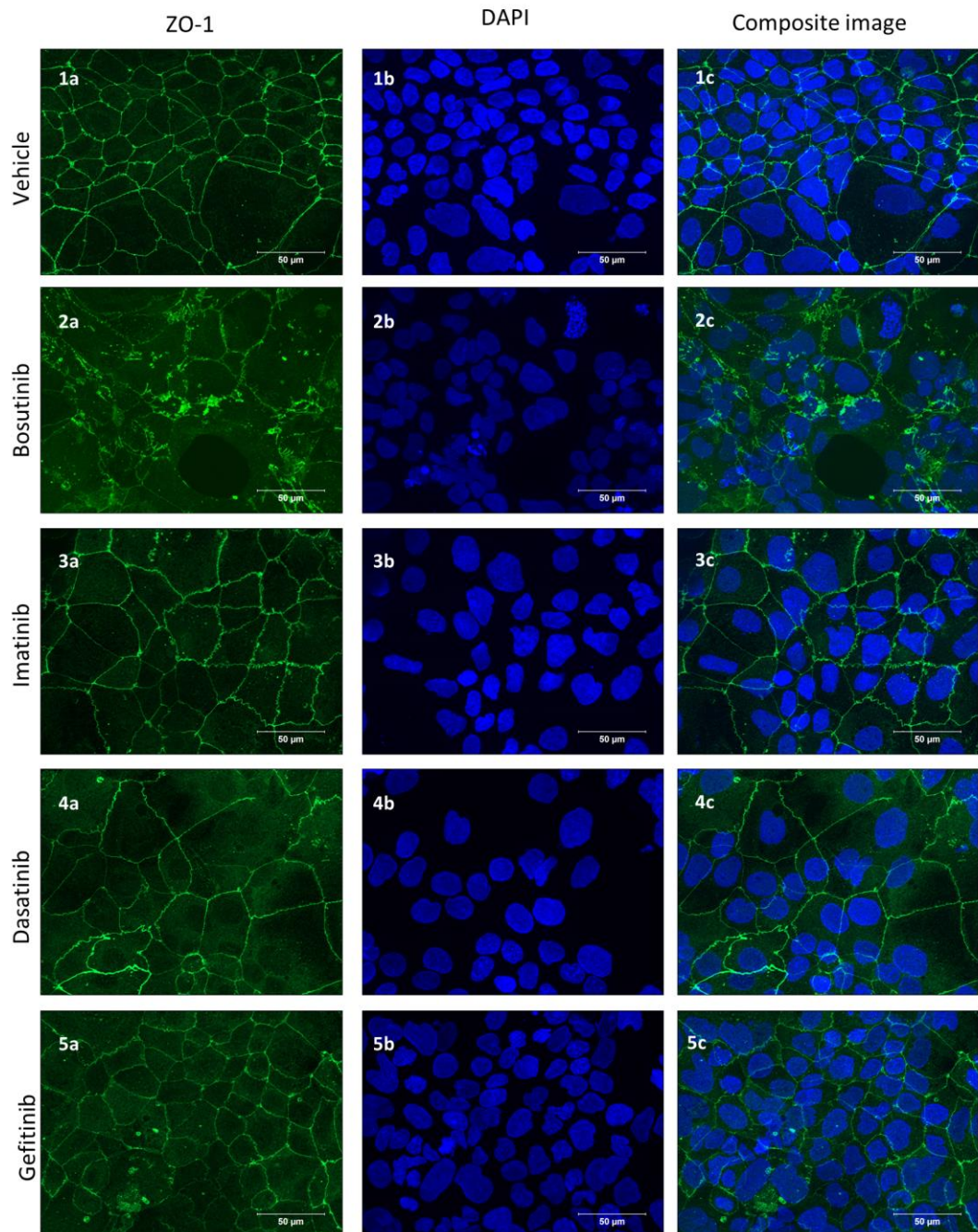


Figure 3.16. Effect of TKIs on localization of ZO-1. Caco-2 cells were incubated with vehicle (1) or 25 μ M bosutinib (2), imatinib (3), dasatinib (4) or gefitinib (5) for 3 h. The localization of ZO-1 (a, green, left column) and nuclei (b, blue, middle column) were analysed by immunofluorescence x40 magnification. Composite images shown in right column (c). Images are representative of 3 independent experiments, and 3 fields of view were taken per experiment.

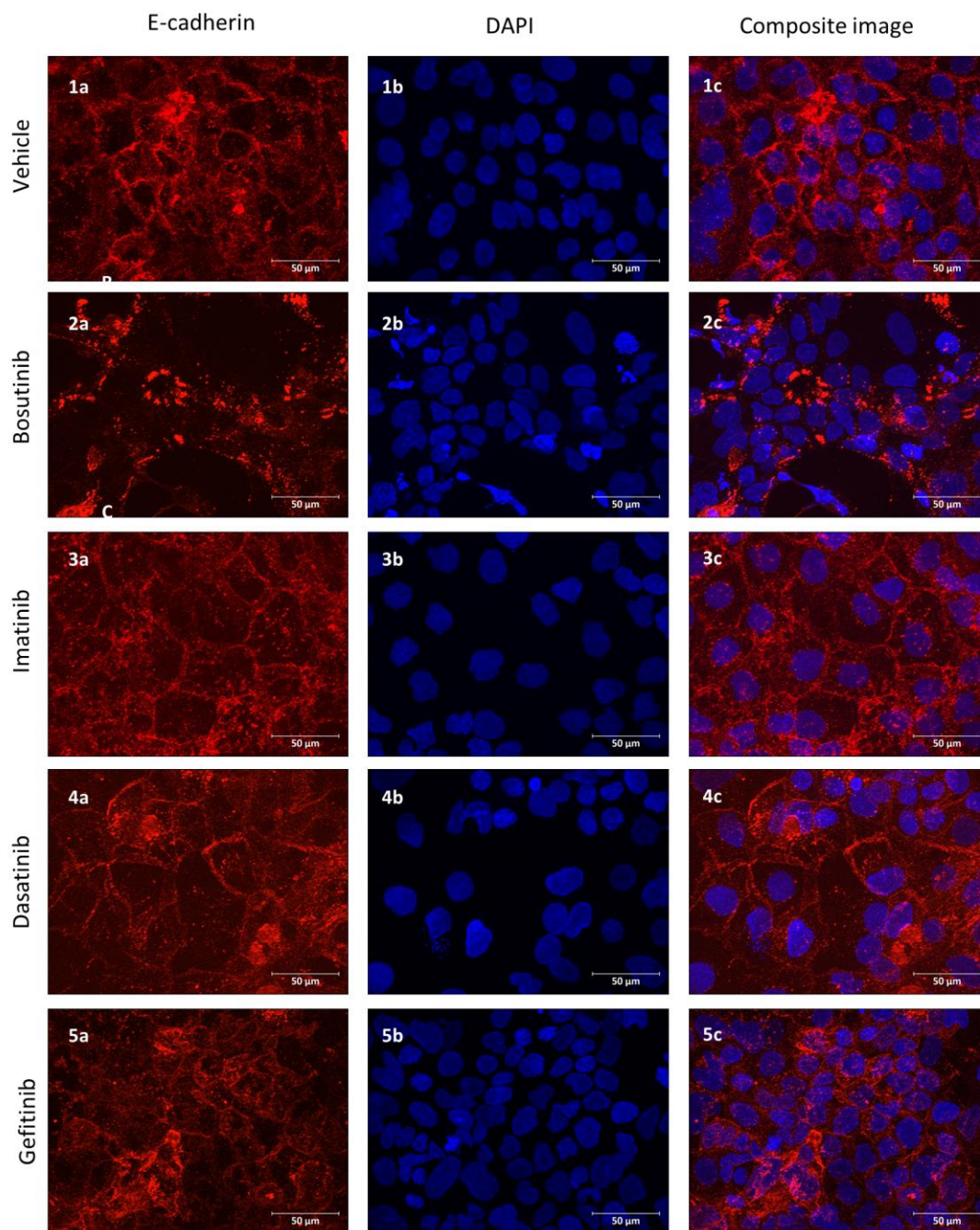


Figure 3.17. Effect of TKIs on localization of E-cadherin. Caco-2 cells were incubated with vehicle (1) or 25 μ M bosutinib (2), imatinib (3), dasatinib (4) or gefitinib (5) for 3 h. The localization of E-cadherin (a, red, left column) and nuclei (b, blue, middle column) were analysed by immunofluorescence x40 magnification. Composite images shown in right column (c). Images are representative of 3 independent experiments, and 3 fields of view were taken per experiment.

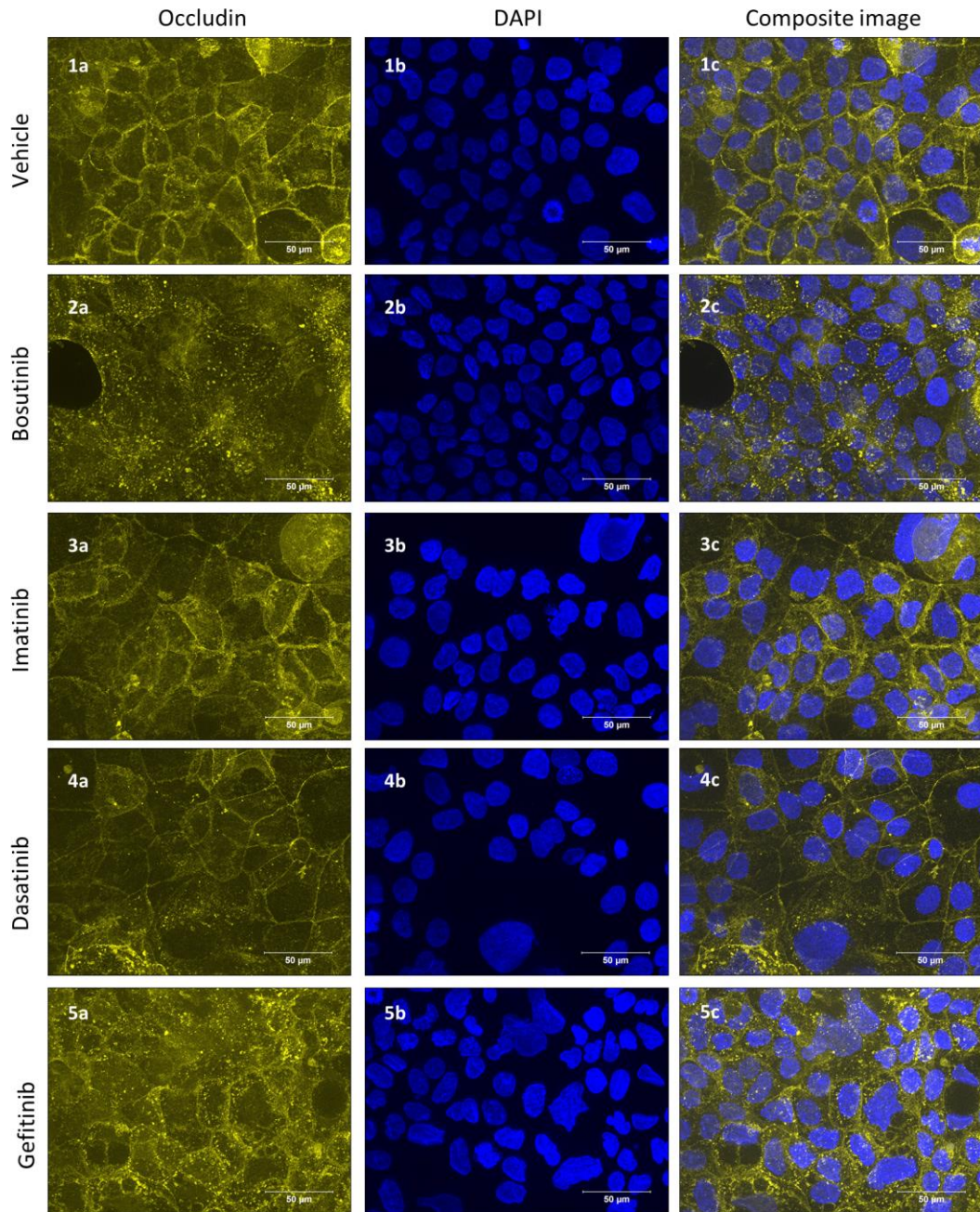


Figure 3.18. Effect of TKIs on localization of occludin. Caco-2 cells were incubated with vehicle (1) or 25 μ M bosutinib (2), imatinib (3), dasatinib (4) or gefitinib (5) for 3 h. The localization of occludin (a, yellow, left column) and nuclei (b, blue, middle column) were analysed by immunofluorescence x40 magnification. Composite images shown in right column (c). Images are representative of 3 independent experiments, and 3 fields of view were taken per experiment.

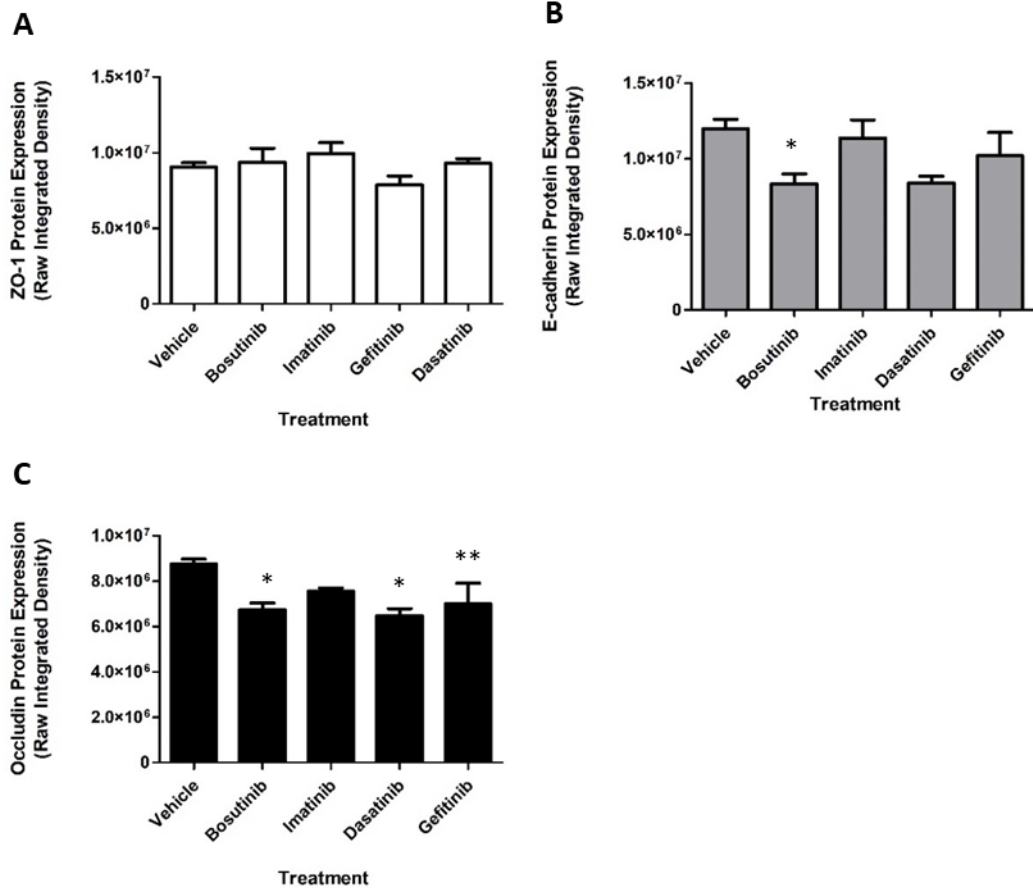


Figure 3.19. Effect of TKIs on protein levels of junction proteins determined by immunofluorescence. Caco-2 cells were incubated with vehicle control or 25 μ M bosutinib, imatinib, dasatinib or gefitinib for 3 h. The levels of ZO-1 (A), E-cadherin (B) and Occludin (C) were determined by measuring raw integrated density (the sum of the pixel intensities) of immunofluorescence images in ImageJ, without DAPI channel. * $p < 0.05$, ** $p < 0.01$ versus vehicle, One-way ANOVA followed by Dunnett's test, mean \pm SEM, N=3, n=3.

3.2.10 Bosutinib causes cytoskeletal rearrangement and cellular retractions in Caco-2 cells

The cytoskeleton plays a key role in maintaining intestinal barrier integrity (López-Posadas *et al.*, 2017); therefore the effect of TKIs on the actin cytoskeleton was assessed. Treatment of Caco-2 cells with 25 μ M bosutinib for 3 h caused changes in the actin cytoskeleton (Fig 3.20B) and cell morphology (Fig 3.21B), whilst dasatinib, imatinib and gefitinib had no effect (Fig 3.20C-E and 1.21C-E).

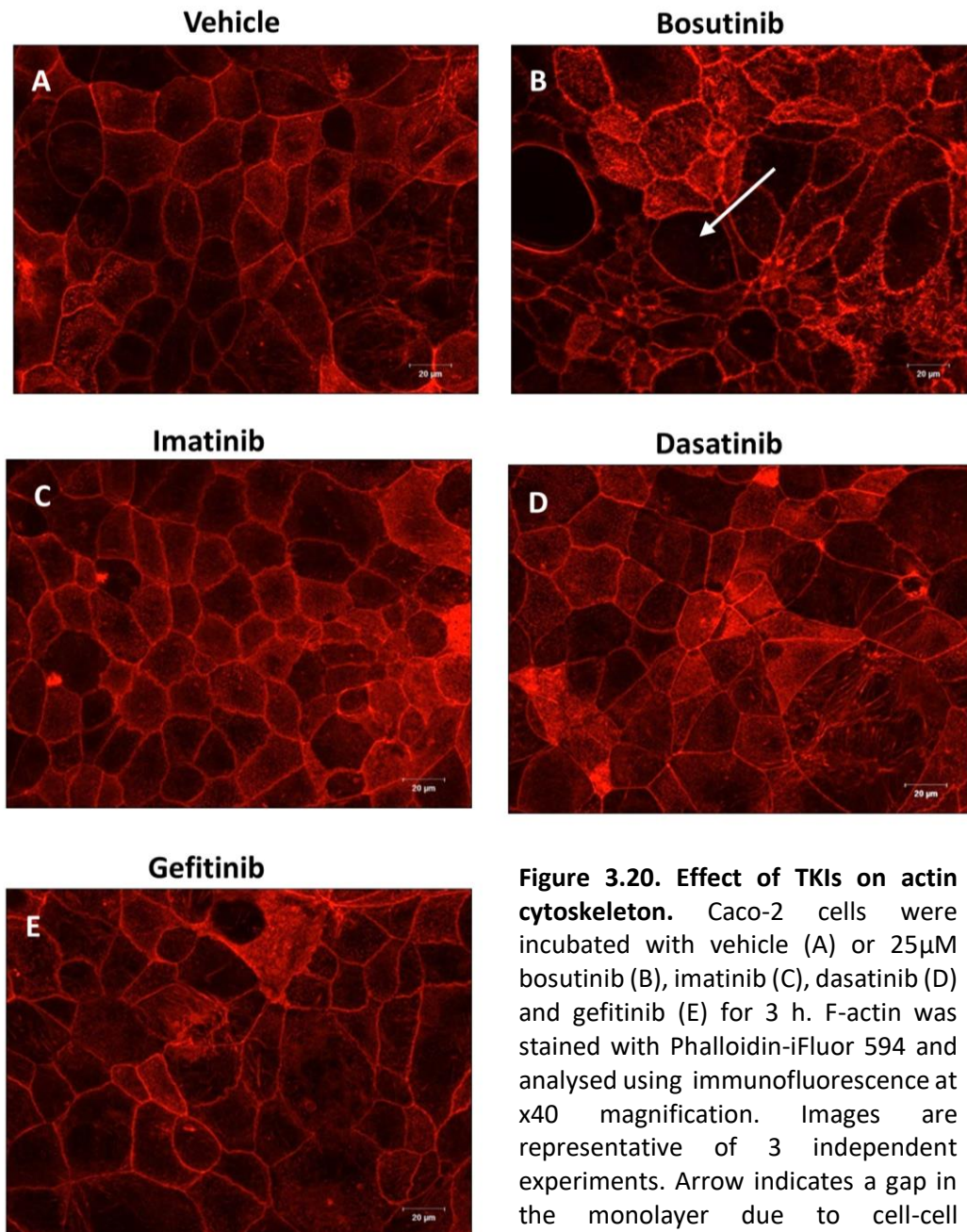


Figure 3.20. Effect of TKIs on actin cytoskeleton. Caco-2 cells were incubated with vehicle (A) or 25µM bosutinib (B), imatinib (C), dasatinib (D) and gefitinib (E) for 3 h. F-actin was stained with Phalloidin-iFluor 594 and analysed using immunofluorescence at x40 magnification. Images are representative of 3 independent experiments. Arrow indicates a gap in the monolayer due to cell-cell dissociation.

Bosutinib-treated cells became “spindle-like” (Fig 3.21B), and cells appeared to “pull-apart” from each other leaving empty spaces (Fig 3.20B and Fig 3.21B, arrow), resembling “cellular retraction”. Interdigitating finger-like projections were formed and other short actin filament structures were visible which may represent intracellular fibres or spikes/protrusions. Moreover, between detached cells, the formation of long actin fibres resembling retraction fibres could be seen (Fig 3.22B, arrows). These morphological changes were not observed in imatinib, dasatinib or gefitinib-treated cells (Fig 3.22C-E).

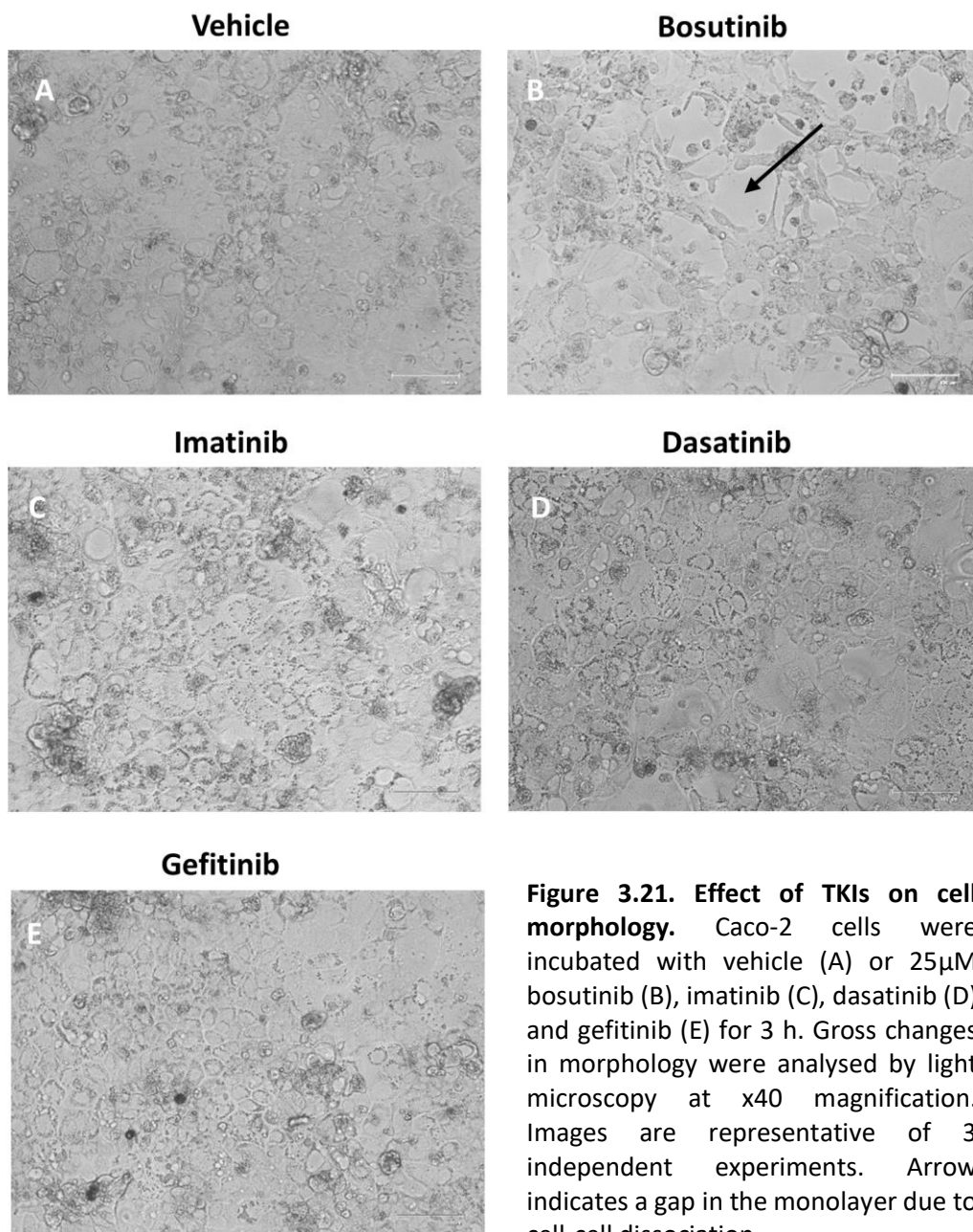


Figure 3.21. Effect of TKIs on cell morphology. Caco-2 cells were incubated with vehicle (A) or 25 μ M bosutinib (B), imatinib (C), dasatinib (D) and gefitinib (E) for 3 h. Gross changes in morphology were analysed by light microscopy at x40 magnification. Images are representative of 3 independent experiments. Arrow indicates a gap in the monolayer due to cell-cell dissociation.

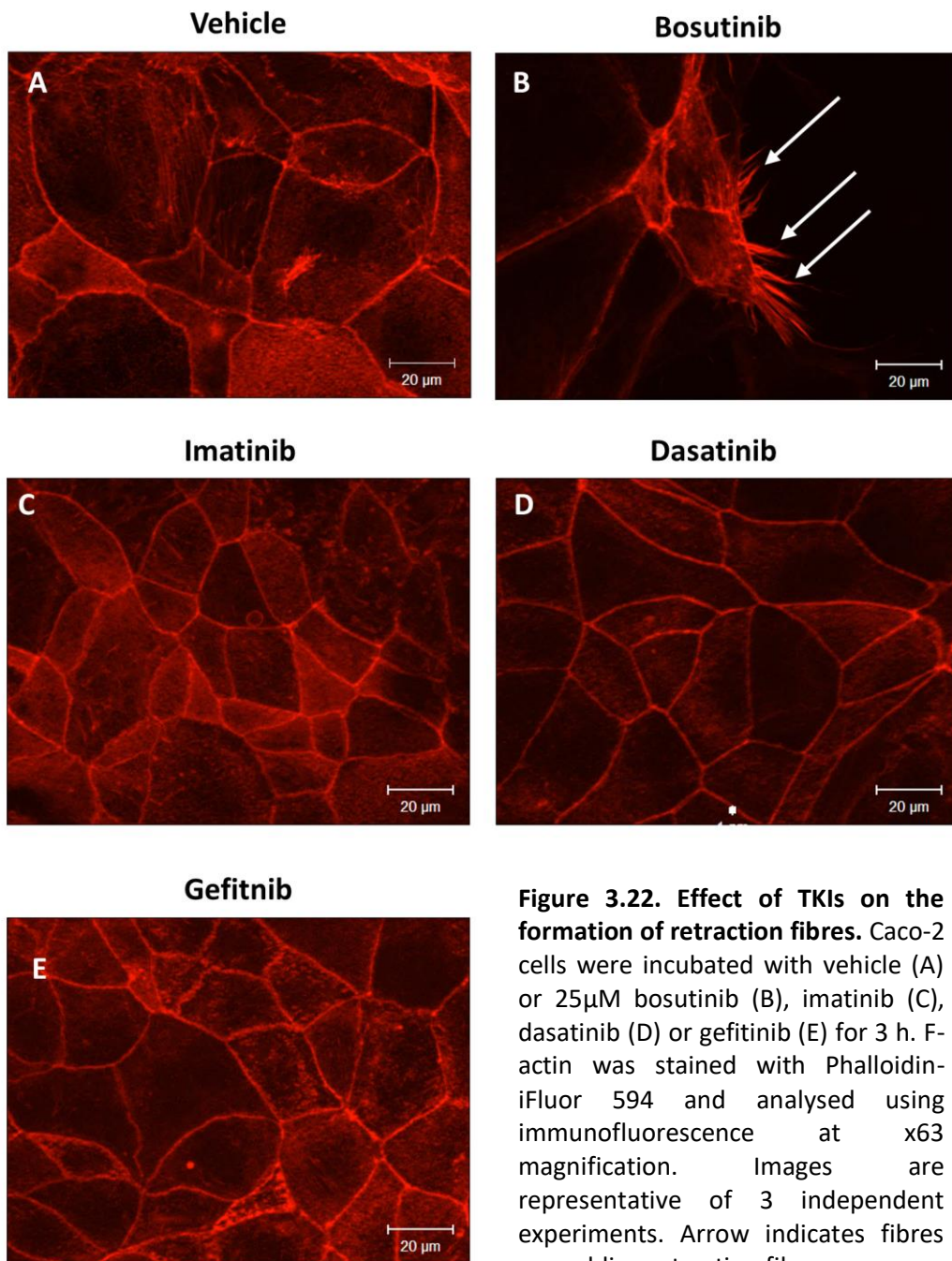


Figure 3.22. Effect of TKIs on the formation of retraction fibres. Caco-2 cells were incubated with vehicle (A) or 25µM bosutinib (B), imatinib (C), dasatinib (D) or gefitinib (E) for 3 h. F-actin was stained with Phalloidin-iFluor 594 and analysed using immunofluorescence at x63 magnification. Images are representative of 3 independent experiments. Arrow indicates fibres resembling retraction fibres.

3.2.11 Bosutinib induces re-localization of occludin when viewed using time-lapse microscopy

To assess the changes in occludin re-localization and actin rearrangement in real time, Caco-2 cells stably expressing Occludin-mEmerald and mCherry-Lifeact were generated through lentiviral transduction. See Methods chapter for more details and Appendices (Fig A.3, 4) for plasmid maps. In brief, mCherry-Lifeact-7 and Occludin-C-14 plasmids, purchased from Addgene, were amplified to generate inserts containing Occludin-mEmerald and mCherry-Lifeact genes, which we termed O1 and L1, respectively. Successful amplification of this insert DNA was demonstrated by gel electrophoresis (Fig 3.23). A second generation lentiviral vector construct plasmid, termed pLJM1 p2A, was restriction digested along with inserts L1 and O1, and insert DNA and construct plasmid ligated.

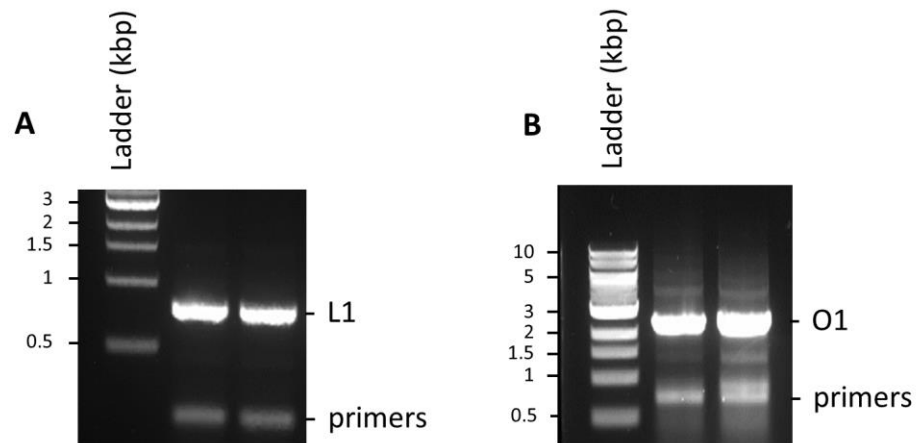


Figure 3.23. Gel electrophoresis of PCR amplification products. PCR products generated from amplification of mCherry-Lifeact-7 to generate insert L1 (798 bp, A) and mEmerald-Occludin-C-14 to generate insert O1 (2353 bp, B) were separated by gel electrophoresis on 1.5% and 0.75% agarose gels, respectively. PCR reactions were run in duplicate (n=2).

The newly formed vectors containing Occludin-mEmerald or mCherry-Lifeact, named pLJM1 P2A-O1 or pLJM1 P2 A-L1, respectively, were transformed into bacteria by heat shock and grown on agar plates with carbenicillin selection. Positive colonies were identified in a colony screen (Fig 3.24). Bacterial transformation was high with plasmid PLJM1 P2A-L1 (6 out of 8 colonies were positive) but low for plasmid pLJM1 P2A-O1 (2 out of the 15 colonies were positive). Generation of desired plasmid sequences for pLJM1-P2A-L1 (colony 5) and pLJM1-P2A-O1 (colony 15) was confirmed by Sanger sequencing (see Appendices, Fig A.5, 6).

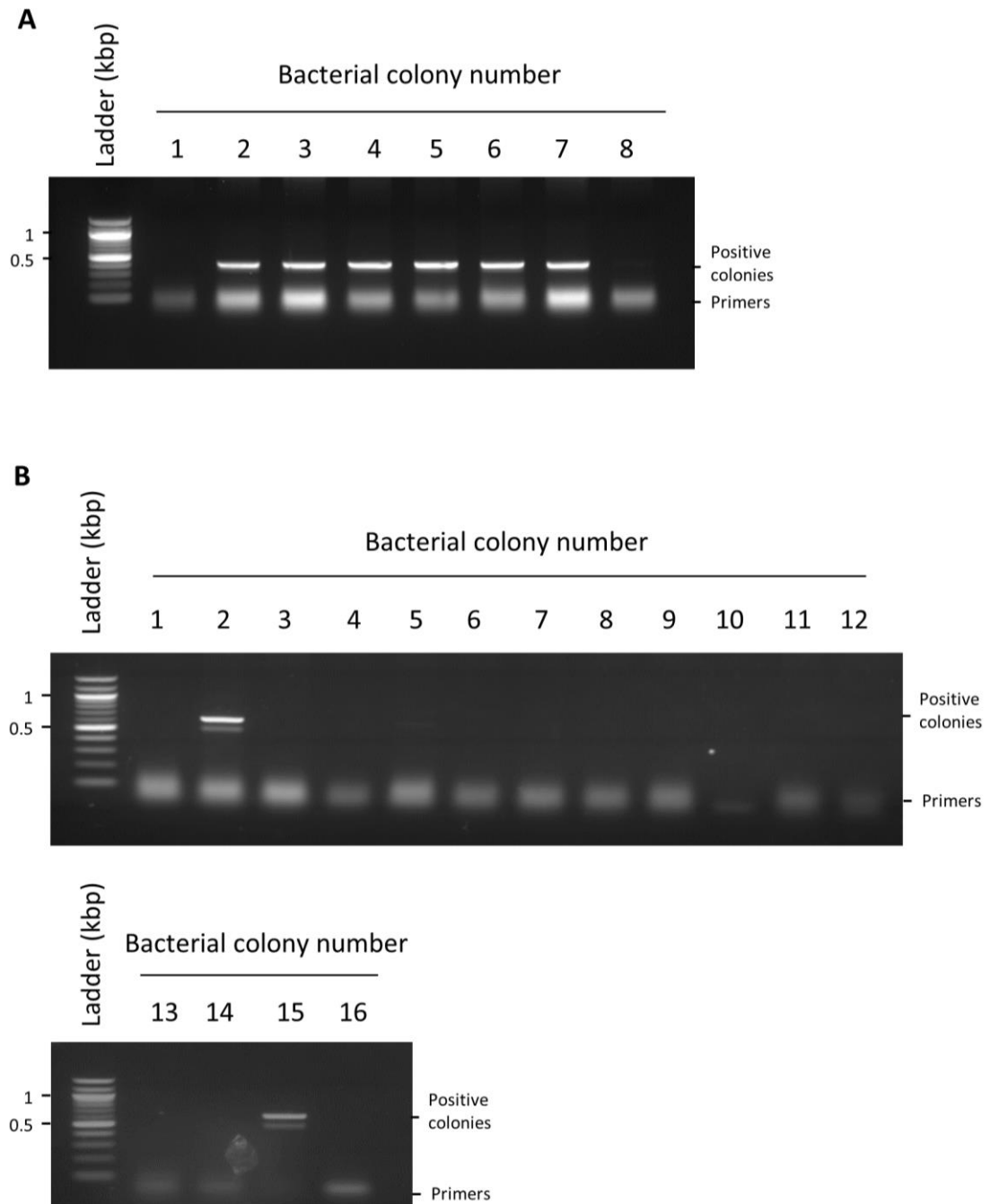


Figure 3.24. Gel electrophoresis of products from colony screening. Bacterial colonies transformed with the pLJM1 P2A-L1 (A), pLJM1 P2A-O1 (B) underwent PCR screening reactions to identify positive colonies. PCR products were run on a 1.5% agarose gel. Expected fragment size were 401 bp and 531 bp for pLJM1 P2A-L1 and pLJM1 P2A-O1, respectively.

Lentivirus was generated by transfection of HEK-293T cells with pLJM1 P2A-L1 or pLJM1 P2A-O1 plasmids along a second-generation lentiviral packaging plasmid and envelope plasmid. Caco-2 cells were transduced with lentivirus and presence of mCherry-Lifeact and Occludin-mEmerald was confirmed by fluorescence microscopy (Fig 3.25). In the majority of cells

where Occludin-mEmerald was expressed, it could be seen to localize at the physiologically relevant location of cell-cell contacts (Fig 3.25D, F); however mCherry-Lifeact did not form actin-like filamentous structures and many globular structures can be seen, suggesting artefacts were present (Fig 3.25C, E), potentially due to off-target binding and fluorescent protein aggregation.

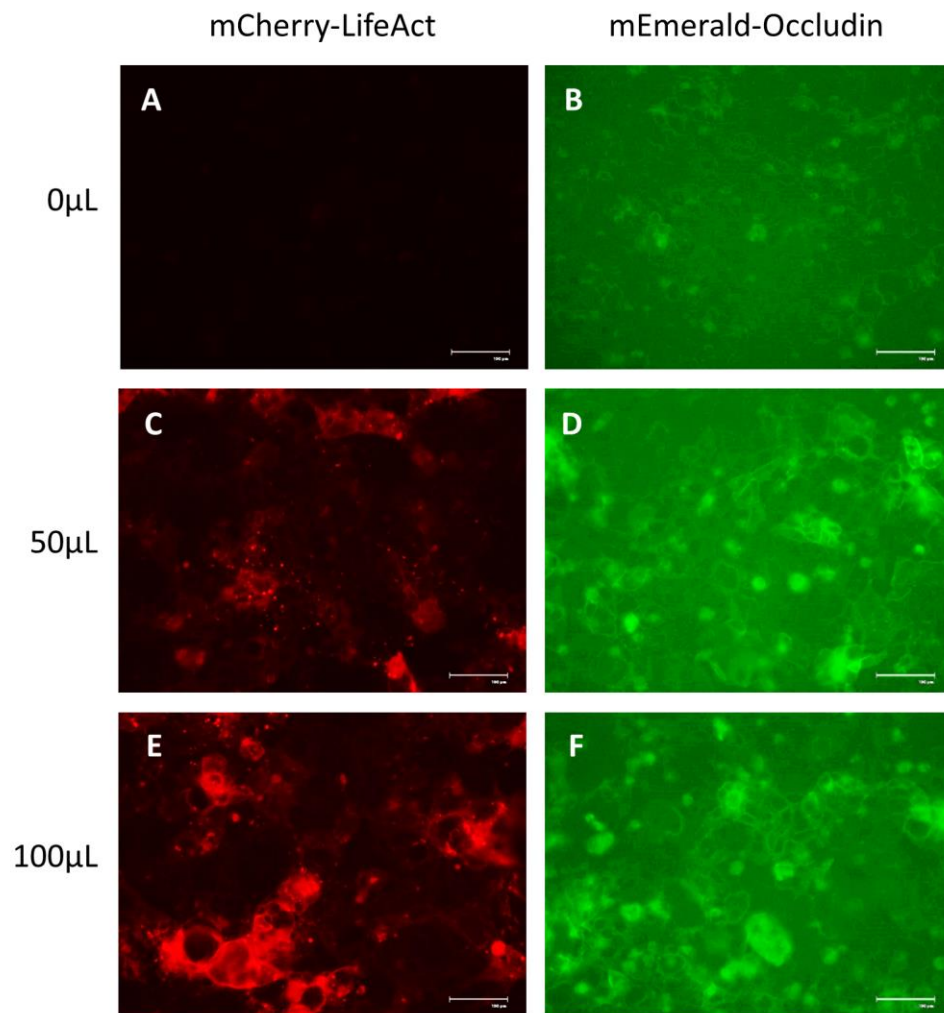


Figure 3.25. Caco-2 cells transduced with lentivirus particles. Caco-2 cells were seeded into 12-well plates at 2×10^5 cells/well and transduced with 0 μ l (A,B), 50 μ l (C,D) or 100 μ l (E,F) of un-titred lentivirus containing mCherry-Lifeact (left column) or mEmerald-Occludin (right column). Images were taken 4 days after transduction and are representative of 3 images at x40 magnification.

Transduced Caco-2 cells were then treated with 25 μ M bosutinib or vehicle and live imaged for 5 h every 5 minutes using fluorescence microscopy with cells being kept under standard culture conditions (37 $^{\circ}$ C, humidified 5% (v/v) CO₂ atmosphere).

Dynamic movement of occludin is seen in both vehicle and bosutinib treated cells as expected (Fig 3.26 and 3.27, see flashdrive for Fig 3.27). Bosutinib caused occludin to rapidly form punctate structures which were internalized, concurrently with membrane invagination. This occurred rapidly ~ 1 h after drug dosing. These gross changes at the cell surface appear to resemble endo/pino-cytosis or reorganisation of the plasma membrane bilayer and lipid rafts. Cells then detached from one another ~ 3 h after drug addition, consistent with immunofluorescence data, whereas the monolayer remained intact in vehicle-treated cells. mCherry-Lifeact imaging is not shown due to the presence of many artefacts and potential off-target binding (Fig 3.25, C, E) (Flores *et al.*, 2019). The decrease in fluorescent intensity seen in vehicle-treated cells is likely due to photo-bleaching, because Western blot data showed the vehicle did not decrease occludin protein levels.

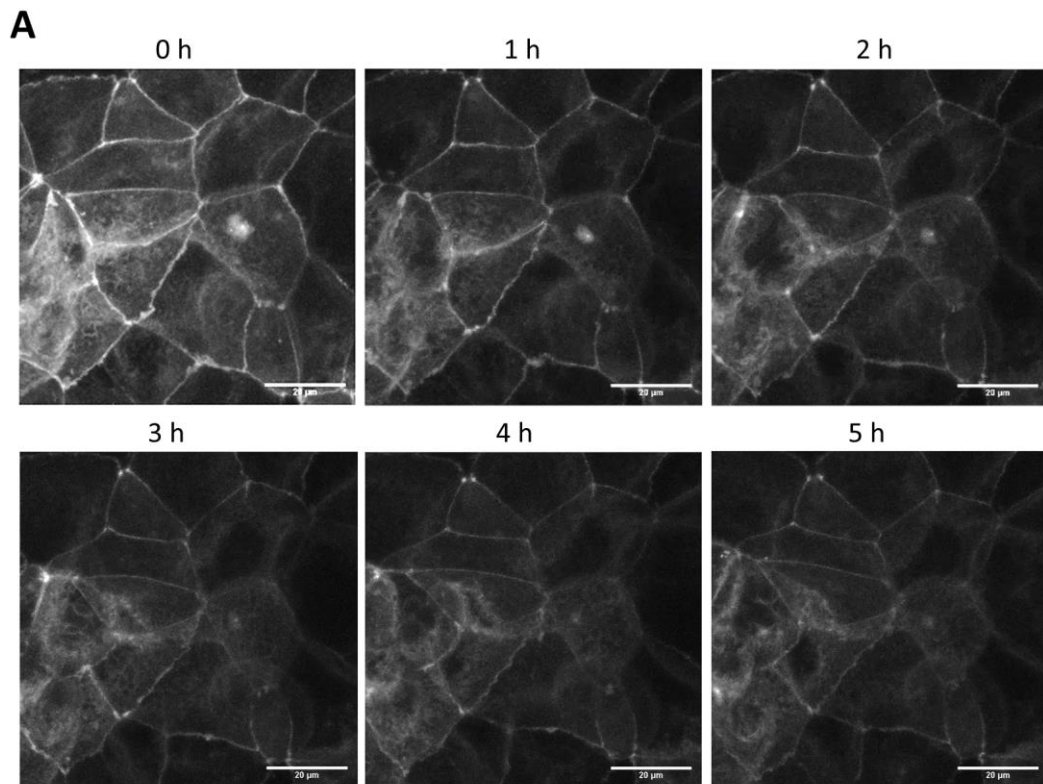


Figure 3.26. Effect of bosutinib on occludin re-localization determined by time-lapse imaging of Caco-2 cells stably expressing mEmerald-occludin (still images). Caco-2 cells were seeded into 4-compartment glass bottom cell culture dishes and differentiated for 10 days. Vehicle (A) or 25 μ M bosutinib (B) was added. Cells were imaged every 5 min for 5 h under standard cell culture conditions (37°C, humidified 5% (v/v) CO₂ atmosphere) using a Zeiss 710 Confocal Microscope at 40x magnification. Only images at hourly intervals are shown (for all images see video). Images are representative of 3 independent experiments.

Figure 3.26. Continues onto the next pages

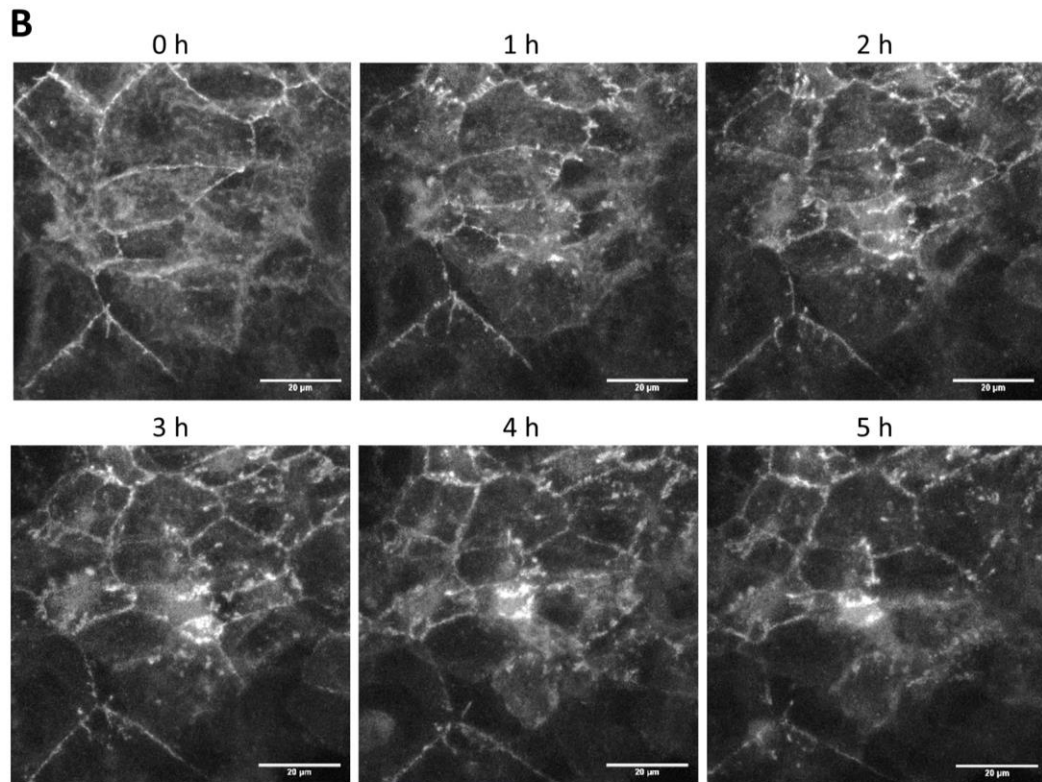


Figure 3.26. Continued

3.3 Summary of results

The main findings from this chapter show that bosutinib was able to: a) increase intestinal permeability and decrease cell-cell adhesion strength at sub-cytotoxic concentrations (this effect was greater than that induced by other TKIs tested); b) decrease E-cadherin and occludin protein levels, most likely by post-transcriptional degradation, and decrease ZO-1 protein levels by a mechanism likely involving decreased transcription; c) induce re-localization of ZO-1, E-cadherin and occludin away from the plasma membrane and into the cytosolic compartment; and d) induces cellular retraction, cytoskeletal rearrangement and formation of contraction fibres.

3.4 Discussion

Intestinal permeability is likely to be a key player in the aetiology of cytotoxic chemotherapy-induced diarrhoea. Chemotherapy-induced increases in paracellular permeability have been shown *in vivo* and in patients, in multiple independent experiments using a variety of different techniques. Increase in gut 'leakiness' – as determined by the lactulose-mannitol test – is seen in cancer patients treated with gefitinib (Melichar, Dvořák, *et al.*, 2010) and 5-FU (Inutsuka *et al.*, 2003). Increased permeability has also been shown during methotrexate

treatment in children with acute lymphoblastic leukaemia, by measuring urine levels of polyethylene glycol after oral administration (Lifschitz *et al.*, 1989). Moreover, 5-FU, irinotecan and methotrexate increase intestinal permeability in both rats and mice (Horie *et al.*, 1998; Maeda *et al.*, 2010; Dong *et al.*, 2014; Maioli *et al.*, 2014; Forsgård *et al.*, 2016).

To test the hypothesis that increased intestinal permeability is important in BCR-ABL inhibitor-induced diarrhoea, we performed *in vitro* experiments using human Caco-2 adenocarcinoma epithelial cells. These cells were exposed to BCR-ABL TKIs which cause diarrhoea to varying frequencies in CML patients: a) bosutinib (70-90%) (Keller *et al.*, 2009; Pfizer, 2014); b) dasatinib (~20%); and c) imatinib (30-50%) (Fullmer *et al.*, 2011; Cohen *et al.*, 2012). We also studied gefitinib, an EGFR inhibitor, as this chemotherapeutic agent has been previously shown to disrupt intestinal intercellular junctions *in vitro* (Hong *et al.*, 2014).

It was found that 25µM bosutinib, when administered apically to a Caco-2 cell monolayer, could rapidly increase paracellular permeability by both the 'leak' and the 'pore' pathways. The effect of bosutinib relative to imatinib appeared to mirror the rapid onset of diarrhoea in the clinic, which occurs within 2-3 days during bosutinib treatment, and after 43 days when patients are receiving imatinib therapy (Kantarjian *et al.*, 2014; Brümmendorf *et al.*, 2015).

Bosutinib administered basolaterally at the therapeutically relevant C_{max} plasma concentration of 400nM had no effect on TEER, suggesting bosutinib-induced increased permeability may be due to local rather than systemic effects. Consistent with this, it has been shown that females and males have similar GI toxicity levels, despite females having several-fold higher circulating plasma levels (Pfizer, 2014).

The apical administration of 25µM TKI was deemed to be pharmacologically relevant because the concentration of bosutinib in the stomach is estimated to be 3.8mM (Pfizer, 2014), which is much greater than the plasma concentration of 150-400nM (Pfizer, 2014). Drug concentrations in the intestinal lumen are much higher than in the plasma because luminal exposure precedes first pass metabolism. At 25µM, bosutinib significantly increased permeability through the 'leak' pathway over the 24h time period studied, whilst 100µM imatinib was required to achieve similar effects. Both dasatinib and gefitinib up to 100µM failed to increase permeation through the 'leak' pathway. To our knowledge, no prior studies have assessed the effect of BCR-ABL inhibitors on intestinal epithelium permeability *in vitro*. However, studies have been performed on patients using gefitinib and imatinib. Gefitinib, given at 250mg or 500mg daily to patients with non-small cell lung cancer (NSCLC) or head and neck carcinoma, increases lactulose/mannitol and lactulose/xylose ratios suggesting

increased intestinal permeability through the size-selective pathway (Melichar, Dvořák, *et al.*, 2010). However, patients with GI stromal tumours (GIST) treated with 400mg imatinib daily do not show an increase in lactulose/mannitol or lactulose/xylose ratio, suggesting no alterations in intestinal permeability (Melichar, Kasparova, *et al.*, 2010). These findings are contradictory to our *in vitro* results and exemplify the common problem of translatability from bench to the patient.

All TKIs tested increased permeation through the 'pore' pathway. This occurred at concentrations as low as 5 μ M for bosutinib, but higher concentrations were required for imatinib (50 μ M), dasatinib (50 μ M) and gefitinib (10 μ M). These observations fit with data suggesting that whilst the 'pore' pathway and the 'leak' pathway are interlinked, they can be controlled independently (Zihni *et al.*, 2016). To our knowledge, this is the first time the effect of BCR-ABL and EGFR inhibitors on intestinal permeation through the charge-selective pathway *in vitro* has been assessed.

We then wished to examine the processes leading to increased permeability. Initially we investigated the ability of TKIs to induce cell death; a potentially simple explanation for increased permeability, by causing cell barrier breakdown (Bojarski *et al.*, 2001; Chen *et al.*, 2017). MTT and CellTitreGlo[®] assays showed bosutinib was the most potent inducer of cell death. However, MTT assays showed a significant, and unexpected, increase in viability at low drug concentrations for all TKIs tested. As Caco-2 cells form a differentiated quiescent cell monolayer which are therefore by nature 'non-dividing', this increase in viability cannot have arisen from an increase in cell number. The apparent increase in viability could be explained by the fact that the MTT assay is not specific for cell viability and is also affected by cellular metabolism. MTT is converted to formazan by the action of NADH-dependent oxidoreductase enzymes; therefore, it is possible these TKIs may increase cellular metabolism leading to an apparent increase in viability. Moreover, MTT assays have previously been shown to underestimate imatinib-induced changes in cell viability in breast and melanoma cell lines (Sims *et al.*, 2009). The CellTitreGlo[®] assay measures the levels of ATP, and is therefore also affected by changes in cellular metabolism, which could explain the slight non-significant increase in viability seen at low concentration of bosutinib and imatinib. To appraise these techniques and determine whether they underestimate cell death, alternative non-metabolic cell death assays such as PARP cleavage, nuclear fragmentation and adenylate kinase release (measured by ToxiLight[™] assay) were also examined. PARP cleavage and nuclear fragmentation occurred at concentrations where there was no significant change in viability determined by MTT, CellTitreGlo[®] or ToxiLight[™] assays

suggesting these latter assays are less sensitive and/or inaccurate methods to determined change in viability. PARP cleavage and nuclear fragmentation occur slightly upstream to cell death which could explain the earlier detection of cell death initiation. Unlike MTT and CellTitreGlo® assays, the ToxiLight™ assay did not induce an apparent increase in viability suggesting a greater validity of this assay.

Bosutinib significantly increased FD-4 flow across the cell monolayer relative to vehicle at a concentration of 25µM at 24 h which is predicted to be sub-cytotoxic by MTT, CellTitreGlo® and ToxiLight™ assay. However, DAPI staining and PARP cleavage indicated some low-level apoptosis at this concentration. These data allow us to postulate the involvement of apoptosis in bosutinib-induced increase in permeability through the size-selective pathway; however, the low level of cell death occurring at 25µM suggests other factors are involved. It is also reasonable to postulate that elevation of cell death markers may be a result of, rather than the cause of, increased permeability (Lugo-Martinez *et al.*, 2009). Imatinib only increased FD-4 flux at 100µM, a concentration shown by CellTitreGlo® to be cytotoxic, suggesting a key mechanism for imatinib-induced increase in FD-4 permeability may be cell death. All TKIs tested decreased TEER at sub-cytotoxic concentrations, allowing us to conclude that cell death is unlikely to be the cause of TKI-induced increases in permeation through the 'pore' pathway.

In addition to cell death, the pathomechanistic basis of increased permeability often involves dissolution of TJ and AJs (Buschmann *et al.*, 2013). Bosutinib (25µM) markedly decreased occludin protein levels whilst ZO-1 and E-cadherin were only slightly decreased. Our data contradicts a study performed on the human colorectal cell line (DLD-1), where bosutinib was shown to increase E-cadherin levels by increasing interaction between E-cadherin and β-catenin (Coluccia *et al.*, 2006). However, the concentration used in the Coluccia *et al.* study was 1.5µM, much lower than the concentration in our experiments which caused TJ and AJ disruption (25µM).

Immunofluorescence data also showed bosutinib decreased levels of intercellular junction proteins and induced a re-localization of occludin. This was consistent with time lapse data collected on Caco-2 cells stably expressing mEmerald-Occludin. The mechanism of this re-localization is unknown but pinocytosis and endocytosis have been postulated (Yu *et al.*, 2008). Decreased occludin plasma membrane levels provide a means through which bosutinib induces an increase in the size-selective pathway (Zihni *et al.*, 2016).

Bosutinib was also capable of inducing cellular retractions and cytoskeletal rearrangement that were not seen with any of the other TKIs tested. This retraction phenotype may be a result of the “unzipping” of the monolayer; inherent tension in the monolayer could cause cells to “pull apart” as TJ and AJ proteins are degraded. In addition, or alternatively, bosutinib could be inducing actomyosin contractions leading to a retraction-like phenotype. This is explored further in chapter 4.

Gefitinib significantly decreased E-cadherin and occludin levels. These findings are consistent with previous studies where gefitinib has been shown to decrease protein levels of TJ and AJ proteins ZO-1 and E-cadherin in IEC-6 cells (Hong *et al.*, 2014). However, as occludin is involved in regulation of the size-selective pathway, it is surprising that 100µM gefitinib did not increase paracellular permeability via the size-selective pathway through increased FD-4 flux. Similar observations were made with dasatinib, which decreased occludin levels at 100µM but which failed to alter permeation through the ‘leak’ pathway. Imatinib did not alter levels of any of the intercellular junction proteins studied. To our knowledge, no literature is available on the effect of imatinib or dasatinib on levels of intestinal ZO-1, E-cadherin or occludin, human or otherwise.

It would be interesting to observe changes in claudins, proteins involved in controlling the charge-selective pathway (Watson *et al.*, 2001), after addition of TKIs. Claudins form gated ion channels and can regulate permeability through channel opening (Krug *et al.*, 2012), a process which can be studied by patch clamp analysis. Changes in levels of claudins can also alter permeability (Zihni *et al.*, 2016). However, there are 26 known claudins (Zihni *et al.*, 2016) and due to time constraints we could not examine these by Western blot; however numerous claudin family members have been implicated in diarrhoea aetiology (Introduction, Table 1.5).

To determine the mechanism of bosutinib-induced decrease in intercellular junction proteins, changes in mRNA and protein levels of TJ and AJ markers were assessed. Bosutinib (25µM) decreased protein levels of E-cadherin, ZO-1 and occludin. Bosutinib did not decrease mRNA levels of *CDH1* and *OCLN* but transiently decreased *TJP1* mRNA levels. This suggests the changes in protein levels of E-cadherin and occludin may occur through post-transcriptional regulation, whereas transcriptional regulation may play a role in bosutinib-induced decrease of ZO-1. It is interesting to note that bosutinib increased *OCLN* mRNA levels despite a fall in protein levels. This suggests a potential compensatory mechanism whereby transcription is increased in an attempt to increase occludin protein levels back to resting

physiological levels. Taken together, our experiments suggest that BCR-ABL inhibitors can increase intestinal permeability and disrupt TJs and AJs integrity.

3.4.1 Limitations and future work

A major limitation of this project was the lack of information on luminal GI concentrations of the TKIs used here; however, plasma concentrations are known. During treatment of CML with daily imatinib at 400mg or 600mg, plasma concentrations are between 2 and 5 μ M (Peng *et al.*, 2005; De Francia *et al.*, 2013). Plasma concentrations of bosutinib, with comparable daily doses of 500mg are much lower than imatinib being between 150-400nM (Pfizer, 2014). Dasatinib-treated CML patients generally have a plasma concentration of \sim 100nM after the standard daily treatment of 100mg (Birch *et al.*, 2013; Wang *et al.*, 2013), whilst gefitinib-treated NSCLC patients have plasma concentrations between 1.6-2.5 μ M when treated with 250mg daily (Nakamura *et al.*, 2010; Miura *et al.*, 2014).

Mathematical modelling to determine physiologically relevant intestinal concentrations would be beneficial, as it is currently not possible to measure drug concentrations in the gut lumen. Several models exist for predicting GI luminal concentrations, and concentrations within enterocytes (Ando *et al.*, 2015). Parameters required for these models are frequently obtainable from the literature or can be predicted by experimentation on intestinal cell lines (Ando *et al.*, 2015). Knowledge of the gut lumen concentrations of TKIs would enable greater confidence in the translatability of our *in vitro* work through the use of physiologically relevant concentrations.

Another limitation of our work was the Caco-2 cell model itself. Caco-2 monolayers are commonly used absorption models in the pharmaceutical industry, partly due to ease of maintenance and their spontaneous differentiation into enterocytes (Antunes *et al.*, 2013). Moreover, bosutinib drug importer OCT-1/SLC22A1 and exporters ABCB1/MDR1 and ABCG2/BCRP are expressed at a similar levels between Caco-2 cells and the human jejunum suggesting cellular drug transport *in vitro* would be similar to humans *in vivo* (Hilgendorf *et al.*, 2007; Brück *et al.*, 2017; Vaessen *et al.*, 2017), in theory resulting in similar intracellular drug concentrations. However, the common monooxygenase metabolic enzyme CYP3A4 has a 871-fold lower expression in Caco-2 cells relative to human jejunum (Vaessen *et al.*, 2017). Moreover, the cancerous origin of Caco-2 cells makes them a poor comparative model for healthy intestinal cells. Caco-2 cells are aneuploid (modal chromosome number of 96) and exhibit chromosome instability with modal chromosome number significantly changing after 20-30 generations (Thompson *et al.*, 2008); therefore a genetic divergence between our

Caco2 cell model and normal healthy cells exists which may limit the translatability of our *in vitro* work to patients.

To overcome the limitations of the Caco-2 cell model, experiments would ideally have been performed on non-cancerous intestinal cells. Most appropriate would be the use of human primary cells but due to difficulty in obtaining human intestinal tissue and maintaining these cells in culture, non-cancerous cell lines would be a more achievable alternative. Cell lines such as FHs 74 Int (ATCC® CCL-241™) and HIEC-6 (ATCC® CRL-3266™) – which are adherent epithelial cell lines derived from human foetal small intestine – are commercially available. Whilst this model has other limitations, such as being relatively immature (as exemplified by a lack of keratin expression), it is reasonable to postulate that findings in this model are more likely to translate to healthy human intestinal epithelium. However, use of cell lines developed from healthy tissue would not overcome the lack of cellular heterogeneity that exists in a 3-dimensional *in vivo* system. Consequently, we assess whether our findings are translatable into 3-dimensional multicellular murine intestinal organoids in chapter 5.

Finally, whilst these findings provide a potential mechanism which could lead to bosutinib-induced diarrhoea, i.e. an increased permeability as a result of TJ and AJ disruption, no conclusions can be made regarding the processes leading to this observed cellular junction dissolution. Further work studying the upstream pathways are performed in chapter 4.

**CHAPTER 4: INVESTIGATING THE
PATHWAYS INVOLVED IN
BOSUTINIB-INDUCED
INTERCELLULAR JUNCTION
DISRUPTION IN CACO-2 CELLS**

4.1 Introduction

In the previous chapter, we demonstrated cancer drugs bosutinib, imatinib, dasatinib and gefitinib can increase paracellular permeability in Caco-2 cells. Bosutinib had the most prominent effect and was also capable of disrupting the actin cytoskeleton, inducing degradation of TJs and AJs, and causing cellular retractions. This chapter aims to elucidate the potential pathways initiated by bosutinib that led to these changes, paying particular attention to pathways involved in occludin degradation and cellular retractions.

There are many signalling cascades involved in the dissolution of intercellular junctions and cellular contractions (both of which can lead to cellular retractions); however, there is significant cross-talk between these pathways and they often converge onto one or more downstream effectors (González-Mariscal *et al.* 2008). Whilst these pathways are not fully elucidated, several of the downstream effector proteins that alter TJ and AJs proteins by cleavage, ubiquitination, phosphorylation, dephosphorylation, endocytosis and degradation are relatively well-established (Fig 4.1) (Ma *et al.*, 2000; Traweger *et al.*, 2002; Rao, 2009; Al-Dasooqi, 2014; Samak *et al.*, 2014).

Downstream effector proteins are known to include matrix metalloproteinases (MMPs), which are zinc-dependent endopeptidases produced as inactive zymogens and converted to active peptidases by cleavage (Al-Dasooqi, 2014). They have been shown to induce proteolysis and alter localisation of TJ and AJ proteins such as E-cadherin (Zuo *et al.*, 2011), occludin (Vermeer *et al.*, 2006; Gorodeski, 2007; Eum *et al.*, 2014), claudins (Vermeer *et al.*, 2006) and ZO-1 (Vermeer *et al.*, 2006; S. Jeong *et al.*, 2012) in a multitude of epithelial cells, including vaginal (Gorodeski, 2007), kidney (S. Jeong *et al.*, 2012), intestinal (Eum *et al.*, 2014; Bein *et al.*, 2015) and airway epithelium (Vermeer *et al.*, 2006). Moreover, MMPs are responsible for the increase in permeability induced by chymase (Groschwitz *et al.*, 2013) and an *N*-acylhomoserine lactone compound (Eum *et al.*, 2014) in Caco-2 BBe and Caco-2 cells, respectively.

As well as cleavage, changes in the phosphorylation status of cellular junction proteins can lead to TJ and AJ disassembly (González-Mariscal *et al.* 2008). During TJ disruption occludin appears to be dephosphorylated on serine and threonine (Ser/Thr) residues and phosphorylated on tyrosine (Tyr) residues (Rao, 2009). Phosphatases such as protein phosphatase 2A (PP2A) can directly interact with the carboxyl tail of occludin located within the cytoplasm, and dephosphorylate serine and threonine residues (which are hyperphosphorylated in intact epithelium) leading to junction disassembly (Nunbhakdi-Craig

et al., 2002; Seth *et al.*, 2007). Some of these phosphatases, such as PP2A, can also indirectly alter occludin phosphorylation, by altering the activity of protein kinase C (PKC) isoforms responsible for the direct phosphorylation of occludin (Fig 4.1, orange pathway) (González-Mariscal *et al.* 2008).

Many kinases also play an active role in TJ and AJ disruption, such as Src which is targeted by both dasatinib (Breccia *et al.*, 2011) and bosutinib (Pfizer, 2014). Studies suggest c-Src can function as both a positive and negative regulator of intercellular junction disassembly. In Caco-2 cells, inhibiting focal adhesion kinase (FAK) on the c-Src activation loop increases intestinal permeability by displacing ZO-1 and occludin from cell borders (Ma *et al.*, 2013). Whereas, direct tyrosine phosphorylation of occludin by c-Src can lead to ubiquitination by the E3 ubiquitin ligase, Itch, followed by degradation via the proteasomal pathway, in an array of epithelial cell lines including human colon HT-29 cells (Fig 4.1, red pathway) (Traweger *et al.*, 2002; Chelakkot *et al.*, 2017).

As well as degradation by the proteasomal pathway, occludin can also be degraded via the lysosomal pathway (Fig 4.1). Evidence for this in Caco-2 cells includes occludin localizing with lysosomal markers, and increased cytoplasmic occludin levels following neutralization of lysosomal pH (Nighot *et al.*, 2017).

In addition to kinases and phosphatases, the actin cytoskeleton is a key regulator of TJ and AJ dynamics. Several cytosolic cell junction proteins, such as ZO-1 and α -catenin, interact directly with actin, connecting TJ and AJ plaques to the peri-junctional actomyosin belt (Zihni *et al.*, 2016). Disruption to the cytoskeleton, through phosphorylation of myosin light chain (MLC) protein can lead to stress fibre formation and increased actomyosin contractility, resulting in TJ disassembly and increased intestinal permeability (Fig 4.1, teal pathway) (Ma *et al.*, 2000; Samak *et al.*, 2014).

A common pathway that is frequently activated during TJ dissolution linked to cytoskeletal disruption is the Rho-ROCK pathway (González-Mariscal *et al.*, 2008). Rho family GTPases are small GTP binding proteins which act as molecular switches, cycling between the active GTP-bound form and the inactive GDP-bound form (González-Mariscal *et al.*, 2008). Ras homolog family member A (RhoA), Ras-related C3 botulinum toxin substrate 1 (Rac) and Cell division control protein 42 homolog (Cdc42) members are all involved in TJ barrier disruption. RhoA has a dominant role in activating Rho-associated protein kinase (ROCK) leading to phosphorylation of MLC (Zandy *et al.*, 2007), actomyosin contractility and subsequent TJ opening (González-Mariscal *et al.*, 2008). RhoA can be activated by pro-inflammatory

cytokines such as Interferon-gamma (INF- γ) (Utech *et al.*, 2005). Activated myosin light chain kinase (MLCK) can also phosphorylate MLC leading to re-localization of TJ proteins (Clayburgh *et al.*, 2004; Lapointe *et al.*, 2011), and has been seen in tumour necrosis factor-alpha (TNF α)-induced alterations in Caco-2 TJ barrier function (Ma *et al.*, 2005). Phosphorylation of MLC due to either ROCK or MLCK activation leading to actomyosin contractility can lead to both cell junction dissolution and cellular contractions.

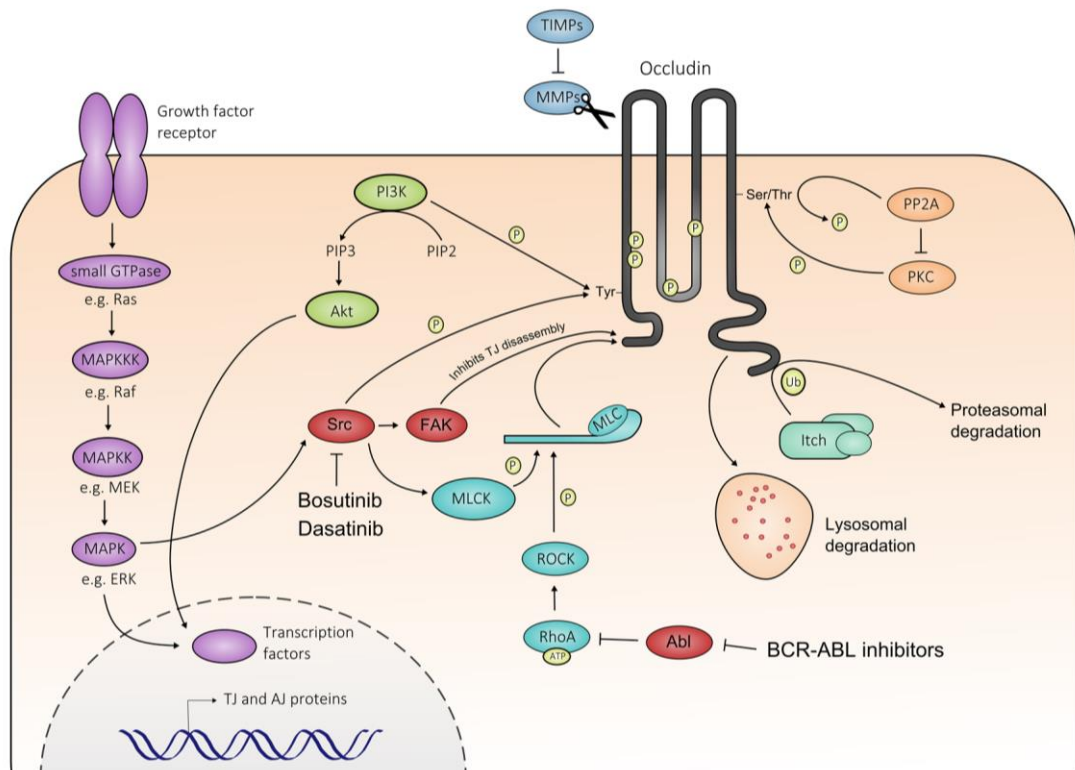


Figure 4.1. Simplification of the signalling pathways involved in increased paracellular permeability. PI3K and Src are involved in phosphorylation of tyrosine occludin residues leading to TJ disruption, whilst phosphatases PP2A and PP1 are involved in dephosphorylation of serine and threonine residues, also leading to TJ disruption. Activation of FAK by Src has been shown to prevent TJ disassembly by an unknown mechanism. Secreted MMPs are involved in occludin cleavage. Occludin can be degraded by both the lysosomal and proteasomal pathway. Phosphorylation of MLC, for example due to RhoA/ROCK signalling, also disrupts TJs (through changes in acto-myosin dynamics). MAPK pathways have a more prominent role in decreasing gene expression of TJ and AJ protein. Abbreviations: ABL, Abelson murine leukaemia viral oncogene homolog 1 protein; FAK, focal adhesion kinase; MAPK(KK), mitogen-activated protein kinase (kinase kinase); MLC(K), myosin light chain (kinase); MMP, matrix metalloproteinases; ROCK, Rho-associated protein kinase; P, phosphate; PI3K, phosphoinositide 3-kinase; PIP2, phosphatidylinositol 4,5-bisphosphate; PIP3, phosphatidylinositol 3,4,5-triphosphate; PKC, protein kinase C; PP2A, protein phosphatase 2A; Ub, ubiquitin; TIMPs, tissue inhibitors of MMPs; Tyr, tyrosine residue; Ser/Thr, serine and threonine residues. Figure produced in Inkscape by S. French.

Another upstream pathway thought to regulate TJ opening is the mitogen-activated protein kinase (MAPK) pathway (González-Mariscal *et al.*, 2008) (Fig 4.1, purple pathway). In this pathway, activation of small GTP binding proteins by growth factor receptors initiates sequential activation of several cytoplasmic Ser/Thr kinases called MAPKs, culminating in phosphorylation of many cytosolic and nucleic proteins (González-Mariscal *et al.*, 2008). The Ras/Raf/MEK1&2/ERK1&2, MLK/MKK3&6/p38 and MLK/MKK4&7/JNK pathways are initiated in response to a vast array of stress stimuli, including oxidative stress and inflammatory cytokines, which can result in decreased barrier function (González-Mariscal *et al.*, 2008). In most cases, this is through altered gene expression of TJ and AJ proteins (Youmba *et al.*, 2012), and therefore not as relevant to our studies on occludin. However, studies in Caco-2 cells have shown activation of c-Jun N-terminal kinase 2 (JNK2) during calcium depletion or cyclic stretch (applying a biaxial repetitive strain to cells) causes redistribution of TJs and AJs proteins away from epithelial junctions (Samak *et al.*, 2014, 2015), providing an alternative mechanism through which the MAPK pathways may increase permeability.

The PI3K/Akt pathway, which can converge onto MAPK pathways (Fig 4.1, green pathway) (Mendoza *et al.*, 2011), is also involved in TJ regulation (González-Mariscal *et al.*, 2008). In this pathway phosphoinositide 3-kinase (PI3K) converts phosphatidylinositol 4,5-bisphosphate (PIP₂) to phosphatidylinositol 3,4,5-triphosphate (PIP₃), causing the activation of Akt which is involved in the degradation of AJ protein β -catenin and reduced expression of TJ and AJ proteins (González-Mariscal *et al.*, 2008). PI3K is associated with the carboxyl tail of occludin in human GI T84 and Caco-2 cells (Nusrat *et al.*, 2000; Sheth *et al.*, 2003). Activation of PI3K – as seen during addition of inflammatory cytokines, such as IFN- γ , (Boivin *et al.*, 2009) or interleukins (ILs) (Ceponis *et al.*, 2000; Suzuki *et al.*, 2011), and oxidative stress (Sheth *et al.*, 2003) – leads to increased permeability, decreased occludin levels and/or redistribution of occludin (Sheth *et al.*, 2003; Boivin *et al.*, 2009).

In summary, effector proteins responsible for TJ and AJ disruption - such as MMPs, kinases and phosphatases - can be activated by several converging and diverging upstream pathways such as the MAPK, PI3K/Akt and Rho-ROCK pathways. These upstream pathways are activated in response to cellular stresses including ER stress, inflammation and oxidative stress which can occur during drug toxicity (González-Mariscal *et al.*, 2008; Hetz, 2012). The small molecule BCR-ABL inhibitor drugs imatinib, dasatinib and nilotinib have been shown to cause oxidative stress (Baran *et al.*, 2013; Damiano *et al.*, 2018) and ER stress (Kerkela *et al.*, 2006; Nakatani *et al.*, 2006; Bellodi *et al.*, 2009; Lin *et al.*, 2013; Lekes *et al.*, 2016; Yang *et al.*,

2018) and this may activate downstream pathways involved in TJ and AJ disruption. This could also result in a cellular retraction phenotype due to release of inherent tension within monolayers causing the cells to separate as cell junctions are degraded. Alternatively, or in addition, the cellular retraction phenotype could be a result of actomyosin contractions, that may be initiated through the Rho-ROCK or MLCK pathway, for example.

In this chapter, we test the hypothesis that bosutinib-induced disruption of intercellular junctions in Caco-2 monolayers involves specific cellular stress pathways. The aims of this chapter were to:

1. Assess the ability of bosutinib and imatinib to induce ER stress and TNF- α release (a pro-inflammatory cytokine)
2. Determine pathways involved in bosutinib-induced cellular retractions using inhibitors of ER stress, inflammation, oxidative stress, cell death, MMPs, ROCK signalling and MLCK activation
3. Determine pathways involved in bosutinib-induced occludin degradation using inhibitors of ER stress, inflammation, oxidative stress, cell death, MMPs, ROCK signalling and MLCK activation
4. To evaluate changes in levels of MMPs and TIMPs induced by bosutinib

4.2 Results

4.2.1 Bosutinib does not induce the release of TNF α

A plethora of studies show TNF α , alone or in combination with other pro-inflammatory cytokines, increase Caco-2 monolayer permeability through re-localization and/or degradation of cell-cell junction proteins such as ZO-1 and occludin (Moran *et al.*, 2012; Al-Sadi *et al.*, 2013; Contreras *et al.*, 2015; Zhang *et al.*, 2016). We therefore tested the hypothesis that bosutinib-induced occludin disruption involved TNF α by first assessing whether bosutinib could induce TNF α release.

Treatment of Caco-2 cells for 24 h with 25 μ M bosutinib or imatinib did not induce the release of TNF α into media (Fig 4.2A, One-way ANOVA, $p < 0.05$); however, 25 μ M dasatinib or gefitinib caused a slight increase in TNF α release (Fig 4.2A, One-way ANOVA, $p < 0.001$). However, levels in the media were still very low, ~3.5pg/mL and ~5pg/mL, for dasatinib and gefitinib, respectively. It is important to note that these values were below the lower limit of quantification (lowest point on the standard curve, 15.6pg/mL, Fig 4,2B), and no positive

control was used for TNF α release from cells, meaning these results should be treated with caution.

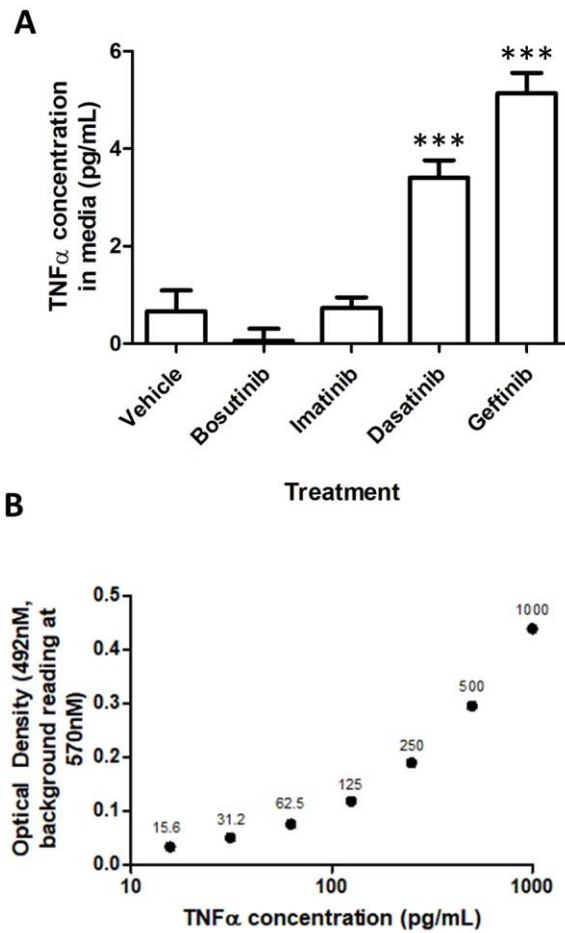


Figure 4.2. Effect of TKIs on TNF α release. Caco-2 cells were incubated with vehicle or 25 μ M bosutinib, dasatinib, imatinib or gefitinib. Growth media was harvested after 24 h and TNF α concentrations determined by ELISA (A). TNF α protein standards (0-1000pg/ml) were added to growth media to generate a standard curve (B). Points are labelled with the TNF α concentration (pg/mL). Due to the logarithmic nature of the graph the optical density (492nm subtract 570nm) of 0pg/ml cannot be shown and was 0.0110. ***p<0.001 versus vehicle, One-way ANOVA followed by Dunnett's post-test, mean \pm SEM, N=3-4, n=3.

4.2.2 Bosutinib does not induce ER stress

ER stress contributes to E-cadherin decrease in intestinal cells treated with the TKI, erlotinib (Fan *et al.*, 2014), and can decrease TEER in Caco-2 cells (Chotikatum *et al.*, 2018). As it was found that bosutinib decreased E-cadherin levels and TEER in chapter 3, we investigated the ability of bosutinib and imatinib to induce ER stress. Two ER stress markers were investigated: - binding immunoglobulin protein (BiP) and C/EBP homologous protein (CHOP) (Cao, 2015). Tunicamycin (10 μ M, 24 h) a *bona fide* inducer of ER stress (Hao *et al.*, 2012) was used as a positive control. Neither 25 μ M bosutinib nor imatinib treatment for up to 24 h increased levels of BiP (Fig 4.3, Dunnett's test, $p > 0.05$). BiP levels appeared slightly elevated after 24 h treatment with imatinib; however, this increase was not significant. CHOP was not detected in either bosutinib or imatinib treated samples. As expected, both BiP (Fig 4.3, Dunnett's test, $p < 0.001$) and CHOP expression was induced with tunicamycin treatment (Fig 4.3).

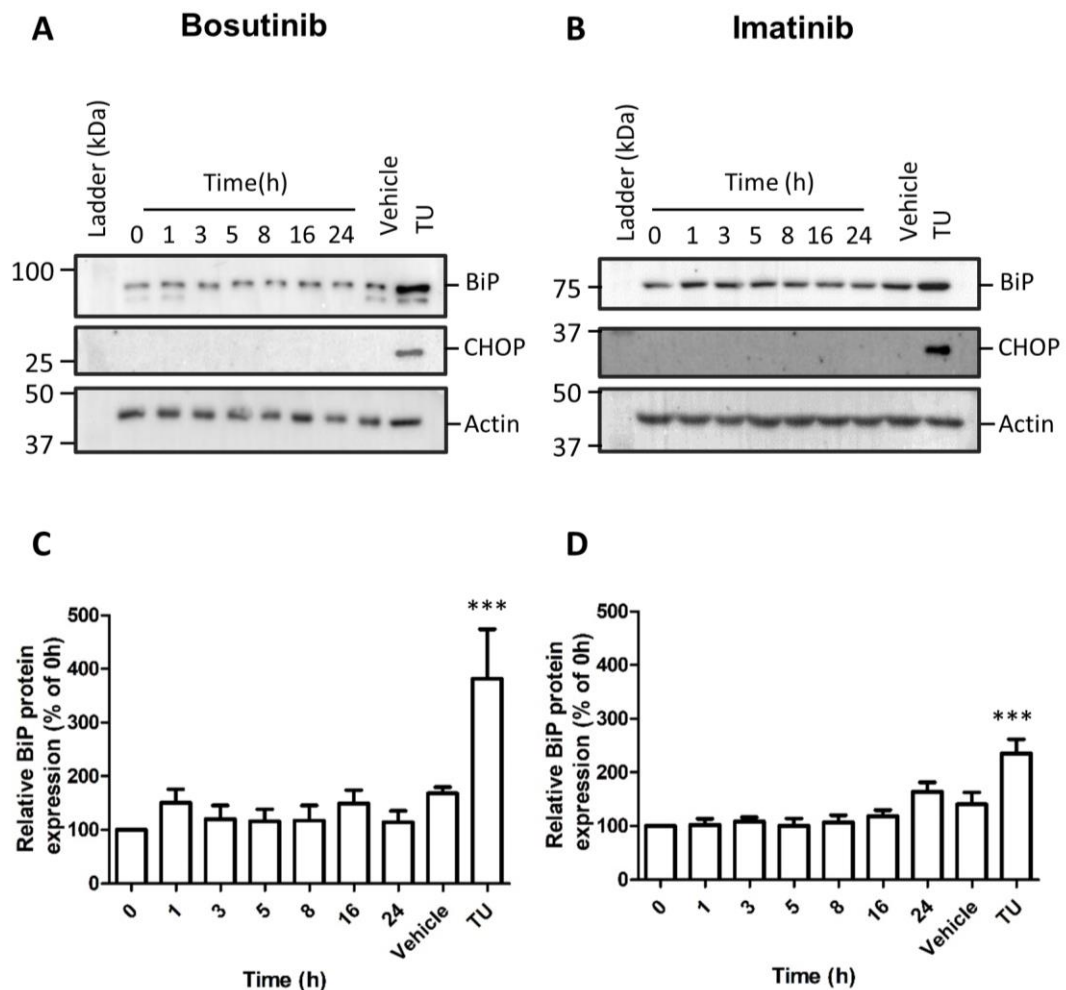


Figure 4.3. Effect of bosutinib and imatinib on levels of ER stress related proteins. Caco-2 cells were incubated with 25 μ M bosutinib (A, C), imatinib (B, D), positive control 10 μ M tunicamycin (TU) or vehicle for 24 h. The expression of BiP and CHOP was analysed by Western blot (A, B). Densitometry analysis was undertaken for BiP and results normalized to actin (C, D). Densitometry analysis was not performed for CHOP. *** $p < 0.001$ versus vehicle, One-way ANOVA followed by Dunnett's test, mean \pm SEM, N=3-4.

4.2.3 Bosutinib-induced cytoskeletal rearrangement and cellular retractions do not involve MLCK

MLCK is known to be involved in TJ reorganization and cytoskeletal rearrangement during cyclic stretch-induced (Samak *et al.*, 2014) and Cytochalasin B-induced (Ma *et al.*, 2000) increase in paracellular permeability in Caco-2 cells. Therefore, we tested whether inhibition of MLCK prevented bosutinib-induced cellular retractions and cytoskeletal rearrangement. Pre-incubation with MLCK inhibitor ML-7 (10 μ M) for 1h failed to prevent bosutinib-induced cytoskeletal rearrangement (Fig 4.4D) or bosutinib-induced cellular retractions (Fig 4.5B, t-test, $p>0.05$).

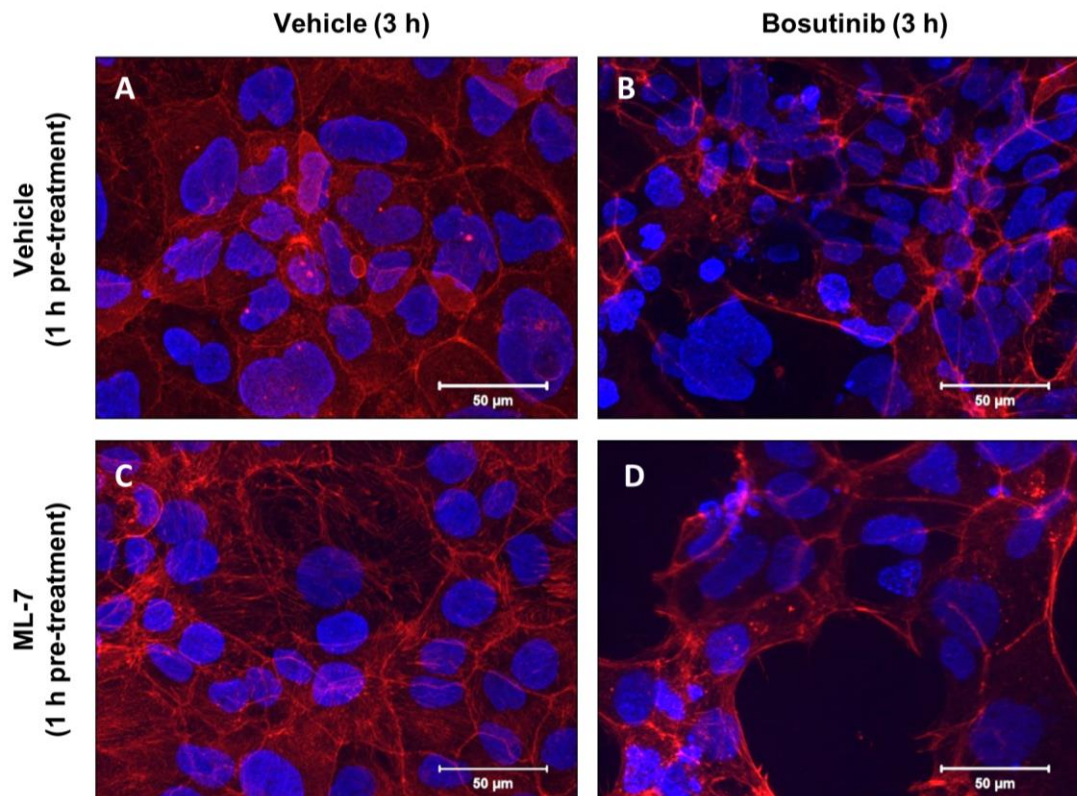


Figure 4.4. Effect of myosin light chain kinase (MLCK) inhibition on bosutinib-induced cytoskeletal rearrangement. Caco-2 cells were pre-treated with vehicle (A,B) or 10 μ M MLCK inhibitor ML-7 (C,D) for 1h then treated with vehicle (A,C) or 25 μ M bosutinib (B,D) for 3 h. Cells were stained for F-actin (red) and nuclei (blue) then analysed by immunofluorescence at 40x magnification. Images are representative of 1 biological experiment with no technical or biological replicates. Three fields of view were taken.

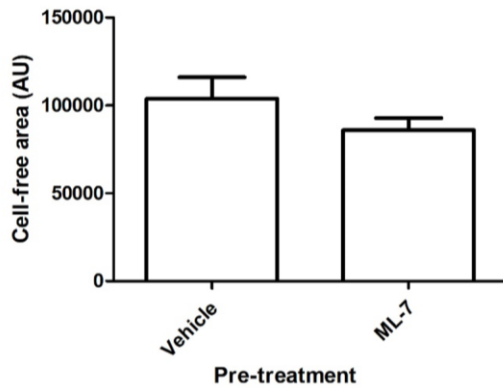


Figure 4.5. Effect of myosin light chain kinase (MLCK) inhibition on bosutinib-induced changes in cellular retractions. Caco-2 cells were pre-treated with 10 μ M MLCK inhibitor (ML-7) or vehicle for 1 h then 25 μ M bosutinib was added for 3 h. Light microscopy images were obtained and cell-free area (extent to which cells had pulled apart i.e. cellular retractions) was determined using the free-hand draw tool in Image J. t-test, mean \pm SEM, N=4, n=3. Abbreviations: AU, arbitrary units. There was no statistical significant difference in cell free area between ML-7 and vehicle pre-treatment.

4.2.4 Bosutinib-induced cellular retractions do not involve Rho kinase activation

A major mechanism of cellular contraction and retraction fibre formation is through RhoA activation leading to ROCK activation (Akhshi *et al.*, 2014). Moreover, ethanol-induced increase in intestinal permeability, cytoskeletal and TJ reorganization is inhibited by Y-27632, a chemical ROCK inhibitor (Elamin *et al.*, 2018). We tested the hypothesis that this signalling pathway was involved in bosutinib-induced cellular retractions by the addition of 10 μ M Y-27632, 1 h prior to treatment with 25 μ M bosutinib or vehicle. Pre-incubation with Y-27632 did not attenuate bosutinib-induced cellular retractions (Fig 4.6, t-test, $p > 0.05$).

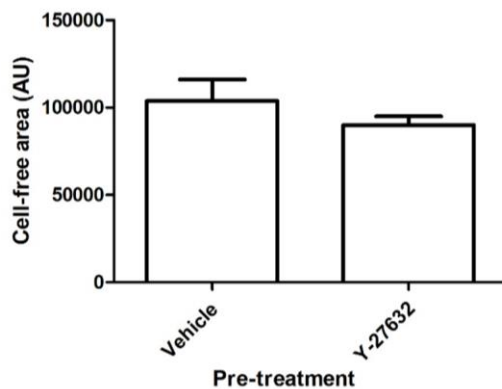


Figure 4.6. Effect of Rho kinase inhibitor Y-27632 on bosutinib-induced changes in cellular retractions. Caco-2 cells were pre-treated with 10 μ M ROCK inhibitor (Y-27632) or vehicle for 1 h then 25 μ M bosutinib was added for 3 h. Three light microscopy images were obtained and cell-free area (extent to which cells had pulled apart i.e. cellular retractions) was determined using the free-hand draw tool in Image J. t-test, mean \pm SEM, N=4, n=3. Abbreviations: AU, arbitrary units. There was no statistical significant difference in cell free area between Y-27632 and vehicle pre-treatment.

4.2.5 Bosutinib decreases occludin levels by protein degradation

Our data showed that bosutinib (25 μ M) decreases occludin protein levels as early as 3 h after treatment (chapter 3, Fig 3.13A and 3.14A), whilst mRNA levels were significantly increased over time (chapter 3, Fig 3.15C). This suggests post-transcriptional modulation of occludin levels by bosutinib, which could occur by decreased translation of the occludin transcript or protein degradation. To investigate this we assessed the turnover of occludin over 24 h using the protein synthesis inhibitor, cycloheximide. Treatment of cells with cycloheximide (10 μ M) did not decrease occludin levels (Fig 4.7) confirming that decreased mRNA levels, or even decreased translation, would not decrease occludin protein levels and that bosutinib must induce protein degradation of occludin. This contradicts a previous study which showed decreased occludin levels in Caco-2 cells around 6-9 h after cycloheximide treatment (Nighot *et al.*, 2017); however, it is unclear whether the cells used were fully differentiated.

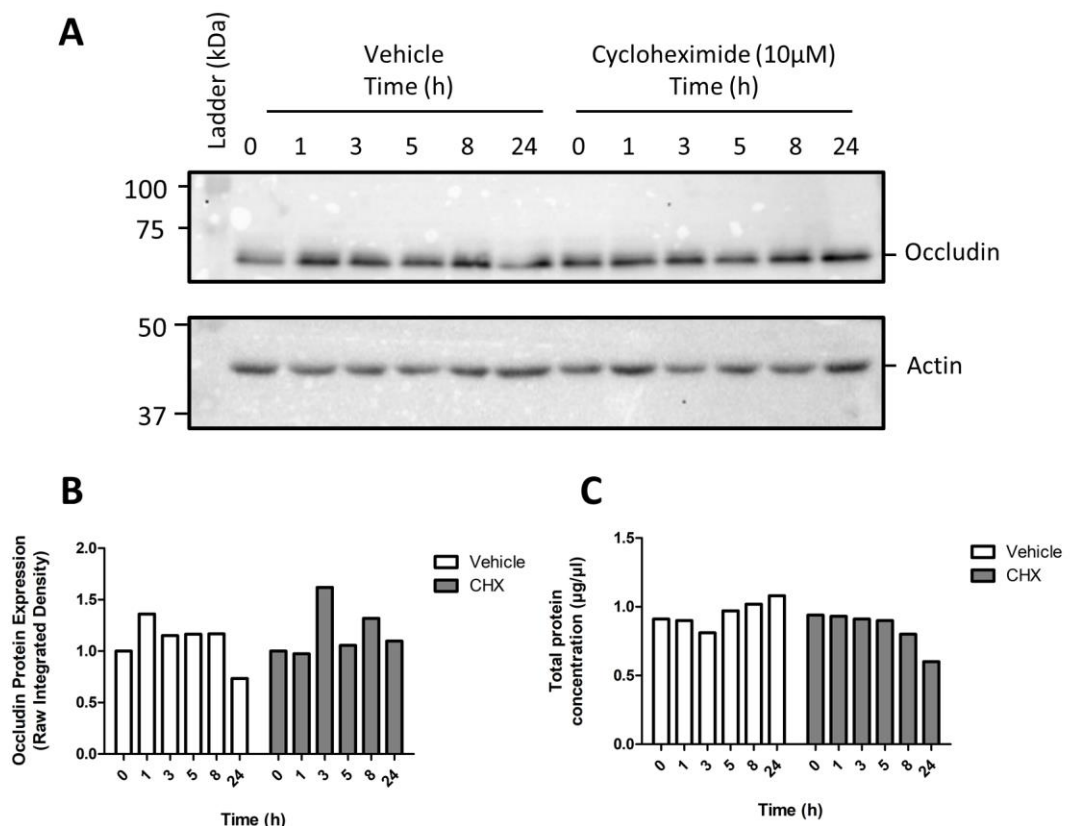


Figure 4.7. Assessment of the half-life of occludin protein using cycloheximide. Caco-2 cells were pre-incubated with vehicle or 10 μ M cycloheximide (CHX) and protein collected at indicated time points. Expression of occludin was analysed by Western blot (A). Densitometry analysis was performed and results normalized to actin (B). Inhibition of protein synthesis by cycloheximide was confirmed by DCTM BioRad protein determination assay (C). N (biological repeats) = 1, n (technical repeats) = 1

4.2.6 Bosutinib-induced degradation of occludin does not involve the lysosomal or proteasomal pathway, but bosutinib-induced cellular retractions involve the proteasomal pathway

Occludin can be degraded by the lysosomal and proteasomal pathway in Caco-2 and HT-29 intestinal cell lines (Chelakkot *et al.*, 2017; Nighot *et al.*, 2017). To explore the mechanism of bosutinib-induced occludin degradation, Caco-2 cells were pre-treated with the lysosomal inhibitors, chloroquine (CQ) (50 μ M), bafilomycin (200nM) and 3-methyladenine (3-MA) (10mM), and the proteasomal inhibitor, MG-132 (50 μ M) for 1 h prior to 25 μ M bosutinib for 3 h. MG-132 did not prevent the significant decrease in occludin (Fig 4.8, Dunnett's test, $p < 0.01$). CQ (Fig 4.8, Dunnett's test, $p < 0.01$), bafilomycin (Fig 4.9, Dunnett's test, $p < 0.01$) and 3-MA (Fig 4.9, Dunnett's test, $p < 0.001$) also failed to prevent a decrease in occludin protein levels.

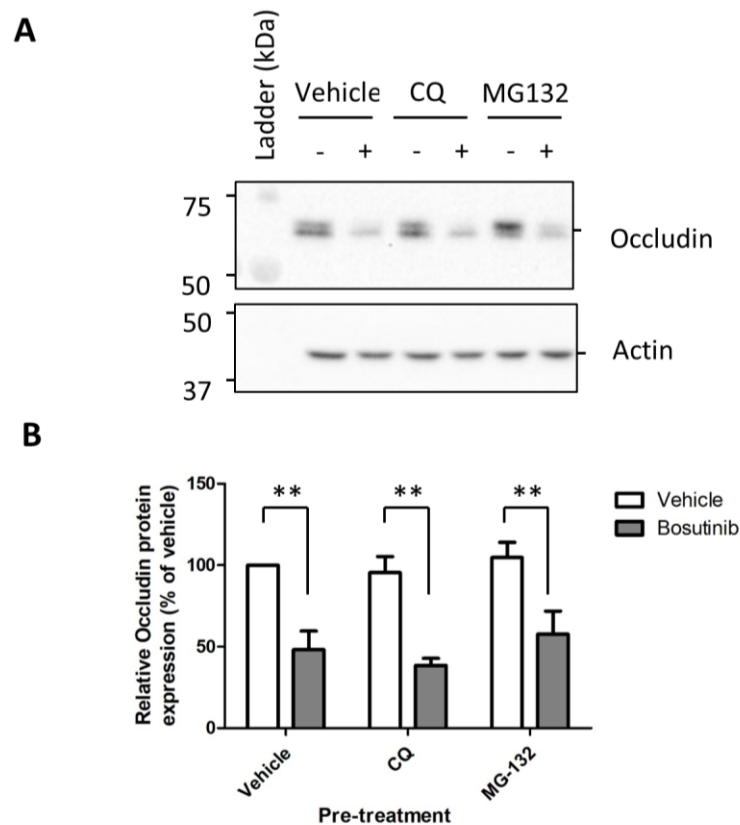


Figure 4.8. Effect of lysosomal inhibitor chloroquine and proteasomal inhibitor MG-132 on bosutinib-induced degradation of occludin. Caco-2 cells were pre-incubated with vehicle, 50 μ M lysosomal inhibitor chloroquine (CQ) or 50 μ M proteasomal inhibitor MG-132 for 1 h then either vehicle control (-) or 25 μ M bosutinib (+) was added for 3 h. Expression of occludin was analysed by Western blot (A). Densitometry analysis was performed and results normalized to actin (B). Significant decreases with bosutinib treatment; ** $p < 0.01$, One-way ANOVA followed by Dunnett's test, mean \pm SEM, N=3-4. CQ and MG-132 pre-treatment did not significantly alter bosutinib-induced reduction in occludin relative to vehicle pre-treatment.

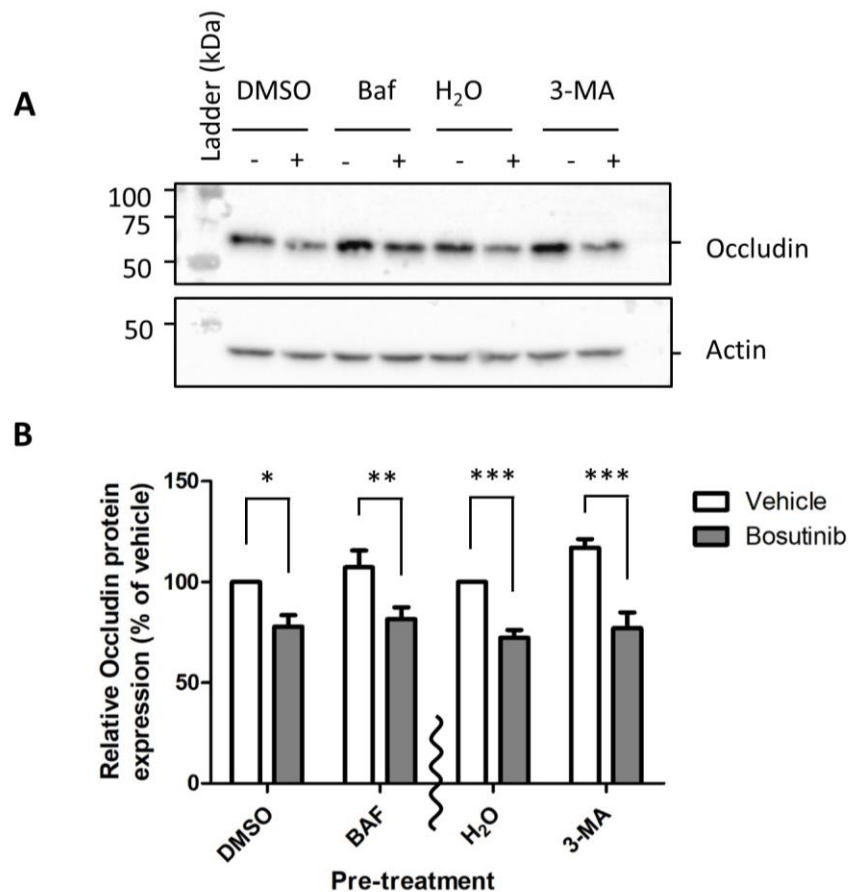


Figure 4.9. Effect of lysosomal inhibitors bafilomycin and 3-methyladenine on bosutinib-induced degradation of occludin. Caco-2 cells were pre-treated with vehicle (DMSO for bafilomycin, H₂O for 3-MA), 10mM lysosomal inhibitor 3-MA or 200nM lysosomal inhibitor bafilomycin (BAF) for 1 h. Then either vehicle (-) or 25µM bosutinib (+) was added for 3 h. Expression of occludin was analysed by Western blot (A). Densitometry analysis was performed and results normalized to actin (B). Significant decreases with bosutinib treatment; *p<0.05, **p<0.01, ***p<0.001, One-way ANOVA followed by Dunnett's test, mean ± SEM, N=3. Baf and 3-MA pre-treatment did not significantly alter bosutinib-induced reduction in occludin relative to vehicle pre-treatment.

Although lysosomal and proteasomal inhibitors failed to prevent bosutinib-induced occludin degradation, it was hypothesized that bosutinib-induced cellular retractions may involve degradation of other cell-cell junction proteins via the proteasomal or the lysosomal pathway. A 1 h pre-treatment of Caco-2 cells with lysosomal inhibitors CQ (50µM), bafilomycin (200nM) or 3-MA (10mM), did not prevent bosutinib-induced changes in morphology i.e. cell-free area did not differ from respective vehicle pre-treatment (Fig 4.10, One-way ANOVA, p>0.05). However, 1 h pre-treatment with the proteasomal inhibitor MG-132 (50µM) reduced the ability for cells to 'pull apart' in the presence of bosutinib (Fig 4.11, t-test, p<0.001).

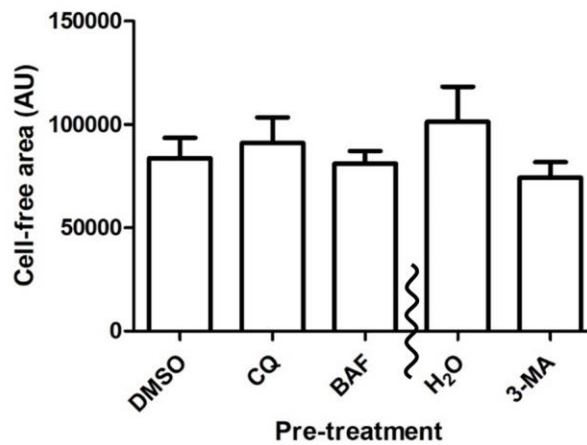


Figure 4.10. Effect of lysosomal inhibitor chloroquine and proteasomal inhibitor MG-132 on bosutinib-induced cellular retractions. Caco-2 cells were pre-treated with 50 μ M chloroquine (CQ), 200nM bafilomycin (BAF), 10mM 3-Methyladenine (3-MA) or vehicle (DMSO for BAF and CQ, H₂O for 3-MA), for 1 h prior to 3 h incubation with 25 μ M bosutinib. Light microscopy images were obtained and cell-free area (extent to which cells had pulled apart) was determined using the free-hand draw tool in Image J. One-way ANOVA, mean \pm SEM, N=3-6, n=3. There was no statistical significant difference in cell free area between CQ, BAF and vehicle (DMSO), nor between 3-MA and vehicle (H₂O).

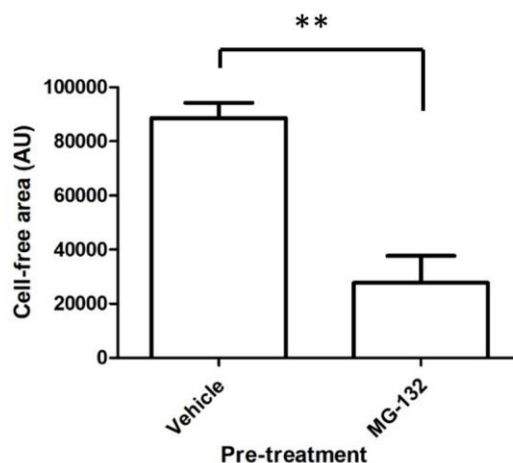


Figure 4.11. Effect of proteasomal inhibitor MG-132 on bosutinib-induced in cellular retractions. Caco-2 cells were pre-treated with 50 μ M MG-132 or vehicle for 1 h prior to 3 h incubation with 25 μ M bosutinib. Light microscopy images were obtained and cell-free area (extent to which cells had pulled apart) was determined using the free-hand draw tool in Image J. ** p <0.01 versus vehicle, t-test, mean \pm SEM, N=3, n=3.

4.2.7 Bosutinib-induced occludin degradation and cellular retractions do not involve ROS signalling

Lipid peroxidation by reoxygenation or hydrogen peroxide (H₂O₂) treatment increases Caco-2 monolayer permeability (Tomita *et al.*, 2002), and in some studies this has been shown to involve re-localization of ZO-1 and occludin away from the plasma membrane (Martín-Venegas *et al.*, 2013; Catanzaro *et al.*, 2015). Consequently, we also explored the role of reactive oxidative species (ROS) signalling in bosutinib-induced occludin degradation and cell morphology alterations.

Inhibition of ROS signalling by a 2 h pre-treatment with the iron-chelating agent deferoxamine mesylate (DEF) (100µM) (Fig 4.12, Dunnett's test, p<0.05) or the antioxidant N-acetylcysteine (NAC) (10mM) (Fig 4.12, Dunnett's test, p<0.01) were unable to prevent bosutinib-induced (25µM, 3 h) occludin protein decrease.

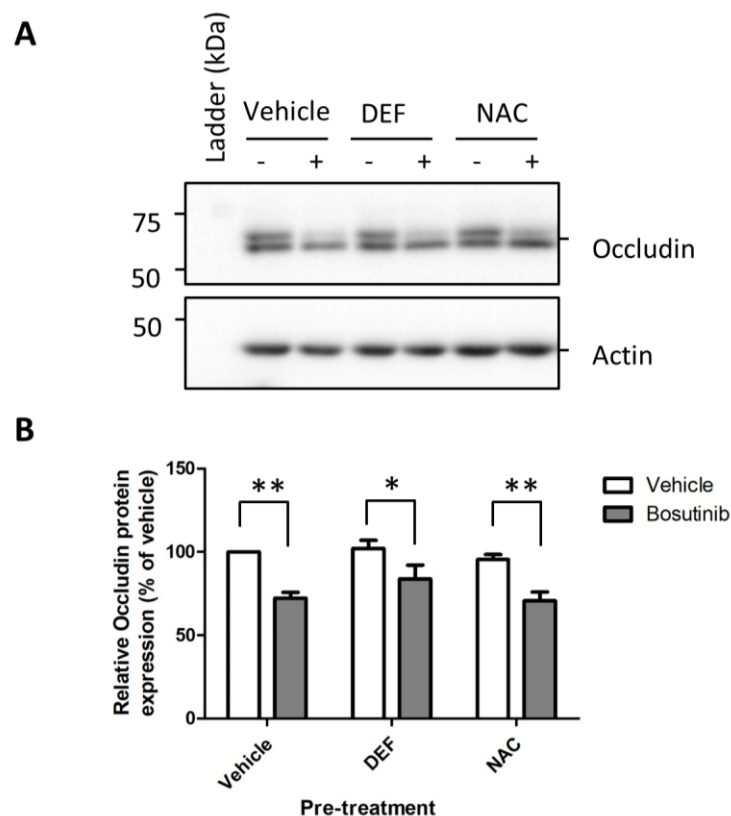


Figure 4.12. Effect of ROS inhibitors on bosutinib-induced degradation of occludin. Caco-2 cells were pre-treated with vehicle, 100µM ROS inhibitor deferoxamine (DEF) or 5mM ROS inhibitor N- acetylcysteine (NAC) for 2 h then either vehicle (-) or 25µM bosutinib (+) was added for 3 h. Expression of occludin was analysed by Western blot (A). Densitometry analysis was performed and results normalized to actin (B). Significant decreases with bosutinib treatment; *p<0.05, **p<0.01, One-way ANOVA followed by Dunnett's test, mean ± SEM, N=4. DEF and NAC pre-treatment did not significantly alter bosutinib-induced reduction in occludin relative to vehicle pre-treatment.

Deferoxamine pre-treated cells displayed slightly higher occludin levels (albeit not significant) after addition of bosutinib, compared to vehicle pre-treated cells (Fig 4.12, Dunnett's test, $p > 0.05$). Therefore, to investigate this further, cells were pre-treated for 2 h with increasing concentrations of deferoxamine (0.25mM to 15mM) to determine the possible contribution of ROS signalling in bosutinib-induced occludin degradation. Increasing concentrations failed to attenuate bosutinib-induced occludin decrease (Fig 4.13, Dunnett's test, $p < 0.05$). However, these results should be interpreted with caution as the bosutinib-induced decrease in occludin was not significant with vehicle pre-treatment.

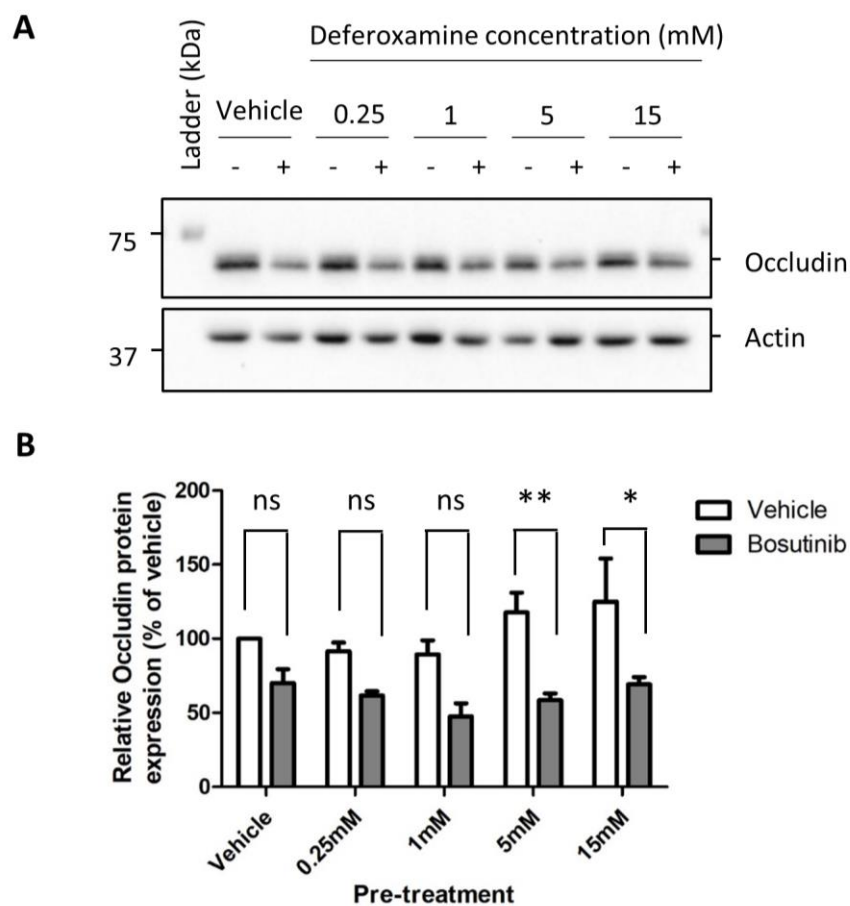


Figure 4.13. Effect of high concentrations of ROS inhibitor deferoxamine on bosutinib-induced occludin degradation. Caco-2 cells were pre-treated with vehicle or deferoxamine (0.25mM-15mM) for 2 h then either vehicle (-) or 25 μ M bosutinib (+) was added for 3 h. Expression of occludin was analysed by Western blot (A). Densitometry analysis was performed and results normalized to actin (B). Significant decreases with bosutinib treatment; * $p < 0.05$, ** $p < 0.01$, One-way ANOVA followed by Dunnett's test, mean \pm SEM, N=5. All concentrations of DEF did not significantly alter bosutinib-induced reduction in occludin relative to vehicle pre-treatment.

Consistent with findings regarding occludin protein levels, neither deferoxamine (100 μ M) nor N-acetylcysteine (10mM) pre-treatment prevented bosutinib-induced cellular retractions (Fig 4.14, One-way ANOVA, $p>0.05$).

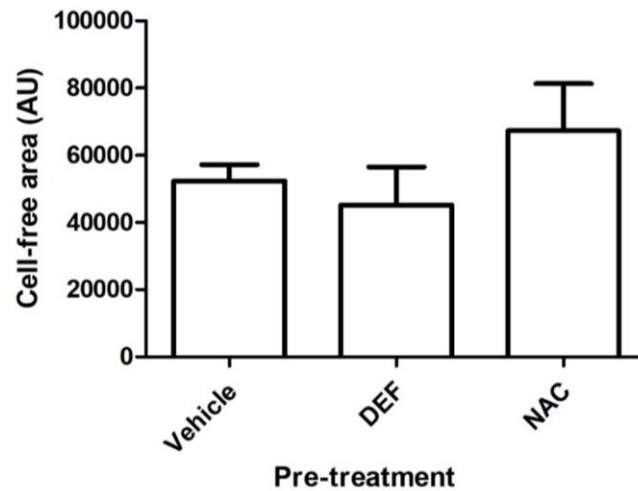


Figure 4.14. Effect of ROS inhibitors on bosutinib-induced cellular retractions. Caco-2 cells were pre-treated with 100 μ M deferoxamine mesylate (DEF), 10mM N-acetylcysteine (NAC) or vehicle for 2 h then 25 μ M bosutinib was added for 3 h. Light microscopy images were obtained and cell-free area (extent to which cells had pulled apart) was determined using the free-hand draw tool in Image J. One-way ANOVA, mean \pm SEM, N=3, n=3. There was no statistical significant difference in cell free area between DEF, NAC and vehicle.

4.2.8 Bosutinib-induced occludin degradation and cellular retractions do not involve cell death pathways

Unsurprisingly, apoptosis can induce an increase in epithelial permeability (Bojarski *et al.*, 2001). Our data showed that 25 μ M bosutinib can induce PARP cleavage and nuclear fragmentation after 3 h (chapter 3; Fig. 1.7A, 1.8). We therefore hypothesized that bosutinib-induced occludin degradation and morphological changes may be linked to cell death. To test this hypothesis, the necroptosis inhibitor necrostatin-1 (50 μ M), oxidative-necrosis inhibitor IM-54 (20 μ M), ferroptosis inhibitor ferrostatin-1 (10 μ M) and pan caspase (apoptosis) inhibitor Z-VAD-FMK (30 μ M) were added to Caco-2 cells 1 h prior to the addition of 25 μ M bosutinib for 3 h.

Cells pre-treated with IM-54, ferrostatin-1 or Z-VAD-FMK maintained a significant decrease in occludin levels after bosutinib treatment (Fig 4.15, Dunnett's test, $p < 0.05$), whilst pre-treatment with necrostatin-1 prevented a significant bosutinib-induced occludin decrease (Fig 4.15, Dunnett's test, $p > 0.05$). However, it is important to note that occludin levels following pre-incubation with necrostatin-1 differed little from the vehicle pre-treatment for both vehicle and bosutinib post-treatment (Fig 4.15, Dunnett's test, $p > 0.05$).

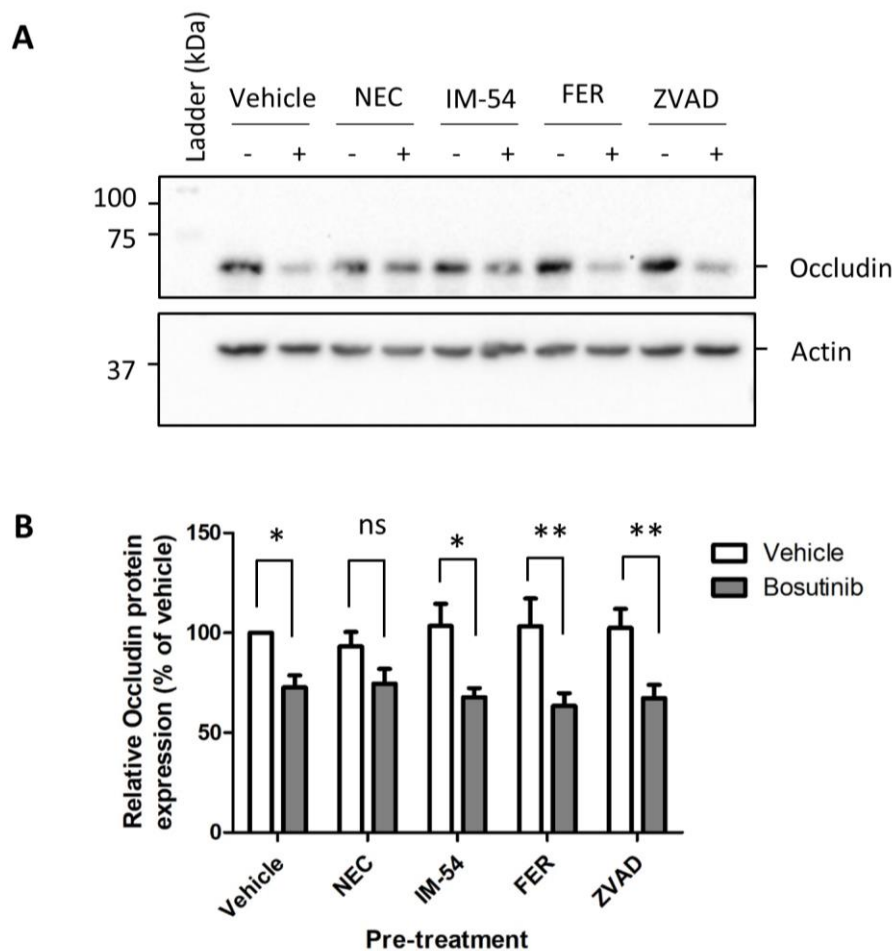


Figure 4.15. Effect of cell death inhibitors on bosutinib-induced degradation of occludin. Caco-2 cells were pre-treated with vehicle, 50 μ M Necrostatin-1, 20 μ M IM-54, 10 μ M Ferrostatin-1, 30 μ M Z-VAD-FMK (ZVAD) for 1 h then either vehicle (-) or 25 μ M bosutinib (+) was added for 3 h. Expression of occludin was analysed by Western blot (A). Densitometry analysis was performed and results normalized to actin (B). Significant decreases with bosutinib treatment; * $p < 0.05$, ** $p < 0.01$, One-way ANOVA followed by Dunnett's test, mean \pm SEM, N=3-4. All cell death inhibitors did not significantly alter bosutinib-induced reduction in occludin relative to vehicle pre-treatment.

Furthermore, none of the cell death inhibitors were able to attenuate bosutinib-induced cellular retractions (Fig 4.16, One-way ANOVA, $p > 0.05$).

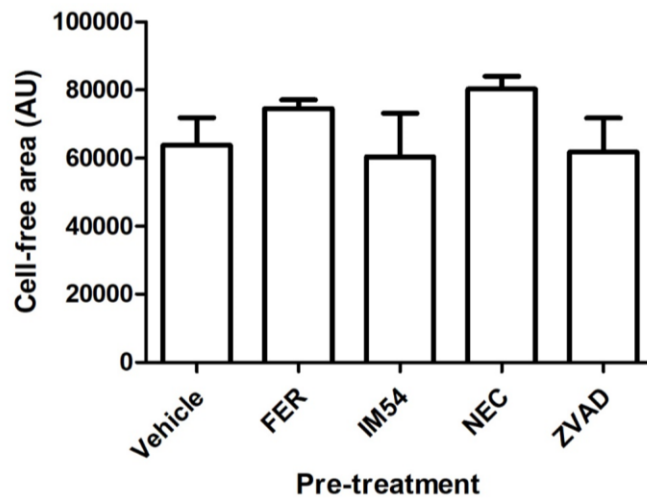


Figure 4.16. Effect of cell death inhibitors on bosutinib-induced cellular retractions. Caco-2 cells were pre-treated with vehicle, 10 μ M ferrostatin-1 (FER), 20 μ M IM-54, 50 μ M necrostatin-1 (NEC), 30 μ M Z-VAD-FMK (ZVAD) for 1 h then 25 μ M bosutinib was added for 3 h. Light microscopy images were obtained and cell-free area (extent to which cells had pulled apart) was determined using the free-hand draw tool in Image J. One-way ANOVA, mean \pm SEM, N=3-5, n=3. There was no statistical significant difference in cell free area between cell death inhibitors and vehicle.

3.4.1 Bosutinib-induced cellular retractions, but not occludin degradation, is attenuated by MMP inhibitor GM6001

MMPs are associated with colitis in rodent models and have a role in TJ modulation (Al-Dasooqi *et al.*, 2010; Trivedi *et al.*, 2013; Ding *et al.*, 2014). It has been shown *Mmp-9^{-/-}* mice have decreased intestinal permeability and higher occludin protein levels than wild type mice (Nighot *et al.*, 2015). Therefore, we assessed the effect of MMP inhibition on bosutinib-induced occludin protein decrease.

Pre-treatment with the pan-MMP inhibitor, GM6001 (10 μ M), for 1 h failed to prevent bosutinib-induced occludin decrease in Caco-2 cells (Fig 4.17, Dunnett's test, $p < 0.05$); the difference between occludin levels in bosutinib treated cells pre-treated with either vehicle or GM6001 was not significant (Fig 4.17, Dunnett's test, $p > 0.05$).

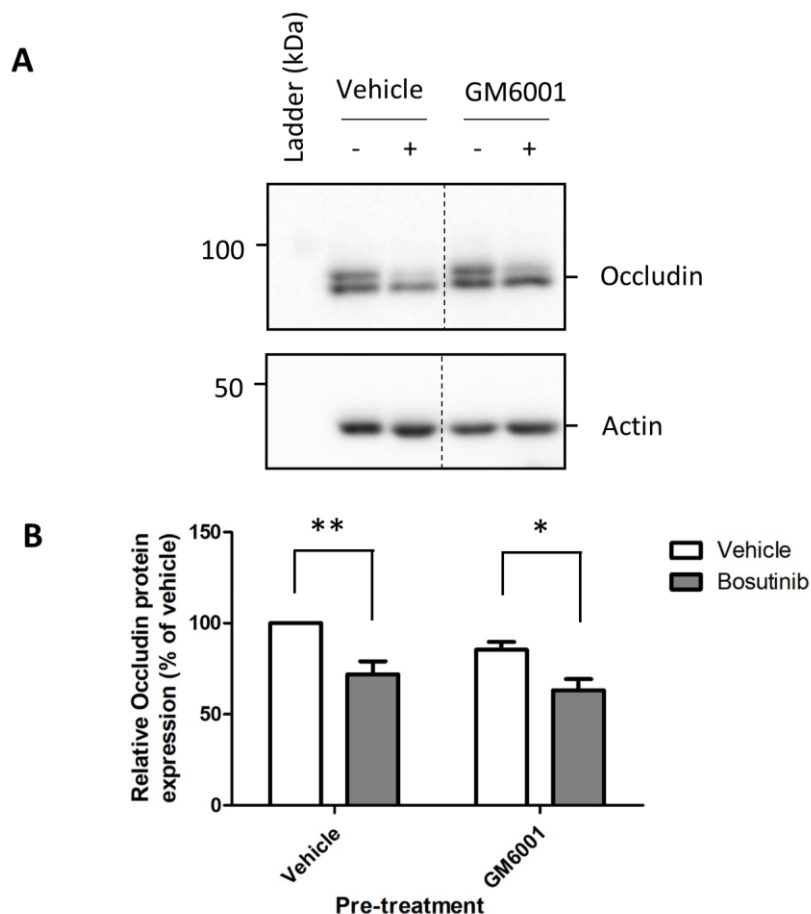


Figure 4.17. Effect of MMP inhibitor GM6001 on bosutinib-induced degradation of occludin. Caco-2 cells were pre-treated with vehicle or 10 μ M GM6001 for 1 h then either vehicle (-) or 25 μ M bosutinib (+) was added for 3 h. Expression of occludin was analysed by Western blot (A). Densitometry analysis was performed and results normalized to actin (B). Dotted lines represent where membranes were cropped. Significant decreases with bosutinib treatment; * $p < 0.05$, ** $p < 0.01$, One-way ANOVA followed by Dunnett's test, mean \pm SEM, N=6. GM6001 pre-treatment did not significantly alter bosutinib-induced reduction in occludin relative to vehicle pre-treatment.

To ensure maximal MMP inhibition, cells were treated with increasing concentrations of GM6001 (50µM - 200µM). Whilst pre-treatment with greater concentrations of GM6001 increased occludin levels (relative to pre-treatment with vehicle) in the presence of bosutinib, these differences were not significant (Fig 4.18, Dunnett's test, $p>0.05$). One hundred micromolar GM6001 pre-treatment prevented the decrease in occludin normally seen with bosutinib treatment (Fig 4.18, Dunnett's test, $p>0.05$); however, this may be due to lower levels of occludin in 100µM GM6001 pre-treated cells relative to vehicle pre-treated cells in the *absence* of bosutinib.

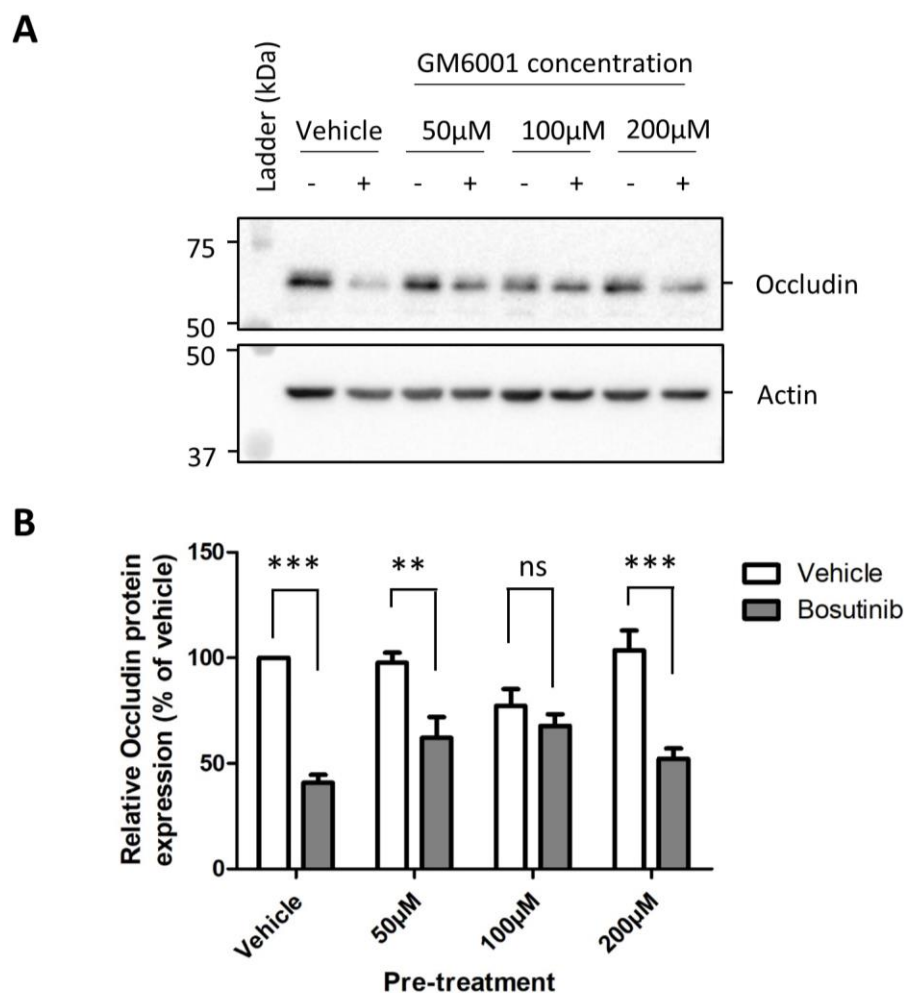


Figure 4.18. Effect of high concentrations of MMP inhibitor GM6001 on bosutinib-induced occludin degradation. Caco-2 cells were pre-treated with vehicle or 50µM-200µM GM6001 for 1 h then either vehicle or 25µM bosutinib was added for 3h. Expression of occludin was analysed by Western blot (A). Densitometry analysis was performed and results normalized to actin (B). Significant decreases with bosutinib treatment; ** $p<0.01$, *** $p<0.001$, One-way ANOVA followed by Dunnett's test, mean \pm SEM, $n=3$. All concentrations of GM6001 did not significantly alter bosutinib-induced reduction in occludin relative to vehicle pre-treatment ($p>0.05$).

We also assessed whether MMP inhibition could prevent bosutinib-induced cellular retractions. GM6001 (10 μ M) was added to cells 1 h prior to 25 μ M bosutinib treatment for 3 h. Pre-incubation with GM6001 significantly attenuated bosutinib-induced increase in cell-free area in Caco-2 cells (Fig 4.19, t-test, $p < 0.05$).

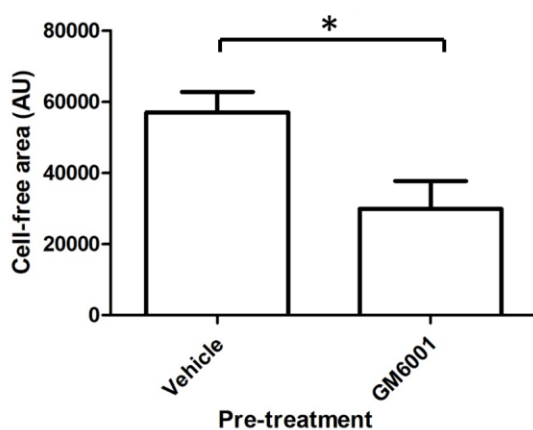


Figure 4.19. Effect of MMP inhibitor GM6001 on bosutinib-induced cellular retractions. Caco-2 cells were pre-treated with 10 μ M GM6001 or vehicle for 1 h then 25 μ M bosutinib was added for 3 h. Light microscopy images were obtained and cell-free area (extent to which cells had pulled apart) was determined using the free-hand draw tool in Image J. * $p < 0.05$ versus vehicle, t-test, mean \pm SEM, N=4, n=3.

4.2.9 Bosutinib decreases levels of TIMP2

As our data suggested MMP inhibition could prevent bosutinib-induced cellular retractions, and it has previously been shown chemotherapy, such as irinotecan, can increase MMP levels in rat intestine (Al-Dasooqi *et al.*, 2010), we hypothesized that bosutinib would increase MMPs levels and/or decrease tissue inhibitor of metalloproteinase (TIMP) levels. An MMP array was used to assess changes in the levels of MMP-1, -2, -3, -8, -9, -10 and -13 as well as TIMPs-1, -2 and -4 in Caco-2 cells both extra-cellularly (i.e. secreted into the growth media), and intra-cellularly. Bosutinib (25 μ M) treatment for 3 h did not appear to drastically alter the levels of secreted MMP and TIMP proteins (Fig 4.20, $n=1$). However, intra-cellular TIMP-2 levels were significantly decreased following bosutinib treatment (Fig 4.20, Dunnett's test, $p < 0.001$).

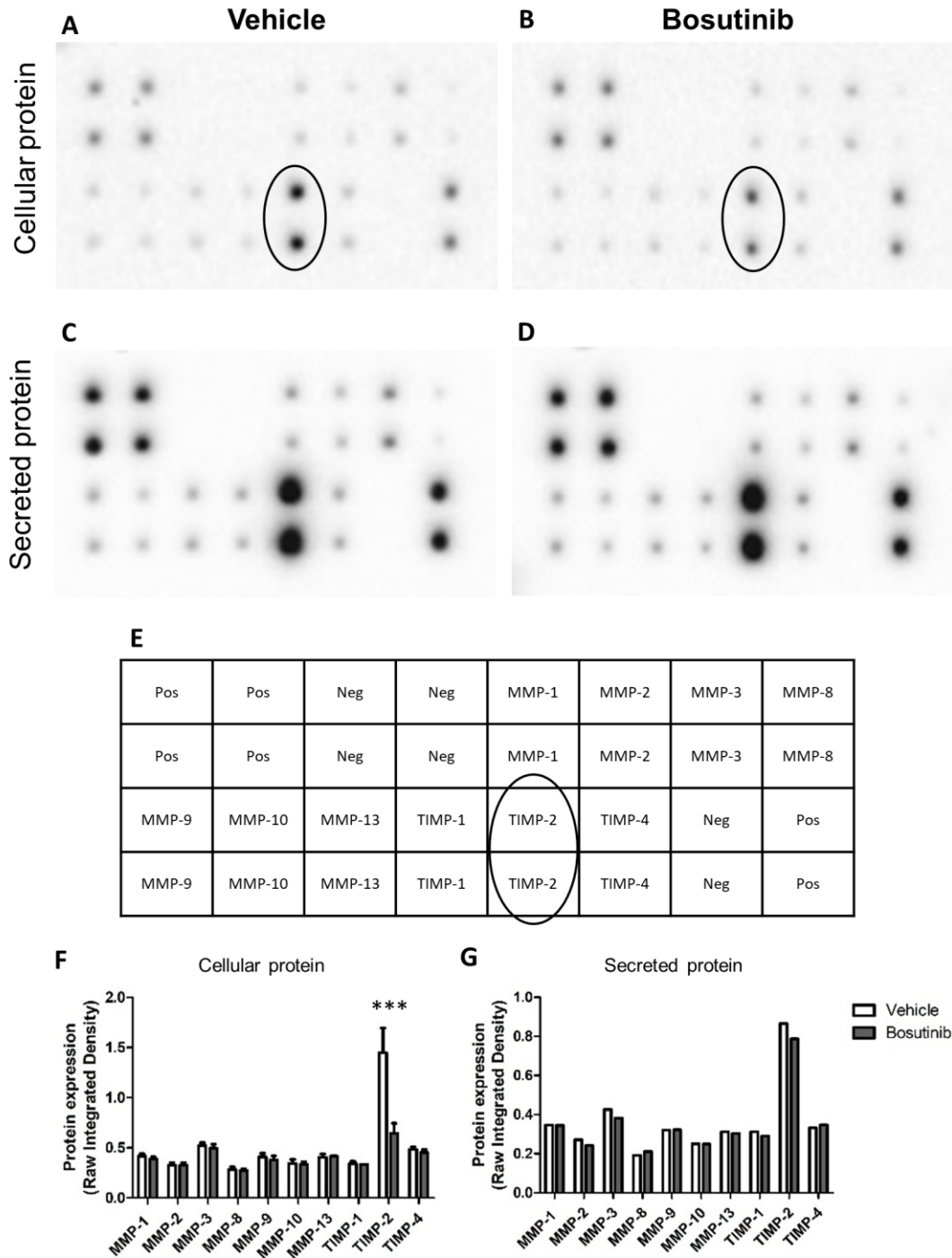


Figure 4.20. Effect of bosutinib on protein levels of MMPs and TIMPs. Caco-2 cells were treated with vehicle (A, C) or 25 μ M bosutinib (B, D) for 3 h. Whole-cell protein lysates and media were harvested to determine level of intracellular protein (A, B, F) and secreted protein (C, D, G), respectively. Protein levels were determined by MMP array (Membrane layout (E)). Densitometry analysis was performed and results normalized to positive control (Pos) after subtraction of background reading negative control (Neg) (F, G). Due to high levels of TIMP-2 secreted protein, a membrane which was not overexposed for TIMP-2 (not shown) was used to determine changes in TIMP-2 secreted protein. *** $p < 0.001$ versus vehicle, One-way ANOVA followed by Dunnett's test, mean \pm SEM, N=1 and 3 for media and protein, respectively.

Western blot analysis of 25 μ M bosutinib-treated Caco-2 cells was used to confirm this finding and to further assess changes in TIMP-2 levels over a 24 h time course. Bosutinib induced a transient ~50% decrease in intra-cellular TIMP-2 protein from 1 h of treatment, which became significant at 3 h (Fig 4.21, Dunnett's test, $p < 0.05$), and was not significant at later time points.

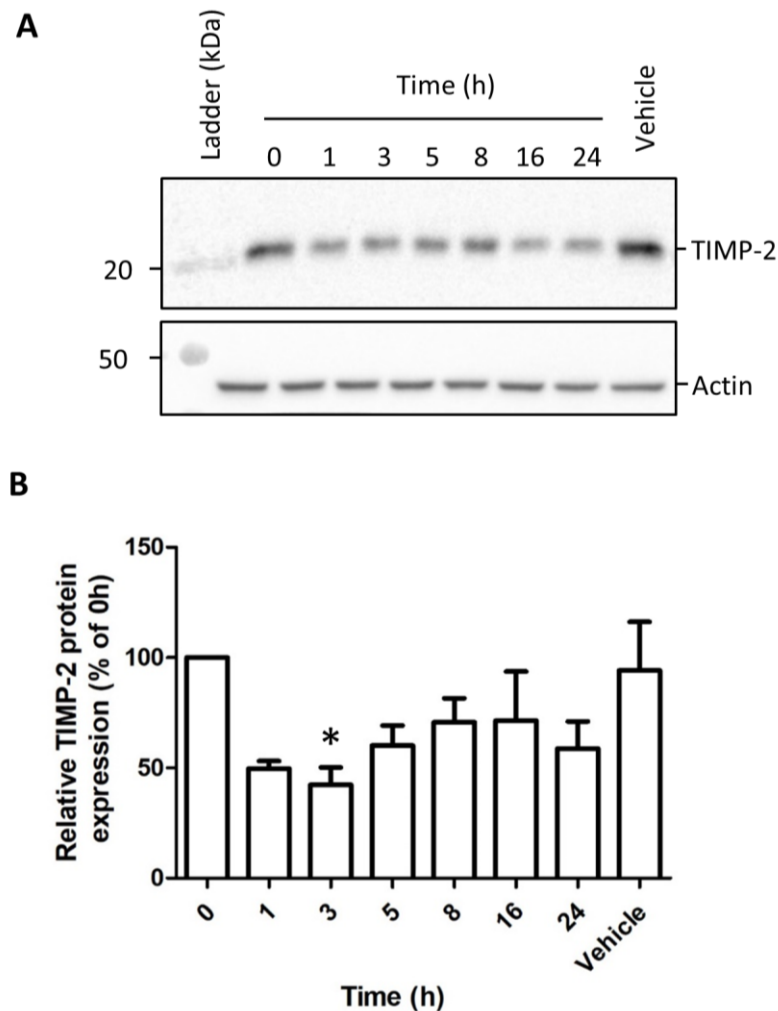


Figure 4.21. Effect of bosutinib on TIMP-2 protein levels. Caco-2 cells were pre-treated with 25 μ M bosutinib or vehicle for up to 24 h. Expression of TIMP-2 was analysed by Western blot (A). Densitometry analysis was performed and results normalized to actin (B). Data are represented as the percentage change relative to 0 h. * $p < 0.05$ versus vehicle, One-way ANOVA followed by Dunnett's test, mean \pm SEM, N=4.

4.3 Summary of results

The main findings from this chapter showed that: a) bosutinib does not induce an inflammatory response through TNF α release; b) bosutinib and imatinib do not promote ER stress; c) bosutinib-induced cellular retractions may involve protein cleavage by MMPs and protein degradation via the proteasomal pathway; d) bosutinib induces occludin protein degradation through a pathway we were unable to identify using our array of pathway inhibitors; and e) bosutinib decreases levels of TIMP-2, an MMP inhibitor.

4.4 Discussion

Inflammation has a key role in chemotherapy-induced diarrhoea. Elevated levels of pro-inflammatory IL-1 β and TNF α are associated with diarrhoea in patients treated with many different forms of chemotherapy including capecitabine, 5-FU combination therapies, carboplatin and gemcitabine (Stringer *et al.*, 2013). Moreover, rodent studies have shown elevated levels of intestinal cytokines including IL-1 β and TNF α following administration of irinotecan, methotrexate or 5-FU (Logan, 2008; Logan *et al.*, 2008, 2009; Melo *et al.*, 2008; Sakai *et al.*, 2013; Yasuda *et al.*, 2013; Hamouda *et al.*, 2017). In Caco-2BBE cells, occludin knockdown prevents TNF α -induced decrease in TEER, suggesting TNF α induces increased permeability through the degradation of occludin (Buschmann *et al.*, 2013). We therefore hypothesized that bosutinib-induced degradation of occludin may involve TNF α release. In our study we did not detect TNF α release following 24h treatment with 25 μ M bosutinib or imatinib; however, TNF α levels were increased with dasatinib and gefitinib treatment (although increase was minimal). Our data is therefore complementary with findings in rat IEC-6 cells which show elevated levels of other pro-inflammatory cytokines, IL-6 and IL-25, following 24 h treatment with 20 μ M gefitinib (Hong *et al.*, 2014). To date, no studies have assessed the direct effect of bosutinib, imatinib or dasatinib on intestinal cytokine levels *in vitro*, *in vivo* or in human tissue.

It is possible that bosutinib may be capable of inducing TNF α release. However this was not detected in our *in vitro* model, possibly due to the absence of a co-culture system containing immune cells such as macrophages, dendritic cells and lymphocytes which are responsible for the majority of cytokine release *in vivo* (Peterson *et al.*, 2014). For our experimental purposes we were interested in determining the mechanism by which bosutinib-induced cell-cell junction rearrangement, as observed in chapter 3, and therefore we did not wish to alter our model. Moreover, Calatayud *et al.* demonstrated it is possible to detect TNF α release in Caco-2 cells by ELISA (Calatayud *et al.*, 2014), providing support for the use of our *in vitro*

Caco-2 model without an immune co-culture system. From these data we can conclude that TNF α release was not responsible for bosutinib-induced changes in permeability in our Caco-2 model.

Another potential mechanism for increased paracellular permeability is ER stress. Tunicamycin, an ER stress inducer, increases permeability in Caco-2 cells (Akiyama *et al.*, 2016); CHOP knockdown prevents E-cadherin degradation in rat IEC-6 cells (Fan *et al.*, 2014), and genome-wide association studies (GWAS) have identified ER stress loci associated with IBD (Kaser *et al.*, 2008; McGovern *et al.*, 2010). Therefore, we hypothesized that bosutinib could induce ER stress in Caco-2 cells leading to increased paracellular permeability.

We chose to assess ER stress by observing changes in the levels of ER stress markers CHOP and BiP. Both these proteins contain ER stress response elements within the vicinity of their transcription start site. Initiation of ER stress by any of the three main interlinking pathways (PERK, IRE1 and ATF4 pathways) leads to upregulation of these markers (Takayanagi *et al.*, 2013).

It was surprising to find that neither imatinib nor bosutinib induced ER stress, considering an array of EGFR and BCR-ABL small molecule TKIs are capable of inducing ER stress. For instance, EGFR inhibitors gefitinib, erlotinib and icotinib (20 μ M, 24h) have been shown to cause ER stress in IEC-6 cells (Fan *et al.*, 2014; Hong *et al.*, 2014); and BCR-ABL inhibitors imatinib, dasatinib and nilotinib resulted in ER stress in non-intestinal epithelial cell types (Kerkela *et al.*, 2006; Nakatani *et al.*, 2006; Bellodi *et al.*, 2009; Lin *et al.*, 2013; Lekes *et al.*, 2016; Yang *et al.*, 2018). These data suggest differing cell type sensitivity to BCR-ABL inhibitor-induced ER stress.

In addition to ER stress, MLCK is another positive regulator of paracellular permeability. Expression of constitutively active MLCK in Caco-2BBE cells was seen to reorganize perijunctional actin along with increased paracellular permeability (Shen *et al.*, 2006); and knockdown of MLCK in Caco-2 cells increases TEER (Clayburgh *et al.*, 2004). However, in our *in vitro* model, MLCK inhibition using ML-7 could not prevent cytoskeletal rearrangements or cellular retractions associated with bosutinib treatment, suggesting that bosutinib does not induce MLCK activation. It is surprising that MLCK did not appear to play a role in bosutinib-induced changes, because Src, which is inhibited by bosutinib, has a relatively well-established role in MLCK regulation in colon cancer cells (Avizienyte *et al.*, 2004, 2005; Khapchaev *et al.*, 2016).

Cell junction disruption through RhoA-ROCK-mediated cellular contractions can be chemically inhibited by Y-27632 (Zandy *et al.*, 2007). Zandy *et al.* (2007) reported inhibition of Abl family kinases, Arg and Abl (for example by imatinib), led to Rho activation, MLCK phosphorylation and AJ disruption in several epithelial cell lines including bladder-derived NBT-II cells and breast-derived MCF-10A cells. However, our data demonstrated that ROCK inhibition by Y-27632 failed to prevent bosutinib-induced cellular retractions suggesting bosutinib does not activate this pathway.

Inhibition of MMPs and proteasomal degradation by MG-132 significantly attenuated cellular retractions. This supports the hypothesis that this retraction phenotype occurred due to the “unzipping” of the monolayer as TJ and AJ proteins were degraded and internalized. As neither ROCK or MLCK inhibitors prevented the change, it is unlikely that actomyosin contractions were involved in the cellular retraction phenotype, unless contractions are initiated by another pathway, for example, cytoskeletal changes induced by the RhoA-mDia pathway (Spiering *et al.*, 2011).

We then focussed on the potential signalling pathways involved in bosutinib-induced occludin degradation. Of the three cell-cell junction proteins we investigated, we decided to focus on occludin as we observed the greatest bosutinib-induced effect with this junction protein. The proposed mechanisms for occludin degradation included degradation via the lysosomal or proteasomal pathway, lipid peroxidation, cell death and proteolysis via MMPs.

Intestinal occludin can be degraded by both the lysosomal and proteasomal pathway (Coëffier *et al.*, 2010; Chelakkot *et al.*, 2017; Nighot *et al.*, 2017). We used several lysosomal inhibitors to reduce the possibility of false-negative data caused by compound off-target effects. For example, 3-MA, a well-known PI3K inhibitor (Wu *et al.*, 2010) which suppresses early stages of autophagy by hindering formation of the autophagosome, has been shown to activate autophagy during nutrient-rich conditions, such as used in our cell model (Wu *et al.*, 2010). None of the lysosomal inhibitors tested – 3-MA, chloroquine or bafilomycin – prevented bosutinib-induced occludin degradation suggesting occludin was not being degraded by the lysosomal pathway.

MG-132, a 26S proteasome inhibitor, which prevents protein degradation by the proteasomal pathway, also failed to prevent occludin degradation. Therefore, no data support the hypothesis that occludin is degraded by either the proteasomal or the lysosomal pathway during bosutinib treatment.

An alternative postulated mechanism for occludin degradation was damage by lipid peroxidation. In this pathway, free-radical lipid peroxides are generated which lead to cellular damage by covalent modification of proteins and DNA, as well as disruption of the cellular structural integrity, for example through oxidation of phospholipid membranes (Gaschler *et al.*, 2017). To test this hypothesis, we used two ROS inhibitors: N-acetylcysteine, a glutathione (free radical scavenger) precursor (Sun, 2010); and deferoxamine mesylate, an iron chelator, which attenuates the generation of highly reactive OH^\cdot by preventing the oxidation of Fe^{2+} by H_2O_2 (Tomita *et al.*, 2002). N-acetylcysteine has been shown to attenuate chenodeoxycholic acid and methotrexate-induced increased permeability in T84 cells and rat intestine, respectively (Maeda *et al.*, 2010; Sarathy *et al.*, 2017).

Neither N-acetylcysteine nor deferoxamine mesylate could prevent bosutinib-induced degradation of occludin. This suggests either bosutinib does not induce lipid peroxidation or that this pathway is not involved in the permeability increase. To our knowledge no studies report small molecule BCR-ABL inhibitor-induced lipid peroxidation in the intestines to support our data. However, several studies show imatinib and dasatinib can cause lipid peroxidation in several cell types such as the CML cell line, K-562 (Baran *et al.*, 2013; Damiano *et al.*, 2018).

A further possible mechanism for bosutinib-induced degradation involves cell death. Our data in chapter 3 showed 25 μM bosutinib caused a small decrease in cell viability, and an increase in PARP cleavage and nuclear fragmentation, indicating low levels of cell death which could be important in bosutinib-induced degradation. As the mechanism of bosutinib-induced cell death is unknown, several cell death inhibitors were used: a) necrostatin-1, which inhibits the necroptosis pathway by inhibiting a key necroptotic effector, receptor-interacting serine/threonine-protein kinase 1 (RIPK1) (Galluzzi *et al.*, 2017); b) ferrostatin-1 which prevents ferroptosis, an iron-dependent cell death mechanism involving lipid peroxidation (Skouta *et al.*, 2014); c) IM-54 which blocks oxidative-induced necrosis (Sodeoka *et al.*, 2010); and d) apoptosis inhibitor Z-VAD-FMK, which irreversibly inhibits caspases by binding to their catalytic site (Ekert *et al.*, 1999). Necrostatin-1 prevented the significant decrease in occludin after addition of bosutinib, whilst none of the other inhibitors had an effect. It is therefore enticing to conclude that necroptosis is involved in bosutinib-induced occludin decrease. However, there was no significant difference in occludin levels between cells pre-treated with vehicle or necrostatin-1 in the presence of bosutinib. This data suggests necrostatin-1 does not prevent occludin decrease and the lack of significance difference

between vehicle and bosutinib treated cells after necrostatin-1 pre-treatment is probably due to experimental variability.

An array of studies have demonstrated the importance of MMPs in controlling intestinal permeability. *Mmp-9^{-/-}* and *Mmp-7/13^{-/-}* mice have decreased sensitivity to dextran sodium sulphate (DSS)-induced and lipopolysaccharide-induced increase in intestinal permeability, respectively (Vandenbroucke *et al.*, 2014; Nighot *et al.*, 2015). MMP inhibitors can prevent increased permeability induced by chymase in Caco-2BBE cells (Groschwitz *et al.*, 2013), a lactone produced by Gram-negative bacteria in Caco-2 cells (Eum *et al.*, 2014) and ischemia in rats (Altshuler *et al.*, 2014). MMPs have also been shown to be increased upon irinotecan treatment in rats (Al-Dasooqi *et al.*, 2010). This led to our final hypothesis that occludin degradation involved protein cleavage by MMPs. The pan MMP inhibitor, GM6001, which reversibly complexes with the conserved zinc active site in MMPs (Levy *et al.*, 1998), attenuated the bosutinib-induced decrease in occludin protein at high concentrations (however, this attenuation was not significant). From these results it was speculated that MMPs may be involved in the bosutinib-induced Caco-2 permeability increase. We tested this hypothesis further by assessing changes in levels of MMP and their endogenous inhibitors, TIMPs. It was found that bosutinib did not alter cellular levels of any of the MMPs tested but significantly decreased levels of TIMP-2. Decreased TIMP-2 levels were confirmed by a time course Western blot which showed a transient decrease in TIMP-2 at 1 and 3 h, occurring earlier than the occludin decrease seen at 3 h; this suggests the TIMP-2 decrease to occur upstream to occludin degradation.

It is important to note that the MMP assay used detects changes in *total* MMP levels i.e. both active MMPs and inactive pro-MMPs. Therefore, whilst no changes in steady state levels of MMPs were found, changes in activation are likely, due to the decreased levels of TIMP-2, a broad-spectrum endogenous MMP inhibitor known to inactivate all of the 23 human MMPs (Brew *et al.*, 2010).

To our knowledge there have been no previous studies on the effect of bosutinib on intestinal TIMP-2 levels, nor on the role of TIMP-2 in intestinal permeability. However, several studies in skin, prostate and lung cancer cell lines have shown positive correlations between TIMP-2 levels and TEER (Choi *et al.*, 2011; Park *et al.*, 2011; J. Jeong *et al.*, 2012; Shin *et al.*, 2013). Furthermore, administration of TIMP-1 to Caco-2 cells has been shown to increase occludin levels (Bein *et al.*, 2015), suggesting a potential causal role of TIMPs in controlling intestine permeability.

Overall, our results provide support for a hypothesis suggesting that MMP activation through TIMP-2 down-regulation may have a role in bosutinib-induced cell junction degradation leading to increased permeability and a “retraction-like” phenotype. However, further work is needed to confirm, or refute, this hypothesis.

4.2.10 Limitations and future work

The major limitations of the general experimental setup, such as the bosutinib concentration and cell line model used, are discussed in chapter 3, whilst limitations and future work more specific to this chapter are highlighted below.

We were surprised to find none of the inhibitors tested significantly prevented the bosutinib-induced occludin decrease considering such a vast array of signalling pathways were assessed, including those involved in ER stress, inflammation, oxidative stress, cell death as well as pathways involving MMPs, ROCK and MLCK. Two possible explanations for this are lack of inhibitor activity or an ineffective concentration. To ascertain greater confidence in these inhibition studies, simultaneous experiments should have been performed to test inhibitor activity. For example, after the addition of ML-7, levels of phospho-MLCK could be probed for by Western blot. However, due to time constraints it was not possible to simultaneously perform these experiments. Alternative explanations are that these pathways may show functional redundancy meaning inhibition of a single pathway would be insufficient to prevent the effects of bosutinib, or bosutinib may activate pathways that were not explored. However, without further data it is only possible to speculate the potential reasons for such a large amount of negative data.

Further to this, it would be useful to perform experiments with additional inhibitors to confirm findings and explore alternative pathways. For example, the JNK inhibitor SP600125 or the formin inhibitor SMIFH2 could be used. It should also be assessed whether ML-7 and Y-27632 can prevent occludin degradation.

Studies here focused on pathways involved in occludin degradation. It would also be interesting to explore the mechanism of bosutinib-induced occludin reorganization. Clathrin-mediated endocytosis (Ivanov *et al.*, 2004) and caveolae/raft-dependent endocytosis (Nighot *et al.*, 2017) have been shown to be involved in cell junction remodelling in human intestinal T84 and Caco-2 cells, respectively. Through disruption to clathrin-coated pit assembly – for example by hypertonic sucrose, cytosolic acidification or phenylarsine oxide – and disruption to lipid rafts by cholesterol sequestration (for example using methyl- β -cyclodextrin), it should

be possible to determine the importance of these two pathways in bosutinib-induced occludin reorganization (Ivanov *et al.*, 2004; Nighot *et al.*, 2017). Co-localization studies assessing spatial-temporal overlap of occludin with caveolin-1 (a caveolae protein) and clathrin could also be performed to support findings from clathrin-coated pit and caveolae disruption (Ivanov *et al.*, 2004; Nighot *et al.*, 2017).

Changes in phosphorylation levels of TJs and AJs proteins by Western blot should be assessed, as changes in the phosphorylation state of TJs and AJs protein can cause disintegration, re-localization, and degradation (Basuroy *et al.*, 2005; Samak *et al.*, 2014, 2015). For example, phosphorylation of occludin due to calcium-depletion occurs during TJ disassembly (Seth *et al.*, 2007).

Our finding that bosutinib-induces a decrease in intracellular TIMP-2 suggests MMPs may be involved in bosutinib-induced increase in permeability. However, further data is required to confirm this. Firstly, it will be necessary to test the hypothesis that bosutinib induces MMP activation. Changes in MMP activity upon bosutinib treatment can be assessed by zymography (Groschwitz *et al.*, 2013). In this technique, samples are run on an acrylamide gel containing an MMP substrate (such as gelatin or casein) and incubated to allow substrate digestion. Protein degradation activity, in this case MMP activity, is then determined by Coomassie staining to identify digested areas. Western blotting could then be undertaken to determine which specific MMPs are activated. It will also be necessary to determine whether secreted TIMP-2 levels are significantly decreased by repeating the MMP array assay to an n of 3, and the effect of TIMP-2 knockdown on occludin levels and MMP activation.

Knockdown studies against known targets of bosutinib, such as Src and Abl, could also be performed and their effect on permeability, TJ protein levels and cytoskeletal rearrangement assessed. Imatinib and Arg/Abl knockdown studies in NBT-II and MCF-10A cells, and Arg/Abl overexpression studies in HeLa cells, provide evidence for a role of Arg/Abl in AJs formation and strengthening (Zandy *et al.*, 2007). Furthermore, Abl has a C-terminal actin binding domain suggesting this protein may have some role in bosutinib-induced changes in the cytoskeleton (Shaul, 2000). Interestingly, this allows us to postulate that inhibition of Arg/Abl could be involved in bosutinib-induced cell junction dissolution; however, if this was the pivotal mechanism involved, we would expect AJ disruption to occur for the other BCR-ABL inhibitors tested (imatinib and dasatinib), which was not the case.

There is more evidence for the involvement of Src than Abl in controlling epithelial cell junction assembly and dissolution, with Src acting as both a positive and negative regulator.

Most studies suggest Src inhibition would prevent TJ disassembly. For example, DSS-induced and cyclic stretch-induced increase in permeability and re-localization of TJ proteins in Caco-2 cells, are prevented by PP2 (Src inhibitor) or Src siRNA (Samak *et al.*, 2014, 2015). However, studies also suggest that inhibition of c-Src can also lead to increased intestinal permeability. For example, inhibiting FAK on the c-Src activation loop increases intestinal permeability by displacing ZO-1 and occludin from cell borders in Caco-2 cells (Ma *et al.*, 2013).

In conclusion, the cascades involved in cell junction disassembly form complex overlapping networks. The main pathways upstream of bosutinib-induced TJ and AJ disintegration remain unknown, but we have shown decreased TIMP-2 levels may be involved. Further studies, such as those discussed above, are required to elucidate these pathways.

**CHAPTER 5: INVESTIGATING THE
MECHANISMS OF TYROSINE
KINASE INHIBITOR-INDUCED
DIARRHOEA USING A MOUSE
ENTEROID MODEL**

5.1 Introduction

TJ involvement in chemotherapy-induced gut toxicity was first hypothesized in 1997 when an increase in intestinal permeability — measured by rhamnose/lactulose permeation — was seen in patients receiving chemotherapy, which corresponded with the onset and duration of diarrhoea (Keefe *et al.*, 1997). TJ disorganisation is now considered to be a common mechanism of chemotherapy-induced GI toxicity. Patients receiving gefitinib (Melichar, Dvořák, *et al.*, 2010), 5-FU (Daniele *et al.*, 2001) and methotrexate (Meng *et al.*, 2016) have compromised barrier integrity. Furthermore, intestinal cell lines show increased permeability and cell-cell junction disruption upon treatment with 5-FU (Buhrmann *et al.*, 2015), methotrexate (Beutheu *et al.*, 2013) and small molecule EGFR inhibitors (Shi *et al.*, 2013; Hong *et al.*, 2014).

In chapter 3, we found bosutinib, imatinib, dasatinib and gefitinib increased permeation through the charge-selective pathway in Caco-2 cell monolayers, but only bosutinib caused a large increase in flux through the size-selective pathway. Moreover, cell junction proteins E-cadherin, ZO-1 and occludin were degraded and re-localized to a much greater extent in bosutinib-treated cells; in imatinib-treated cells this effect was absent, and in dasatinib and gefitinib treated cells the effect was limited to occludin. These findings correlate well with clinical diarrhoea occurrence, i.e. the frequency of diarrhoea in bosutinib-treated patients (Kantarjian *et al.*, 2014; Brümmendorf *et al.*, 2015) is much higher than patients receiving imatinib (Kantarjian *et al.*, 2010; Brümmendorf *et al.*, 2015), dasatinib (Kantarjian *et al.*, 2010) or gefitinib (Shi *et al.*, 2013). However, the physiological relevance of these findings is unknown and difficult to interpret due to issues of translatability of cell line studies — preclinical cell line data are often inconsistent with patient sample data.

Human immortalized cell lines were first developed in 1951 (Gey *et al.*, 1952) and since then hundreds of somatic cell lines have been generated, including those modelling enterocytes, such as Caco-2 cells (Lea, 2015). These cell lines overcame several limitations associated with patient-based research, such as ethical concerns and limited access to patient material. However, the issue of translatability was often challenged and is still a common problem today.

Low-level translatability is prevalent during GI toxicity in *in vitro* studies. GI models were generally developed for estimating oral drug absorption (Antunes *et al.*, 2013; Li *et al.*, 2013; Huang *et al.*, 2014) and increasing understanding of GI physiology (Sung *et al.*, 2011) and development (Kim *et al.*, 2005; Spence *et al.*, 2011; Feng *et al.*, 2013; McCracken *et al.*, 2014),

rather than studying toxicity. The lack of a reliable *in vitro* model is demonstrated by the fact that limited pre-clinical *in vitro* predictive GI toxicity screening is currently undertaken during drug discovery and development. However, alternative more complex and translatable models, called organoids, are under development and showing promise (Fatehullah *et al.*, 2016).

Organoids are microscopic organ-like 3-dimensional cultures which resemble *in vivo* structure and recapitulate the multiple cellular tissue phenotype. Organoids contain stem cells which undergo self-renewal and differentiation into many of the cell types present in the primary tissue, with a similar cellular abundance to *in vivo*. Within intestinal organoids (which when developed from the small intestines are called enteroids), long-lived stem cells reside near the base of intestinal crypts which produce progenitor cells called transit-amplifying cells. These cells migrate upwards towards the villus region and differentiate into epithelium cell types including enteroendocrine cells, enterocytes and goblet cells (Sato *et al.*, 2009) (Fig 5.1), whilst Paneth cells migrate downwards towards the base of the crypt. Upon reaching the villus tip, cells are shed into the enclosed enteroid centre, which models the lumen. Organoids are most commonly developed from primary tissue or induced pluripotent stem cells (Zachos *et al.*, 2016), and like cell lines, can be expanded and maintained in culture through routine passaging (Sato *et al.*, 2011).

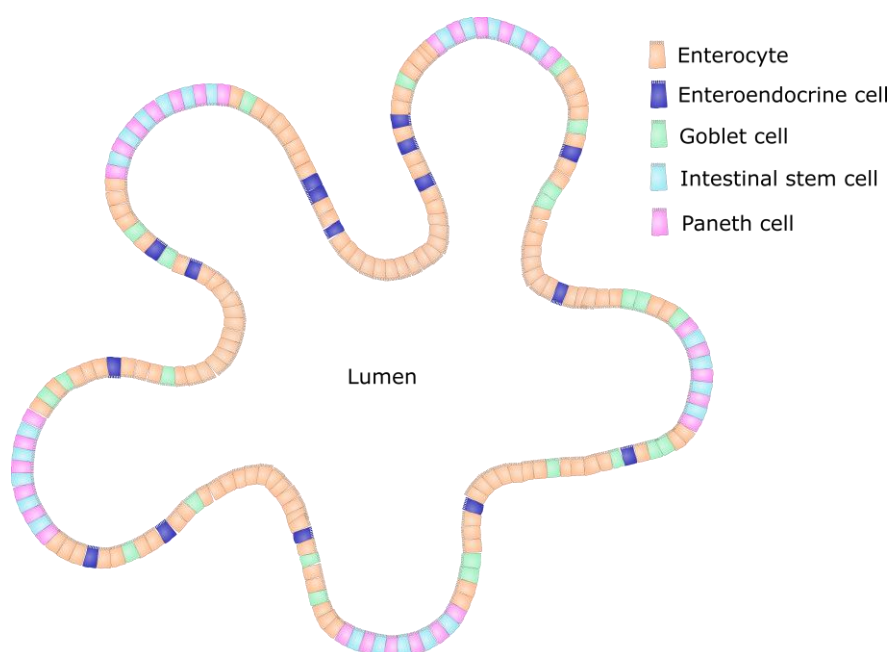


Figure 5.1. Schematic of an intestinal organoid. Figure showing the major intestinal cell types present within small intestinal organoids developed from both rodent models and humans. Diagram produced in Inkscape by S. French.

The use of these complex multi-cellular models gives scope to develop a deeper understanding of drug-induced intestinal pathogenesis, because the pathophysiological mechanism of drug-induced GI injury involves cross-talk between many cell types (Sultani *et al.*, 2012), something which cannot be modelled in cell line monocultures. Moreover, gene expression studies, including those examining drug metabolism and transporter genes, have shown that the profiles in GI organoids are similar to that in normal tissue *in vivo* (Bijmans *et al.*, 2017; Lu *et al.*, 2017), whereas in Caco-2 cells, this is not the case (Vaessen *et al.*, 2017).

Whilst the capability of intestinal organoids to predict and model GI toxicity needs further evaluation, several studies suggest intestinal organoids may be a more effective *in vitro* tool for studying GI toxicity than cell lines. In human, rat, mouse and canine intestinal organoids, toxicity IC₅₀ values for common colorectal chemotherapies reportedly correlate well with species-matched *in vivo* and clinical data. For example, human organoids showed greater sensitivity to irinotecan than oxaliplatin, which are associated with up to 40% and 4% grade 3/4 diarrhoea within the clinic, respectively (Hoyle *et al.*, 2016, 2018). Treatment of mouse enteroids with xenobiotic nuclear receptor agonists causes induction of genes linked to metabolism and transport, a finding translatable from mouse *in vivo* studies (Lu *et al.*, 2017). Moreover, a study by Peters *et al.* (2019) exemplified how non-cancerous and multi-cellular models are more translatable than cell line models. In this study it was found that a multicellular co-culture model of the intestinal epithelium containing human epithelial primary cells seeded onto a transwell containing fibroblasts, could more accurately predict the diarrhoeagenic capability of drugs, and had more physiologically relevant TEER values than a Caco-2 transwell model (Peters *et al.*, 2019).

In 2009, a relatively simple organoid culturing system was developed in the Clevers' laboratory in The Netherlands, which recapitulated the endogenous intestinal stem cell niche through use of Matrigel supplemented with growth factors Noggin, R-spondin and EGF, which allowed the maintenance, growth and propagation of intestinal organoids (Sato *et al.*, 2009). Since then the number of publications on organoid research has increased exponentially (Davies, 2018).

The Clevers' group also developed a simple assay to carry out drug screening for chloride secretion activity, specifically cystic fibrosis transmembrane regulator (CFTR) current activity, in organoids (Dekkers *et al.*, 2013). In this assay, human and mouse intestinal organoids were found to swell upon addition of forskolin, a CFTR activator, and this was prevented by addition of CFTR inhibitors. Through measuring forskolin-induced current changes on human

rectal sample biopsies using a micro-Ussing chamber, it was concluded that forskolin-induced swelling indicated *in vivo* chloride secretion and represented a translatable model for measuring chloride secretion.

We therefore used this organoid culture system to determine whether our data on Caco-2 cells in chapter 3 were translatable into an enteroid model, and to test the physiological relevance of our *in vitro* findings. We also aim to evaluate the ability of TKIs to induce ion secretion, a common diarrhoea pathogenesis mechanism, using the assay developed by Dekkers *et al.* (Dekkers *et al.*, 2013).

In this chapter, we test the hypothesis that BCR-ABL inhibitors bosutinib, imatinib and dasatinib, and EGFR inhibitor gefitinib, increase permeability and ion secretion in mouse enteroids. The aims of this chapter were to:

1. Validate our enteroid model by confirming the presence of major intestinal cell types.
2. Assess the cytotoxicity of bosutinib, imatinib, dasatinib and gefitinib in the enteroid model.
3. Evaluate the effect of bosutinib, imatinib, dasatinib and gefitinib on enteroid permeability and localization of cell-cell junction protein.
4. Determine the ability of bosutinib, imatinib, dasatinib and gefitinib to induce enteroid ion secretion.

5.2 Results

5.2.1 The BALB/c mouse enteroid model expresses relevant epithelial cell types

To determine the translatability of findings from a two-dimensional Caco-2 monolayer model into a 3-dimensional more physiological model, experiments were performed on organoids generated from the proximal intestine of male BALB/c mice aged between 8 and 12 weeks.

Firstly, the suitability of the enteroid model was assessed by confirming the presence of principal intestinal cell types by immunohistochemistry. Positively stained cells, as indicated by black arrows, were seen for all four cell-type markers tested: a) Paneth cells stain positive for the anti-microbial peptide, lysozyme (Ho *et al.*, 1989) (Fig 5.2A); b) goblet cells stain positive for the mucosal secretory protein trefoil factor 3 (TFF3) (Langer *et al.*, 1999) (Fig 5.2B); c) enteroendocrine cells stain positive for the neuroendocrine secretory protein chromogranin A (CgA) (Ho *et al.*, 1989) (Fig 5.2C); and d) tuft cells stain positive for the

microtubule-associated kinase double cortin like kinase 1 (DCLK1) (Gerbe *et al.*, 2011) (Fig 5.2D).

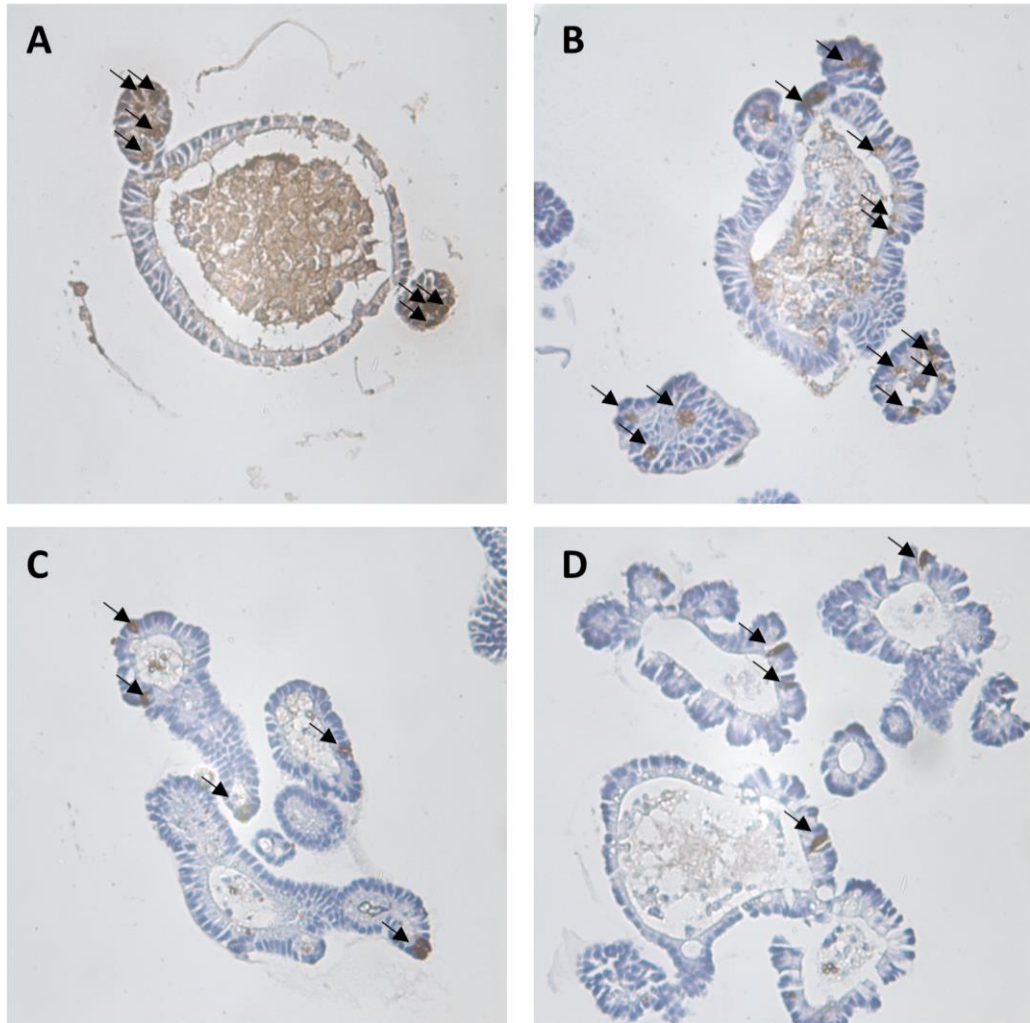


Figure 5.2. Epithelial cell types present in the mouse enteroid model. Male BALB/c mouse proximal intestinal organoids were treated with vehicle for 4 h then 3 3' Diamino-benzidine (DAB)-stained for Paneth cell marker lysozyme (A), goblet cell marker TFF3 (B), enteroendocrine cell marker CgA (C) and tuft cell marker DCLK1 (D) and counter stained with haematoxylin. Black arrows indicate positive stained cells. Cells within the enteroid lumen represent shedded cells. Data are representative of 3 independent experiments where 3-6 enteroids were imaged per experiment.

5.2.2 Bosutinib increases permeability in mouse enteroids

Firstly, we wished to determine whether TKI-induced increase in paracellular permeability in Caco-2 cells (chapter 3; Fig 3.3, 3.4) also occurred in our organoid model.

Murine enteroids, were injected with 4kDa FITC-dextran (FD-4) and the ability of TKIs to induce leakage was assessed over 4 h by measuring the mean fluorescence intensity remaining within the organoid lumen (Fig 5.3). Due to technical constraints, it was not possible to simultaneously inject TKIs and FD-4 into the enteroid lumen, to dose the enteroids at the apical surface. Instead, TKI drug exposure was restricted to the basal aspect of the enteroid, through addition of drug into the growth media, thus mimicking systemic drug exposure. Enteroids were monitored for 4 h, rather than 24 h as in the Caco-2 experiments, because higher levels of basal FD-4 leakage resulted in decreased assay sensitivity beyond 4 h (Thompson, 2019). EGTA was used as a positive control (Leslie *et al.*, 2015).

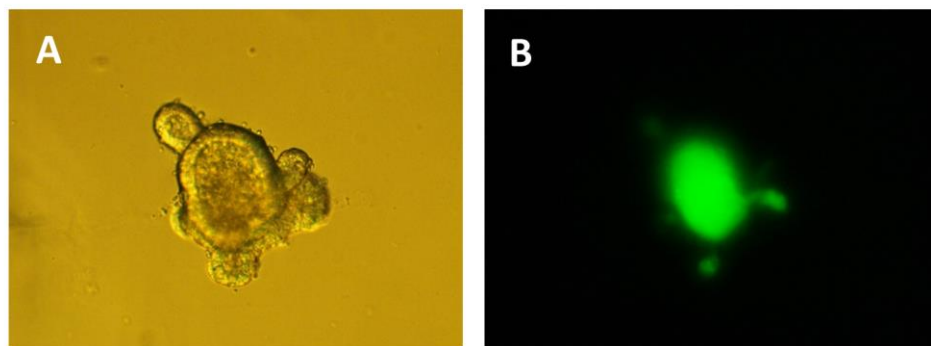


Figure 5.3. Enteroid lumen injected with FITC-dextran. Representative image of a BALB/c mouse enteroid injected with 10mg/mL 4kDa FITC-dextran as viewed under bright field microscopy (A) and fluorescence microscopy (B).

Bosutinib (10 μ M) and EGTA (2mM) significantly increased enteroid permeability (Fig 5.4, Dunnett's test, $p < 0.001$) as determined by comparing the area under the curve (AUC) to the vehicle. Imatinib (10 μ M) and gefitinib (10 μ M) treatment had no effect on enteroid permeability (Fig 5.4B, D; Dunnett's test, $p > 0.05$). Leakage of FD-4 from dasatinib-treated (10 μ M) enteroids was slightly increased relative to the vehicle, however, this difference only approached significance (Fig 5.4C, Dunnett's test, $p = 0.067$).

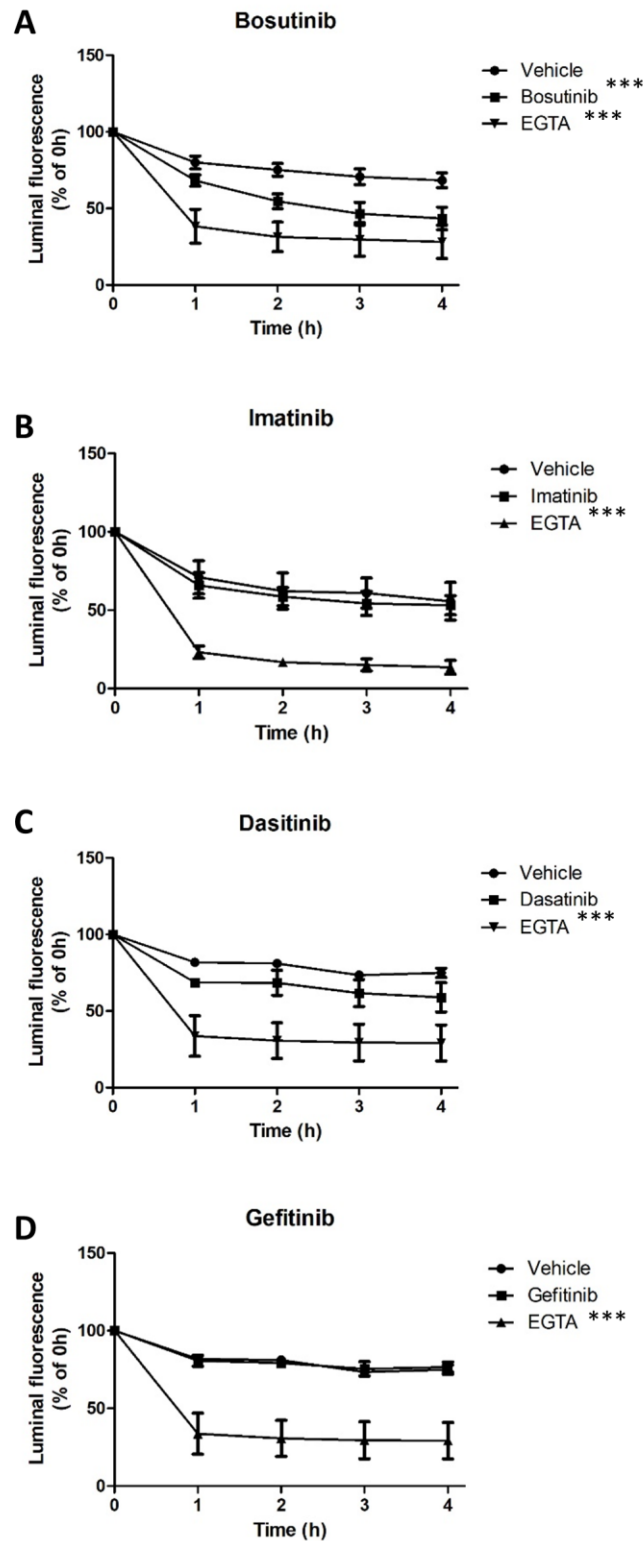


Figure 5.4. Effect of TKIs on paracellular permeability. Male BALB/c mouse enteroids were injected with 10mg/mL 4kDa FITC-dextran (FD-4). Enteroids were incubated with vehicle, 10 μ M bosutinib (A), 10 μ M imatinib (B), 10 μ M dasatinib (C), 10 μ M gefitinib (D) or 2mM EGTA (positive control). Over time, luminal fluorescent intensity of enteroids was measured to determine the percentage of FD-4 leakage. ***p<0.001 versus vehicle, One-way ANOVA followed by Dunnett's post-test of area under the curve, mean \pm SEM, N (biological repeats) = 3-5, n (enteroids per biological repeat) = 2-5.

5.2.3 Bosutinib is cytotoxic to mouse enteroids

Similarly to the Caco-2 *in vitro* experiments, TKI-induced changes in viability were assessed in enteroids to determine whether increases in permeability were due to cell death.

Cell death was initially assessed using ToxiLight™ assay that semi-quantitatively measures enteroid adenylate kinase release, an end-point marker of cell death. Incubation of enteroids with bosutinib or imatinib (0.1-10 μ M) for 4 h did not induce the release of adenylate kinase (Fig 5.5A, B; One-way ANOVA, $p > 0.05$). Dasatinib and gefitinib treatment for 4 h caused a slight increase in adenylate kinase release but this was not significant (Fig 5.5C, D; One-way ANOVA, $p > 0.05$). Enteroids were also treated for 24 h to allow direct comparison to the 24 h Caco-2 ToxiLight™ assay data (chapter 3, Fig 3.10). In our enteroid model, 10 μ M bosutinib and gefitinib significantly increased cell death at 24 h (Fig 5.5A, D); and dasatinib-induced cell death from 0.1 μ M in a dose-dependent manner (Fig 5.5C). Imatinib did not induce cell death at any of the concentrations tested at 24 h (Fig 5.5B).

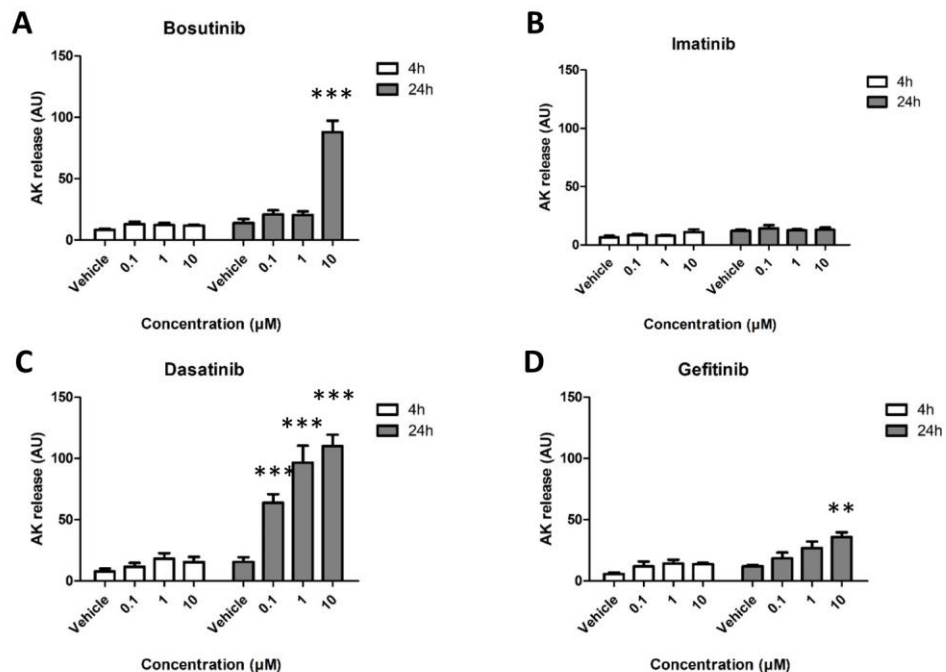


Figure 5.5. Effect of TKIs on cell viability determined by ToxiLight™ assay after 4 and 24 h. Male BALB/c mouse enteroids were treated with vehicle or 0.1-10 μ M bosutinib (A), imatinib (B), dasatinib (C) or gefitinib (D) for 4 h or 24 h. Cell viability was determined by ToxiLight™ assay, which measures adenylate kinase (AK) release, and normalised to area occupied by all enteroids as determined in ImageJ. ** $p < 0.01$, *** $p < 0.001$ versus vehicle, One-way ANOVA followed by Dunnett's post-test, mean \pm SEM, N (biological repeats) = 3-4.

Changes in enteroid circularity were also assessed as a crude measure of cell death. It has previously been shown that circularity positively correlates with caspase-3 activation, a marker of cell death (Fig 5.6) (Jones *et al.*, 2019). Moreover, disruption to organoid morphology is a validated method for studying cell death (Grabinger *et al.*, 2014).

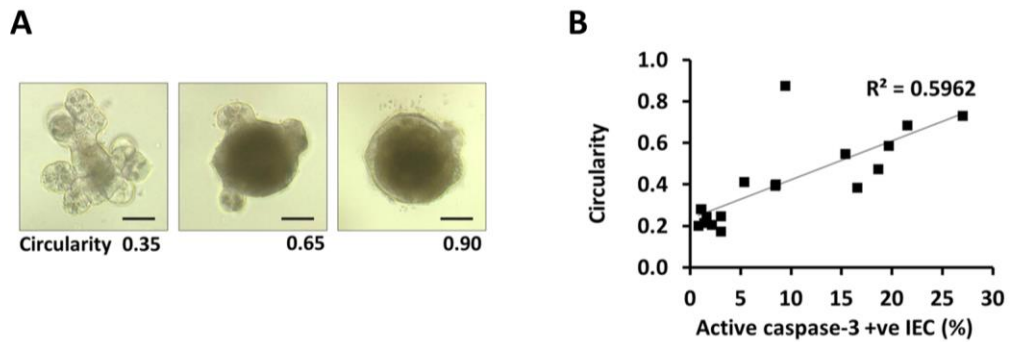


Figure 5.6. Correlation between enteroid death determined by caspase-3 activation and enteroid circularity. Male C57BL/6 mouse enteroids were dosed with 100ng/mL TNF α for up to 24 h. Presence of active caspase-3 positive cells was determined by immunochemistry (representative image not shown). Percentage of active caspase-3 positive intestinal epithelial cells (active caspase-3+ve IEC) was calculated as the number of positive stained cells divided by the total number of cells within the epithelium. Circularity was determined by drawing around enteroids in ImageJ, as shown by the yellow lines (A). Circularity was correlated against active caspase-3+ve IEC (B). $R^2 = 0.5962$, Spearman's rank correlation coefficient N (biological repeats) = 1, n (enteroids per biological repeat) = 17. Figures were obtained from Jones *et al.*, 2019, with permissions for use being granted by Dr. Duckworth, University of Liverpool.

Consistent with ToxiLight™ data, bosutinib, imatinib and gefitinib (10µM) did not significantly increase circularity after 4 h treatment (Fig 5.7, Dunnett's test, $p > 0.05$). However, dasatinib (10µM) induced an increase in circularity (Fig 5.7, Dunnett's test, $p < 0.05$) at 4 h.

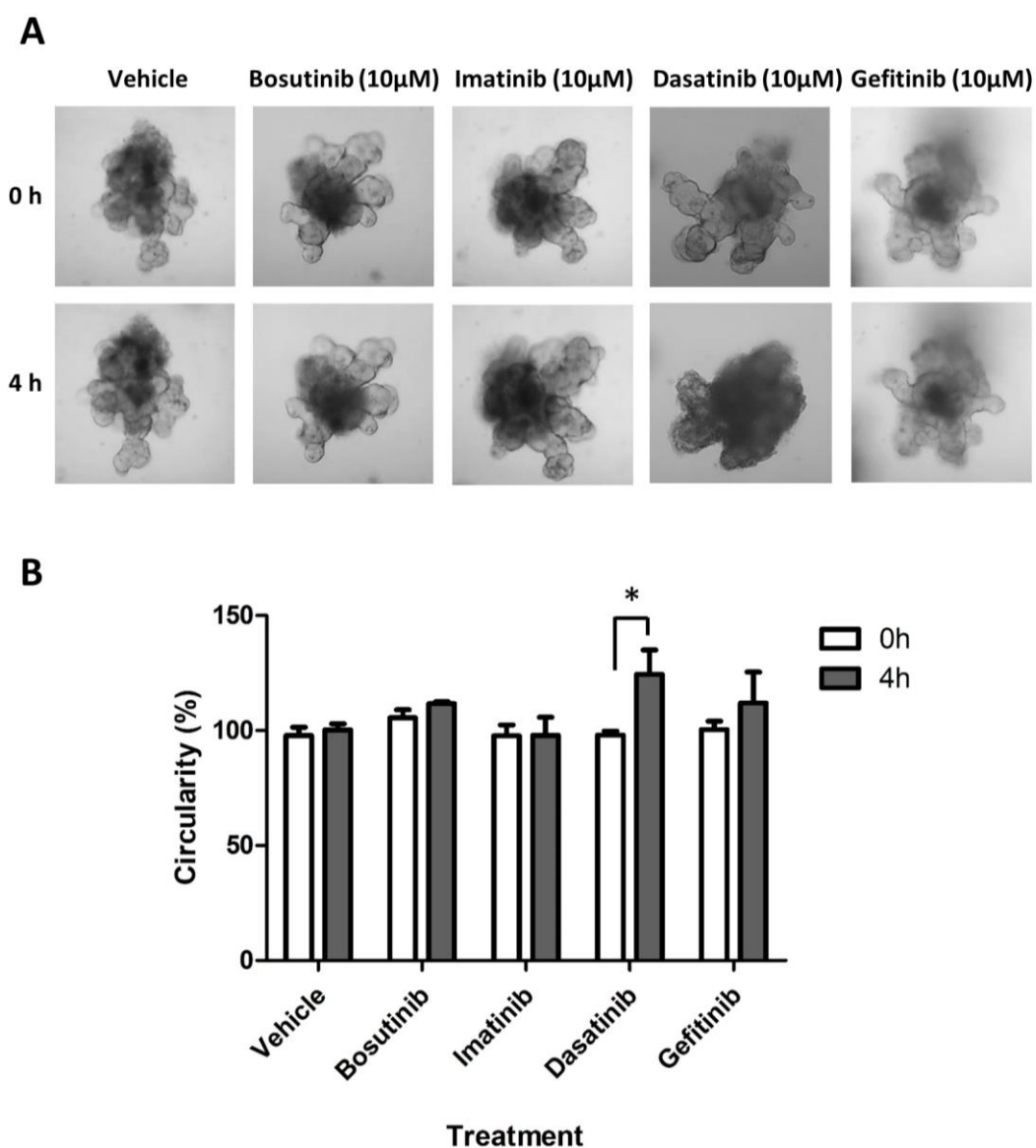


Figure 5.7. Effect of TKIs on cell viability determined by circularity after 4 h. Male BALB/c mouse enteroids were treated with vehicle or 10µM bosutinib, 10µM imatinib, 10µM dasatinib or 10µM gefitinib for 4 h. Light microscopy images were obtained (A) and enteroid death determined by change in enteroid circularity assessed in Image J, as a percentage relative to time zero (B). * $p < 0.05$ versus 0 h, One-way ANOVA followed by Dunnett's post-test, mean \pm SEM, N (biological repeats) = 3-6, n (enteroids per biological repeat) = 4-7.

After 24 h treatment, imatinib still failed to increase circularity (Fig 5.8C, Dunnett's test, $p>0.05$) whereas a significant increase in circularity was observed with 10 μ M bosutinib (Fig 5.8B, Dunnett's test, $p>0.01$), 0.1-10 μ M dasatinib (Fig 5.8D, Dunnett's test, $p<0.01$), and 1-10 μ M gefitinib (Fig 5.8E, Dunnett's test, $p<0.05$) in a dose-dependent manner.

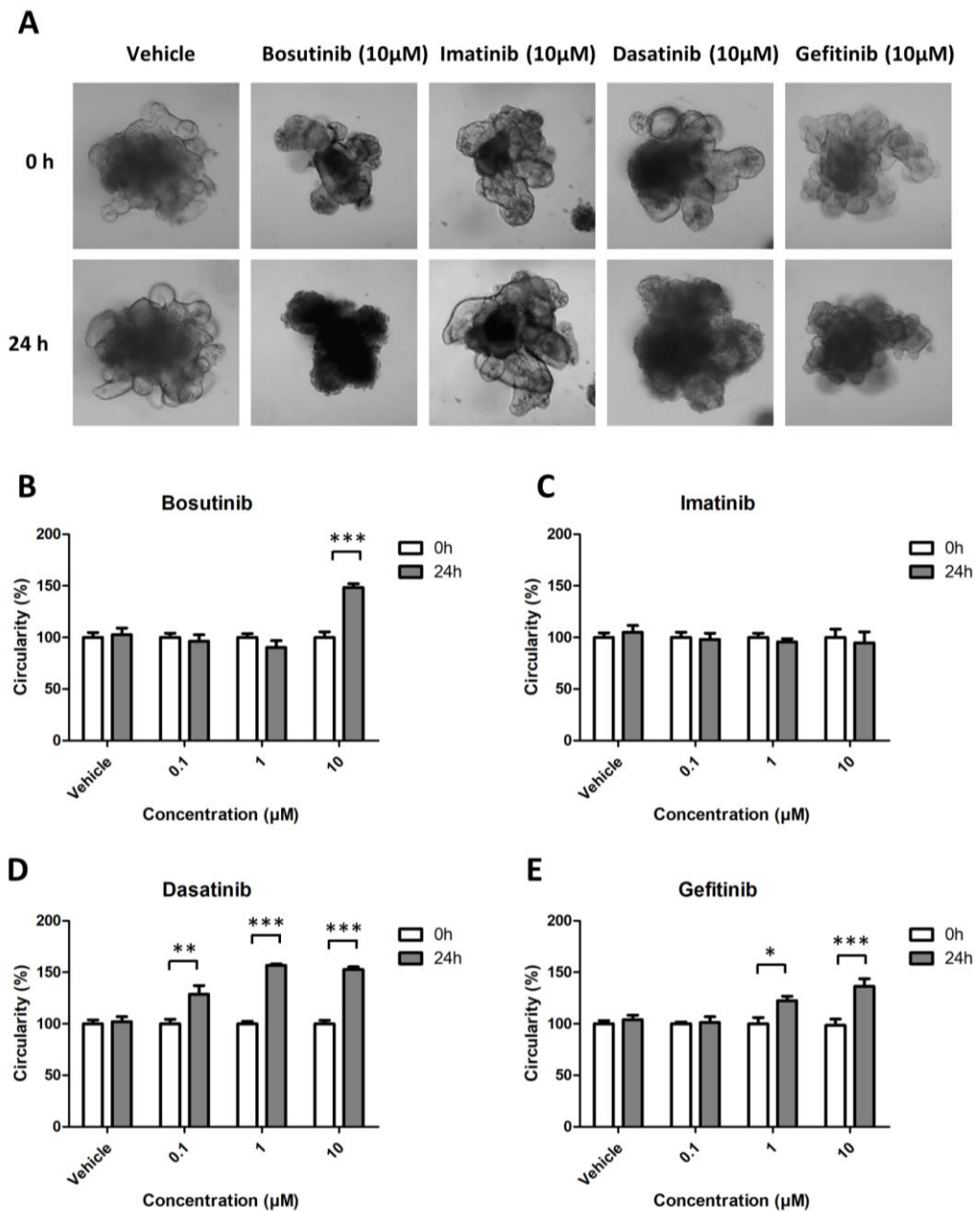


Figure 5.8. Effect of TKIs on cell viability determined by circularity after 24 h. Male BALB/c mouse enteroids were treated with 0.1-1 μ M bosutinib, imatinib, dasatinib, gefitinib or vehicle for 24 h. Light microscopy images were obtained (A, only shown for 10 μ M) and enteroid death determined by change in enteroids circularity assessed in Image J, as a percentage relative to time zero for bosutinib (B), imatinib (C), dasatinib (D) and gefitinib (E). * $p<0.05$, ** $p<0.01$, *** $p<0.001$ versus 0 h, One-way ANOVA followed by Dunnett's post-test, mean \pm SEM, N (biological repeats) = 3-6, n (enteroids per biological repeat) = 6-10.

To validate the circularity assay as an assessment of cell death, data from the ToxiLight™ assay and circularity assay were plotted against each other to assess correlation strength. The 24 h time point was chosen rather than the 4 h time point, because a greater degree of cell death was seen with this time point. A strong positive correlation was seen between adenylate kinase release and circularity (Fig 5.9, Spearman's rank correlation coefficient, $R^2 = 0.8462$) with 1 μ M and 10 μ M gefitinib appearing to be slight outliers.

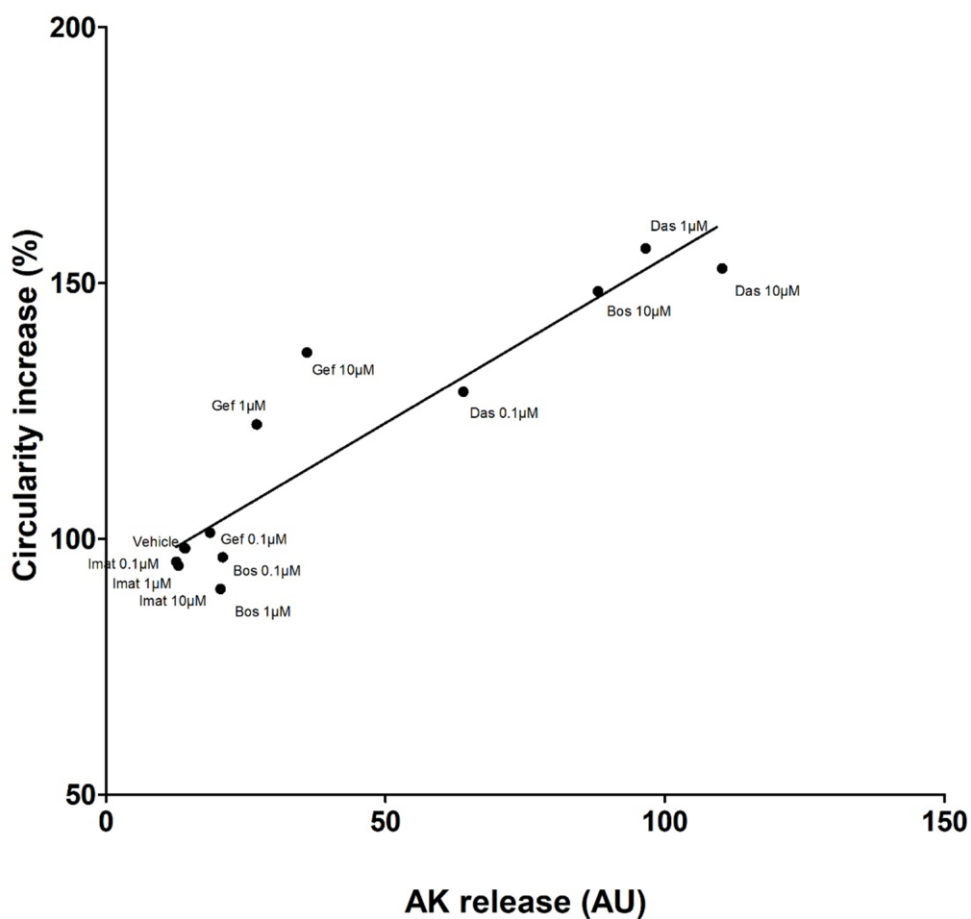


Figure 5.9. Correlation between enteroid death determined by ToxiLight™ assay and enteroid circularity. Male BALB/c mouse enteroids were dosed with up to 10 μ M bosutinib, 10 μ M imatinib, 10 μ M dasatinib, 10 μ M gefitinib or vehicle 24 h (Fig 3.7E). Enteroid death was determined by percentage circularity increase (drawing round enteroids in image J), and adenylate kinase (AK) release (ToxiLight™ assay). $R^2 = 0.8462$, Spearman's rank correlation coefficient, mean (SEM not shown for clarity), N (biological repeats) = 3-6, Spearman's rank correlation coefficient.

Active caspase-3 staining of enteroids treated with 10 μ M bosutinib and imatinib for 4 h was also undertaken to assess cell death, and more specifically apoptosis. Inconsistent with circularity and ToxiLight™ results, bosutinib treatment significantly increased active caspase-3 levels; ~8% of cells were active caspase-3 positive, compared to ~0.5% of cells in vehicle treated enteroids (Fig 5.10B, D; Dunnett's test, $p < 0.01$). Imatinib treatment did not increase caspase-3 cleavage and was similar to vehicle control (Fig 5.10C, D; Dunnett's test, $p > 0.05$).

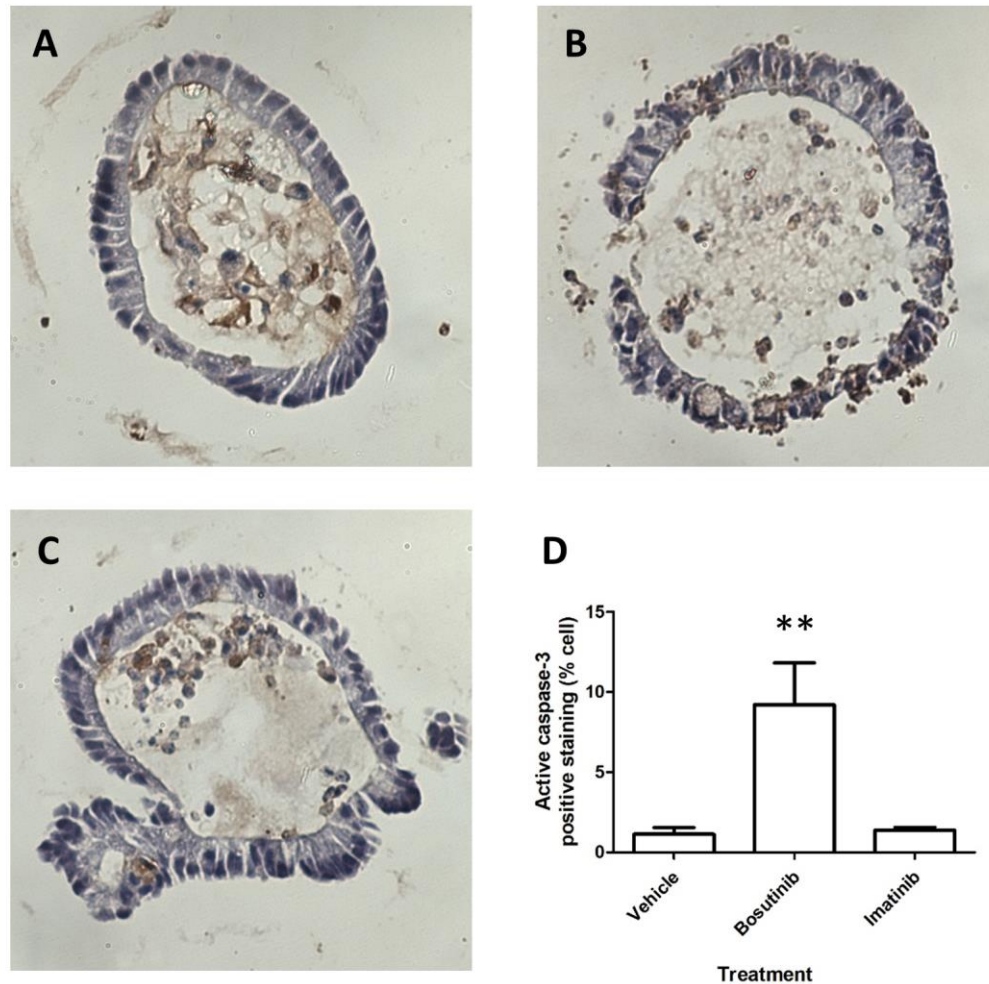


Figure 5.10. Quantification of the number of apoptotic cells in bosutinib and imatinib treated enteroids using active caspase-3 staining. Male BALB/c mouse enteroids were treated with vehicle (A), 10 μ M bosutinib (B) or 10 μ M imatinib (C) for 4 h. Enteroids were 3,3'-Diamino-benzidine (DAB)-stained for active caspase-3 and counterstained with haematoxylin. The percentage of cells staining positive for active caspase-3 within the epithelium was determined relative to the total number of cells (D). Cells within the enteroid lumen (shedded epithelial cells) were not included in the analysis. ** $p < 0.01$ versus vehicle, One-way ANOVA test followed by Dunnett's post-test, mean \pm SEM, N (biological repeat) = 3, n (enteroids per biological repeat) = 5-8.

Haematoxylin and eosin (H&E) staining was undertaken to assess for gross morphological changes and barrier disruption. Epithelial layer disruption occurred in some (Fig 5.11D), but not all (Fig 5.11C), 10 μ M bosutinib-treated enteroids, whilst all enteroids treated with 10 μ M imatinib (Fig 5.11B) appeared indistinct from vehicle treated enteroids (Fig 5.11A).

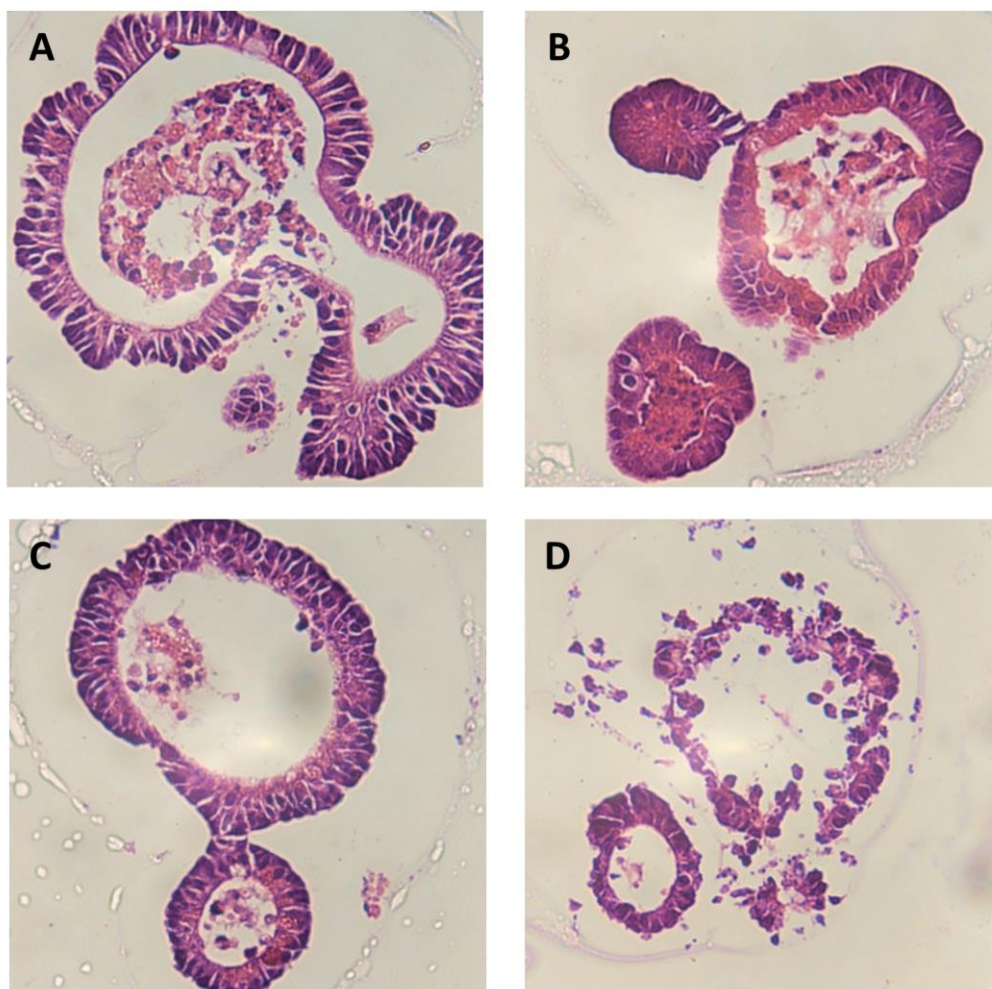


Figure 5.11. Effect of bosutinib and imatinib on enteroid epithelium layer integrity. Male BALB/c mouse enteroids were treated with vehicle (A), 10 μ M imatinib (B) or 10 μ M bosutinib (C and D) for 4 h and gross changes were assessed by haematoxylin & eosin staining. Images are representative of three independent experiments where 3-6 enteroids were imaged per experiment.

5.2.4 Bosutinib does not alter levels of intercellular junction proteins

TJ and AJ proteins are very important in controlling paracellular permeability (Zihni *et al.*, 2016). In Caco-2 cells, bosutinib (at concentrations which significantly increased permeability) decreased levels of a) cytosolic TJ and AJ protein, ZO-1; b) AJ transmembrane protein E-cadherin; and c) TJ transmembrane protein, occludin (chapter 3, Fig 3.13, 3.14). However, imatinib did not induce this change (chapter 3; Fig 3.13, 3.14); therefore, the levels of these proteins were assessed after the addition of bosutinib or imatinib in enteroids to determine whether the mechanistic basis of bosutinib-induced gut 'leakiness' was translatable.

Neither treatment of bosutinib nor imatinib (10 μ M) for 4 h altered levels of occludin, E-cadherin or ZO-1 (Fig 5.12, One-way ANOVA, $p > 0.05$). However, large variability between biological repeats was seen, as indicated by the large SEM bars.

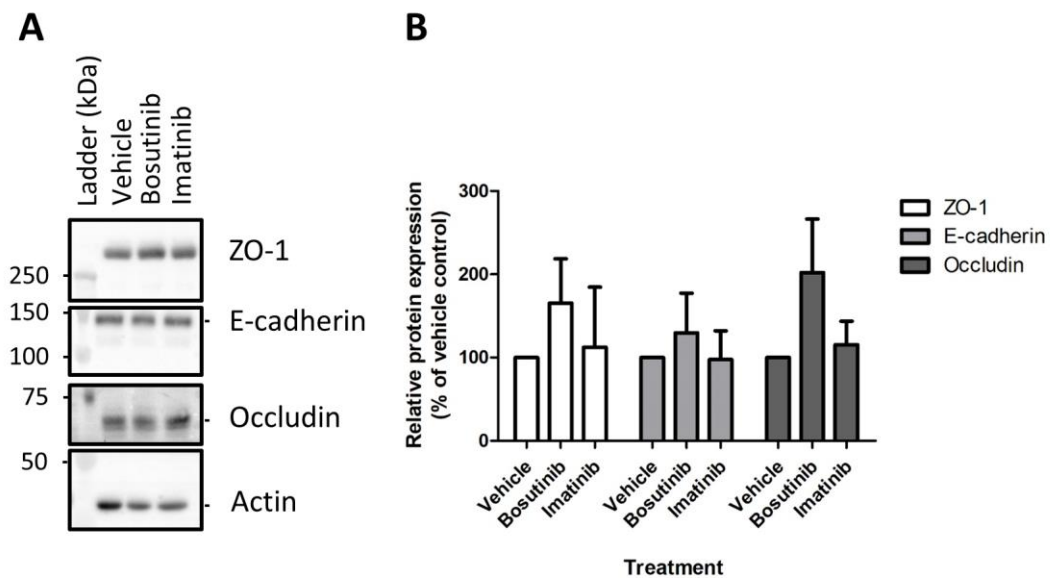


Figure 5.12. Effect of bosutinib and imatinib on tight junction and adherens junction protein levels. Male BALB/c mouse enteroids were incubated with 10 μ M bosutinib, 10 μ M imatinib or vehicle for 4 h. Expression of ZO-1, E-cadherin and occludin was analysed by Western blot (A). Densitometry analysis was performed and results normalized to actin (B). One-way ANOVA followed by Dunnett's post-test, mean \pm SEM, N (biological repeats) = 3.

5.2.5 Bosutinib induces the re-localization of occludin

In addition to altering protein levels, it was previously shown that bosutinib induces re-localization of ZO-1, E-cadherin and occludin away from cell-cell contacts in Caco-2 cells (chapter 3, Fig 3.16-3.18); therefore, the translatability of these results into enteroids was assessed. Enteroids were treated with bosutinib or imatinib (10 μ M) for 4 h and localization of the above-mentioned junction proteins were viewed using immunofluorescence. In vehicle-treated cells, E-cadherin and occludin were mainly observed at plasma membrane. No detectable changes in E-cadherin localization were observed after treatment with either TKI (Fig 5.13); however, occludin re-localized away from the plasma membrane in some bosutinib-treated enteroids (Fig 5.14). It is important to note that this change was not consistent across all bosutinib-treated organoids, as in some bosutinib-treated organoids no change was seen. In the majority of cells, ZO-1 staining does not appear to localize to cell-cell contacts even in vehicle treated organoids (potentially due to off-target binding), making the effect of bosutinib and imatinib on ZO-1 localization difficult to interpret (Fig 5.15).

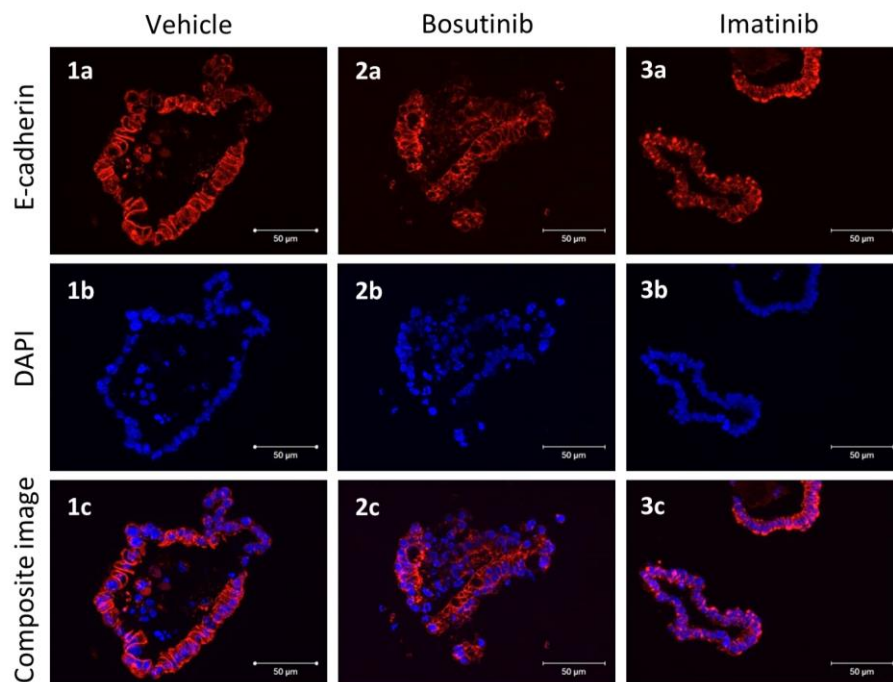


Figure 5.13. Effect of bosutinib and imatinib on localization of E-cadherin. Male BALB/c mouse enteroids were incubated with vehicle (1), 10 μ M bosutinib (2) or 10 μ M imatinib (3) for 4 h. Localization of E-cadherin (a, red) and nuclei (b, blue) were analysed by immunofluorescence. Composite images shown in the lower panel (c). Images are representative of 3 independent experiments where 3-4 enteroids were imaged per experiment.

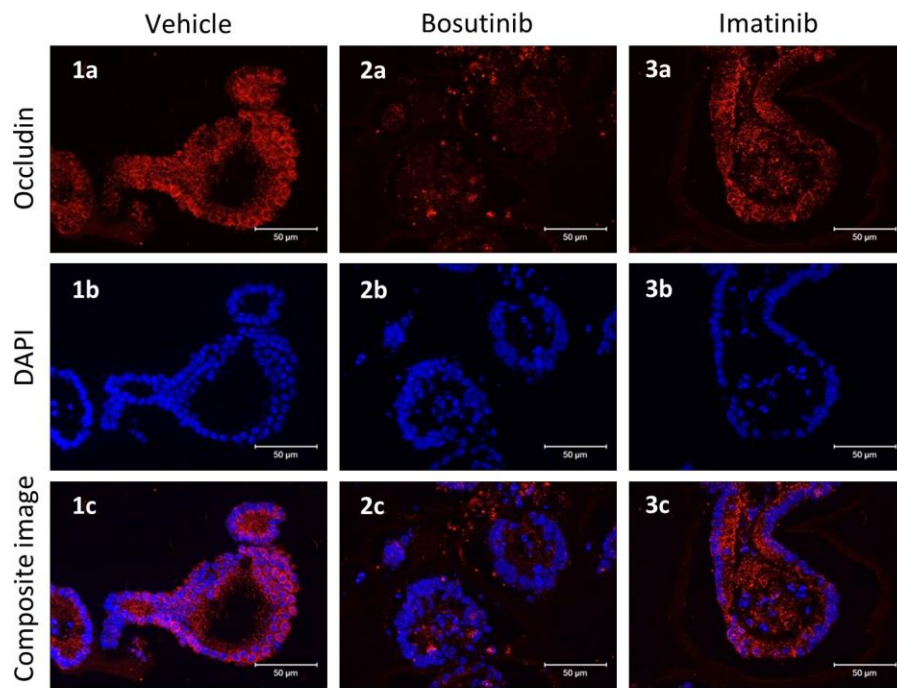


Figure 5.14. Effect of bosutinib and imatinib on localization of occludin. Male BALB/c mouse enteroids were incubated with vehicle (1), 10 μ M bosutinib (2) or 10 μ M imatinib (3) for 4 h. Localization of occludin (a, red) and nuclei (b, blue) were analysed by immunofluorescence. Composite images shown in lower panels (c). Images are representative of 3 independent experiments where 3-4 enteroids were imaged per experiment.

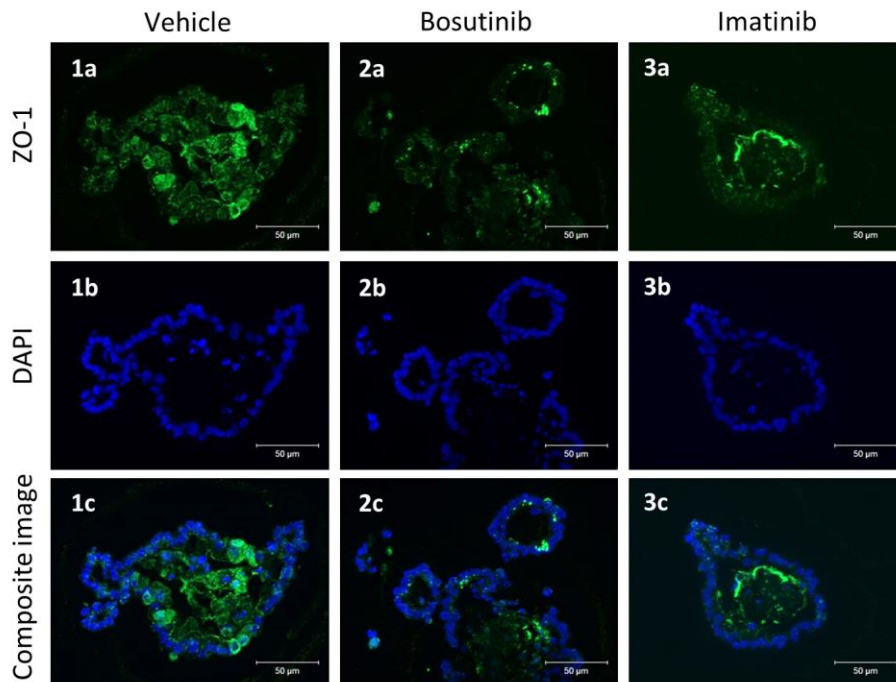


Figure 5.15. Effect of bosutinib and imatinib on localization of ZO-1. Male BALB/c mouse enteroids were incubated with vehicle (1), 10 μ M bosutinib (2) or 10 μ M imatinib (3) for 4 h. Localization of ZO-1 (a, green) and nuclei (b, blue) were analysed by immunofluorescence. Composite images shown in lower panels (c). Images are representative of 3 independent experiments where 3-4 enteroids were imaged per experiment.

5.2.6 Tyrosine kinase inhibitors do not induce enteroid swelling, an indicator of ion secretion

It has previously been shown that ion secretion causes enteroid swelling leading to an increase in enteroid volume, measured as area in a 2-dimensional imaging system (Dekkers *et al.*, 2013). To assess whether TKIs induce ion secretion in enteroids, swelling was assessed by measuring enteroid area of still images obtained by bright-field microscopy, initially over a 30 min time period. Bosutinib, imatinib, dasatinib and gefitinib (10 μ M) and vehicle treatment did not cause organoid swelling (Fig 5.16, One-way ANOVA, $p > 0.05$), indicating the TKIs tested do not initiate chloride secretion. Forskolin, a known activator of the cystic fibrosis transmembrane regulator (CFTR) which induces cAMP-dependent chloride secretion (Dekkers *et al.*, 2013), was used as a positive control. Forskolin (5 μ M) rapidly induced enteroid swelling (Fig 5.16, One-way ANOVA, $p > 0.05$).

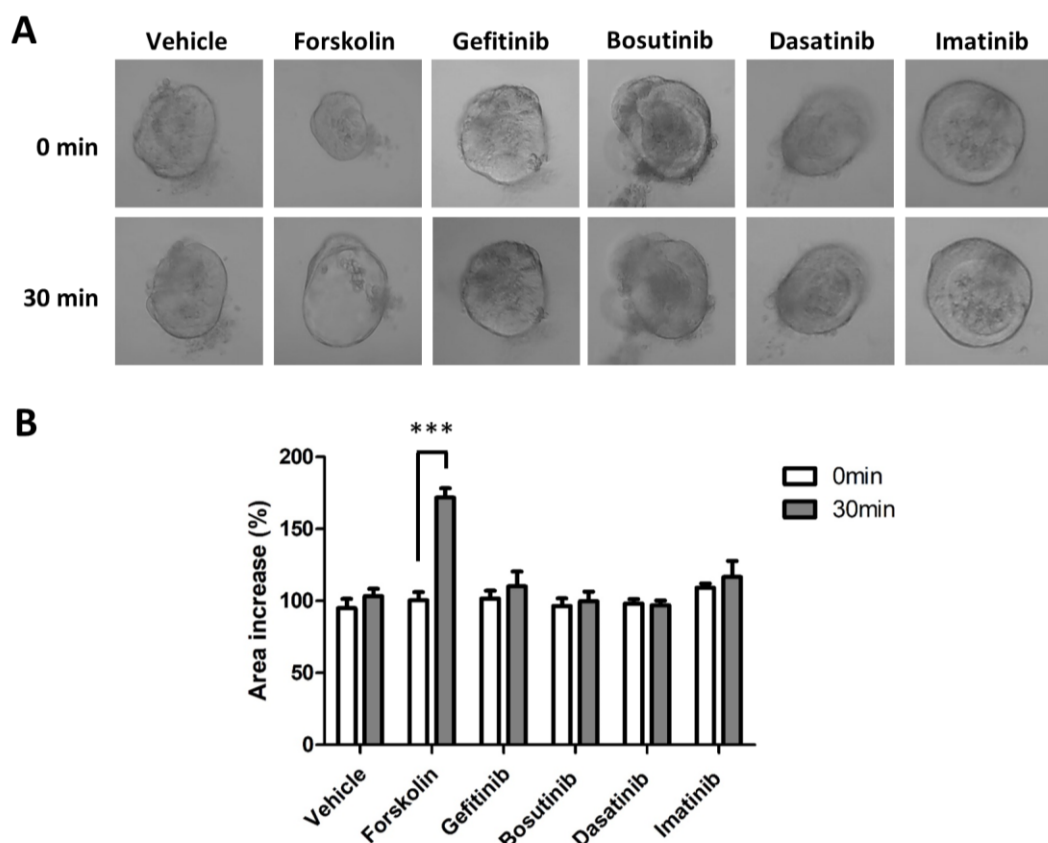


Figure 5.16. Effect of TKIs on enteroid swelling after 30 min. Male BALB/c mouse enteroids were incubated with vehicle, positive control 5 μ M forskolin, 10 μ M gefitinib, 10 μ M dasatinib, 10 μ M imatinib or 10 μ M bosutinib. Static images were obtained by light microscopy at 0 min and 30 min time points (A). Enteroid swelling was assessed by percentage area increase, in ImageJ, relative to 0 min time point (B). *** $p < 0.001$ versus 0 min, One-way ANOVA followed by Dunnett's post-test, mean \pm SEM, N (biological repeats) = 3, n (enteroids per biological repeat) = 5-8.

Chloride ion secretion is hypothesized to be a key mechanism in EGFR inhibitor-induced diarrhoea (Van Sebille *et al.*, 2015), and the kinetics of chloride secretion varies between secretagogues (Van Sebille *et al.*, 2015); therefore, swelling of enteroids treated with gefitinib, an EGFR inhibitor, was assessed over a longer period of time (Fig 5.16).

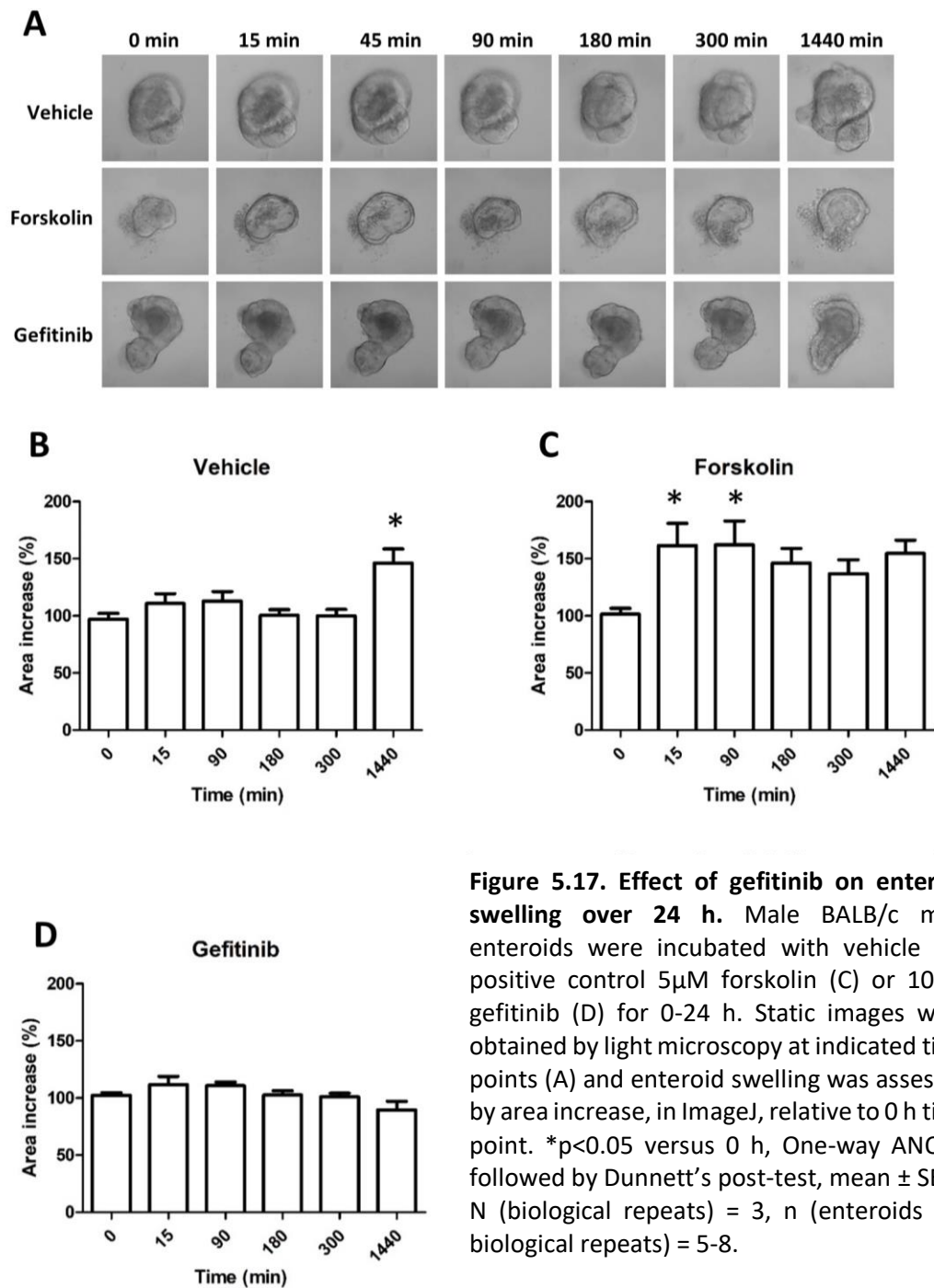


Figure 5.17. Effect of gefitinib on enteroid swelling over 24 h. Male BALB/c mice enteroids were incubated with vehicle (B), positive control 5 μ M forskolin (C) or 10 μ M gefitinib (D) for 0-24 h. Static images were obtained by light microscopy at indicated time points (A) and enteroid swelling was assessed by area increase, in ImageJ, relative to 0 h time point. * $p < 0.05$ versus 0 h, One-way ANOVA followed by Dunnett's post-test, mean \pm SEM, N (biological repeats) = 3, n (enteroids per biological repeats) = 5-8.

Again forskolin (5 μ M) was used as a positive control and was seen to significantly increase enteroid area, relative to time zero, at 15 and 90 min (Fig 5.17C, Dunnett's test, $p < 0.05$). Area was not significantly increased beyond 180 min of treatment (Fig 5.17C, Dunnett's test,

$p > 0.05$). Gefitinib ($10\mu\text{M}$) did not significantly increase organoid area at any of the time periods studied (Fig 5.17D, One-way ANOVA, $p > 0.05$). However, after 24 h (1440 min) treatment with gefitinib, the enteroid lumen appeared enlarged, although no increase in area was seen (Fig 5.17A). Area of enteroids treated with vehicle was significantly increased after 24 h (Fig 5.17D, Dunnett's test, $p < 0.05$); however, this is likely to represent organoid growth rather than swelling.

5.3 Summary of results

The main findings from this chapter was that bosutinib induced an increase in FD-4 flux through the size-selective permeation pathway that was translatable from the human Caco-2 *in vitro* model into the mouse enteroid *ex vivo* model. The underlying mechanism of permeability increase was only partially translatable from the Caco-2 model to the enteroid model: rearrangement of occludin was seen in both models, but bosutinib failed to alter protein levels of cell-cell junction proteins or localization of E-cadherin and ZO-1 in the enteroid model. It was also shown that Caco-2 cells and mouse enteroids had different relative sensitivities to cell death induced by different TKIs, with the enteroid model being more sensitive overall. Finally, it was shown that bosutinib, imatinib and dasatinib did not cause enteroid swelling suggesting these TKIs do not induced chloride ion secretion, whereas further studies are required to determine whether gefitinib elicits chloride secretion.

5.4 Discussion

Findings in several models are more likely to translate into humans than those in a single model; for example toxicity predictions based on *in vivo* studies in both non-rodent and rodent models show higher concordance with human toxicity than those on rodents alone (Olson *et al.*, 2000). Therefore, in this chapter we used a second, arguably more physiologically relevant model, to ascertain an indication of the translatability of our *in vitro* findings.

Proximal small intestinal organoids were chosen to assess translatability from Caco-2 cells. The Caco-2 cell line differentiates into a monolayer of absorptive enterocytes as found in the small intestines, despite being derived from colorectal cancer cells (Hidalgo *et al.*, 1989), and therefore small intestinal organoids (enteroids) were deemed most appropriate. A mouse model was used due to limited access to patient samples; however, mice intestinal development and immune response is comparable to humans making them a relatively good model for GI studies (Jiminez *et al.*, 2015). Furthermore, mouse enteroids have previously

been shown to contain the major relevant cell types of the intestinal epithelial layer (Sato *et al.*, 2009).

Before our translatability studies were undertaken, the validity of our model was assessed by probing for several intestinal epithelial cell type markers using immunohistochemistry. Consistent with previous studies the presence of Paneth, goblet, enteroendocrine and tuft cells was confirmed (Sato *et al.*, 2009).

In enteroids, bosutinib induced an increase in paracellular permeability through the size-selective pathway; a result which was translatable from our Caco-2 cell model. Lower concentrations of bosutinib were capable of inducing an increase in permeability in the enteroid model (10 μ M) than in the Caco-2 model (25 μ M), potentially due to the non-cancerous origin of the former model. Gefitinib failed to significantly increase permeability in enteroids, consistent with findings in Caco-2 cells. Imatinib was also unable to significantly increase permeability at 10 μ M in enteroids, in concordance with sub-apoptotic concentrations (10 μ M – 50 μ M) in Caco-2 cells failing to increase permeability. Dasatinib-induced increase in FD-4 leakage approached significance in enteroids. This finding was inconsistent with our Caco-2 cell studies, where concentrations as high as 100 μ M failed to increase size-selective paracellular permeability.

To our knowledge there are no reported studies assessing the effect of TKIs on enteroid permeability, and, as discussed in chapter 3, no published data regarding the effect of BCR-ABL inhibitors on intestinal epithelial cell permeability. However, oral administration of bosutinib, imatinib and dasatinib were seen to increase gut *endothelial* permeability in C57BL/6J mice, with these changes being significant with dasatinib only (Kreutzman *et al.*, 2017). Some studies have been performed using EGFR inhibitors: erlotinib increases intestinal permeability in rat IEC-6 cells; and gefitinib can decrease levels of E-cadherin and ZO-1, again in IEC-6 cells, at similar concentrations used in our experiment (Fan *et al.*, 2014; Hong *et al.*, 2014). Whilst our study did not assess change in levels of E-cadherin and ZO-1 upon gefitinib treatment, it can be postulated that decreases in these proteins did not occur in our enteroid model, because no changes in permeability were seen.

As with the Caco-2 cell model, it was then determined whether concentrations which caused an increase in enteroid permeability induced cell death, and therefore contributed to the mechanism of this permeability increase. The concentration of bosutinib causing a significant increase in enteroid permeability, 10 μ M, caused low-level cell death that was detectable in some enteroid assays. The ToxiLight™ assay and circularity assay failed to detect changes

whereas a significant increase in caspase-3 cleavage by immunohistochemistry was detected. This could be explained by the differences in assay sensitivity; for example, both the ToxiLight™ and circularity assay measure endpoint cell death whereas caspase-3 cleavage occurs upstream of this pathway.

Circularity is a novel method to measure small intestinal organoid cytotoxicity (Dr Carrie Duckworth, unpublished data); therefore, the validity of this assay was investigated through comparison to results from the ToxiLight™ assay. A strong positive correlation was seen between circularity and adenylate kinase (AK) release, across different TKIs using a range of drug concentrations. However, increase in circularity is not specific to cell death. For example, luminal swelling, such as that induced by forskolin (Dekkers *et al.*, 2013), would lead to increased circularity. However, in this assay gross morphological signs of apoptosis can be assessed, such as loss of crypt architecture and a “grainy-like” opaque appearance, to give greater confidence that the cause of circularity increase is enteroid death. However, for this reason, circularity score should not be used as a standalone method to quantify cell death.

From these cell death assays, we can conclude bosutinib (10µM) induces a low level of cell death and this may have some involvement in increasing enteroid permeability. This is consistent with our findings in the Caco-2 model.

However, unlike in the Caco-2 model, in the enteroid model, dasatinib was the most cytotoxic TKI (whereas, in the Caco-2 model, bosutinib caused the greatest level of cell death). There are many possible reasons for these differences in drug response between our Caco-2 and enteroid models including: a) species-specific differences; b) differences in drug sensitivity between cancer and non-cancer cells; c) apical versus basolateral administration; d) homogenous versus a heterogenous mix of cell types; and e) a 2-dimensional versus a 3-dimensional growth system. Unsurprisingly, and consistent with the permeability studies, lower TKI concentrations were required to induce cell death in the enteroid model compared to the Caco-2 model.

In the Caco-2 model it was found that decreased cell junction protein levels and re-localization away from the plasma membrane occurred, likely contributing to increased permeability; therefore, we assessed whether these findings were translatable into our enteroid model. However, differences in levels and localization of TJ and AJ proteins between biological repeats made results difficult to interpret for both immunofluorescence and Western blot data. This is potentially due to differences in the maturity level and size of

enteroids between biological repeats and wells – which can affect levels and localization of cell junction proteins (In *et al.*, 2016). Immunofluorescent staining illustrated that some organoids only expressed these proteins at the cell-cell contacts, indicative of maturation, whereas others expressed these proteins along the entirety of the plasma membrane, demonstrating enteroid variability. However, in some biological repeats, bosutinib induced a clear re-localization of occludin away from the plasma membrane that was not seen with imatinib. Densitometry analysis of Western blot data revealed high variability in relative protein levels between biological repeats with no overall trend being observed. From these results it is possible to speculate that TJ re-localization and the low level of cell-death observed may contribute to bosutinib-induced increase in enteroid permeability, but it is not possible to draw conclusions on changes in protein levels. This is the first time the effect of BCR-ABL inhibitors on AJ and TJs has been investigated, and consequently these findings cannot be compared to others.

Overall, these data show our major permeability findings in Caco-2 cells were translatable into enteroids with some differences in toxicity sensitivity. Studies highlighting the role of permeability in other forms of chemotherapy-induced diarrhoea, such as 5-FU and methotrexate, have been translatable from Caco-2 monolayers (Yumba *et al.*, 2012; Wang *et al.*, 2015) into rodent *in vivo* models (Southcott *et al.*, 2008; Maioli *et al.*, 2014) and cancer patients (Daniele *et al.*, 2001; Meng *et al.*, 2016), giving greater confidence that our findings may be relevant to TKI-treated patients.

Diarrhoea is often multi-factorial; therefore, next we wished to assess whether an alternative mechanism to increased permeability was involved. Secretion is important in removal of toxins and maintaining appropriate fluidity for motility in normal gut function (Barrett *et al.*, 2000). However, excess secretion, or decreased absorption, causes an accumulation of ions such as Na⁺, Cl⁻ and HCO₃⁻ within the intestinal lumen resulting in secretory diarrhoea, due to movement of fluids into the intestinal lumen (Field, 2003; Thiagarajah *et al.*, 2015).

A simple assay developed by Dekkers *et al.* investigating personalized medicine approaches for cystic fibrosis (Dekkers *et al.*, 2013), can be adapted to identify compounds that may induce secretory diarrhoea. Dekkers found that forskolin caused swelling of human intestinal organoids, due to chloride channel activity, and that patient-matched organoids could potentially be used as a model to predict sensitivity to CFTR-restoring drugs. Hence, we ascertained the ability of TKIs to act as secretagogues, through their ability to activate enteroid swelling. None of the BCR-ABL inhibitors tested induced swelling over the 30 min

period studied and, to our knowledge, no previous studies have assessed the ability of TKIs to induce secretion in organoids. However, Src, which is inhibited by bosutinib and dasatinib (Keller *et al.*, 2009; Fullmer *et al.*, 2011), is involved in chloride secretion. INF- γ and H₂O₂ attenuate secretagogue-induced chloride secretion in human colonic T84 cells through activation of Src (Uribe *et al.*, 2002; Chappell *et al.*, 2008), and Src inhibition potentiates carbachol-induced chloride secretion in T84 cells (Keely *et al.*, 2000). Therefore, it was surprising that bosutinib and dasatinib had no effect on organoid swelling. However, herbimycin A – which, similarly to bosutinib and dasatinib, inhibits both c-Abl and c-Src – does not increase chloride secretion in T84 monolayers (Illek *et al.*, 1996).

Several studies have suggested a role for ErbB, a family of four tyrosine kinase receptors including EGFR (ErbB1), in inhibition of chloride secretion, which has led to the chloride secretion hypothesis for EGFR inhibitors (Van Seville *et al.*, 2015). Direct activation of EGFR by TGF α or EGF can inhibit carbachol-induced chloride secretion in T84 colonic epithelial cells (McCole *et al.*, 2007) and EGF pre-treatment inhibits carbachol- or forskolin-induced ion transport changes in mouse colon *ex vivo* (McCole *et al.*, 2005). Indirect activation of EGFR can also inhibit chloride secretion (carbachol initially activates chloride secretion but a negative feedback loop is subsequently initiated, involving Src-induced EGFR transactivation, leading to inhibition of apical calcium-dependent chloride channels in T84 colonic epithelial cells) (McCole *et al.*, 2007). Moreover, several studies have shown inhibition of EGFR can lead to chloride secretion. Lapatinib, an EGFR and ErbB2 TKI, leads to reduced serum chloride levels in rats, suggestive of intestinal chloride secretion (Bowen *et al.*, 2012). Genistein, an EGFR inhibitor, prevents EGF-induced inhibition of calcium-activated chloride secretion in colonic epithelial cells (Uribe *et al.*, 1996; Keely *et al.*, 1999).

Due to the array of evidence pointing towards the involvement of EGFR in chloride secretion, we tested whether the EGFR inhibitor, gefitinib, could elicit secretion over a longer time period (after initial data found no evidence for chloride secretion after 30 min). No increase in area was observed upon treatment over a 24 h window which is consistent with findings that the EGFR inhibitors, tyrphostinA23, tyrphostinA51 and erbstatin, do not increase chloride secretion in T84 monolayers (Illek *et al.*, 1996). However, the increased luminal size seen after 24 h treatment suggests gefitinib may initiate slow, low-level chloride secretion, even though enteroid area did not increase. Further experimentation, discussed below, will be necessary to determine whether gefitinib can cause chloride secretion. To our knowledge no previous studies have assessed the effect of bosutinib, imatinib, dasatinib or gefitinib on intestinal secretion *in vitro* or in enteroids.

5.4.1 Limitations and future work

In addition to the limitations discussed in chapter 3 – such as the paucity of knowledge on gut luminal drug concentrations – the enteroid model used in this chapter has several limitations. Although enteroids contain the epithelial cell types derived from the crypt stem cells (Zachos *et al.*, 2016), they lack a diverse array of cell types – such as myofibroblasts, smooth muscle cells, stromal, enteric immune and neural cells, as well as an intestinal microbiota – which are present in the intestine *in vivo*. Enteroids are also deficient in true villus structures, exemplified by mRNA profiles containing many more crypt-specific genes than villus-specific genes (Middendorp *et al.*, 2014), and form a non-physiological closed spherical structure.

The closed spherical morphology of enteroids is not only problematic in terms of its non-physiological structure, it also makes luminal administration of drugs technically challenging. In our experiments test drugs were applied to the basolateral side, mimicking systemic drug exposure. However, small molecule TKIs are given orally (Kantarjian *et al.*, 2010; Shi *et al.*, 2013; Brümmendorf *et al.*, 2015), which would result in an initial luminal exposure, followed by a systemic exposure (at lower concentration) once absorbed across the GI epithelium into the blood stream. This distinction is important because application of drugs to the apical or basolateral side can induce different effects. For example, basolateral administration of carbachol to xenografts can increase ion secretion but apical administration cannot (Bertelsen *et al.*, 2004); whilst only basolateral administration of PAR-2 activating peptides can increase chloride secretion in intestinal cells (van der Merwe *et al.*, 2018). However, carbachol and PAR-2 activating-peptides exhibit their effects extracellularly, whilst bosutinib, imatinib, dasatinib and gefitinib induce their effects intracellularly; therefore, it is not unreasonable to suggest apical and basolateral administration of these TKIs could lead to comparable changes, assuming similar uptake at both apical and basal aspects. To overcome the limitations of basolateral drug administration non-spherical GI micro-tissue could be utilised. This has previously been implemented by culturing organoids on scaffolds within a transwell format (Wang *et al.*, 2017). This would also enable changes in the charge-selective permeation pathway to be assessed by TEER measurements, which to our knowledge is unfeasible in organoids, due to the closed-spherical structure preventing micro-electrode access to the lumen (Kim *et al.*, 2018).

We confirmed the presence of Paneth cells, goblet cells, enteroendocrine cells and tuft cells in our model, giving us some confidence of the validity of our model. However, the presence

of Lrg5+ stem cells, absorptive enterocytes and M-cells was not assessed. To our knowledge, it is possible to detect Lrg5+ stem cells by PCR and RNA *in situ* hybridization (Foulke-Abel *et al.*, 2016; Chandra *et al.*, 2019), however it can be assumed that these cells exist owing to the continued growth of the enteroids, with differentiated cell types, in culture. The presence of absorptive enterocytes may be confirmed using antibodies against sucrose-isomaltase (Saxena *et al.*, 2016), but were assumed to be present in our model. Finally, previous studies using mature M-cell marker such as GP2 (Glycoprotein 2) have shown that mouse enteroids rarely contain these cells (Wood *et al.*, 2016). Whilst the presence of several relevant cell types was identified in our enteroid model, the species-origin of these organoids – mouse rather than human – restricts translatability.

There is a paucity of studies on the concordance between toxicities in human and animal models, especially rodent models. The limited literature suggests *in vivo* animal models (including rodent and non-rodent combined) as a whole are good predictors of GI toxicity, correlating with 62-85% of human toxicity data (Olson *et al.*, 2000; Tamaki *et al.*, 2013). However, rodent models alone are a much poorer model of this form of toxicity; only 46% of drugs inducing GI toxicity in humans also induce toxicity in rodents (Olson *et al.*, 2000). This is exemplified by the high rate of GI-related adverse events seen in Phase I (23%) and Phase III (67%) human trials (Redfern *et al.*, 2010). Moreover, mouse and human intestinal organoids developed from the same intestinal segments have disparities in gene expression profiles (Middendorp *et al.*, 2014). Overall this suggests findings in mouse enteroids may not be applicable to human enteroids; however, positive results were found in our human cell line in chapter 3, providing confidence that our findings are relevant to humans.

In addition to the enteroid model, some of the assays performed have limitations. For example, the enteroid 'swelling' assay used may not be sensitive to low level increases in secretion, and requires an intact epithelial layer to allow luminal accumulation of water. We showed that bosutinib, and to some extent dasatinib, increased enteroid permeability and therefore this assay may be unsuitable to assess chloride ion secretion for these drugs. Not all time points studied showed a significant area increase upon treatment with positive control forskolin (potentially due to organoid bursting as luminal pressure increased). This – along with the fact that chloride secretion has variable kinetics (through the Ca²⁺-dependent delayed mechanism or and the cAMP-dependent rapid mechanisms) (Van Sebille *et al.*, 2015) – highlights the importance of examining changes in area at regular time intervals with this assay. As well as observing multiple time points, assay sensitivity could be improved through

fluorescently labelling live cells using calcein and measuring changes in luminal area, rather than the whole enteroid area, by confocal microscopy (Dekkers *et al.*, 2013).

Alternative assays to measure changes in ion transport in organoids may be explored, especially for compounds known to compromise epithelial integrity. Changes in intracellular pH using two-photon microscopy with a pH-sensitive dye such as SNARF-4F, can provide information on H⁺ exchange particularly for apical NHE3 activity, a transporter which absorbs Na⁺ and extrudes H⁺ (Foulke-Abel *et al.*, 2016). Microelectrode analysis can also be undertaken to determine changes in membrane potential at the basolateral membrane (Liu *et al.*, 2012). Finally, observing shrinkage of individual cells observed under high-level magnification can give an indication of chloride ion efflux (Liu *et al.*, 2012).

We attempted to perform a colorimetric chloride secretion assay developed by Tang *et al.* (Tang *et al.*, 2004) in Caco-2 cells (data not shown) to ascertain the translatability of our findings in enteroids. However, due to the very high variability between replicates, we were not able to optimize the assay; therefore, we cannot make a comparison between our cell line and enteroid model.

In addition to further studies on ion secretion, future experimentation on TJ and AJ protein levels and localization are required. To overcome the effect of variability, many biological repeats would be required, or experimentation could be performed on organoids developed from single Lgr5⁺ stem cells before passage (rather than enteroids developed from crypts and passaged, as in our model) to prevent differences in maturity. It would also be interesting to determine changes in the actin cytoskeleton upon bosutinib treatment, to ascertain whether the finding of bosutinib-induced actin rearrangement in Caco-2 cells was translatable to enteroids. Instead of immunofluorescent staining, which appeared to show some off-target fluorescence, organoids could be generated from transgenic mice expressing fluorescently-labelled AJ and TJ or cytoskeletal proteins to observe changes in real-time. This has previously been performed to allow lineage tracing by labelling Lgr5⁺ cells with green fluorescent protein (GFP) (Sato *et al.*, 2009). Alternatively, organoids could be transfected with fluorescently labelled proteins using electroporation or liposome-mediated techniques. This technique has been successfully performed using bacterial artificial chromosomes containing GFP-labelled proteins (TUBB5 and H2A) (Schwank *et al.*, 2013).

Finally, it will be necessary to appraise findings by assessing translatability into other models. A protocol developed by Sato *et al.* enables the robust culturing of human enteroids and

colonoids (Sato *et al.*, 2011); however, due to lack of access to patient samples we are unable to perform experiments using human organoids.

Next, we will determine the relevance of our research in a BALB/c mouse *in vivo* model. Mice will be dosed with bosutinib (250-1000mg/kg) by oral gavage for 4 h, and after culling, small intestine and colon will be harvested. Experimentation will involve observing apoptosis induction through staining for active caspase-3, assessing gross pathological changes by H&E and determining changes in localization of TJs and AJs by immunohistochemistry. Changes in intestinal permeability can be assessed by detecting plasma or urine levels of orally administration of markers such as FITC-dextran (Dong *et al.*, 2014), phenol red (Nariya *et al.*, 2009), iohexol (Forsgård *et al.*, 2016) or lactulose and mannitol (Southcott *et al.*, 2008). Alternatively changes in intestinal permeability can be measured *ex vivo* using an Ussing chamber (Dong *et al.*, 2014) or by the FITC-dextran permeation everted sac method (Maeda *et al.*, 2010). Positive findings *in vivo* would enable greater confidence of the clinical relevance of our data.

**CHAPTER 6: A GENOME-WIDE
ASSOCIATION STUDY (GWAS) TO
IDENTIFY GENETIC MARKERS OF
DASATINIB-INDUCED DIARRHOEA**

6.1 Introduction

There is a large degree of evidence suggesting single nucleotide polymorphisms (SNPs) are involved in susceptibility to diarrhoea, including chemotherapy-induced diarrhoea (Table 6.1 and 6.2) and diarrhoeal diseases, such as irritable bowel syndrome with diarrhoea (IBS-D) (Beyder *et al.*, 2014), ulcerative colitis (Silverberg *et al.*, 2009) and Crohn's disease (Barrett *et al.*, 2008).

The majority of genetic factors associated with chemotherapy-induced diarrhoea have been characterized through candidate gene studies focusing on transporters, metabolizing enzymes and targets specific to the drug of interest (Table 6.1). For example, candidate gene studies have shown that the frequency of gefitinib-induced diarrhoea is affected by polymorphisms within the gefitinib drug exporter, ATP-binding cassette super-family G member 2 (ABCG2), (Cusatis *et al.*, 2006; Lemos *et al.*, 2011) and the gefitinib drug target, epidermal growth factor receptor (EGFR) (Rudin *et al.*, 2008; Giovannetti *et al.*, 2010).

However, two genome-wide association studies (GWAS) have been undertaken, which identified genetic markers associated with diarrhoea induced by chemotherapy treatment (Table 6.2). These studies, unlike candidate gene studies, allowed identification of novel genes with previously unknown links to the pharmacokinetics or pharmacodynamics of the drug.

Han *et al.* (2013), identified three loci previously unknown to be associated with irinotecan-induced diarrhoea (grade 3) in patients with non-small-cell lung cancer (NSCLC) (Han *et al.*, 2013). Chromosome 8 open reading frame 34 (*C8orf34*), which encodes a protein similar to cyclic AMP (cAMP)-dependent protein kinase regulators, was identified. Whilst no previous studies have implicated *C8orf34*, in the pathogenesis of diarrhoea, cAMP is a well-known intracellular regulator of intestinal ion secretion (Field, 2003) and further studies identified cAMP accumulation as a potential mechanism of irinotecan-induced secretory diarrhoea (Moon *et al.*, 2015). *FLJ41856* also associated with the diarrhoea phenotype; a poorly annotated pseudogene with weak similarity to carcinoembryonic antigen-related cell adhesion molecule 5, a clinical biomarker for GI cancers involved in tumour development and cell adhesion (Beauchemin *et al.*, 2013). Finally, phospholipase C- β 1 (*PLCB1*), a gene encoding an intracellular signal transducer previously shown to be associated with severe ulcerative colitis (Haritunians *et al.*, 2010), also associated with irinotecan-induced diarrhoea.

Table 6.1. Summary of a literature search identifying SNPs significantly associated with chemotherapy-induced diarrhoea in candidate gene studies. Abbreviations: *ABCG2*, ATP-binding cassette subfamily G member 2; *ABCB1*, ATP-binding cassette subfamily B member 1; *CCND1*, Cyclin D1; *CES1*, Carboxylesterase 1; *CYP1A2*, Cytochrome P450 1A2; *CYP3A5*, Cytochrome P450 3A5; *DPYD*, Dihydropyrimidine dehydrogenase; *ERCC2*, Excision repair 2; *EGFR*, Epidermal Growth Factor Receptor; *MTHFR*, Methylenetetrahydrofolate reductase; NSCLC, Non-small-cell lung cancer; *UGT1A*, Uridine diphosphate glucuronosyltransferase; *UMPS*, Uridine monophosphate synthetase. *denotes where ancestry is inferred by study location.

Gene	SNP	Disease	Ancestry	Treatment	Association (Diarrhoea grade)	Odds Ratio	P-value	Reference	
<i>ABCG2</i>	rs7699188	NSCLC	Majority Caucasian*	Gefitinib	Grades 2-3	Not stated	<0.01	(Lemos <i>et al.</i> , 2011)	
	rs2231142	NSCLC	Caucasian	Gefitinib	Any grade	Not stated	0.0046	(Cusatis <i>et al.</i> , 2006)	
<i>ABCB1</i>	rs1045642	Colorectal cancer	Majority Caucasian*	Irinotecan	Any grade	0.177	0.01	(Cortejoso <i>et al.</i> , 2013)	
		Breast cancer	Majority Asian*	Docetaxel and Doxorubicin	Grade 3-4	3.3	0.017	(Kim <i>et al.</i> , 2015)	
		Small-cell lung cancer	North American ancestry	Irinotecan and Cisplatin	Grade ≥3	3.9	0.01	(Lara <i>et al.</i> , 2009)	
	rs1128503	Predominantly colon cancer	Majority Caucasian*	Capecitabine	Grade ≥3	Not stated	0.018	(Garcia-Gonzalez <i>et al.</i> , 2015)	
	rs2032582								
	rs1045642	Colorectal cancer	Canadian	Irinotecan	Severe	0.43	0.001	(Chen <i>et al.</i> , 2015)	
	rs3749438								
rs10937158									
<i>CCND1</i>	rs9344	Rectal cancer	Majority Chinese*	Capecitabine with or without oxaliplatin	Severe	1.66	0.038	(Qiao <i>et al.</i> , 2013)	
<i>CES1</i>	rs2244613	Metastatic colorectal cancer	Majority Caucasian	Irinotecan, 5-fluorouracil and Leucovorin	Grades 2-3	0.29	<0.05	(Teft <i>et al.</i> , 2015)	
<i>CYP1A2</i>	rs2069521	Advanced NSCLC	Chinese ancestry	Erlotinib, Gefitinib or Icotinib	Digestive tract injury		0.0585	(Ruan <i>et al.</i> , 2016)	
<i>CYP3A5</i>	rs776746	NSCLC, head and neck cancer, ovarian cancer	Majority North American ancestry*	Erlotinib	Any grade	3.77	0.07	(Rudin <i>et al.</i> , 2008)	
<i>DPYD</i>	rs7548189	Colon or rectum cancer	Caucasian	Capecitabine with or without bevacizumab	grade 0-1 vs grade 2 vs grade 3-4	1.18	1.54 x 10 ⁻⁵	(Rosmarin <i>et al.</i> , 2015)	
	rs1202243					1.18	1.11 x 10 ⁻⁵		
	rs1801265	Metastatic gastroesophageal cancer	Majority Caucasian*	Epirubicin, Cisplatin and Capecitabine	Grades 1-3	Not stated	0.023	(Joerger <i>et al.</i> , 2015)	
	rs17376848						0.058		
	rs67376798						0.028		
		rs67376798	Stage II colon cancer	Mixed population	5-fluorouracil combination therapies	Grade ≥3	Not stated	0.003	(Lee <i>et al.</i> , 2014)
		rs3918290	Colorectal cancer	Majority Chinese*	5-fluorouracil, Leucovorin and Oxaliplatin	Grade 3-4	Not stated	0.04	(Cai <i>et al.</i> , 2014)

Table 6.1 Continued								
DPYD	rs56038477	Colorectal cancer	Majority Caucasian*	Capecitabine	Grade 3-4	Not stated	0.006	(Deenen <i>et al.</i> , 2011)
	rs3918290						0.01	
	rs1801160						0.02	
	rs67376798						0.02	
ERCC2	rs13181	Colorectal cancer	Majority Caucasian*	Irinotecan	Any grade	19.4	0.033	(Cortejoso <i>et al.</i> , 2013)
EGFR	rs712829	NSCLC, head and neck cancer, ovarian cancer	Majority North American ancestry*	Erlotinib	Any grade	Not stated	0.009	(Rudin <i>et al.</i> , 2008)
	rs712830						0.008	
	rs712830	NSCLC	Caucasian	Gefitinib	Grade 0-1 vs Grade 2-3	Not stated	<0.01	(Giovannetti <i>et al.</i> , 2010)
	rs712829						<0.01	
	rs11543848						0.02	
hsa-mir-4751	rs8667	Acute lymphoblastic leukaemia	Spanish Children	Spanish standard LAL-SHOP 94/99/2005	Grade 2-4	12.83	0.0005	(Umerez <i>et al.</i> , 2018)
MTHFR	rs1801131	Metastatic colorectal cancer	Majority Caucasian*	Capecitabine	Grade 3-4	Not stated	0.041	(Van Huis-Tanja <i>et al.</i> , 2013)
	rs1801133	Metastatic colorectal cancer	Majority Caucasian	5-fluorouracil, Leucovorin and Oxaliplatin	Grade 3-4	Not stated	0.02	(Chua <i>et al.</i> , 2009)
	rs1801133	Acute lymphoblastic leukaemia	Egyptians Children	Methotrexate	Grade 3-4	Not stated	<0.0001	(Tantawy <i>et al.</i> , 2010)
UGT1A9	rs17868320	Solid tumours	Majority Caucasian	Sorafenib	Grade ≥2	14.33	0.015	(Boudou-Rouquette <i>et al.</i> , 2012)
UGT1A1	rs3064744	Colorectal cancer	Caucasian	Irinotecan	Severe	1.84	0.002	(Iyer <i>et al.</i> , 2002)
UMPS	rs1801019	Advanced rectal cancer	Asian	Tegafur-uracil and Leucovorin	Grade ≥2	10.76	0.018	(Kim <i>et al.</i> , 2017)

The study by Takahashi *et al.* (2014) identified potassium voltage-gated channel subfamily KQT member 5 (*KCNQ5*), a gene encoding a channel which controls GI motility (Schwake *et al.*, 2003), to be associated with irinotecan-induced diarrhoea. Whilst this locus did not attain genome-wide significance, it is biologically plausible because selective *KCNQ4/5* blockers have been shown to increase intestinal motility and *KCNQ4/5* suggested to be a therapeutic target for constipation predominant irritable bowel syndrome (IBS-C) (Jepps *et al.*, 2009). As irinotecan activates acetylcholine signaling (Hyatt *et al.*, 2005) and *KCNQ5* is inhibited by acetylcholine (Pérez *et al.*, 2010), Takahashi suggested irinotecan inhibited *KCNQ5*, through activation of this pathway. These two studies exemplify how GWAS can aid mechanistic understanding and identify novel avenues to be further explored.

Table 6.2. Summary of a literature search identifying SNPs significantly associated with chemotherapy-induced diarrhoea in genome-wide association studies. 95% CI show 95% confidence intervals. Abbreviations: *C8orf34*, Chromosome 8 Open Reading Frame 34; *CEACAM22P*, Carcinoembryonic antigen-related cell adhesion molecule 2 (pseudogene); *PLC-β1* Phospholipase C beta 1; *KCNQ5*, Potassium voltage-gated channel subfamily KQT member 5; NSCLC, Non-small cell lung cancer.

Gene	SNP	Disease	Ancestry	Treatment	Association	Odds Ratio (95% CI)	P-value	Reference
<i>C8orf34</i>	rs1517114	Advanced NSCLC	Korean	Discovery and replication cohort: Irinotecan, with Cisplatin or Capecitabine	Grade 3 diarrhoea	4.1 (2.1-8.0)	8.5 x10 ⁻⁶	(Han <i>et al.</i> , 2013)
<i>FLJ41856</i>	rs1661167					4.0 (2.0-7.9)	1.9 x10 ⁻⁵	
<i>PLCB1</i>	rs2745761					4.8 (2.3-10.0)	6.4x10 ⁻⁶	
<i>KCNQ5</i>	rs9351963	Cancer (type not stated)	Japanese	Discovery cohort: Irinotecan monotherapy Replication cohort: Irinotecan monotherapy or combined therapy	Grade ≥ 2 diarrhoea	3.1 (1.8-5.6)	3.31x10 ⁻⁵	(Takahashi <i>et al.</i> , 2014)

In addition to furthering our mechanistic understanding, identification of prognostic genetic factors aids personalized health care. Variants with high sensitivity and specificity can be used in a clinical setting to predict individuals at risk of severe to life-threatening adverse drug reactions. For example, pre-emptive testing for *UGT1A1**6 and *UGT1A1**28 is recommended by the Pharmaceuticals and Medical Devices Agency in Japan prior to irinotecan treatment, to identify individuals at increased risk of severe adverse drug reactions (ADRs), such as high-grade diarrhoea. Individuals with these polymorphisms undergo slower degradation of the active irinotecan metabolite, SN-38, and require dose-reduction (Etienne-Grimaldi *et al.*,

2015). However, to our knowledge, there are currently no widely used genetic tests to determine the likelihood of drug-induced diarrhoea within the UK.

Similar to the genetic variants discussed above, variants associated with ADRs are often specific to the pharmacological action of the drug. In this way, associated variants from one class of chemotherapy are unlikely to be applicable to other classes of chemotherapy. This – along with the complex multi-mechanistic basis of chemotherapy-induced diarrhoea and lack of standardized phenotypes – means the large majority of genetic factors contributing to GI ADRs remain unknown. For example, no genetic determinants of Bcr-Abl inhibitor-induced diarrhoea are currently known.

By identifying genetic polymorphisms associated with dasatinib-induced diarrhoea, it may be possible to gain a greater understanding of the mechanism(s) of diarrhoea induced by Bcr-Abl inhibitors. In this chapter, the hypothesis that there are genetic determinants which significantly alter the likelihood of dasatinib-induced diarrhoea in patients with chronic myeloid leukaemia (CML) was tested. The aims of the chapter were to:

1. Perform a GWAS to identify SNPs associated with dasatinib-induced diarrhoea using a discovery cohort of 145 patients from the SPIRIT2 trial.
2. Assess imputation accuracy of suggestive or genome-wide significant imputed SNPs using PCR-based genotyping.
3. Validate GWAS discovery cohort findings in a replication cohort of a further 137 SPIRIT2 trial patients using PCR-based genotyping.
4. Analyse the biological plausibility of candidate SNPs by literature searches.

6.2 Results

6.2.1 Patient characteristics

Patients within the discovery and replication cohort were from the SPIRIT2 trial and received 100mg oral dasatinib daily (chapter 2, Section 2.6). Demographic data for the 145 discovery cohort patients used in the GWAS are summarised in Table 6.3, along with demographics of the 137 patients studied in the replication cohort. Patients within the replication cohort did not overlap with those in the discovery cohort. Patient ethnicity was not catalogued, but as the study was conducted in the UK the subjects were largely considered to be Caucasian. Patients with non-Caucasian genomic ancestry were excluded from the discovery cohort through principal component analysis (n=16). Neither age (t-test, $p=0.403$), gender (Chi-

squared test, $p=0.132$) nor body mass index (BMI) (t-test, $p=0.497$) showed univariate association with the diarrhoea phenotype in the discovery cohort. Within the replication cohort neither gender (Chi-squared test, $p=0.5031$) nor BMI (t-test, $p=0.399$) were significantly associated with diarrhoea; however, age (t-test, $p=0.0325$) was significantly associated with this phenotype.

Table 6.3. SPIRIT2 trial patient demographics of the discovery and replication cohorts. Patients within the discovery and replication cohort received 100mg dasatinib daily. Patient information on age, gender and body mass index (BMI) was collected and occurrence and grade of diarrhoea were logged according to the Common Terminology Criteria for Adverse Events (CTCAE) system.

	Discovery cohort	Replication cohort
Patient number, n	145	137
Median age years (range)	56 (18-88)	52 (21-89)
Gender		
Male, n (%)	89 (61%)	90 (66%)
Female, n (%)	56 (39%)	47 (34%)
BMI, mean (range)	27.6 (19.2 – 44.2)	26.5 (18.5 – 43.9)
Diarrhoea incidence, n (%)	40 (28%)	33 (23%)
Diarrhoea grade, n (%)		
1	27 (68%)	24 (73%)
2	8 (20%)	8 (24%)
3	1 (3%)	1 (3%)
4	0 (0%)	0 (0%)
Unknown	4 (10%)	0 (0%)

6.2.2 SNPs significantly associated with dasatinib-induced diarrhoea in the discovery cohort

Genome-wide association analysis identified five SNPs associated with dasatinib-induced diarrhoea at the genome-wide level (Fig 6.1, $p < 5 \times 10^{-8}$). All five SNPs were imputed. rs187843272 was located within the intronic region of the gene coding for amino adipate-semialdehyde dehydrogenase (*AASDH*) on chromosome 4q57.2 (Fig 6.2B, $p = 9.85 \times 10^{-9}$). The other four variants – rs12422992, rs201379970, rs12424256 and rs61708525 – were located as a cluster on chromosome 12q94.6 within the intronic region of plexin C1 (*PLXNC1*). rs12424256 exhibited the lowest p-value (Fig 6.2A, $p = 4.22 \times 10^{-9}$) and is in linkage disequilibrium with rs61708525 ($r^2=0.61$, $D'=0.93$).

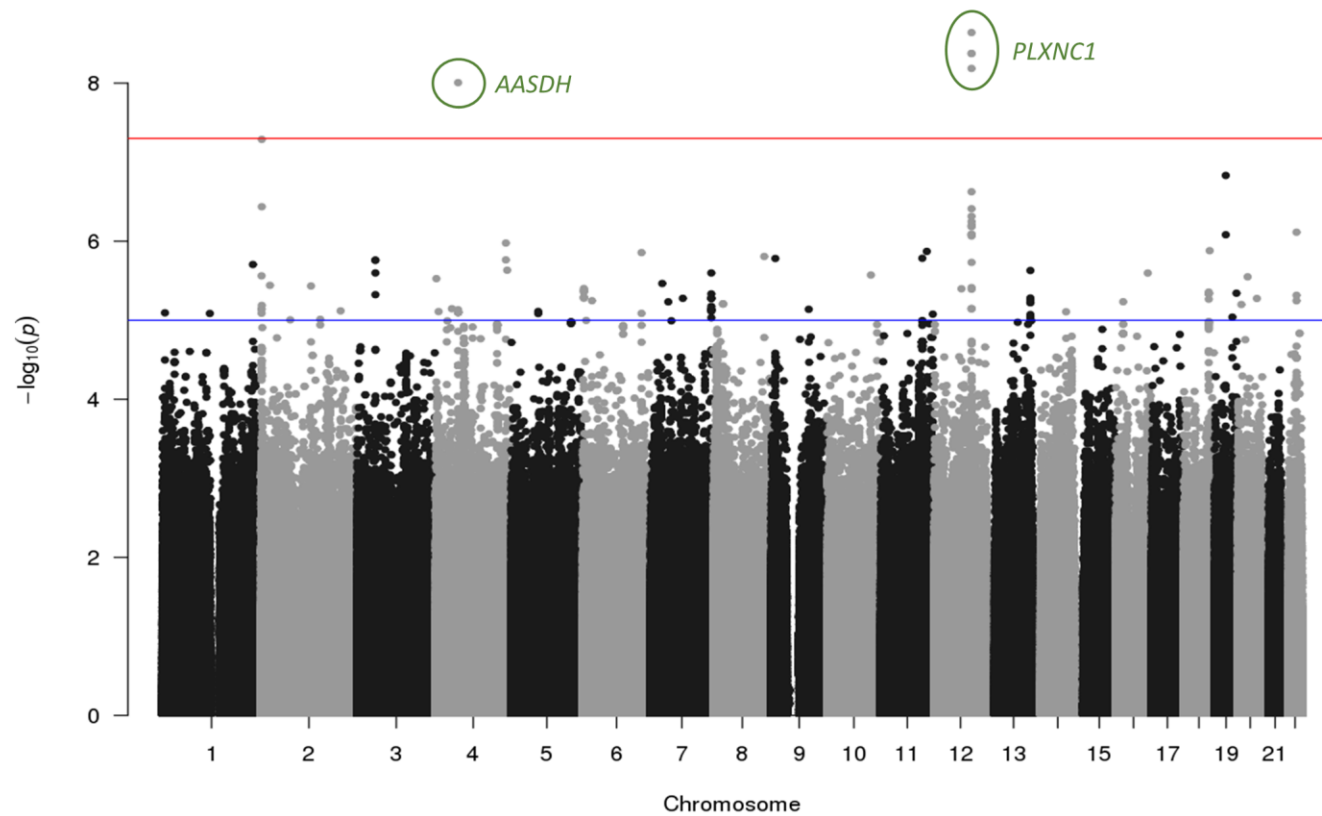


Figure 6.1. Genome-wide Manhattan plot showing SNPs linked to dasatinib-induced diarrhoea. $-\log_{10} P$ values of SNPs plotted against their chromosomal location for the genome-wide association study performed on the discovery cohort. Horizontal red line indicates genome-wide significance (p -value = 5×10^{-8}) and horizontal blue line indicates suggestive significance (p -value = 1×10^{-5}). The genes in which the SNPs that reached genome-wide significance reside are labelled in green.

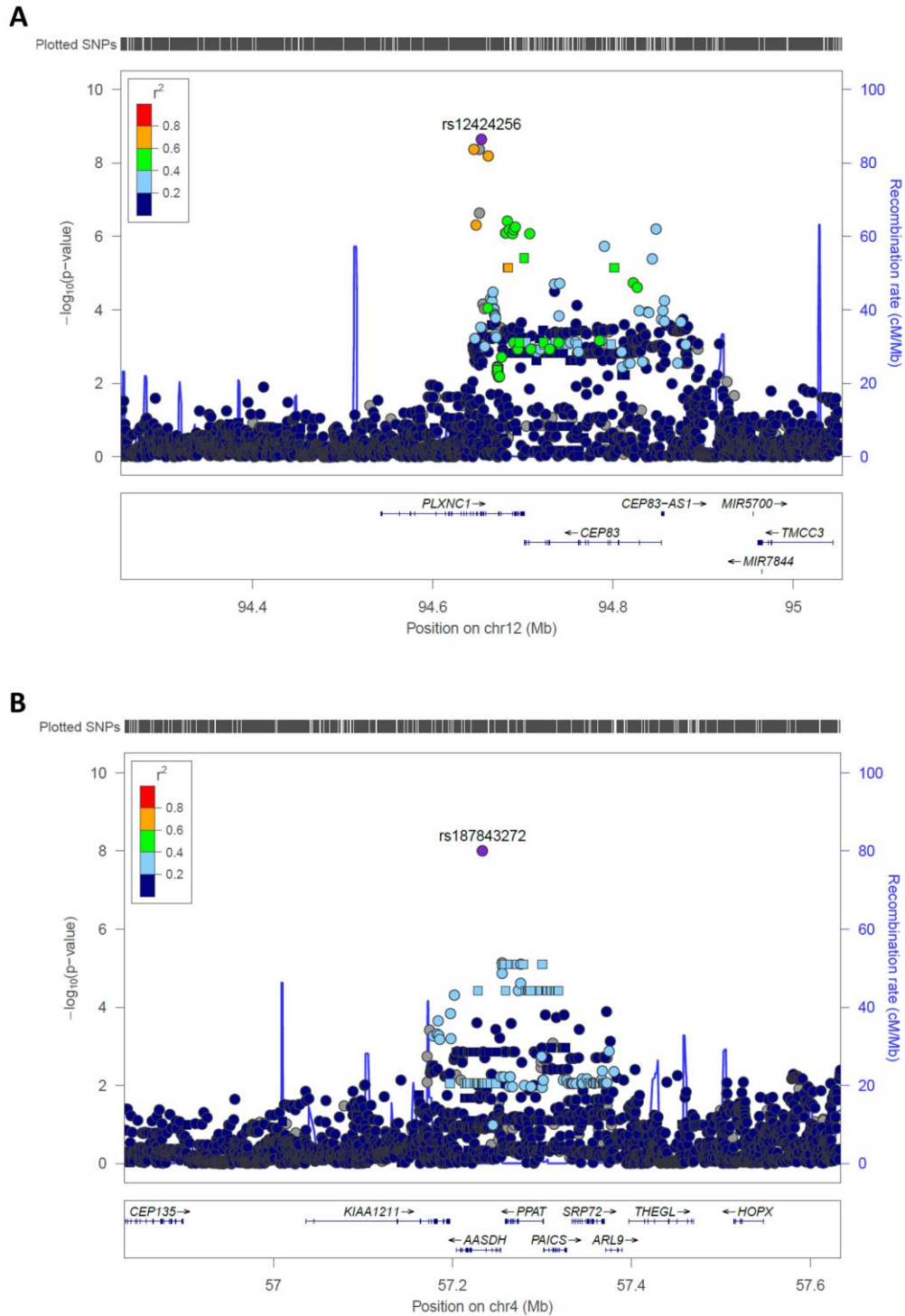


Figure 6.2. Regional association plots and recombination rates for chromosomal regions showing associations with dasatinib-induced diarrhoea at the genome-wide significance level. SNP towers appearing in Manhattan plot on chromosome 12 (A) and 4 (B) are shown. Each circle represents an imputed SNP, whilst each square represents a genotyped SNP. The index SNP is shown in purple. The extent of linkage disequilibrium (r^2) is colour graded as shown in the top left box. Blue lines represent the genetic recombination rate (cM/Mb) and the lower box indicates the genes coded for at this chromosome location.

SNPs reaching suggestive significance levels ($p < 1 \times 10^{-5}$) were seen in several other regions. Those with clear 'towers' in the regional plots were located on chromosome 2q1.8, 3q46.2, 6q2.9, 7q153.8 and 13q109.5 (Fig 6.3A-E). On chromosome 2q1.8, an intronic SNP (rs6760938) within myelin transcription factor 1 like (*MYT1L*) was the most significant SNP ($p = 2.74 \times 10^{-6}$, Fig 6.3A). On chromosome 3q46.2 the most significant SNP was rs35636998 which resides within the intronic region of C-C chemokine receptor type 3 (*CCR3*) ($p = 2.52 \times 10^{-6}$, Fig 6.3B). rs73718779 reached highest significance within the 6q2.9 chromosomal region and is located within the intronic region of serine protease inhibitors (serpin) family B member 6 (*SERPINB6*) ($p = 3.97 \times 10^{-6}$, Fig 6.3C). On chromosome 7q153.8, rs6975293, a SNP located within a non-coding transcript exon region of dipeptidyl peptidase like 6 (*DPP6*) was the most significant ($p = 2.52 \times 10^{-6}$, Fig 6.3D). Finally, rs9559427 located within the intronic region of myosin XVI (*MYO16*) reached highest significance on chromosome 13q109.5 ($p = 2.35 \times 10^{-6}$, Fig 6.3E).

A summary of the most significant SNP within each 'tower' found to associate with dasatinib-induced diarrhoea at the suggestive ($p < 1 \times 10^{-5}$) and genome-wide significance ($p < 5 \times 10^{-8}$) levels is shown in Table 6.4. Of the seven SNPs highlighted in the regional plots above, rs187843272 on chromosome 4q57.2 is not shown in the table and was not investigated further because the 'stand-alone' nature of this SNP (low correlation with neighbouring SNPs) suggests it is a false positive (Fig 6.2B).

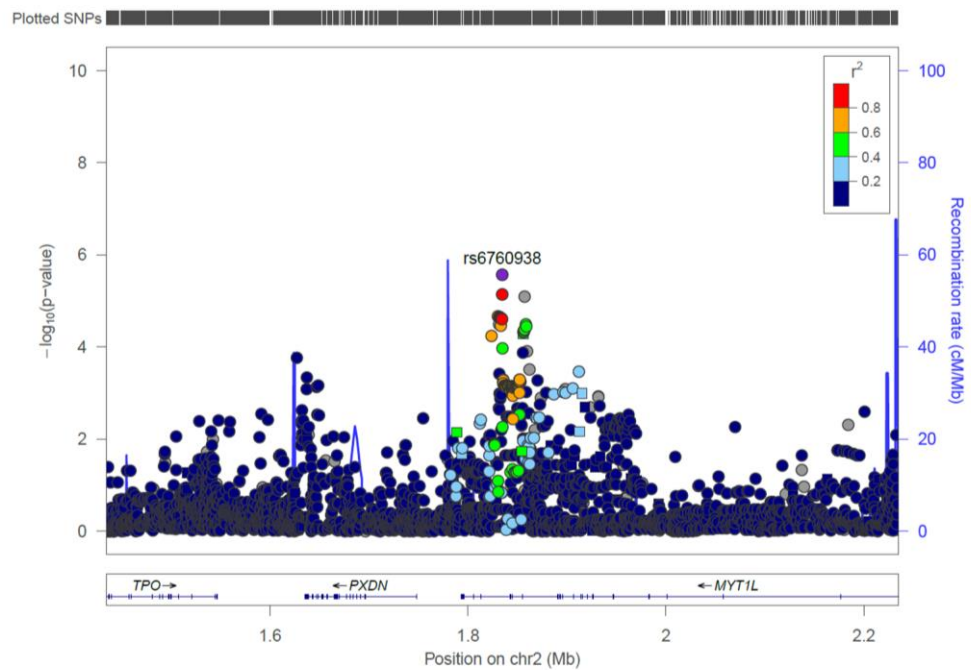
A

Figure 6.3. Regional association plots and recombination rates for chromosomal regions showing associations with dasatinib-induced diarrhoea at the suggestive significance level. SNP towers appearing in Manhattan plot on chromosome 2 (A), 3 (B), 6 (C), 7 (D) and 13 (E) are shown. Each circle represents an imputed SNP, whilst each square represents a genotyped SNP. The index SNP is shown in purple. The extent of linkage disequilibrium (r^2) is colour graded as shown in the top box. Blue lines represent the genetic recombination rate (cM/Mb) and the lower box indicates the genes coded for at this chromosome location.

Figure 6.3 continues onto next page

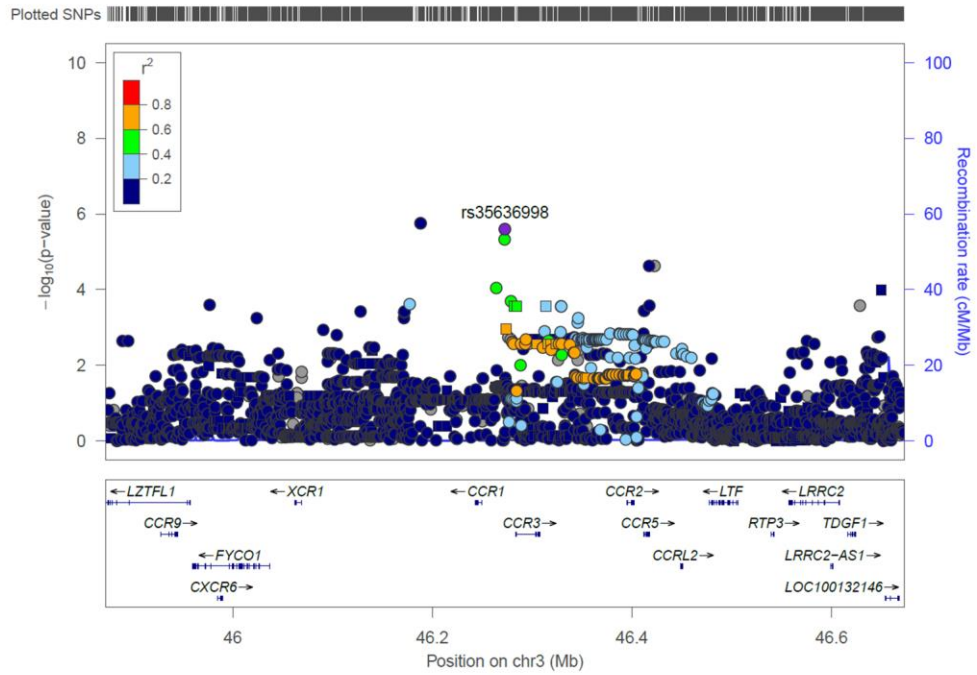
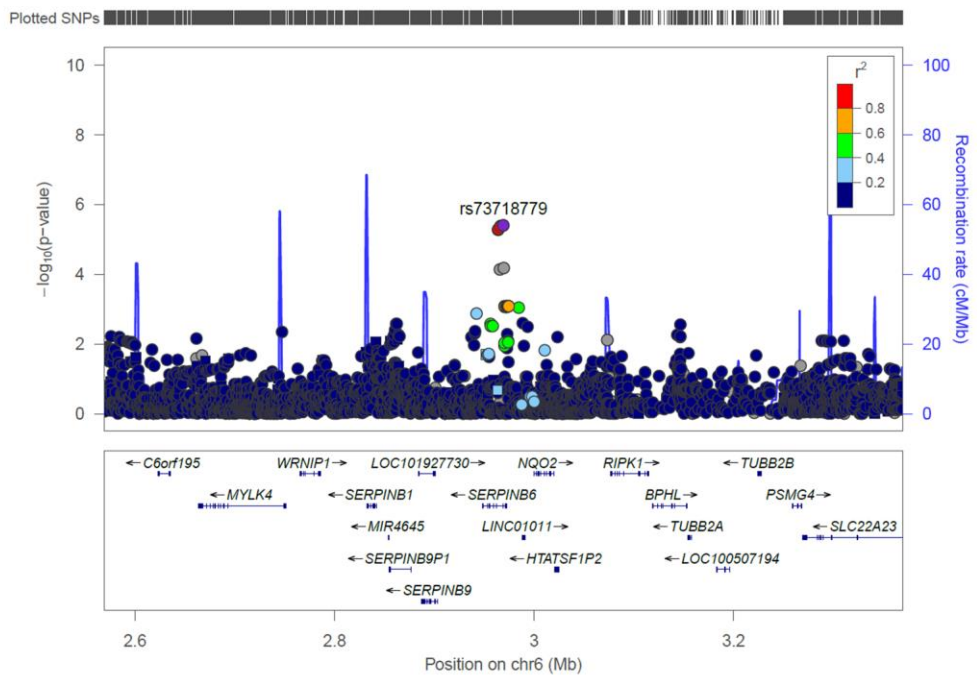
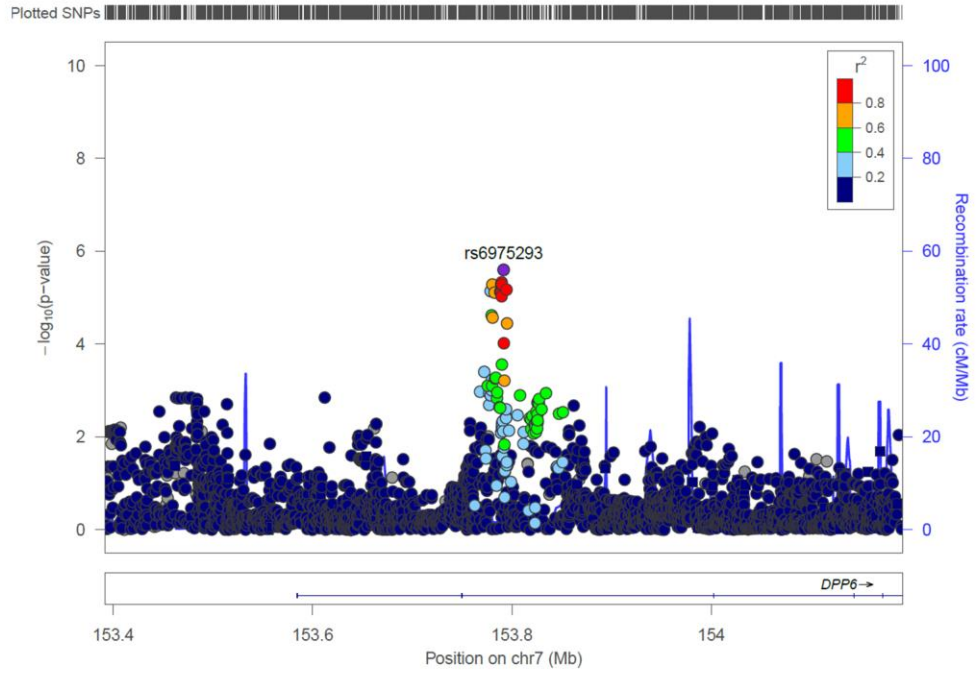
B**C**

Figure 6.3 continues onto next page

D



E

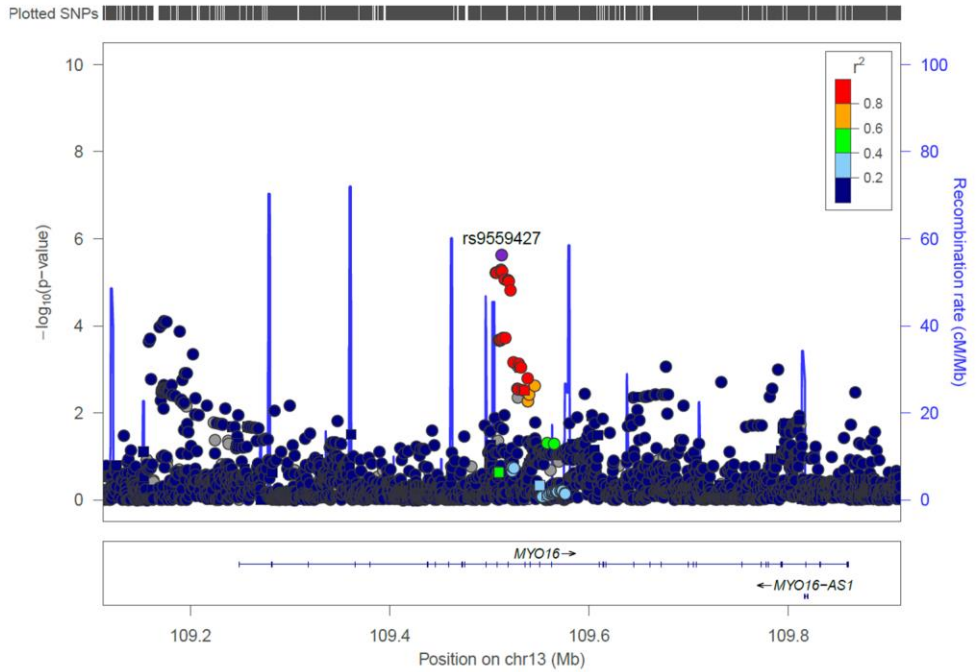


Figure 6.3 continued

Table 6.4. Index SNPs associated with dasatinib-induced diarrhoea at suggestive ($p < 1 \times 10^{-5}$) and genome-wide ($p < 5 \times 10^{-8}$) significance levels. Base pair (bp) position and location are based on human genome build GRCh37. Chr denotes chromosome number. MAF denotes minor allele frequency in cases (patients experiencing diarrhoea) and controls (patients not experiencing diarrhoea). INFO score is a prediction score of imputation accuracy. Imputed SNPs were analysed in dosage format. P-value indicates the SNPs association with dasatinib-induced diarrhoea. *MAF based on imputed dosage is close to zero therefore it is likely there were no carriers of this minor allele.

SNP	Chr	BP position	Gene	Location	Effect (minor) allele	Reference (major) allele	MAF		Allelic odds ratio	P-value of association	INFO score (%)
							Cases (n=40)	Controls (n=105)			
rs12424256	12	94654057	<i>PLXNC1</i>	intron	T	C	0.525	0.159	5.0956	4.22×10^{-9}	97.6
rs9559427	13	109512417	<i>MYO16</i>	intron	T	C	0.0001*	0.15	0.00027	2.35×10^{-6}	97.9
rs35636998	3	46272723	<i>CCR3</i>	intron	G	A	0.325	0.130	3.373	2.52×10^{-6}	95.2
rs6975293	7	153791767	<i>DPP6</i>	Non-coding transcript exon	G	C	0.288	0.524	0.44484	2.52×10^{-6}	48.6
rs6760938	2	1834745	<i>MYT1L</i>	intron	C	T	0.590	0.272	3.5792	2.74×10^{-6}	93.0
rs73718779	6	2969278	<i>SERPINB6</i>	intron	T	C	0.025	0.143	0.15389	3.97×10^{-6}	98.8

6.2.3 Validation of imputed SNPs in the discovery cohort using PCR-based genotyping methods

The six SNPs with the most significant p-value of association within each 'tower' (index SNPs) were imputed (Table 6.4); therefore, patients from the discovery cohort were genotyped for these specific SNPs by Taqman™ or KASP™ assay, to assess imputation accuracy.

All genotyped SNPs were in Hardy-Weinberg Equilibrium (HWE) (Table 6.5, $p > 1 \times 10^{-3}$), and showed clear genotype clusters (example plot in chapter 2, Fig 2.5) with relatively high call rate (>95%); suggesting accurate genotyping. SNPs with high INFO score (Table 6.4), a prediction of imputation accuracy, exhibited high concordance between the imputed and genotyped SNPs (Table 6.5). rs6765293 had a low INFO score (48.6%) indicating poor imputation, which was reflected in the low concordance between genotype predicted by imputation and genotype determined by PCR-based genotyping (47.6%) (Table 6.4). Moreover, rs6975293 is a palindromic SNP which codes for a G to C nucleotide change with a MAF of 49%, causing difficulty in differentiating between the forward and reverse strands which can lead to errors in SNP assay design.

Table 6.5. Confirmation of imputation accuracy of the discovery cohort using Taqman™ or KASP™ genotyping. MAF denotes minor allele frequency in cases (patients experiencing diarrhoea) and controls (patients not experiencing diarrhoea). P-values were calculated by performing logistic regression in PLINK assuming an additive mode of inheritance. Concordance with imputation was calculated as the percentage of matching patient genotypes predicted by imputation and determined by PCR-based genotyping.

SNP	Call rate (%)	Effect (minor) allele	Reference (major) allele	MAF		Allelic odds ratio	P-value of association	Concordance with imputation (%)	HWE P-value
				Cases (n=40)	Controls (n=105)				
rs12424256	95.6	T	C	0.474	0.159	4.803	3.46×10^{-6}	95.6	0.2532
rs9559427	96.2	T	C	0	0.141	N/A	N/A	98.1	0.0387
rs35636998	96.9	G	A	0.302	0.125	4.21	2.48×10^{-4}	93.2	0.0765
rs6975293	97.5	G	C	0.275	0.485	0.4225	2.75×10^{-3}	47.6	0.3085
rs6760938	97.6	C	T	0.600	0.304	3.409	3.18×10^{-5}	93.3	0.3765
rs73718779	97.5	T	C	0.025	0.142	0.1481	1.087×10^{-2}	100	0.6802

Odds ratios were similar between the genome-wide association study and our validation study (Table 6.4 and 6.5). However, p-values were different for rs9559427, rs25636998, rs73718779. This is probably due to the different statistical tests performed: in the genome-wide association study, genotypes are used in dosage format due to imputation, rather than absolute genotype values which are generated from PCR-based genotyping methods.

All six SNPs, excluding rs955942, reached significance at the $p < 0.05$ level (Table 6.5) and were therefore taken forward into the replication cohort. It was not possible to calculate the odds ratio or p-value of association for rs955942, because none of the diarrhoea cases carried the T allele. However, as the minor allele frequency (MAF) of control patients was 0.141 and much greater than control patients, this SNP was taken forward into the replication cohort.

6.2.4 Validation of SNPs in the replication cohort failed to confirm findings in the discovery cohort

The significance of SNPs identified and validated in the discovery cohort was investigated through a replication study using the replication cohort; 137 dasatinib-treated patients from the SPIRIT2 trial which were not used in the discovery cohort. The demographic characteristics of these patients were similar to those in the discovery cohort (Table 6.1); however, slightly fewer patients experienced diarrhoea (23% in contrast to 28%).

Table 6.6. Assessment of selected associated SNPs in replication cohort. MAF denotes minor allele frequency in cases (patients experiencing diarrhoea) and controls (patients not experiencing diarrhoea). P-values and odds ratios were calculated by performing a logistic regression in PLINK assuming an additive mode of inheritance with age, which significantly associated with the diarrhoea phenotype, set as a covariate.

SNP	Call rate (%)	Effect (minor) allele	Reference (major) allele	MAF		Allelic odds ratio	P-value of association	HWE p-value
				Cases (n=33)	Controls (n=104)			
rs12424256	98.5	T	C	0.166	0.191	0.9301	0.8416	0.3995
rs9559427	97.1	T	C	0.129	0.092	1.508	0.3620	0.3823
rs35636998	98.6	G	A	0.125	0.122	1.189	0.6970	0.6931
rs6975293	95.9	G	C	0.411	0.455	0.9005	0.6996	0.0435
rs6760938	92.8	C	T	0.266	0.320	0.7527	0.4054	0.8284
rs73718779	98.5	T	C	0.125	0.106	1.330	0.4927	0.2065

Patient DNA was genotyped using the Taqman™ or KASP™ assays as described for the discovery cohort. Genotype call rates for all SNPs were relatively high (>90%), clear clusters formed (example plot in chapter 2, Fig 2.5) and all passed HWE ($p > 1 \times 10^{-3}$) (Table 6.6) suggesting accurate genotyping.

No SNP associations were confirmed for diarrhoea versus non-diarrhoea patients in the replication cohort. The allelic odds ratio for all six SNPs (rs12424256, rs9559427, rs35636998, rs6975293, rs6760938, rs73718779) were close to 1, and P-values were not significant ($p > 0.3$) (Table 6.6).

6.3 Summary of results

The genome-wide association study performed in this chapter identified 4 SNPs, within the intronic region of the *PLXNC1* gene, significantly associated with dasatinib-induced diarrhoea at a genome-wide significance level ($p < 5 \times 10^{-8}$). The same genome-wide association study identified SNPs — within *MYO16*, *CCR3*, *DPP6*, *MYT1L* and *SERPINB6* genes — associated with dasatinib-induced diarrhoea at the suggestive significance level ($p < 1 \times 10^{-5}$). SNPs with the lowest p-value of association from each chromosomal region were taken forward into the replication cohort; however, we failed to find significant associations within this cohort.

6.3.1 Discussion

GWAS and candidate gene studies have identified many genetic variants associated with chemotherapy-induced diarrhoea (Table 6.1 and 6.2). However, to our knowledge this is the first report of a GWAS to identify genetic determinants of susceptibility to diarrhoea induced by the tyrosine kinase inhibitor, dasatinib.

Our study identified SNPs within *PLXNC1* (plexin C1), a protein-coding gene, to be significantly associated with dasatinib-induced diarrhoea at the genome-wide significance level. This semaphorin 7A receptor is involved in controlling adherence (Tamagnone *et al.*, 1999; Scott *et al.*, 2008, 2009; König *et al.*, 2014) and inflammation (Comeau *et al.*, 1998; Morote-Garcia *et al.*, 2012; König *et al.*, 2014), and is expressed on many inflammatory cells – T cells, B cells, monocytes, dendritic cells, neutrophils and platelets (König *et al.*, 2014). However, whilst both plexin C1 and its cognate ligand sema7A, are expressed at the protein level in the gut (Uhlen *et al.*, 2015), to date no studies have assessed the role of plexin C1 in the gut. It has been shown, however that DSS treatment to model colitis in BALB/c mice induces an increase in sema7a (Cho *et al.*, 2015); however, the extent to which this contributed to the colitis phenotype was not explored.

Five other regions within protein coding genes were also identified as significantly associated with dasatinib-induced diarrhoea at the suggestive significance level. These genes were *MYT1L*, *CCR3*, *SERPINB6*, *DPP6* and *MYO16*. It was interesting to note that no SNPs within dasatinib transporters or metabolism genes were found to be associated with dasatinib-induced diarrhoea. This could reflect the limitations of the study (see section below). Transporter and metabolism gene polymorphisms are frequently associated with adverse events (Table 6.1), likely due to higher intracellular drug concentrations.

MYT1L, a cysteine-cysteine zinc finger transcription factor involved in neurogenesis (Vierbuchen *et al.*, 2010) with incredibly low to no expression in small intestines and colon (Uhlen *et al.*, 2015), lacked any obvious link to the pathogenesis of diarrhoea. *MYO16* – a myosin protein, involved in brain development (Liu *et al.*, 2015) – has not been detected in the GI tract (Uhlen *et al.*, 2015) and also lacked any obvious biological plausibility.

SERPINB6, however, is highly expressed in the intestines (Uhlen *et al.*, 2015) and strong expression has been shown in colonic mast cells (Strik *et al.*, 2004). *SERPINB6* is a cytoplasmic protein which inhibits trypsin-like proteases, such as mast cell β -tryptase. It is thought that this inhibition aids neutralization of ectopic intracellular proteases, which can be released into the cytoplasm due to internalization and faults in degranulation. Mast cell degranulation leading to the release of proinflammatory mediators, such as histamine, can induce hypersecretion and hypermotility leading to diarrhoea (Ramsay *et al.*, 2010). Moreover, several studies have shown an increase in mast cell number in patients with IBS-D and chronic intractable diarrhoea (Ramsay *et al.*, 2010), suggesting biological plausibility of this locus.

DPP6 is a peptidase protein (that lacks peptidase activity (Strop *et al.*, 2004)) which physically associates with and increases cell surface expression of potassium voltage-gated channel subfamily D member 2 (*KCND2* or *Kv4.2*) (Soh *et al.*, 2008; Seikel *et al.*, 2009). *KCND2* is responsible for producing dendritic A-type currents, a current which is activated after hyperpolarization and regulates neuronal excitability (Amberg *et al.*, 2003). *Kv4.2*, along with *Kv4.3*, are likely major contributors to the A-type currents within smooth muscle, including that within the GI tract (Amberg *et al.*, 2003). *KCNQ5*, another potassium voltage-gated channel, has been shown to be associated with irinotecan-induced diarrhoea (grade ≥ 2) in a GWAS study (Takahashi *et al.*, 2014), and it was suggested that this was through altered susceptibility to irinotecan-induced gut motility.

CCR3 – a chemokine receptor expressed on inflammatory cells including T-helper cells – is known to have a role in the pathogenesis of diarrhoea. Three studies have shown genetic

variants within CCR3 are linked to celiac disease (Dubois *et al.*, 2010; Trynka *et al.*, 2011; Garner *et al.*, 2014), and CCR3 overexpression occurs in ulcerative colitis (Manousou *et al.*, 2010). The minor allele variant of the index SNP (rs35636998), that was found to be associated with increased frequency of dasatinib-induced diarrhoea, increases expression of CCR3 and 2 in whole blood (GTEx-Consortium, 2013). T cell expansion has been linked to dasatinib-induced high grade diarrhoea (Mustjoki *et al.*, 2009), and therefore, it could be hypothesized that rs35636998 may affect susceptibility to dasatinib-induced T-cell expansion thereby affecting the incidence of diarrhoea.

Within each genetic region, the index SNP (that was identified in the GWAS discovery cohort) was not found to be significantly related to the incidence of dasatinib-induced diarrhoea in the replication cohort. This suggests either the initial results were false positives or that we failed to detect true associations in the second cohort, due to the limitations of the study (discussed below).

From our results it is tempting to speculate that dasatinib-induced diarrhoea has a genetic component. For example, CCR3, DPP6 and SERPINB6 have biologically plausible links to diarrhoea pathogenesis, suggesting certain polymorphisms within this region could alter susceptibility to dasatinib-induced diarrhoea. However, this conclusion should be treated with caution as we were unable to validate these candidate SNPs in our replication cohort.

6.4 Limitations and future work

One of the main limitations of our study, which is common to GWAS, was the small sample size. Our discovery cohort consisted of 145 patients (40 cases and 105 controls), meaning the study likely had insufficient power to detect all genome-wide associations. Dasatinib-induced diarrhoea is likely a complex and multifactorial phenotype; the diarrhoeal mechanisms in one set of patients may be overlapping but distinct to another set, both within the same diarrhoeal grade and between grades. This decreases the power of the study, meaning a large sample size is especially important. Susceptibility to dasatinib-induced diarrhoea is also likely to be influenced by other non-genetic components, which it has not been possible to study, such as diet and microbiome.

Another common problem, which was also true for our study, was the issue of phenotyping. Dasatinib-induced diarrhoea is not a clear-cut phenotype and the CTCAE, used to categorize diarrhoea into grades 1 to 5, is highly subjective. Further increasing subjectivity was the fact that the diarrhoea grade assigned was based on patient reporting. Moreover, in some cases,

it can be difficult to determine whether the adverse event is caused by the drug. Whilst we excluded patients for which diarrhoea was unlikely to be caused by dasatinib (due to patient co-morbidities, chapter 2, Fig 2.4), we cannot be absolutely confident that dasatinib was the cause of diarrhoea for the remaining patients. This lack of non-subjective standardized phenotyping can make replication between different cohorts and independent studies challenging. The requirement for more standardized phenotype definitions to identify genetic determinants of GI toxicity has been noted previously (Carr *et al.*, 2017).

A more objective approach, would include using a marker of GI epithelial damage, for example histological scoring of GI damage or faecal calprotectin levels (a biomarker for intestinal inflammation) (Manceau *et al.*, 2017). This would increase the power of the study, however, would cause bias towards specific diarrhoeal mechanisms. For example, a GWAS for drug-induced GI damage would fail to detect genetic associations linked to diarrhoeal mechanism involved in secretion and dysmotility. However, using diarrhoea as the case phenotype enables a more generalised unbiased approach and is arguably more clinically relevant.

An additional limitation is the lack of patient quality control with the replication cohort, despite patient quality control being performed in the GWAS. In this way, co-founding variables or population sub-structure could be present decreasing validity of results. Moreover, fewer patients experienced diarrhoea in the replication cohort, decreasing the power of this cohort.

Future work should include sub-analysis of a larger cohort using higher grade diarrhoea only. The majority of candidate gene and GWAS studies which have successfully identified SNPs associated with chemotherapy-induced diarrhoea focused on higher grade toxicity (Table 6.1 and 6.2). The use of high-grade diarrhoea only, will likely give the study greater power, as diarrhoeal mechanisms may differ between low and high grade (see section 1.4.4 Inflammation and ER stress). Furthermore, SNPs associated with higher-grade diarrhoea will be of greater clinical relevance; enabling identification of patients who require alternative treatment due to the risk of potentially fatal chemotherapy-induced GI toxicities. The use of a larger sample size would give the study greater power and allow association tests to be performed only on patients with high-grade diarrhoea.

The biological plausibility of any SNPs found to associate in both the discovery and replication cohort should be analysed thoroughly. For SNPs within or near genes, pathway analysis should be undertaken using web servers such as GeneMANIA (genemania.org) and STRING

(String-db.org). Analysis of metabolic pathways linked to genes could be examined using KEGG PATHWAY database (genome.jp/kegg/pathway.html) and PathCards (pathcards.genecards.org). Whether SNPs within 5' untranslated and promoter regions affect gene expression and transcription factor binding should be analysed using RegulomeDB (regulomedb.org) and GTEx Portal (gtexportal.org). It would also be interesting to determine whether SNPs within intronic regions alter splicing, for example by using the online tool Human Splicing Finder (umd.be/HSF). For SNPs within protein coding exons, the effect on amino acid sequence should be determined.

CHAPTER 7: FINAL DISCUSSION

7.1 General discussion

Diarrhoea is a common ADR in patients receiving oral anti-cancer TKIs (Keller *et al.*, 2009; Fullmer *et al.*, 2011; Cohen *et al.*, 2012; Shi *et al.*, 2013; Brümmendorf *et al.*, 2015). This adverse event can be dose-limiting resulting in treatment discontinuation or dose-reduction, (Cortes *et al.*, 2010; Kantarjian *et al.*, 2014) which may lead to decreased treatment efficacy (Carr *et al.*, 2017).

Patients presenting with diarrhoea are treated with anti-diarrhoeal therapies which are decades old (Carr *et al.*, 2017). The most commonly used treatments are antimotility agents which increase intestinal transit time, and hence increase sodium ion and water reabsorption. Loperamide, a μ -opioid receptor agonist, is an over-the-counter licensed antimotility drug used for mild diarrhoea. However, μ -opioid agonists have a narrow therapeutic index and potential side effects including nausea, vomiting and abdominal pain (Markland *et al.*, 2015).

Moreover, these commonly administered anti-diarrhoeal agents often do not target the mechanism through which diarrhoea is occurring (in many cases diarrhoea pathogenesis does not solely involve increased motility, see chapter 1); therefore, treatment can be ineffective (Cortes *et al.*, 2010). The need for more definitive diarrhoeal treatments is recognised in the clinic and pharmaceutical setting, and more specific strategies are under development. These include NKCC1 inhibitors, K^+ channel inhibitors and NHE3 agonists which are appropriate for the treatment of diarrhoea with a secretory mechanism (Thiagarajah *et al.*, 2015). Specific anti-diarrhoeal therapies are already available in a few cases of drug-induced diarrhoea. For example, crofelemer, a dual CFTR and CaCC inhibitor, is used to attenuate diarrhoea induced by HIV therapy (Thiagarajah *et al.*, 2015).

However, the paucity in mechanistic understanding of drug-induced GI toxicity, particularly for targeted chemotherapies, hinders the development and identification of more specific and effective management strategies. Therefore, this project aimed to investigate the mechanism of TKI-induced diarrhoea.

In chapter 3 it was found that the TKIs bosutinib, dasatinib, imatinib and gefitinib induced barrier dysfunction and increased intestinal permeability in an *in vitro* model of the human intestinal epithelium (Caco-2 cells), with bosutinib inducing the greatest barrier disruption compared to the other TKIs tested. Bosutinib also caused degradation and rearrangement of TJ and AJ proteins, and this likely contributed to decreased barrier integrity. This loss of

intestinal barrier function has been shown to increase susceptibility to infection and bacterial translocation in chemotherapy-treated rats (Song *et al.*, 2006; Nakao *et al.*, 2012). Treatment with a non-specific anti-diarrhoeal, such as loperamide to increase transit time, would not protect from decreased barrier integrity, and the potential secondary effect of intestinal bacterial infection. This further highlights the need for targeted diarrhoea therapy.

The differences in intestinal barrier responses to TKIs within the same class (i.e. BCR-ABL inhibitors used for CML treatment) – degradation and rearrangement of cell junction proteins occurred after addition of bosutinib but not imatinib – can be seen for other drug classes. For example, EGFR inhibitors gefitinib and erlotinib decrease ZO-1 and E-cadherin levels in rat IEC-6 cells, but icotinib at the same concentration has no effect (Fan *et al.*, 2014; Hong *et al.*, 2014). This discrepancy is potentially due to the differing off-target proteins of drugs within the same inhibitor class, as well as the different IC50s that these drugs display towards their target protein. Bosutinib has a lower IC50 than imatinib and many more off-target proteins including the Src family kinases and MAPKs (Rix *et al.*, 2009; Kitagawa *et al.*, 2013).

After identification of bosutinib-induced barrier dysfunction as a potential diarrhoea mechanism, we then examined the upstream pathways, to enable identification of possible drug targets. First, we assessed cell death; a common process in increased intestinal permeability (Bojarski *et al.*, 2001; Chen *et al.*, 2017) and cytotoxic chemotherapy-induced diarrhoea (Keefe *et al.*, 2000; Sonis *et al.*, 2004). Only low levels of cell death were seen at concentrations causing bosutinib-induced permeability increases, supporting the hypothesis that the predominant diarrhoeal mechanism of targeted chemotherapies, such as BCR-ABL inhibitors, is unlikely to involve direct intestinal damage (however this cannot be ruled out as a possible secondary effect) (Van Sebille *et al.*, 2015).

We therefore hypothesized that bosutinib was targeting specific pathways, by inhibiting off-target or on-target kinases, involved in controlling TJ and AJ disassembly. To test this, a plethora of pathway inhibitors – including inhibitors of MMPs, ER stress, oxidative stress, cytoskeletal rearrangement, and proteasomal and lysosomal degradation – were investigated for their ability to prevent bosutinib-induced occludin degradation. None of these inhibitors significantly attenuated bosutinib-induced occludin degradation. However, we detected a significant and rapid decrease in TIMP-2 levels upon addition of bosutinib, enabling us to speculate involvement of the TIMP-MMP pathway (TIMPs are endogenous inhibitors of MMPs) in bosutinib-induced barrier disruption. This hypothesis was supported by the fact that a broad spectrum MMP inhibitor, GM6001, was able to prevent bosutinib-

induced cellular retractions. There is also strong evidence for the involvement of MMPs in TJ and AJ degradation within the intestines – MMPs are involved in TJ modulation during intestinal permeability increases in rodent models (Al-Dasooqi *et al.*, 2010; Trivedi *et al.*, 2013; Ding *et al.*, 2014; Vandenbroucke *et al.*, 2014; Nighot *et al.*, 2015), and Caco-2 cells (Groschwitz *et al.*, 2013; Eum *et al.*, 2014).

The fact that the pathways involved in bosutinib-induced barrier dysfunction were not fully elucidated exemplifies the high complexity of interlinking signalling pathways involved in TJ and AJ disassembly (González-Mariscal *et al.*, 2008; Zihni *et al.*, 2014, 2016). Some pathways may be redundant and only become activated when other pathways are inhibited, and certain proteins can act as both positive and negative regulators of cell junction disassembly (dependent on their phosphorylation status, conformational state and cellular environment). For example, *activation* of Src by dextran sulphate sodium (DSS) treatment (to model colitis) causes TJ disruption and increased permeability in Caco-2 cells (Samak *et al.*, 2015), but *inhibiting* Src-induced FAK activation increases permeability in the same cell line (Ma *et al.*, 2013).

This complexity is further exacerbated by the large number of off-target kinases inhibited by bosutinib (Rix *et al.*, 2009), and the fact that kinase profiling has not been undertaken in intestinal cells. Further knowledge of the bosutinib intestinal kinase inhibition spectrum and bioinformatics analysis will likely be required to identify relevant targets to be tested for their involvement in bosutinib-induced barrier disruption.

Next, we attempted to ascertain the physiological relevance of our findings in the two-dimensional Caco-2 cell *in vitro* model by determining the translatability of our results into a 3-dimensional multicellular intestinal organoid (enteroid) model. Human tissue was not available for this project; therefore, organoids were cultured from BALB/c mouse proximal small intestinal tissue. However, mouse enteroids, unlike Caco-2 cells, recapitulate an *in vivo* 3-dimensional intestinal structure and contains the major cell types of the intestinal epithelial layer (Sato *et al.*, 2009) making them more physiologically relevant in this regard.

Using a previously developed enteroid permeability assay (Leslie *et al.*, 2015), similar to the FITC-dextran permeability assay used on Caco-2 cells in this project, we demonstrated that the bosutinib-induced permeability increase was translatable to our enteroid model. The mechanism of this permeability increase was likely similar, but not identical, to that in the Caco-2 model. In both the Caco-2 and enteroid model, the permeability increase occurred at a concentration causing occludin rearrangement and a low level of cell death (that was only

detected in the more sensitive viability assays, such as active caspase-3 staining). However, unlike in the Caco-2 model, we failed to detect rearrangement of ZO-1 and E-cadherin or decreased cell junction protein levels in the enteroid model. Overall, results from this chapter show the majority of our findings in chapter 3 on the Caco-2 cell line are translatable into a model that was more physiologically relevant in terms of its non-cancerous origin, cellular heterogeneity and 3-dimensional structure.

In chapter 6, a GWAS was performed as an unbiased approach to identify genes associated with dasatinib-induced diarrhoea, and therefore potentially develop a better mechanistic understanding of TKI-induced diarrhoea. Six SNPs were identified, two with biological relevance (within the *DPP6* and *CCR3* genes), in the discovery cohort at the suggestive significance level. *DPP6* encodes a transmembrane protein that belongs to a family of serine proteases, and binds to and regulates the level of KCND2, a potassium channel involved in regulating neuronal excitability within the GI tract (Amberg *et al.*, 2003). *CCR3* codes for a chemokine receptor with strong links to diarrhoea-associated diseases including celiac disease (Dubois *et al.*, 2010; Trynka *et al.*, 2011; Garner *et al.*, 2014), and ulcerative colitis (Manousou *et al.*, 2010). Moreover, *SERPINB6* encodes a serine protease inhibitor – expressed in mast cells, macrophages and activated neutrophils – that likely has a protective role against cell death induced by lysosomal leakage (Strik *et al.*, 2004). This enabled us to hypothesise that dasatinib-induced diarrhoea may involve dysmotility and inflammation, providing further avenues which could be experimentally explored *in vitro* and *in vivo*.

However, we were unable to confirm the associations of *DPP6* and *CCR3* with dasatinib-induced diarrhoea in a replication cohort. This may be due to the lower incidence of diarrhoea seen in this replication cohort, thus giving this cohort relatively lower power to identify associations than the discovery cohort. Lack of replication could also suggest the trait (dasatinib-induced diarrhoea) has a highly complex and multi-factorial pathogenesis that may differ between patients and include non-genetic factors, such as diet and the microbiome, which could not be factored into the analysis.

7.2 Future studies and implications

Data presented here provides strong evidence for the involvement of barrier dysfunction in diarrhoea induced by bosutinib, and potentially other TKIs such as dasatinib and gefitinib. However, it will be necessary to assess the physiological and clinical relevance of findings in patients, by determining the translatability of increased paracellular permeability into patients. Several non-invasive techniques, such as the lactulose/mannitol test (Inutsuka *et*

al., 2003; Melichar, Dvořák, *et al.*, 2010), exist for determining changes in intestinal permeability in patients. Permeability measurements in CML patients receiving TKIs should be correlated with the diarrhoea phenotype to give an indication of the contribution of the barrier dysfunction to the diarrhoea phenotype.

To gain further support for the cellular junction dissolution mechanism, studies observing changes in cellular junction proteins should be performed on human intestinal organoids. Changes in localization of cell junction proteins may be observed in real time using organoids transfected with fluorescently-labelled TJ/AJ proteins; a technique which has been successfully employed in human organoids to generate intestinal organoids expressing fluorescently-labelled histone (specially histone H2A) (Schwank *et al.*, 2013). Alternatively, immunofluorescence staining of TJs could be performed on human duodenal biopsies taken from patients before and after chemotherapeutic treatment (Karczewski *et al.*, 2010). As human samples were not available for this project, we will undertake whole mouse *in vivo* work to further understand the translatability of our findings at a whole-systems level. Mice will be given TKIs by oral gavage and have their proximal small intestine examined for signs of tight junction dissolution by immunofluorescence staining, cell death using active caspase-3 staining and changes in gross pathology by H&E staining.

Whilst data presented here show that bosutinib is capable of disrupting Caco-2 monolayer and enteroid epithelial barrier integrity, the pathways leading to this remain largely unknown. However, our preliminary findings of decreased TIMP2 levels following bosutinib treatment, offers the suggestion of MMP pathway involvement. Further studies assessing the importance of MMP activation in this process will be essential to accept or refute our hypothesis of MMP-induced TJ and AJ disruption.

Finally, assessment of compounds for their ability to prevent intestinal barrier dysfunction at the pre-clinical and clinical stages will be required. Currently no FDA-approved treatments exist to maintain barrier function, neither for the treatment of GI disorders nor the prevention of drug-induced GI toxicity (Odenwald *et al.*, 2017). However, larazotide acetate has been shown to attenuate Caco-2 barrier dysfunction caused by gliadin and *Vibrio cholerae* zonula occludens toxin (Gopalakrishnan *et al.*, 2012) and is currently in clinical trials for the treatment of coeliac disease (Leffler *et al.*, 2015). Larazotide acetate prevents gluten-induced release of zonulin (Khaleghi *et al.*, 2016), a protein which initiates a signalling pathway leading to increased intestinal permeability; therefore, larazotide acetate is unlikely to be effective at preventing TJ and AJ dissolution initiated by other pathways.

Probiotics, however, have been shown to increase TJ and AJ protein levels under an array of different conditions (Bron *et al.*, 2017). Administration of *Lactobacillus plantarum*, a bacteria found in fermented foods and the GI tract, to the duodenum by feeding catheter in healthy patients increases localization of ZO-1 and occludin to TJ structures (Bron *et al.*, 2017). Several *in vitro* and *in vivo* models, including models of colitis, have demonstrated specific probiotics can have a beneficial effect on intestinal barrier function by increasing expression of TJ and AJ proteins such as occludin and E-cadherin (Bron *et al.*, 2017). One study showed the probiotic *Lactobacillus rhamnosus* significantly decreased grade 3/4 diarrhoea in colorectal cancer patients treated with 5-FU (Touchefeu *et al.*, 2014); however, strong evidence for probiotic-induced barrier repair is lacking due to inconsistent findings across studies (Touchefeu *et al.*, 2014).

It is also worth noting, as our data point towards a hypothesis whereby MMP activation leads to bosutinib-induced diarrhoea, that several MMP inhibitors are in clinical and pre-clinical trials for treatment of an array of cancer types, including breast and colorectal cancer (Winer *et al.*, 2018). MMPs are well-known mediators of tumour growth and metastasis; however, the role of MMPs in barrier dysfunction also make them a candidate target for treatment of chemotherapy-induced diarrhoea (Al-Dasooqi *et al.*, 2014). A recent study by Gibson *et al.* showed selective MMP-9/-12 inhibition using AZD3342 delayed diarrhoea onset and reduced tumour growth in methotrexate-treated Dark Agouti rats (Gibson *et al.*, 2019), suggesting MMP inhibition should be explored further as a potential co-treatment to increase efficacy and decrease the incidence of lower GI ADRs.

Taken together, our results support a hypothesis that bosutinib-induced diarrhoea is mediated by barrier dysfunction involving cellular junction dissolution and increased paracellular permeability, possibly through the MMP pathway, and this warrants further investigation *in vitro*, *in vivo* and in patients.

REFERENCES

- Abbas, R. *et al.* (2016) 'Clinical pharmacokinetics and pharmacodynamics of bosutinib', *Clinical Pharmacokinetics*, 55(10), pp. 1191–1204. doi: 10.1007/s40262-018-0679-9.
- Adachi, M. *et al.* (2006) 'Normal establishment of epithelial tight junctions in mice and cultured cells lacking expression of ZO-3, a tight-junction MAGUK protein', *Molecular and Cellular Biology*, 26(23), pp. 9003–9015. doi: 10.1128/MCB.01811-05.
- Agarwal, R. *et al.* (1994) 'Pathophysiology of potassium absorption and secretion by the human intestine', *Gastroenterology*, 107(2), pp. 548–571. doi: 10.1016/0016-5085(94)90184-8.
- Akshsi, T. K. *et al.* (2014) 'Microtubules and actin crosstalk in cell migration and division', *Cytoskeleton*, 7(1), pp. 1–23. doi: 10.1002/cm.21150.
- Akiyama, T. *et al.* (2016) 'Bifidobacteria prevent tunicamycin-induced endoplasmic reticulum stress and subsequent barrier disruption in human intestinal epithelial Caco-2 monolayers', *PLoS ONE*, 11(9), p. e0162448. doi: 10.1371/journal.pone.0162448.
- Al-Dasooqi, N. *et al.* (2010) 'Matrix metalloproteinases are possible mediators for the development of alimentary tract mucositis in the dark agouti rat.', *Experimental Biology and Medicine*, 235(10), pp. 1244–56. doi: 10.1258/ebm.2010.010082.
- Al-Dasooqi, N. *et al.* (2014) 'Gastrointestinal mucositis: the role of MMP-tight junction interactions in tissue injury', *Pathology and Oncology Research*, 20(3), pp. 485–491. doi: 10.1007/s12253-013-9733-y.
- Al-Dasooqi, N. (2014) 'Matrix metalloproteinases and gut toxicity following cytotoxic cancer therapy', *Current Opinion in Supportive and Palliative Care*, 8(2), pp. 164–169. doi: 10.1097/SPC.0000000000000049.
- Al-Sadi, R. *et al.* (2008) 'Mechanism of IL-1 β -induced increase in intestinal epithelial tight junction permeability', *The Journal of Immunology*, 180(8), pp. 5653–5661. doi: 10.4049/jimmunol.180.8.5653.
- Al-Sadi, R. *et al.* (2013) 'TNF- α modulation of intestinal epithelial tight junction barrier is regulated by ERK1/2 activation of Elk-1', *The American Journal of Pathology*, 183(6), pp. 1871–1884. doi: 10.1016/j.ajpath.2013.09.001.
- Altshuler, A. E. *et al.* (2014) 'Transmural intestinal wall permeability in severe ischemia after enteral protease inhibition', *PLoS ONE*, 9(5), pp. 1–14. doi: 10.1371/journal.pone.0096655.
- Amberg, G. C. *et al.* (2003) 'A-type potassium currents in smooth muscle', *American Journal of Physiology: Cell Physiology*, 284(3), pp. C583–C595. doi: 10.1152/ajpcell.00301.2002.
- Ando, H. *et al.* (2015) 'A new physiologically-based pharmacokinetic model for the prediction of gastrointestinal drug absorption: translocation model.', *Drug Metabolism and Disposition*, 43(4), pp. 590–602. doi: 10.1124/dmd.114.060038.
- Antunes, F. *et al.* (2013) 'Establishment of a triple co-culture *in vitro* cell models to study intestinal absorption of peptide drugs', *European Journal of Pharmaceutics and Biopharmaceutics*, 83(3), pp. 427–435. doi: 10.1016/j.ejpb.2012.10.003.

- Appiah-Kubi, K. *et al.* (2017) 'Platelet-derived growth factor receptors (PDGFRs) fusion genes involvement in hematological malignancies', *Critical Reviews in Oncology/Hematology*, 109(301), pp. 20–34. doi: 10.1016/j.critrevonc.2016.11.008.
- Arijs, I. *et al.* (2011) 'Mucosal gene expression of cell adhesion molecules, chemokines, and chemokine receptors in patients with inflammatory bowel disease before and after infliximab treatment', *The American Journal of Gastroenterology*, 106(4), pp. 748–761. doi: 10.1038/ajg.2011.27.
- Artursson, P. *et al.* (2001) 'Caco-2 monolayers in experimental and theoretical predictions of drug transport', *Advanced Drug Delivery Reviews*, 46(1–3), pp. 27–43. doi: 10.1016/S0169-409X(00)00128-9.
- Avizienyte, E. *et al.* (2004) 'Src SH3/2 domain-mediated peripheral accumulation of Src and phospho-myosin is linked to deregulation of E-cadherin and the epithelial-mesenchymal transition', *Molecular Biology of the Cell*, 15(6), pp. 2794–2803. doi: 10.1091/mbc.E03.
- Avizienyte, E. *et al.* (2005) 'The Src-induced mesenchymal state in late-stage colon cancer cells', *Cells Tissues Organs*, 179, pp. 73–80. doi: 10.1159/000084511.
- Ayehunie, S. *et al.* (2013) 'A new organotypic 3-D small intestinal tissue model reconstructed from primary human cells', *Toxicology Letters*, 221, p. S88. doi: 10.1016/j.toxlet.2013.05.108.
- Baran, Y. *et al.* (2013) 'The roles of macromolecules in imatinib resistance of chronic myeloid leukemia cells by Fourier transform infrared spectroscopy', *Biomedicine and Pharmacotherapy*, 67(3), pp. 221–227. doi: 10.1016/j.biopha.2012.12.001.
- Barker, N. *et al.* (2008) 'The intestinal stem cell', *Genes & Development*, 22(14), pp. 1856–1864. doi: 10.1101/gad.1674008.1856.
- Barrett, J. C. *et al.* (2008) 'Genome-wide association defines more than thirty distinct susceptibility loci for Crohn's disease', *Nature Genetics*, 40(8), pp. 955–962. doi: 10.1038/NG.175.
- Barrett, K. E. *et al.* (2000) 'Chloride secretion by the intestinal epithelium: molecular basis and regulatory aspects.', *Annual Review of Physiology*, 62(1), pp. 535–572. doi: 10.1146/annurev.physiol.62.1.535.
- Barrett, K. E. (2018) 'Mapping the Duodenal Crypt-Villus Transport Axis', *Cellular and Molecular Gastroenterology and Hepatology*, 5(4), pp. 642–644. doi: 10.1016/j.jcmgh.2018.02.010.
- Basuroy, S. *et al.* (2005) 'Acetaldehyde disrupts tight junctions and adherens junctions in human colonic mucosa: protection by EGF and L-glutamine', *American Journal of Physiology: Gastrointestinal and Liver Physiology*, 289(2), pp. 367–375. doi: 10.1152/ajpgi.00464.2004.
- Beauchemin, N. *et al.* (2013) 'Carcinoembryonic antigen-related cell adhesion molecules (CEACAMs) in cancer progression and metastasis', *Cancer and Metastasis Reviews*, 32(3–4), pp. 643–671. doi: 10.1007/s10555-013-9444-6.
- Bein, A. *et al.* (2015) 'TIMP-1 inhibition of occludin degradation in Caco-2 intestinal cells: a potential protective role in necrotizing enterocolitis.', *Pediatric Research*, 77(5), pp. 649–655. doi: 10.1038/pr.2015.26.
- Bellodi, C. *et al.* (2009) 'Targeting autophagy potentiates tyrosine kinase inhibitor-induced

cell death in Philadelphia chromosome-positive cells, including primary CML stem cells', *The Journal of Clinical Investigation*, 119(5), pp. 1109–1123. doi: 10.1172/JCI35660.

Bertelsen, L. S. *et al.* (2004) 'Prolonged interferon- γ exposure decreases ion transport, NKCC1, and Na⁺-K⁺-ATPase expression in human intestinal xenografts in vivo', *The American Journal of Physiology: Gastrointestinal and Liver Physiology*, 286(1), pp. G157–65. doi: 10.1152/ajpgi.00227.2003 [pii].

Bertiaux-Vanda, N. *et al.* (2011) 'The expression and the cellular distribution of the tight junction proteins are altered in irritable bowel syndrome patients with differences according to the disease subtype', *The American Journal of Gastroenterology*, 106(12), pp. 2165–2173. doi: 10.1038/ajg.2011.257.

Bertolotti, A. *et al.* (2001) 'Increased sensitivity to dextran sodium sulfate colitis in IRE1 β -deficient mice', *The Journal of Clinical Investigation*, 107(5), pp. 585–593. doi: 10.1172/JCI11476.

Beutheu, S. *et al.* (2013) 'Glutamine and arginine improve permeability and tight junction protein expression in methotrexate-treated Caco-2 cells', *Clinical Nutrition*, 32(5), pp. 863–869. doi: 10.1016/j.clnu.2013.01.014.

Beyder, A. *et al.* (2014) 'Loss-of-function of the voltage-gated sodium channel NaV1.5 (channelopathies) in patients with irritable bowel syndrome', *Gastroenterology*, 146(7), pp. 1659–1668. doi: 10.1053/j.gastro.2014.02.054.

Bijsmans, I. T. G. W. *et al.* (2017) 'Characterization of stem cell-derived liver and intestinal organoids as a model system to study nuclear receptor biology', *Biochimica et Biophysica Acta*, 1863(3), pp. 687–700. doi: 10.1016/j.bbadis.2016.12.004.

Birch, M. *et al.* (2013) 'Simple methodology for the therapeutic drug monitoring of the tyrosine kinase inhibitors dasatinib and imatinib', *Biomedical Chromatography*, 27(3), pp. 335–342. doi: 10.1002/bmc.2796.

Boivin, M. A. *et al.* (2009) 'Mechanism of interferon- γ -induced increase in T84 intestinal epithelial tight junction', *Journal of Interferon & Cytokine Research*, 29(1), pp. 45–54. doi: 10.1089/jir.2008.0128.

Bojarski, C. *et al.* (2001) 'Permeability of human HT-29/B6 colonic epithelium as a function of apoptosis', *Journal of Physiology*, 535(2), pp. 541–552. doi: 10.1111/j.1469-7793.2001.00541.x.

Boudou-Rouquette, P. *et al.* (2012) 'Early sorafenib-induced toxicity is associated with drug exposure and UGT1A9 genetic polymorphism in patients with solid tumors: a preliminary study', *PLoS ONE*, 7(8), pp. 1–9. doi: 10.1371/journal.pone.0042875.

Boulares, A. H. *et al.* (1999) 'Role of poly(ADP-ribose) polymerase (PARP) cleavage in apoptosis', *The Journal of Biological Chemistry*, 274(33), pp. 22932–22940.

Bowen, J. M. *et al.* (2007) 'Irinotecan changes gene expression in the small intestine of the rat with breast cancer', *Cancer Biology Therapy*, 59(3), pp. 337–348. doi: 10.1007/s00280-006-0275-9.

Bowen, J. M. *et al.* (2012) 'Development of a rat model of oral small molecule receptor tyrosine kinase inhibitor-induced diarrhea', *Cancer Biology and Therapy*, 13(13), pp. 1269–1275. doi: 10.4161/cbt.21783.

- Breccia, M. *et al.* (2011) 'Activity and safety of dasatinib as second-line treatment or in newly diagnosed chronic phase chronic myeloid leukemia patients.', *BioDrugs: Clinical Immunotherapeutics, Biopharmaceuticals and Gene Therapy*, 25(3), pp. 147–57. doi: 10.2165/11591840-000000000-00000.
- Brew, K. *et al.* (2010) 'The tissue inhibitors of metalloproteinases (TIMPs): an ancient family with structural and functional diversity', *Biochimica et Biophysica Acta*, 1803(1), pp. 55–71. doi: 10.1016/j.bbamcr.2010.01.003.
- Bron, P. A. *et al.* (2017) 'Can probiotics modulate human disease by impacting intestinal barrier function?', *British Journal of Nutrition*, 117(1), pp. 93–107. doi: 10.1017/S0007114516004037.
- Brück, S. *et al.* (2017) 'Caco-2 cells – expression, regulation and function of drug transporters compared with human jejunal tissue', *Biopharmaceutics & Drug Disposition*, 38(2), pp. 115–126. doi: 10.1002/bdd.2025.
- Bruewer, M. *et al.* (2003) 'Proinflammatory cytokines disrupt epithelial barrier function by apoptosis-independent mechanisms.', *Journal of Immunology*, 171(11), pp. 6164–6172. doi: 10.4049/jimmunol.171.11.6164.
- de Bruïne, A. P. *et al.* (1992) 'NCI-H716 cells as a model for endocrine differentiation in colorectal cancer', *Virchows Archiv. B Cell Pathology Including Molecular Pathology*, 62(1), pp. 311–320. doi: 10.1007/BF02899698.
- Brümmendorf, T. *et al.* (2015) 'Bosutinib versus imatinib in newly diagnosed chronic-phase chronic myeloid leukaemia: results from the 24-month follow-up of the BELA trial', *British Journal of Haematology*, 168(1), pp. 69–81. doi: 10.1111/bjh.13108.
- Buhrmann, C. *et al.* (2015) 'Resveratrol induces chemosensitization to 5-fluorouracil through up-regulation of intercellular junctions, epithelial-to-mesenchymal transition and apoptosis in colorectal cancer', *Biochemical Pharmacology*, 98(1), pp. 51–68. doi: 10.1016/j.bcp.2015.08.105.
- Burton, P. R. *et al.* (2007) 'Genome-wide association study of 14,000 cases of seven common diseases and 3,000 shared controls', *Nature*, 447(7145), pp. 661–678. doi: 10.1038/nature05911.
- Buschmann, M. M. *et al.* (2013) 'Occludin OCEL-domain interactions are required for maintenance and regulation of the tight junction barrier to macromolecular flux', *Molecular Biology of the Cell*, 24(19), pp. 3056–3068. doi: 10.1091/mbc.E12-09-0688.
- Cai, X. *et al.* (2014) 'The role of IVS14+1 G > A genotype detection in the dihydropyrimidine dehydrogenase gene and pharmacokinetic monitoring of 5-fluorouracil in the individualized adjustment of 5-fluorouracil for patients with local advanced and metastatic colorectal cancer', *European Review for Medical and Pharmacological Sciences*, 18(8), pp. 1247–58.
- Calatayud, M. *et al.* (2014) 'Trivalent arsenic species induce changes in expression and levels of proinflammatory cytokines in intestinal epithelial cells', *Toxicology Letters*, 224(1), pp. 40–46. doi: 10.1016/j.toxlet.2013.09.016.
- Cao, S. S. (2015) 'Endoplasmic reticulum stress and unfolded protein response in inflammatory bowel disease', *Inflammatory Bowel Diseases*, 21(3), pp. 636–644. doi: 10.1097/mib.0000000000000238.

- Carpenter, A. E. *et al.* (2006) 'CellProfiler: image analysis software for identifying and quantifying cell phenotypes', *Genome Biology*, 7(10), p. R100.1-R100.11. doi: 10.1186/gb-2006-7-10-r100.
- Carr, D. F. *et al.* (2017) 'Towards better models and mechanistic biomarkers for drug-induced gastrointestinal injury', *Pharmacology and Therapeutics*, 172, pp. 181–194. doi: 10.1016/j.pharmthera.2017.01.002.
- Carrasco-Pozo, C. *et al.* (2013) 'Polyphenols protect the epithelial barrier function of Caco-2 cells exposed to indomethacin through the modulation of occludin and zonula occludens-1 expression', *Journal of Agricultural and Food Chemistry*, 61(22), pp. 5291–5297. doi: 10.1021/jf400150p.
- Catanzaro, D. *et al.* (2015) '*Boswellia serrata* preserves intestinal epithelial barrier from oxidative and inflammatory damage', *PLoS ONE*, 10(5), pp. e0125375–e012390. doi: 10.1371/journal.pone.0125375.
- Ceponis, P. J. M. *et al.* (2000) 'Interleukins 4 and 13 increase intestinal epithelial permeability by a phosphatidylinositol 3-kinase pathway', *The Journal of Biological Chemistry*, 275(37), pp. 29132–29137. doi: 10.1074/jbc.M003516200.
- Chandra, L. *et al.* (2019) 'Derivation of adult canine intestinal organoids for translational research in gastroenterology', *BMC Biology*, 17(33), pp. 1–21. doi: 10.1186/s12915-019-0652-6.
- Chappell, A. E. *et al.* (2008) 'Hydrogen peroxide inhibits Ca²⁺-dependent chloride secretion across colonic epithelial cells *via* distinct kinase signaling pathways and ion transport proteins', *The FASEB Journal*, 22(6), pp. 2023–2036. doi: 10.1096/fj.07-099697.
- Chelakkot, C. *et al.* (2017) 'Intestinal epithelial cell-specific deletion of PLD2 alleviates DSS-induced colitis by regulating occludin', *Scientific Reports*, 7(1), pp. 1573–1588. doi: 10.1038/s41598-017-01797-y.
- Chen, S. *et al.* (2015) 'ABCC5 and ABCG1 polymorphisms predict irinotecan-induced severe toxicity in metastatic colorectal cancer patients', *Pharmacogenetics and Genomics*, 25(12), pp. 573–583. doi: 10.1097/FPC.0000000000000168.
- Chen, W. Y. *et al.* (2017) 'Acrolein disrupts tight junction proteins and causes endoplasmic reticulum stress-mediated epithelial cell death leading to intestinal barrier dysfunction and permeability', *The American Journal of Pathology*, 187(12), pp. 2686–2697. doi: 10.1016/j.ajpath.2017.08.015.
- Chey, W. Y. *et al.* (2001) 'Colonic motility abnormality in patients with irritable bowel syndrome exhibiting abdominal pain and diarrhea', *American Journal of Gastroenterology*, 96(5), pp. 1499–1506. doi: 10.1016/S0002-9270(01)02367-X.
- Cho, J. Y. *et al.* (2015) 'β-caryophyllene attenuates dextran sulfate sodium-induced colitis in mice *via* modulation of gene expression associated mainly with colon inflammation', *Toxicology Reports*, 2, pp. 1039–1045.
- Choi, Y. J. U. N. *et al.* (2011) 'Inhibition of cell motility and invasion by HangAmDan-B in NCI-H460 human non-small cell lung cancer cells', *Oncology Reports*, 26, pp. 1601–1608. doi: 10.3892/or.2011.1440.
- Chotikatum, S. *et al.* (2018) 'Inflammation induced ER stress affects absorptive intestinal

epithelial cells function and integrity', *International Immunopharmacology*, 55(January), pp. 336–344. doi: 10.1016/j.intimp.2017.12.016.

Chow, J. Y. C. *et al.* (2007) 'Role of protein phosphatase 2A in calcium-dependent chloride secretion by human colonic epithelial cells', *American Journal of Physiology: Cell Physiology*, 292(1), pp. C452–C459. doi: 10.1152/ajpcell.00034.2006.

Chua, W. *et al.* (2009) 'Molecular markers of response and toxicity to FOLFOX chemotherapy in metastatic colorectal cancer', *British Journal of Cancer*, 101(6), pp. 998–1004. doi: 10.1038/sj.bjc.6605239.

Cilloni, D. *et al.* (2012) 'Molecular pathways: BCR-ABL', *Clinical Cancer Research*, 18(4), pp. 930–937. doi: 10.1158/1078-0432.CCR-10-1613.

Clayburgh, D. R. *et al.* (2004) 'A differentiation-dependent splice variant of myosin light chain kinase, MLCK1, regulates epithelial tight junction permeability', *The Journal of Biological Chemistry*, 279(53), pp. 55506–55513. doi: 10.1074/jbc.M408822200.

Coëffier, M. *et al.* (2010) 'Increased proteasome-mediated degradation of occludin in irritable bowel syndrome.', *The American Journal of Gastroenterology*, 105(5), pp. 1181–1188. doi: 10.1038/ajg.2009.700.

Cohen, M. H. *et al.* (2002) 'Approval summary for imatinib mesylate capsules in the treatment of chronic myelogenous leukemia', *Clinical Cancer Research*, 8(5), pp. 935–942.

Cohen, M. H. *et al.* (2012) 'Approval summary: imatinib mesylate for one or three years in the adjuvant treatment of gastrointestinal stromal tumors.', *The Oncologist*, 17(7), pp. 992–7. doi: 10.1634/theoncologist.2012-0109.

Coluccia, A. M. L. *et al.* (2006) 'SKI-606 decreases growth and motility of colorectal cancer cells by preventing pp60 (c-Src)-dependent tyrosine phosphorylation of beta-catenin and its nuclear signaling', *Cancer Research*, 66(4), pp. 2279–2286. doi: 10.1158/0008-5472.CAN-05-2057.

Comeau, M. R. *et al.* (1998) 'A poxvirus-encoded semaphorin induces cytokine production from monocytes and binds to a novel cellular semaphorin receptor, VESPR', *Immunity*, 8(4), pp. 473–482.

Contreras, T. C. *et al.* (2015) '(–)-Epicatechin in the prevention of tumor necrosis alpha-induced loss of Caco-2 cell barrier integrity', *Archives of Biochemistry and Biophysics*, 573, pp. 84–91. doi: 10.1016/j.abb.2015.01.024.

Cook, D. *et al.* (2014) 'Lessons learned from the fate of AstraZeneca's drug pipeline: a five-dimensional framework.', *Nature Reviews. Drug discovery*, 13(6), pp. 419–31. doi: 10.1038/nrd4309.

Cortejoso, L. *et al.* (2013) 'Differential toxicity biomarkers for irinotecan- and oxaliplatin-containing chemotherapy in colorectal cancer', *Cancer Chemotherapy and Pharmacology*, 71(6), pp. 1463–1472. doi: 10.1007/s00280-013-2145-6.

Cortes, J. E. *et al.* (2010) 'Safety and efficacy of bosutinib (SKI-606) in patients (pts) with chronic phase (CP) chronic myeloid leukemia (CML) following resistance or intolerance to imatinib (IM).', *Journal of Clinical Oncology*, 28(15_suppl), pp. 6502–6502. doi: 10.1200/jco.2010.28.15_suppl.6502.

- Cusatis, G. *et al.* (2006) 'Pharmacogenetics of ABCG2 and adverse reactions to gefitinib', *Journal of the National Cancer Institute*, 98(23), pp. 1739–1742. doi: 10.1093/jnci/djj469.
- Czito, B. G. *et al.* (2006) 'Increased toxicity with gefitinib, capecitabine, and radiation therapy in pancreatic and rectal cancer: phase I trial results', *Journal of Clinical Oncology*, 24(4), pp. 656–662. doi: 10.1200/JCO.2005.04.1749.
- Dalile, B. *et al.* (2019) 'The role of short-chain fatty acids in microbiota-gut-brain communication', *Nature Reviews Gastroenterology and Hepatology*, 16(8), pp. 461–478. doi: 10.1038/s41575-019-0157-3.
- Damiano, S. *et al.* (2018) 'Effects of antioxidants on apoptosis induced by dasatinib and nilotinib in K562 cells', *Journal of Cellular Biochemistry*, 119(January), pp. 4845–4854. doi: 10.1002/jcb.26686.
- Daniele, B. *et al.* (2001) 'Oral glutamine in the prevention of fluorouracil induced intestinal toxicity: a double blind, placebo controlled, randomised trial', *Gut*, 48(1), pp. 28–33.
- Das, P. *et al.* (2012) 'Comparative tight junction protein expressions in colonic Crohn's disease, ulcerative colitis, and tuberculosis: a new perspective', *Virchows Arch: An International Journal of Pathology*, 460(3), pp. 261–270. doi: 10.1007/s00428-012-1195-1.
- Davies, J. A. (2018) *Organs and Organoids*. 1st edn. Edited by J. A. Davies *et al.* Academic Press Inc., pp. 1-284. doi: 10.1016/B978-0-12-812636-3.00001-8.
- Deenen, M. J. *et al.* (2011) 'Relationship between single nucleotide polymorphisms and haplotypes in DPYD and toxicity and efficacy of capecitabine in advanced colorectal cancer', *Clinical Cancer Research*, 17(10), pp. 3455–3468. doi: 10.1158/1078-0432.CCR-10-2209.
- Dekkers, J. F. *et al.* (2013) 'A functional CFTR assay using primary cystic fibrosis intestinal organoids', *Nature Medicine*, 19(7), pp. 939–945. doi: 10.1038/nm.3201.
- Delaneau, O. *et al.* (2013) 'Improved whole-chromosome phasing for disease and population genetic studies', *Nature Methods*, 10(1), pp. 5–6. doi: 10.1038/nmeth.2307.
- Ding, H. *et al.* (2014) 'Effect of homocysteine on intestinal permeability in rats with experimental colitis, and its mechanism', *Gastroenterology Report*, 2(3), pp. 215–220. doi: 10.1093/gastro/gou022.
- Dong, C. X. *et al.* (2014) 'The intestinal epithelial insulin-like growth factor-1 receptor links glucagon-like peptide-2 action to gut barrier function', *Endocrinology*, 155(2), pp. 370–379. doi: 10.1210/en.2013-1871.
- Dubois, P. C. A. *et al.* (2010) 'Multiple common variants for celiac disease influencing immune gene expression', *Nature Genetics*. Nature Publishing Group, 42(4), pp. 295–302. doi: 10.1038/ng.543.
- Dyer, J. *et al.* (2002) 'Expression of monosaccharide transporters in intestine of diabetic humans', *American Journal of Physiology: Gastrointestinal and Liver Physiology*, 282(2), pp. 241–248. doi: 10.1152/ajpgi.00310.2001.
- Ekert, P. G. *et al.* (1999) 'Caspase inhibitors', *Cell Death and Differentiation*, 6(11), pp. 1081–1086. doi: 10.1038/sj.cdd.4400594.
- Elamin, E. *et al.* (2018) 'Ethanol disrupts intestinal epithelial tight junction integrity through

intracellular calcium-mediated Rho/ROCK activation', *American Journal of Physiology: Gastrointestinal and Liver Physiology*, 306(8), pp. 677–685. doi: 10.1152/ajpgi.00236.2013.

Engle, M. J. *et al.* (1998) 'Caco-2 cells express a combination of colonocyte and enterocyte phenotypes', *Journal of Cellular Physiology*, 174(3), pp. 362–369. doi: 10.1002/(SICI)1097-4652(199803)174:3<362::AID-JCP10>3.0.CO;2-B.

Erkut, M. *et al.* (2010) 'A case of acute colitis with severe rectal bleeding in a patient with chronic myeloid leukemia after dasatinib use', *Acta Haematologica*, 123(4), pp. 205–206. doi: 10.1159/000306070.

Eskazan, A. E. *et al.* (2014) 'Acute colitis presenting with hematochezia in a patient with chronic myeloid leukemia during dasatinib therapy', *The Turkish Journal of Gastroenterology*, 25(Suppl 1), p. 233. doi: 10.5152/tjg.2014.5281.

Etienne-Grimaldi, M. C. *et al.* (2015) 'UGT1A1 genotype and irinotecan therapy: general review and implementation in routine practice', *Fundamental and Clinical Pharmacology*, 29(3), pp. 219–237. doi: 10.1111/fcp.12117.

Eum, S. Y. *et al.* (2014) 'Disruption of epithelial barrier by quorum-sensing N-3-(oxododecanoyl)-homoserine lactone is mediated by matrix metalloproteinases', *American Journal of Physiology: Gastrointestinal and Liver Physiology*, 306(11), pp. G992–G1001. doi: 10.1152/ajpgi.00016.2014.

European Medicines Agency (2018) 'Bosulif Assessment Report [Online]', *European Medicines Agency Science Medicines Health*. Available at: ema.europa.eu/en/documents/variation-report/bosulif-h-c-2373-ii-0025-g-epar-assessment-report-variation_en.pdf (Accessed 1 April 2020).

Fan, L. *et al.* (2014) 'Erlotinib promotes endoplasmic reticulum stress-mediated injury in the intestinal epithelium.', *Toxicology and Applied Pharmacology*, 278(1), pp. 45–52. doi: 10.1016/j.taap.2014.04.015.

Farooqi, A. A. *et al.* (2015) 'Platelet-derived growth factor (PDGF) signalling in cancer: rapidly emerging signalling landscape', *Cell Biochemistry and Function*, 33(5), pp. 257–265. doi: 10.1002/cbf.3120.

Fatehullah, A. *et al.* (2016) 'Organoids as an in vitro model of human development and disease', *Nature Cell Biology*, 18(3), pp. 246–254. doi: 10.1038/ncb3312.

Feng, R. *et al.* (2013) 'Indian hedgehog mediates gastrin-induced proliferation in stomach of adult mice', *Gastroenterology*, 147(3), pp. 655–666. doi: 10.1053/j.gastro.2014.05.006.

Field, M. *et al.* (1972) 'Effect of cholera enterotoxin on ion transport across isolated ileal mucosa.', *Journal of Clinical Investigation*, 51(4), pp. 796–804. doi: 10.1172/JCI106874.

Field, M. (2003) 'Intestinal ion transport and the pathophysiology of diarrhea', *The Journal of Clinical Investigation*, 111(7), pp. 931–943. doi: 10.1172/JCI200318326.

Finkbeiner, S. R. *et al.* (2015) 'Generation of tissue-engineered small intestine using embryonic stem cell-derived human intestinal organoids', *Biology Open*, 4(11), pp. 1462–1472. doi: 10.1242/bio.013235.

Flores, L. R. *et al.* (2019) 'Lifeact-GFP alters F-actin organization, cellular morphology and biophysical behaviour', *Scientific Reports*, 9(1), pp. 1–13. doi: 10.1038/s41598-019-40092-w.

- Forsgård, R. A. *et al.* (2016) 'Intestinal permeability to iohexol as an in vivo marker of chemotherapy-induced gastrointestinal toxicity in Sprague-Dawley rats', *Cancer Chemotherapy and Pharmacology*, 78(4), pp. 863–874. doi: 10.1007/s00280-016-3150-3.
- Foulke-Abel, J. *et al.* (2016) 'Human enteroids as a model of upper small intestinal ion transport physiology and pathophysiology', *Gastroenterology*, 150(3), pp. 638–649. doi: 10.1053/j.gastro.2015.11.047.
- De Francia, S. *et al.* (2013) 'Plasma and intracellular imatinib concentrations in patients with chronic myeloid leukemia', *Therapeutic Drug Monitoring*, 36(3), pp. 410–420. doi: 10.1097/FTD.000000000000013.
- Fullmer, A. *et al.* (2011) 'Dasatinib for the treatment of chronic phase chronic myeloid leukemia', *Expert Reviews in Hematology*, 4(3), pp. 253–260. doi: 10.2217/cpr.13.43.
- Furuse, M. *et al.* (2001) 'Conversion of zonulae occludentes from tight to leaky strand type by introducing claudin-2 into Madin-Darby canine kidney I cells', *The Journal of Cell Biology*, 153(2), pp. 263–272.
- Galluzzi, L. *et al.* (2017) 'Necroptosis: mechanisms and relevance to disease', *Annual Review of Pathology: Mechanisms of Disease*, 12, pp. 103–130. doi: 10.1146/annurev-pathol-052016-100247.
- Garcia-Gonzalez, X. *et al.* (2015) 'Variants in CDA and ABCB1 are predictors of capecitabine-related adverse reactions in colorectal cancer', *Oncotarget*, 6(8), pp. 6422–6430.
- Gareau, M. G. *et al.* (2013) 'Fluid and electrolyte secretion in the inflamed gut: novel targets for treatment of inflammation-induced diarrhea', *Current Opinion in Pharmacology*, 13(6), pp. 895–899. doi: 10.1016/j.coph.2013.08.014.
- Garner, C. *et al.* (2014) 'Genome-wide association study of celiac disease in North America confirms FRMD4B as new celiac locus', *PLoS ONE*, 9(7), p. e101428. doi: 10.1371/journal.pone.0101428.
- Gaschler, M. M. *et al.* (2017) 'Lipid peroxidation in cell death', *Biochemical and Biophysical Research Communications*, 482(3), pp. 419–425. doi: 10.1016/j.bbrc.2016.10.086.
- Gerbe, F. *et al.* (2011) 'Distinct ATOH1 and Neurog3 requirements define tuft cells as a new secretory cell type in the intestinal epithelium', *The Journal of Cell Biology*, 192(5), pp. 767–780. doi: 10.1083/jcb.201010127.
- Gey, G. O. *et al.* (1952) 'Tissue culture studies of the proliferative capacity of cervical carcinoma and normal epithelium', *Cancer Research*, 12, pp. 264–265.
- Gibson, R. J. *et al.* (2019) 'Selective MMP inhibition, using AZD3342, to reduce gastrointestinal toxicity and enhance chemoefficacy in a rat model', *Chemotherapy*, 63(5), pp. 284–292. doi: 10.1159/000495470.
- Giovannetti, E. *et al.* (2010) 'Association of polymorphisms in AKT1 and EGFR with clinical outcome and toxicity in non-small cell lung cancer patients treated with gefitinib', *Molecular Cancer Therapeutics*, 9(3), pp. 581–593. doi: 10.1158/1535-7163.mct-09-0665.
- González-Mariscal, L. *et al.* (2008) 'Crosstalk of tight junction components with signaling pathways', *Biochimica et Biophysica Acta*, 1778(3), pp. 729–756. doi:

10.1016/j.bbamem.2007.08.018.

Gopalakrishnan, S. *et al.* (2012) 'Larazotide acetate regulates epithelial tight junctions in vitro and in vivo', *Peptides*, 35(1), pp. 86–94. doi: 10.1016/j.peptides.2012.02.015.

Gorodeski, G. I. (2007) 'Estrogen decrease in tight junctional resistance involves matrix-metalloproteinase-7-mediated remodeling of occludin', *Endocrinology*, 148(1), pp. 218–231. doi: 10.1210/en.2006-1120.

Grabinger, T. *et al.* (2014) 'Ex vivo culture of intestinal crypt organoids as a model system for assessing cell death induction in intestinal epithelial cells and enteropathy', *Cell Death and Disease*, 15(5), p. e1228. doi: 10.1038/cddis.2014.183.

Greaves, P. *et al.* (2004) 'First dose of potential new medicines to humans: how animals help', *Nature Reviews Drug Discovery*, 3(3), pp. 226–236. doi: 10.1038/nrd1329.

Greenspon, J. *et al.* (2011) 'Sphingosine-1-phosphate regulates the expression of adherens junction protein E-Cadherin and enhances intestinal epithelial cell barrier function', *Digestive Diseases and Sciences*, 56(5), pp. 1342–1353. doi: 10.1007/s10620-010-1421-0.

Groschwitz, K. R. *et al.* (2013) 'Chymase-mediated intestinal epithelial permeability is regulated by a protease-activating receptor/matrix metalloproteinase-2-dependent mechanism', *American Journal of Physiology - Gastrointestinal and Liver Physiology*, 304(5), pp. G479–G489. doi: 10.1152/ajpgi.00186.2012.

Grundy, D. *et al.* (2012) *Neural control of gastrointestinal function*. 1st edn. Edited by D. N. Granger *et al.* Morgan & Claypool Publishers., pp. 1-136. doi: 10.4199/C00048ED1V01Y201111ISP030.

GTEEx-Consortium (2013) 'The genotype-tissue expression (GTEEx) project', *Nature Genetics*, 45(6), pp. 580–585. doi: 10.1038/ng.2653.

Gunawardene, A. R. *et al.* (2011) 'Classification and functions of enteroendocrine cells of the lower gastrointestinal tract', *International Journal of Experimental Pathology*, 92(4), pp. 219–231. doi: 10.1111/j.1365-2613.2011.00767.x.

Hamada, K. *et al.* (2010) 'Zonula occludens-1 alterations and enhanced intestinal permeability in methotrexate-treated rats', *Cancer Chemotherapy and Pharmacology*, 66(6), pp. 1031–1038. doi: 10.1007/s00280-010-1253-9.

Hamada, K. *et al.* (2013) 'Disruption of ZO-1/claudin-4 interaction in relation to inflammatory responses in methotrexate-induced intestinal mucositis', *Cancer Chemotherapy and Pharmacology*, 72(4), pp. 757–765. doi: 10.1007/s00280-013-2238-2.

Hammel, H. T. *et al.* (2005) 'Osmosis and solute-solvent drag: fluid transport and fluid exchange in animals and plants', *Cell Biochemistry and Biophysics*, 42(3), pp. 277–345. doi: 10.1385/CBB:42:3:277.

Hamouda, N. *et al.* (2017) 'Apoptosis, Dysbiosis and Expression of Inflammatory Cytokines are Sequential Events in the Development of 5-Fluorouracil-Induced Intestinal Mucositis in Mice', *Basic and Clinical Pharmacology and Toxicology*, 121(3), pp. 159–168. doi: 10.1111/bcpt.12793.

Han, J.-Y. *et al.* (2013) 'A genome-wide association study for irinotecan-related severe toxicities in patients with advanced non-small-cell lung cancer', *Pharmacogenomics*. Nature

Publishing Group, 13(5), pp. 417–422. doi: 10.1038/tpj.2012.24.

Hao, X. *et al.* (2012) 'Berberine ameliorates pro-inflammatory cytokine-induced endoplasmic reticulum stress in human intestinal epithelial cells in vitro', *Inflammation*, 35(3), pp. 841–849. doi: 10.1007/s10753-011-9385-6.

Haritunians, P. T. *et al.* (2010) 'Genetic predictors of medically refractory ulcerative colitis', *Inflammatory Bowel Diseases*, 16(11), pp. 1830–1840. doi: 10.1016/j.cortex.2009.08.003.

Hetz, C. (2012) 'The unfolded protein response: controlling cell fate decisions under ER stress and beyond', *Nature Reviews Molecular Cell Biology*. Nature Publishing Group, 13(2), pp. 89–102. doi: 10.1038/nrm3270.

Hida, T. *et al.* (2009) 'Gefitinib for the treatment of non-small-cell lung cancer', *Expert Review of Anticancer Therapy*, 9(1), pp. 17–35. doi: 10.1586/14737140.9.1.17.

Hidalgo, I. J. *et al.* (1989) 'Characterization of the human colon carcinoma cell line (Caco-2) as a model system for intestinal epithelial permeability', *Gastroenterology*, 96(2), pp. 736–749. doi: 10.1016/S0016-5085(89)80072-1.

Hilgendorf, C. *et al.* (2007) 'Expression of thirty-six drug transporter genes in human intestine, liver, kidney, and organotypic cell lines', *Drug Metabolism and Disposition*, 35(8), pp. 1333–1340. doi: 10.1124/dmd.107.014902.

Hinnebusch, B. F. *et al.* (2004) 'Enterocyte differentiation marker intestinal alkaline phosphatase is a target gene of the gut-enriched Kruppel-like factor.', *American Journal of Physiology: Gastrointestinal and Liver physiology*, 286(1), pp. G23-30. doi: 10.1152/ajpgi.00203.2003.

Ho, S. B. *et al.* (1989) 'Cell lineage markers in premalignant and malignant colonic mucosa', *Gastroenterology*, 97(2), pp. 392–404.

Hong, S. *et al.* (2014) 'EGFR inhibitor-driven endoplasmic reticulum stress-mediated injury on intestinal epithelial cells.', *Life Sciences*, 119(1–2), pp. 28–33. doi: 10.1016/j.lfs.2014.10.008.

Horie, T. *et al.* (1998) 'Docosahexaenoic acid exhibits a potent protection of small intestine from methotrexate-induced damage in mice', *Life Sciences*, 62(15), pp. 1333–1338. doi: 10.1016/S0024-3205(98)00067-8.

Howie, B. N. *et al.* (2009) 'A flexible and accurate genotype imputation method for the next generation of genome-wide association studies', *PLoS Genetics*, 5(6), pp. 1–15. doi: 10.1371/journal.pgen.1000529.

Hoyle, S. *et al.* (2016) 'Validation of human, rat and mouse intestinal organoid models as preclinical screens to assess GI toxicity in novel oncology drug development', *European Journal of Cancer*, 69(Supplement 1), p. S77. doi: 10.1016/S0959-8049(16)32823-4.

Hoyle, S. M. *et al.* (2018) 'Validation of a canine intestinal organoid model as a preclinical screen to assess GI toxicity in novel oncology drug development', *Proceedings: AACR Annual Meeting 2018*, 78(13), p. 3870. doi: 10.1158/1538-7445.AM2018-3870.

Hu, M. *et al.* (2004) *Use of Caco-2 cell monolayers to study drug absorption and metabolism, Optimization in Drug Discovery*. doi: 10.1385/1-59259-800-5:019.

Hu, S. *et al.* (2007) 'Translational inhibition of colonic epithelial heat shock proteins by IFN- γ

and TNF- α in intestinal inflammation', *Gastroenterology*, 133(6), pp. 1893–1904. doi: 10.1053/j.gastro.2007.09.026.

Huang, Z. *et al.* (2014) 'A 3-D artificial colon tissue mimic for the evaluation of nanoparticle-based drug delivery system', *Molecular Pharmaceutics*, 11(7), pp. 2051–2061. doi: 10.1021/mp400723j.

Van Huis-Tanja, L. H. *et al.* (2013) 'MTHFR polymorphisms and capecitabine-induced toxicity in patients with metastatic colorectal cancer', *Pharmacogenetics and Genomics*, 23(4), pp. 208–218. doi: 10.1097/FPC.0b013e32835ee8e1.

Hussaarts, K. *et al.* (2019) 'Clinically relevant drug interactions with multikinase inhibitors: a review', *Therapeutic Advances in Medical Oncology Review*, 11(2s), pp. 1–34. doi: 10.1177/1758835918818347.

Hyatt, J. L. *et al.* (2005) 'Inhibition of acetylcholinesterase by the anticancer prodrug CPT-11', *Chemico-Biological Interactions*, 157–158(1), pp. 247–252. doi: 10.1016/j.cbi.2005.10.033.

Illek, B. *et al.* (1996) 'Alternate stimulation of apical CFTR by genistein in epithelia.', *American Journal of Physiology*, 270(24), pp. C265–C275.

Imura, Y. *et al.* (2010) 'Micro total bioassay system for ingested substances: assessment of intestinal absorption, hepatic metabolism, and bioactivity', *Analytical Chemistry*, 82(24), pp. 9983–9988. doi: 10.1021/ac100806x.

In, J. G. *et al.* (2016) 'Human mini-guts: new insights into intestinal physiology and host-pathogen interactions', *Nature Reviews Gastroenterology and Hepatology*, 13(11), pp. 633–642. doi: 10.1038/nrgastro.2016.142.

Inutsuka, S. *et al.* (2003) 'Assessment of the intestinal permeability following postoperative chemotherapy for human malignant disease', *European Surgical Research*, 35(1), pp. 22–25. doi: 10.1159/000067037.

Iqbal, N. *et al.* (2014) 'Imatinib: a breakthrough of targeted therapy in cancer', *Chemotherapy Research and Practice*, 2014(1), pp. 1–9. doi: 10.1155/2014/357027.

Ivanov, A. I. *et al.* (2004) 'Endocytosis of epithelial apical junctional proteins by a clathrin-mediated pathway into a unique storage compartment', *Molecular Biology of the Cell*, 15(January), pp. 176–188. doi: 10.1091/mbc.E03.

Iyer, L. *et al.* (2002) 'UGT1A1*28 polymorphism as a determinant of irinotecan disposition and toxicity', *Pharmacogenomics Journal*, 2(1), pp. 43–47.

Jandhyala, S. M. *et al.* (2015) 'Role of the normal gut microbiota', *World Journal of Gastroenterology*, 21(29), pp. 8836–8847. doi: 10.3748/wjg.v21.i29.8787.

Jeong, J. *et al.* (2012) 'Inhibition of migration and invasion of LNCaP human prostate carcinoma cells by cordycepin through inactivation of Akt', *International Journal of Oncology*, 40(5), pp. 1697–1704. doi: 10.3892/ijo.2012.1332.

Jeong, S. *et al.* (2012) 'Interaction of clusterin and matrix metalloproteinase-9 and its implication for epithelial homeostasis and inflammation', *American Journal of Pathology*, 180(5), pp. 2028–2039. doi: 10.1016/j.ajpath.2012.01.025.

Jepps, T. A. *et al.* (2009) 'Molecular and functional characterization of Kv7K+ channel in

murine gastrointestinal smooth muscles', *American Journal of Physiology-Gastrointestinal and Liver Physiology*, 297(1), pp. G107–G115. doi: 10.1152/ajpgi.00057.2009.

Jimenez, J. A. *et al.* (2015) 'Animal models to study acute and chronic intestinal inflammation in mammals', *Gut Pathogens*, 7(29), pp. 1–31. doi: 10.1186/s13099-015-0076-y.

Joerger, M. *et al.* (2015) 'Germline TYMS genotype is highly predictive in patients with metastatic gastrointestinal malignancies receiving capecitabine-based chemotherapy', *Cancer Chemotherapy and Pharmacology*, 75(4), pp. 763–772. doi: 10.1007/s00280-015-2698-7.

Johansson, M. E. V. *et al.* (2011) 'The two mucus layers of colon are organized by the MUC2 mucin, whereas the outer layer is a legislator of host-microbial interactions', *Proceedings of the National Academy of Sciences of the United States of America*, 108(Suppl. 1), pp. 4659–4665. doi: 10.1073/pnas.1006451107.

Jones, L. G. *et al.* (2019) 'NF- κ B2 signalling in enteroids modulates enterocyte responses to secreted factors from bone marrow-derived dendritic cells', *Cell Death and Disease*, 10(12), p. 896. doi: 10.1038/s41419-019-2129-5.

Jung, P. *et al.* (2011) 'Isolation and *in vitro* expansion of human colonic stem cells', *Nature Medicine*, 17(10), pp. 1225–1227. doi: 10.1038/nm.2470.

Kaeffer, B. (2002) 'Mammalian intestinal epithelial cells in primary culture: a mini-review', *In Vitro Cellular & Developmental Biology: Animal*, 38(3), pp. 123–134. doi: 10.1290/1071-2690(2002)038<0123:miecip>2.0.co;2.

Kantarjian, H. *et al.* (2010) 'Dasatinib versus imatinib in newly diagnosed chronic myeloid leukemia', *The New England Journal of Medicine*, 362(24), pp. 2260–2270.

Kantarjian, H. M. *et al.* (2014) 'Bosutinib safety profile and management of toxicities in leukemia patients with resistance or intolerance to imatinib and other tyrosine kinase inhibitors', *Blood*, 132(9), pp. 1309–1318. doi: 10.1182/blood-2013-07-513937.

Karczewski, J. *et al.* (2010) 'Regulation of human epithelial tight junction proteins by *Lactobacillus plantarum* in vivo and protective effects on the epithelial barrier', *American Journal of Physiology: Gastrointestinal and Liver Physiology*, 298(6), pp. G851–G859. doi: 10.1152/ajpgi.00327.2009.

Kaser, A. *et al.* (2008) 'XBP1 links ER stress to intestinal inflammation and confers genetic risk for human inflammatory bowel disease', *Cell*, 134(5), pp. 743–756. doi: 10.1016/j.cell.2008.07.021.

Kauffman, A. L. *et al.* (2013) 'Alternative functional *in vitro* models of human intestinal epithelia', *Frontiers in Pharmacology*, 4(79), pp. 1–18. doi: 10.3389/fphar.2013.00079.

Keefe, D. M. K. *et al.* (1997) 'Effect of high-dose chemotherapy on intestinal permeability in humans', *Clinical Science*, 92(4), pp. 385–389.

Keefe, D. M. K. *et al.* (2000) 'Chemotherapy for cancer causes apoptosis that precedes hypoplasia in crypts of the small intestine in humans', *Gut*, 47(5), pp. 632–637. doi: 10.1136/gut.47.5.632.

Keely, S. J. *et al.* (1999) 'ErbB2 and ErbB3 receptors mediate inhibition of calcium-dependent chloride secretion in colonic epithelial cells', *Journal of Biological Chemistry*, 274(47), pp.

33449–23454. doi: 10.1074/jbc.274.47.33449.

Keely, S. J. *et al.* (2000) 'Carbachol-stimulated transactivation of epidermal growth factor receptor and mitogen-activated protein kinase in T84 cells is mediated by intracellular Ca²⁺, PYK-2, and p60 src*', *Journal of Biological Chemistry*, 275(17), pp. 12619–12625.

Keller, G. *et al.* (2009) 'Bosutinib: a dual SRC/ABL kinase inhibitor for the treatment of chronic myeloid leukemia.', *Expert Review of Hematology*, 2(5), pp. 489–497. doi: 10.1586/ehm.09.42.

Kerkela, R. *et al.* (2006) 'Cardiotoxicity of the cancer therapeutic agent imatinib mesylate', *Nature Medicine*, 12(8), pp. 908–916. doi: 10.1038/nm1446.

Keshav, S. *et al.* (2013) *The Gastrointestinal System at a Glance*. 2nd edn. Edited by F. Goodgame *et al.* Wiley-Blackwell., pp. 1-120.

Khaleghi, S. *et al.* (2016) 'The potential utility of tight junction regulation in celiac disease: Focus on larazotide acetate', *Therapeutic Advances in Gastroenterology*, 9(1), pp. 37–49. doi: 10.1177/1756283X15616576.

Khalil, H. A. *et al.* (2016) 'A novel culture system for adult porcine intestinal crypts', *Cell and Tissue Research*, 365(1), pp. 123–134. doi: 10.1007/s00441-016-2367-0.

Khapchaev, A. Y. *et al.* (2016) 'Myosin light chain kinase MYLK1: anatomy, interactions, functions, and regulation', *Biochemistry (Moscow)*, 81(13), pp. 1676–1697.

Khoury, H. J. *et al.* (2012) 'Bosutinib is active in chronic phase chronic myeloid leukemia after imatinib and dasatinib and/or nilotinib therapy failure H.', *Leukemia*, 119(15), pp. 3403–3412. doi: 10.1182/blood-2011-11-390120.

Khoury, H. J. *et al.* (2018) 'Practical management of toxicities associated with bosutinib in patients with Philadelphia chromosome-positive chronic myeloid leukemia', *Annals of Oncology*, 29(3), pp. 578–587. doi: 10.1093/annonc/mdy019.

Kiela, P. *et al.* (2009) 'Ion transport in the intestine', *Current Opinion in Gastroenterology*, 25(2), pp. 87–91. doi: 10.1016/j.physbeh.2017.03.040.

Kim, B. M. *et al.* (2005) 'The stomach mesenchymal transcription factor Barx1 specifies gastric epithelial identity through inhibition of transient Wnt signaling', *Developmental Cell*, 8(4), pp. 611–622. doi: 10.1016/j.devcel.2005.01.015.

Kim, G. *et al.* (2018) 'Integration of sensors in gastrointestinal organoid culture for biological analysis', *Cellular and Molecular Gastroenterology and Hepatology*, 6(1), pp. 123–131. doi: 10.1016/j.jcmgh.2018.03.002.

Kim, H. J. *et al.* (2015) 'ABCB1 polymorphism as prognostic factor in breast cancer patients treated with docetaxel and doxorubicin neoadjuvant chemotherapy', *Cancer Science*, 106(1), pp. 86–93. doi: 10.1111/cas.12560.

Kim, S. Y. *et al.* (2017) 'A phase II study of preoperative chemoradiation with tegafur-uracil plus leucovorin for locally advanced rectal cancer with pharmacogenetic analysis', *Radiation Oncology*, 12(1), pp. 1–9. doi: 10.1186/s13014-017-0800-5.

Kitagawa, D. *et al.* (2013) 'Activity-based kinase profiling of approved tyrosine kinase inhibitors', *Genes to Cells*, 18(2), pp. 110–122. doi: 10.1111/gtc.12022.

- Kmira, Z. (2013) 'Severe hemorrhagic colitis in a patient with chronic myeloid leukemia in the blastic phase after dasatinib use', *World Journal of Gastrointestinal Pathophysiology*, 4(3), p. 59. doi: 10.4291/wjgp.v4.i3.59.
- Konig, K. *et al.* (2014) 'The plexin C1 receptor promotes acute inflammation', *European Journal of Immunology*, 44(9), pp. 2648–2658. doi: 10.1002/eji.201343968.
- Kreutzman, A. *et al.* (2017) 'Dasatinib reversibly disrupts endothelial vascular integrity by increasing non-muscle myosin II contractility in a ROCK-dependent manner', *Clinical Cancer Research*, 23(21), pp. 6697–6708. doi: 10.1158/1078-0432.CCR-16-0667.
- Krug, S. M. *et al.* (2012) 'Charge-selective claudin channels', *Annals of The New York Academy of Sciences*, 1257(1), pp. 20–28. doi: 10.1111/j.1749-6632.2012.06555.x.
- Krug, S. M. *et al.* (2014) 'Tight junction, selective permeability, and related diseases', *Seminars in Cell and Developmental Biology*, 36, pp. 166–176. doi: 10.1016/j.semcdb.2014.09.002.
- Lacal, P. M. *et al.* (2018) 'Therapeutic implication of vascular endothelial growth factor receptor-1 (VEGFR-1) targeting in cancer cells and tumor microenvironment by competitive and non-competitive inhibitors', *Pharmacological Research*, 136, pp. 97–107. doi: 10.1016/j.phrs.2018.08.023.
- Langer, G. *et al.* (1999) 'Secretory peptides TFF1 and TFF3 synthesized in human conjunctival goblet cells', *Investigative Ophthalmology & Visual Science*, 40(10), pp. 2220–2224.
- Lapointe, T. K. *et al.* (2011) 'Interleukin-18 facilitates neutrophil transmigration via myosin light chain kinase-dependent disruption of occludin, without altering epithelial permeability', *The American Journal of Physiology: Gastrointestinal and Liver Physiology*, 4(302), pp. 343–351. doi: 10.1152/ajpgi.00202.2011.
- Lara, P. N. *et al.* (2009) 'Phase III trial of irinotecan/cisplatin compared with etoposide/cisplatin in extensive-stage small-cell lung cancer: clinical and pharmacogenomic results from SWOG S0124', *Journal of Clinical Oncology*, 27(15), pp. 2530–2535. doi: 10.1200/JCO.2008.20.1061.
- Latorre, R. *et al.* (2016) 'Enteroendocrine cells: a review of their role in brain-gut communications', *Neurogastroenterology and Motility*, 28(5), pp. 620–630. doi: 10.1111/nmo.12754.
- Lea, T (2015) *The impact of food bioactives on health: in vitro and ex vivo models*. 1st edn. Edited by K. Verhoeckx *et al.* Springer, Cham., pp 1-341. doi: 10.1007/978-3-319-16104-4_26.
- Lee, A. M. *et al.* (2014) 'DPYD variants as predictors of 5-fluorouracil toxicity in adjuvant colon cancer treatment', *Journal of the National Cancer Institute*, 106(12). doi: 10.1093/jnci/dju298.
- Lee, M. *et al.* (2005) 'Scaffold fabrication by indirect three-dimensional printing', *Biomaterials*, 26(20), pp. 4281–4289. doi: 10.1016/j.biomaterials.2004.10.040.
- Leffler, D. A. *et al.* (2015) 'Larazotide acetate for persistent symptoms of celiac disease despite a gluten-free diet: A randomized controlled trial', *Gastroenterology*, 148(7), pp. 1311–1319.e6. doi: 10.1053/j.gastro.2015.02.008.
- Lekes, D. *et al.* (2016) 'Nilotinib induces ER stress and cell death in H9c2 cells', *Physiology*

Research, 65(Suppl 4), pp. S505–S514.

Lemos, C. *et al.* (2011) 'Impact of ABCG2 polymorphisms on the clinical outcome and toxicity of gefitinib in non-small-cell lung cancer patients', *Pharmacogenomics*, 12(2), pp. 159–170. doi: 10.2217/pgs.10.172.

Leslie, J. L. *et al.* (2015) 'Persistence and toxin production by *Clostridium difficile* within human intestinal organoids result in disruption of epithelial paracellular barrier function', *Infection and Immunity*, 83(1), pp. 138–145. doi: 10.1128/IAI.02561-14.

Levy, D. E. *et al.* (1998) 'Matrix metalloproteinase inhibitors: a structure-activity study', *Journal of Medicinal Chemistry*, 41(2), pp. 199–223. doi: 10.1021/jm970494j.

Li, G. Z. *et al.* (2019) 'Targeted therapy and personalized medicine in gastrointestinal stromal tumors: drug resistance, mechanisms, and treatment strategies', *Oncotargets and Therapy*, 12(1), pp. 5123–5133. doi: 10.2147/ott.s180763.

Li, N. *et al.* (2013) 'Development of an improved three-dimensional *in vitro* intestinal mucosa model for drug absorption evaluation', *Tissue Engineering Part C: Methods*, 19(9), pp. 708–719. doi: 10.1089/ten.tec.2012.0463.

Li, S. (2008) 'Src-family kinases in the development and therapy of Philadelphia chromosome-positive chronic myeloid leukemia and acute lymphoblastic leukemia', *Leukemia and Lymphoma*, 49(1), pp. 19–26. doi: 10.1080/10428190701713689.

Liang, G. H. *et al.* (2014) 'Molecular aspects of tight junction barrier function', *Current Opinion in Pharmacology*, 19(1), pp. 84–89. doi: 10.1016/j.coph.2014.07.017.

Lifschitz, C. H. *et al.* (1989) 'Low-dose methotrexate-induced changes in intestinal permeability determined by polyethylene glycol polymers', *Journal of Pediatric Gastroenterology and Nutrition*, 9(3), pp. 301–306. doi: 10.1097/00005176-198910000-00007.

Lima-Júnior, R. C. P. *et al.* (2014) 'Targeted inhibition of IL-18 attenuates irinotecan-induced intestinal mucositis in mice', *British Journal of Pharmacology*, 171(9), pp. 2335–2350. doi: 10.1111/bph.12584.

Lin, Yu-chin *et al.* (2013) 'Metformin sensitizes anticancer effect of dasatinib in head and neck squamous cell carcinoma cells through AMPK-dependent ER stress', *Oncotarget*, 5(1), pp. 298–308.

Liu, J. *et al.* (2012) 'Functional Cftr in crypt epithelium of organotypic enteroid cultures from murine small intestine', *American Journal of Physiology: Cell Physiology*, 302(10), pp. C1492–C1503. doi: 10.1152/ajpcell.00392.2011.

Liu, Y. F. *et al.* (2015) 'Autism and intellectual disability-associated KIRREL3 interacts with neuronal proteins MAP1B and MYO16 with potential roles in neurodevelopment', *PLoS ONE*, 10(4), p. e0123106. doi: 10.1371/journal.pone.0123106.

Logan, R. M. (2008) 'Characterisation of mucosal changes in the alimentary tract following administration of irinotecan: implications for the pathobiology of mucositis', *Cancer Chemotherapy and Pharmacology*, 62(1), pp. 33–41. doi: 10.1007/s00280-007-0570-0.

Logan, R. M. *et al.* (2008) 'Serum levels of NFkappaB and pro-inflammatory cytokines following administration of mucotoxic drugs', *Cancer Biology & Therapy*, 7(7), pp. 1139–45.

doi: 10.4161/cbt.7.7.6207.

Logan, R. M. *et al.* (2009) 'Is the pathobiology of chemotherapy-induced alimentary tract mucositis influenced by the type of mucotoxic drug administered?', *Cancer Chemotherapy and Pharmacology*, 63(2), pp. 239–251. doi: 10.1007/s00280-008-0732-8.

Lopes, G. L. *et al.* (2015) 'Identifying activating mutations in the *EGFR* gene: prognostic and therapeutic implications in non-small cell lung cancer', *Jornal Brasileiro de Pneumologia*, 41(2), pp. 365–375. doi: 10.1111/anae.12918.

López-Posadas, R. *et al.* (2017) 'Interplay of GTPases and cytoskeleton in cellular barrier defects during gut inflammation', *Frontiers in Immunology*, 8, p. 1240. doi: 10.3389/fimmu.2017.01240.

Lu, W. *et al.* (2017) 'Crypt organoid culture as an in vitro model in drug metabolism and cytotoxicity studies', *Drug Metabolism and Disposition*, 45(7), pp. 748–754. doi: 10.1124/dmd.117.075945.

Lugo-Martinez, V.-H. *et al.* (2009) 'Epidermal growth factor receptor is involved in enterocyte anoikis through the dismantling of E-cadherin-mediated junctions', *American Journal of Physiology: Gastrointestinal and Liver Physiology*, 296(2), pp. 235–244. doi: 10.1152/ajpgi.90313.2008.

Ma, T. Y. *et al.* (2000) 'Cytochalasin B modulation of Caco-2 tight junction barrier: role of myosin light chain kinase.', *American Journal of Physiology: Gastrointestinal and Liver Physiology*, 279(5), pp. G875-85. doi: 10.1152/ajpgi.2000.279.5.G875.

Ma, T. Y. *et al.* (2004) 'TNF- α -induced increase in intestinal epithelial tight junction permeability requires NF- κ B activation', *American Journal of Physiology: Gastrointestinal and Liver Physiology*, 286(3), pp. G367–G376. doi: 10.1152/ajpgi.00173.2003.

Ma, T. Y. *et al.* (2005) 'Mechanism of TNF- α modulation of Caco-2 intestinal epithelial tight junction barrier: role of myosin light-chain kinase protein expression', *American Journal of Physiology: Gastrointestinal and Liver Physiology*, 288(3), pp. G422-30. doi: 10.1152/ajpgi.00412.2004.

Ma, Y. *et al.* (2013) 'Focal adhesion kinase regulates intestinal epithelial barrier function via redistribution of tight junction.', *Biochimica et Biophysica Acta*, 1832(1), pp. 151–159. doi: 10.1016/j.bbadis.2012.10.006.

Maeda, T. *et al.* (2010) 'Oxidative stress and enhanced paracellular permeability in the small intestine of methotrexate-treated rats', *Cancer Chemotherapy and Pharmacology*, 65(6), pp. 1117–1123. doi: 10.1007/s00280-009-1119-1.

Maioli, T. U. *et al.* (2014) 'Pretreatment with *Saccharomyces boulardii* does not prevent the experimental mucositis in Swiss mice', *Journal of Negative Results in Biomedicine*, 13(6), pp. 1–8. doi: 10.1186/1477-5751-13-6.

Mäki-Nevala, S. *et al.* (2013) 'Mutated ephrin receptor genes in non-small cell lung carcinoma and their occurrence with driver mutations-targeted resequencing study on formalin-fixed, paraffin-embedded tumor material of 81 patient', *Genes Chromosomes Cancer*, 52(12), pp. 1141–1149. doi: 10.1002/gcc.

Malagola, M. *et al.* (2016) 'Tyrosine kinase inhibitors in Ph+ acute lymphoblastic leukaemia: facts and perspectives', *Annals of Hematology*, 95(5), pp. 681–693. doi: 10.1007/s00277-016-

2617-y.

Manceau, H. *et al.* (2017) 'Fecal calprotectin in inflammatory bowel diseases: update and perspectives', *Clinical Chemistry and Laboratory Medicine*, 55(4), pp. 474–483. doi: 10.1515/cclm-2016-0522.

Manousou, P. *et al.* (2010) 'Increased expression of chemokine receptor CCR3 and its ligands in ulcerative colitis: the role of colonic epithelial cells in in vitro studies', *Clinical and Experimental Immunology*, 162(2), pp. 337–347. doi: 10.1111/j.1365-2249.2010.04248.x.

Mao, Y. *et al.* (1996) 'The effects of *Lactobacillus* strains and oat fiber on methotrexate-induced enterocolitis in rats', *Gastroenterology*, 111(2), pp. 334–344. doi: 10.1053/gast.1996.v111.pm8690198.

Markland, A. D. *et al.* (2015) 'Loperamide versus psyllium fiber for treatment of fecal incontinence: the fecal incontinence prescription (Rx) management (FIRM) randomized clinical trial', *Diseases of the Colon and Rectum*, 58(10), pp. 983–993. doi: 10.1097/DCR.0000000000000442.

Marks, L. *et al.* (2013) 'An evaluation of the non-invasive faecal pellet assessment method as an early drug discovery screen for gastrointestinal liability', *Journal of Pharmacological and Toxicological Methods*, 68(1), pp. 123–136. doi: 10.1016/j.vascn.2013.03.006.

Martín-Venegas, R. *et al.* (2013) 'The methionine precursor DL-2-hydroxy-(4-methylthio) butanoic acid protects intestinal epithelial barrier function', *Food Chemistry*, 141(3), pp. 1702–1709. doi: 10.1016/j.foodchem.2013.04.081.

Matos, J. E. *et al.* (2007) 'Role of cholinergic-activated KCa1.1 (BK), KCa3.1 (SK4) and KV7.1 (KCNQ1) channels in mouse colonic Cl⁻ secretion', *Acta Physiologica*, 189(3), pp. 251–258. doi: 10.1111/j.1748-1716.2006.01646.x.

Mawe, G. M. *et al.* (2013) 'Serotonin signalling in the gut—functions, dysfunctions and therapeutic targets.', *Nature Reviews. Gastroenterology & Hepatology*, 10(8), pp. 473–486. doi: 10.1038/nrgastro.2013.105.

McCole, D. F. *et al.* (2005) 'Epidermal growth factor partially restores colonic ion transport responses in mouse models of chronic colitis.', *Gastroenterology*, 129(2), pp. 591–608. doi: 10.1016/j.gastro.2005.06.004.

McCole, D. F. *et al.* (2007) 'Consequences of direct versus indirect activation of epidermal growth factor receptor in intestinal epithelial cells are dictated by protein-tyrosine phosphatase 1B', *Journal of Biological Chemistry*, 282(18), pp. 13303–13315. doi: 10.1074/jbc.M700424200.

McCormack, P. L. *et al.* (2011) 'Dasatinib: a review of its use in the treatment of chronic myeloid leukaemia and Philadelphia chromosome-positive acute lymphoblastic leukaemia', *Drugs*, 71(13), pp. 1771–1795. doi: 10.2165/11206790-000000000-00000.

McCracken, K. W. *et al.* (2014) 'Modelling human development and disease in pluripotent stem-cell-derived gastric organoids', *Nature*, 516(7531), pp. 400–404. doi: 10.1038/nature13863.

McGovern, D. P. B. *et al.* (2010) 'Genome-wide association identifies multiple ulcerative colitis susceptibility loci', *Nature Genetics*, 11(1), pp. 28–29. doi: 10.1038/ng.549.

- McQuade, R. M. *et al.* (2016) 'Chemotherapy-induced constipation and diarrhea: Pathophysiology, current and emerging treatments', *Frontiers in Pharmacology*, 7, p. 414. doi: 10.3389/fphar.2016.00414.
- Melichar, B., Dvořák, J., *et al.* (2010) 'Intestinal permeability, vitamin A absorption and serum alpha-tocopherol during therapy with gefitinib', *Scandinavian Journal of Clinical and Laboratory Investigations*, 70(3), pp. 180–187. doi: 10.3109/00365511003653581.
- Melichar, B., Kasparova, M., *et al.* (2010) 'Intestinal permeability, vitamin A absorption and serum alpha-tocopherol in gastrointestinal stromal tumor patients treated with imatinib', *Journal of Nutritional Science and Vitaminology*, 56(6), pp. 347–352.
- Melo, M. L. P. *et al.* (2008) 'Role of cytokines (TNF- α , IL-1 β and KC) in the pathogenesis of CPT-11-induced intestinal mucositis in mice: effect of pentoxifylline and thalidomide', *Cancer Chemother Pharmacol*, 61(5), pp. 775–784. doi: 10.1007/s00280-007-0534-4.
- Mendoza, M. C. *et al.* (2011) 'The Ras-ERK and PI3K-mTOR pathways: cross-talk and compensation', *Trends in Biochemical Sciences*, 36(6), pp. 320–328. doi: 10.1016/j.tibs.2011.03.006.The.
- Meng, Y. *et al.* (2016) 'Evaluating intestinal permeability by measuring plasma endotoxin and diamine oxidase in children with acute lymphoblastic leukemia treated with high-dose methotrexate', *Anticancer Agent in Medicinal Chemistry*, 16(3), pp. 387–392.
- van der Merwe, J. Q. *et al.* (2018) 'EGF receptor transactivation and MAP kinase mediate proteinase-activated receptor-2-induced chloride secretion in intestinal epithelial cells', *American Journal of Physiology: Gastrointestinal and Liver Physiology*, 294(2), pp. G441–G451. doi: 10.1152/ajpgi.00303.2007.
- Messersmith, W. A. *et al.* (2004) 'Phase I trial of irinotecan, infusional 5-fluorouracil, and leucovorin (FOLFIRI) with erlotinib (OSI-774): early termination due to increased toxicities', *Clinical Cancer Research*, 10(19), pp. 6522–6527. doi: 10.1158/1078-0432.CCR-04-0746.
- Middendorp, S. *et al.* (2014) 'Adult stem cells in the small intestine are intrinsically programmed with their location-specific function', *Stem Cells*, 32(5), pp. 1083–1091. doi: 10.1002/stem.1655.
- van Midwoud, P. M. *et al.* (2010) 'A microfluidic approach for *in vitro* assessment of interorgan interactions in drug metabolism using intestinal and liver slices', *Lab on a chip*, 10(20), pp. 2778–2786. doi: 10.1039/c0lc00043d.
- Miller, H. *et al.* (2007) 'Intestinal M cells: The fallible sentinels?', *World Journal of Gastroenterology*, 13(10), pp. 1477–1486. doi: 10.3748/wjg.v13.i10.1477.
- Mita, A. *et al.* (2018) 'Correlation of plasma concentration and adverse effects of bosutinib: standard dose or dose-escalation regimens of bosutinib treatment for patients with chronic myeloid leukemia', *Experimental Hematology and Oncology*. BioMed Central, 7(9), pp. 1–8. doi: 10.1186/s40164-018-0101-1.
- Miura, M. *et al.* (2014) 'A limited sampling strategy for estimation of the area under the plasma concentration-time curve of gefitinib', *Therapeutic Drug Monitoring*, 36(1), pp. 24–29. doi: 10.1097/FTD.0b013e31829dabbc.
- Moon, C. *et al.* (2013) 'Development of a primary mouse intestinal epithelial cell monolayer culture system to evaluate factors that modulate IgA transcytosis', *Mucosal Immunology*,

7(4), pp. 818–828. doi: 10.1038/mi.2013.98.

Moon, C. *et al.* (2015) 'Compartmentalized accumulation of cAMP near complexes of multidrug resistance protein 4 (MRP4) and cystic fibrosis transmembrane conductance regulator (CFTR) contributes to drug-induced diarrhea', *Journal of Biological Chemistry*, 290(18), pp. 11246–11257. doi: 10.1074/jbc.M114.605410.

Moran, G. W. *et al.* (2012) 'GLP-2 enhances barrier formation and attenuates TNF α -induced changes in a Caco-2 cell model of the intestinal barrier', *Regulatory Peptides*, 178, pp. 95–101. doi: 10.1016/j.regpep.2012.07.002.

Morote-Garcia, J. C. *et al.* (2012) 'Endothelial Semaphorin 7A promotes neutrophil migration during hypoxia', *Proceedings of the National Academy of Sciences of the United States of America*, 109(35), pp. 14146–14151. doi: 10.1073/pnas.1202165109.

Mowat, A. M. *et al.* (2014) 'Regional specialization within the intestinal immune system', *Nature Reviews Immunology*, 14(10), pp. 667–685. doi: 10.1038/nri3738.

Moy, B. *et al.* (2007) 'Lapatinib-associated toxicity and practical management recommendations', *The Oncologist*, 12(7), pp. 756–765. doi: 10.1634/theoncologist.12-7-756.

Mustjoki, S. *et al.* (2009) 'Clonal expansion of T/NK-cells during tyrosine kinase inhibitor dasatinib therapy', *Leukemia*, 23(8), pp. 1398–1405. doi: 10.1038/leu.2009.46.

Nagafuchi, A. *et al.* (1994) 'The roles of catenins in the cadherin-mediated cell adhesion: functional analysis of E-Cadherin-alpha catenin fusion molecules', *The Journal of Cell Biology*, 127(1), pp. 235–245. doi: 10.1083/jcb.127.1.235.

Nakamura, Y. *et al.* (2010) 'Pharmacokinetics of gefitinib predicts antitumor activity for advanced non-small cell lung cancer', *Journal of Thoracic Oncology*. International Association for the Study of Lung Cancer, 5(9), pp. 1404–1409. doi: 10.1097/JTO.0b013e3181e59a7b.

Nakao, T. *et al.* (2012) 'Irinotecan injures tight junction and causes bacterial translocation in rat', *Journal of Surgical Research*, 173(2), pp. 341–347. doi: 10.1016/j.jss.2010.10.003.

Nakatani, H. *et al.* (2006) 'STI571 (Glivec) induces cell death in the gastrointestinal stromal tumor cell line, GIST-T1, via endoplasmic reticulum stress response', *International Journal of Molecular Medicine*, 71(14), pp. 893–897.

Nariya, M. *et al.* (2009) 'Comparison of enteroprotective efficacy of triphala formulations (Indian herbal drug) on methotrexate-induced small intestinal damage in rats', *Phytotherapy Research*, 23(8), pp. 1092–1098. doi: 10.1002/ptr.

Nighot, P. K. *et al.* (2015) 'Matrix metalloproteinase 9-induced increase in intestinal epithelial tight junction permeability contributes to the severity of experimental DSS colitis', *American Journal of Physiology: Gastrointestinal and Liver Physiology*, 309(12), pp. G988–G997. doi: 10.1152/ajpgi.00256.2015.

Nighot, P. K. *et al.* (2017) 'Chloride channel ClC-2 enhances intestinal epithelial tight junction barrier function via regulation of caveolin-1 and caveolar trafficking of occludin', *Experimental Cell Research*, 352(1), pp. 113–122. doi: 10.1016/j.yexcr.2017.01.024.

Nunbhakdi-Craig, V. *et al.* (2002) 'Protein phosphatase 2A associates with and regulates atypical PKC and the epithelial tight junction complex', *The Journal of Cell Biology*, 158(5), pp.

967–978. doi: 10.1083/jcb.200206114.

Nusrat, A. *et al.* (2000) 'The coiled-coil domain of occludin can act to organize structural and functional elements of the epithelial tight junction*', *The Journal of Biological Chemistry*, 275(38), pp. 29816–29822. doi: 10.1074/jbc.M002450200.

Odenwald, M. A. *et al.* (2017) 'The intestinal epithelial barrier: A therapeutic target?', *Nature Reviews Gastroenterology and Hepatology*. Nature Publishing Group, 14(1), pp. 9–21. doi: 10.1038/nrgastro.2016.169.

Oliver, F. J. *et al.* (1998) 'Importance of poly(ADP-ribose) polymerase and its cleavage in apoptosis', *The Journal of Biological Chemistry*, 273(50), pp. 33533–33539.

Olson, H. *et al.* (2000) 'Concordance of the toxicity of pharmaceuticals in humans and in animals', *Regulatory Toxicology and Pharmacology*, 32(1), pp. 56–67. doi: 10.1006/rtp.2000.1399.

Oshima, T. *et al.* (2008) 'Changes in the expression of claudins in active ulcerative colitis', *Gastroenterology*, 23(Suppl 2), pp. S146-150. doi: 10.1111/j.1440-1746.2008.05405.x.

Papadopoulos, N. *et al.* (2018) 'The PDGF/PDGFR pathway as a drug target', *Molecular Aspects of Medicine*, 62(Aug), pp. 75–88. doi: 10.1016/j.mam.2017.11.007.

Park, H. S. *et al.* (2011) 'Inhibition of matrix metalloproteinase activities and tightening of tight junctions by diallyl disulfide in AGS human gastric carcinoma cells', *Journal of Food Science*, 76(4), pp. T105–T111. doi: 10.1111/j.1750-3841.2011.02114.x.

Parsons, S. J. *et al.* (2004) 'Src family kinases, key regulators of signal transduction', *Oncogene*, 23(48 REV. ISS. 7), pp. 7906–7909. doi: 10.1038/sj.onc.1208160.

Peng, B. *et al.* (2005) 'Clinical pharmacokinetics of imatinib', *Clinical Pharmacokinetics*, 44(9), pp. 879–894. doi: 10.2165/00003088-200544090-00001.

Pérez, C. *et al.* (2010) 'Phospholipase C-mediated inhibition of the M-potassium current by muscarinic-receptor activation in the vestibular primary-afferent neurons of the rat', *Neuroscience Letters*, 468(3), pp. 238–242. doi: 10.1016/j.neulet.2009.11.004.

Peters, M. F. *et al.* (2019) 'Human 3D gastrointestinal microtissue barrier function as a predictor of drug-induced diarrhea', *Toxicological Sciences*, 168(1), pp. 3–17. doi: 10.1093/toxsci/kfy268.

Peters, S. *et al.* (2014) 'Oral epidermal growth factor receptor tyrosine kinase inhibitors for the treatment of non-small cell lung cancer: Comparative pharmacokinetics and drug-drug interactions', *Cancer Treatment Reviews*, 40(8), pp. 917–926. doi: 10.1016/j.ctrv.2014.06.010.

Peterson, L. W. *et al.* (2014) 'Intestinal epithelial cells: regulators of barrier function and immune homeostasis.', *Nature Reviews. Immunology*, 14(3), pp. 141–53. doi: 10.1038/nri3608.

Pfizer (2014) *Investigator's brochure bosutinib (PF-05208763; SKI-606)*, Confidential document obtainable upon request and under agreement.

Poritz, L. S. *et al.* (2011) 'Increase in the tight junction protein claudin-1 in intestinal inflammation', *Digestive Diseases and Sciences*, 56(10), pp. 2802–2809. doi: 10.1007/s10620-

011-1688-9.

Prasad, S. *et al.* (2005) 'Inflammatory processes have differential effects on claudins 2, 3 and 4 in colonic epithelial cells', *Laboratory Investigation*, 85(9), pp. 1139–1162. doi: 10.1038/labinvest.3700316.

Pruim, R. J. *et al.* (2010) 'LocusZoom: regional visualization of genome-wide association scan results', *Bioinformatics*, 26(18), pp. 2336–2337. doi: 10.1093/bioinformatics/btq419.

Purcell, S. *et al.* (2007) 'PLINK: a tool set for whole-genome association and population-based linkage analyses', *The American Journal of Human Genetics*, 81(3), pp. 559–575. doi: 10.1086/519795.

Pusch, J. *et al.* (2011) 'The physiological performance of a three-dimensional model that mimics the microenvironment of the small intestine', *Biomaterials*, 32(30), pp. 7469–7478. doi: 10.1016/j.biomaterials.2011.06.035.

Qiao, Y. *et al.* (2013) '[Impact of CCND1 A870G polymorphism on acute adverse events in postoperative rectal cancer patients treated with adjuvant concurrent chemoradiotherapy].', *Zhonghua Zhong Liu Za Zhi [Chinese Journal of Oncology]*, 35(4), pp. 268–272. doi: 10.3760/cma.j.issn.0253-3766.2013.04.006.

Ramsay, D. B. *et al.* (2010) 'Mast cells in gastrointestinal disease', *Gastroenterology and Hepatology*, 6(12), pp. 772–777.

Rao, R. (2009) 'Occludin phosphorylation in regulation of epithelial tight junctions', *Annals of New York Academy of Sciences*, 1165, pp. 62–68. doi: 10.1111/j.1749-6632.2009.04054.x.

Redfern, W. S. *et al.* (2010) 'Impact and frequency of different toxicities throughout the pharmaceutical life cycle', *The Toxicologist*, 114(S1), p. 1081.

Refaat, B. *et al.* (2015) 'Vitamin D3 enhances the tumouricidal effects of 5-fluorouracil through multipathway mechanisms in azoxymethane rat model of colon cancer', *Journal of Experimental & Clinical Cancer Research*, 34(71), pp. 1–15. doi: 10.1186/s13046-015-0187-9.

Rinninella, E. *et al.* (2019) 'What is the healthy gut microbiota composition? A changing ecosystem across age, environment, diet, and diseases', *Microorganisms*, 7(1), pp. 14–36. doi: 10.3390/microorganisms7010014.

Rix, L. L. R. *et al.* (2009) 'Global target profile of the kinase inhibitor bosutinib in primary chronic myeloid leukemia cells', *Leukemia*, 23(3), pp. 477–485. doi: 10.1038/leu.2008.334.

Rix, U. *et al.* (2007) 'Chemical proteomic profiles of the BCR-ABL inhibitors imatinib, nilotinib, and dasatinib reveal novel kinase and nonkinase targets', *Blood*, 110(12), pp. 4055–4063. doi: 10.1182/blood-2007-07-102061.

Rosmarin, D. *et al.* (2015) 'A candidate gene study of capecitabine-related toxicity in colorectal cancer identifies new toxicity variants at *DPYD* and a putative role for *ENOSF1* rather than *TYMS*', *Gut*, 64(1), pp. 111–120. doi: 10.1136/gutjnl-2013-306571.

Ruan, Y. *et al.* (2016) 'Genetic association of curative and adverse reactions to tyrosine kinase inhibitors in chinese advanced non-small cell lung cancer patients', *Scientific Reports*, 6, p. 23368. doi: 10.1038/srep23368.

Rudin, C. M. *et al.* (2008) 'Pharmacogenomic and pharmacokinetic determinants of erlotinib

- toxicity', *Journal of Clinical Oncology*, 26(7), pp. 1119–1127. doi: 10.1200/JCO.2007.13.1128.
- Rugo, H. S. *et al.* (2019) 'The characterization, management, and future considerations for ErbB-family TKI-associated diarrhea', *Breast Cancer Research and Treatment*, 175(1), pp. 5–15. doi: 10.1007/s10549-018-05102-x.
- Sakai, H. *et al.* (1997) 'Thromboxane A₂, released by the anti-tumour drug irinotecan, is a novel stimulator of Cl⁻ secretion in isolated rat colon', *Journal of Physiology*, 505(1), pp. 133–144. doi: 10.1111/j.1469-7793.1997.133bc.x.
- Sakai, H. *et al.* (2013) '5-Fluorouracil induces diarrhea with changes in the expression of inflammatory cytokines and aquaporins in mouse intestines', *PLoS ONE*, 8(1), pp. 1–10. doi: 10.1371/journal.pone.0054788.
- Samak, G. *et al.* (2014) 'Cyclic stretch disrupts apical junctional complexes in Caco-2 cell monolayers by a JNK-2-, c-Src-, and MLCK-dependent mechanism', *American Journal of Physiology: Gastrointestinal and Liver Physiology*, 306(11), pp. 947–958. doi: 10.1152/ajpgi.00396.2013.
- Samak, G. *et al.* (2015) 'Calcium/Ask1/MKK7/JNK2/c-Src signalling cascade mediates disruption of intestinal epithelial tight junctions by dextran sulfate sodium', *Biomedical Journal*, 465(3), pp. 503–515. doi: 10.1042/BJ20140450.
- Sambuy, Y. *et al.* (2005) 'The Caco-2 cell line as a model of the intestinal barrier: influence of cell and culture-related factors on Caco-2 cell functional characteristics', *Cell Biology and Toxicology*, 21(1), pp. 1–26. doi: 10.1007/s10565-005-0085-6.
- Sarathy, J. *et al.* (2017) 'The Yin and Yang of bile acid action on tight junctions in a model colonic epithelium', *Physiological Reports*, 5(10), pp. 1–24. doi: 10.14814/phy2.13294.
- Sato, T. *et al.* (2009) 'Single Lgr5 stem cells build crypt-villus structures *in vitro* without a mesenchymal niche.', *Nature*, 459(7244), pp. 262–5. doi: 10.1038/nature07935.
- Sato, T. *et al.* (2011) 'Long-term expansion of epithelial organoids from human colon, adenoma, adenocarcinoma, and Barrett's epithelium', *Gastroenterology*, 141(5), pp. 1762–1772. doi: 10.1053/j.gastro.2011.07.050.
- Satoh, M. *et al.* (1992) 'Role of poly(ADP-ribose) formation in DNA repair', *Nature Letters*, 356(6367), pp. 356–358.
- Sattler, M. *et al.* (2003) 'Mutated tyrosine kinases as therapeutic targets in myeloid leukemias', *Advances in Experimental Medicine and Biology*, 532, pp. 121–140. doi: 10.1007/978-1-4615-0081-0_11.
- Saxena, K. *et al.* (2016) 'Human intestinal enteroids: a new model to study human rotavirus infection, host restriction, and pathophysiology', *Journal of Virology*, 90(1), pp. 43–56. doi: 10.1128/JVI.01930-15.
- Schindelin, J. *et al.* (2012) 'Fiji: an open-source platform for biological-image analysis.', *Nature Methods*, 9(7), pp. 676–682. doi: 10.1038/nmeth.2019.
- Schneider, C. A. *et al.* (2012) 'NIH Image to ImageJ: 25 years of image analysis.', *Nature Methods*, 9(7), pp. 671–675. doi: 10.1038/nmeth.2089.
- Schwake, M. *et al.* (2003) 'A carboxy-terminal domain determines the subunit specificity of

KCNQ K⁺ channel assembly', *EMBO Reports*, 4(1), pp. 76–81. doi: 10.1038/sj.embor.embor715.

Schwank, G. *et al.* (2013) 'Generation of BAC transgenic epithelial organoids', *PLoS One*, 8(10), p. e76871. doi: 10.1371/journal.pone.0076871.

Scott, G. A. *et al.* (2008) 'Semaphorin 7a promotes spreading and dendricity in human melanocytes through β 1-integrins', *Journal of Investigative Dermatology*, 128(1), pp. 151–161. doi: 10.1038/sj.jid.5700974.

Scott, G. A. *et al.* (2009) 'Plexin C1, a receptor for semaphorin 7A, inactivates cofilin and is a potential tumor suppressor for melanoma progression', *Journal of Investigative Dermatology*, 129(4), pp. 954–963. doi: 10.1038/jid.2008.329.

Van Seville, Y. Z. A. *et al.* (2015) 'ErbB small molecule tyrosine kinase inhibitor (TKI) induced diarrhoea: chloride secretion as a mechanistic hypothesis', *Cancer Treatment Reviews*, 41(7), pp. 646–652. doi: 10.1016/j.ctrv.2015.05.011.

Seidler, U. E. (2013) 'Gastrointestinal HCO₃⁻ transport and epithelial protection in the gut: new techniques, transport pathways and regulatory pathways', *Current Opinion in Pharmacology*, 13(6), pp. 900–908. doi: 10.1016/j.coph.2013.10.001.

Seikel, E. *et al.* (2009) 'Convergent modulation of Kv4.2 channel R subunits by structurally distinct DPPX and KChIP auxiliary subunits', *Biochemistry*, 48(24), pp. 5721–5730. doi: 10.1021/bi802316m.

Sener, Y. *et al.* (2019) 'TKI-related platelet dysfunction does not correlate with bleeding in patients with chronic phase-chronic myeloid leukemia with complete hematological response', *Clinical and Applied Thrombosis/Hemostasis*, 25, pp. 1–6. doi: 10.1177/1076029619858409.

Seth, A. *et al.* (2004) 'L-Glutamine ameliorates acetaldehyde-induced increase in paracellular permeability in Caco-2 cell monolayer', *American Journal of Physiology: Gastrointestinal and Liver Physiology*, 287(3), pp. G510–G517. doi: 10.1152/ajpgi.00058.2004.

Seth, A. *et al.* (2007) 'Protein phosphatases 2A and 1 interact with occludin and negatively regulate the assembly of tight junctions in the Caco-2 cell monolayer*', *The Journal of Biological Chemistry*, 282(15), pp. 11487–11498. doi: 10.1074/jbc.M610597200.

Shaul, Y. (2000) 'c-Abl: activation and nuclear targets', *Cell Death and Differentiation*, 7(1), pp. 10–16. doi: 10.1038/sj.cdd.4400626.

Shen, L. *et al.* (2006) 'Myosin light chain phosphorylation regulates barrier function by remodeling tight junction structure', *Journal of Cell Science*, 119(10), pp. 2095–2106. doi: 10.1242/jcs.02915.

Sheth, P. *et al.* (2003) 'Role of phosphatidylinositol 3-kinase in oxidative stress-induced disruption of tight junctions*', *The Journal of Biological Chemistry*, 278(49), pp. 49239–49245. doi: 10.1074/jbc.M305654200.

Shi, Y. *et al.* (2013) 'Icotinib versus gefitinib in previously treated advanced non-small-cell lung cancer (ICOGEN): a randomised, double-blind phase 3 non-inferiority trial', *The Lancet Oncology*, 14(10), pp. 953–961. doi: 10.1016/S1470-2045(13)70355-3.

Shin, D. Y. *et al.* (2013) 'Inhibiting invasion into human bladder carcinoma 5637 cells with

diallyl trisulfide by inhibiting matrix metalloproteinase activities and tightening tight junctions', *International Journal of Molecular Sciences*, 14(10), pp. 19911–19922. doi: 10.3390/ijms141019911.

Shkoda, A. *et al.* (2007) 'Interleukin-10 blocked endoplasmic reticulum stress in intestinal epithelial cells: impact on chronic inflammation', *Gastroenterology*, 132(1), pp. 190–207. doi: 10.1053/j.gastro.2006.10.030.

Silverberg, M. S. *et al.* (2009) 'Ulcerative colitis-risk loci on chromosomes 1p36 and 12q15 found by genome-wide association study', *Nature Genetics*, 41(2), pp. 216–220. doi: 10.1038/ng.275.

Sims, J. T. *et al.* (2009) 'MTT assays cannot be utilized to study the effects of STI571/Gleevec on the viability of solid tumor cell lines', *Cancer Chemotherapy and Pharmacology*, 64(3), pp. 629–633. doi: 10.1007/s00280-009-1004-y.

Skouta, R. *et al.* (2014) 'Ferrostatins inhibit oxidative lipid damage and cell death in diverse disease models', *Journal of the American Chemical Society*, 136(12), pp. 4551–4556. doi: 10.1021/ja411006a.

Soares, P. M. G. *et al.* (2008) 'Gastrointestinal dysmotility in 5-fluorouracil-induced intestinal mucositis outlasts inflammatory process resolution', *Cancer Chemotherapy and Pharmacology*, 63(1), pp. 91–98. doi: 10.1007/s00280-008-0715-9.

Soares, P. M. G. *et al.* (2013) 'Inflammatory intestinal damage induced by 5-fluorouracil requires IL-4', *Cytokine*, 61(1), pp. 46–49. doi: 10.1016/j.cyto.2012.10.003.

Sodeoka, M. *et al.* (2010) 'Development of selective inhibitors of necrosis', *The Chemical Record*, 10(5), pp. 308–314. doi: 10.1002/tcr.201000031.

Soh, H. *et al.* (2008) 'ISA channel complexes include four subunits each of DPP6 and Kv4.2', *Journal of Biological Chemistry*, 283(22), pp. 15072–15077. doi: 10.1074/jbc.M706964200.

Soletti, R. C. *et al.* (2013) 'Immunohistochemical analysis of retinoblastoma and β -catenin as an assistant tool in the differential diagnosis between Crohn's disease and ulcerative colitis', *PloS One*, 8(8), p. e70786. doi: 10.1371/journal.pone.0070786.

Song, D. *et al.* (2006) 'Confirmation and prevention of intestinal barrier dysfunction and bacterial translocation caused by methotrexate', *Digestive Diseases and Sciences*, 51(9), pp. 1549–1556. doi: 10.1007/s10620-005-9058-0.

Song, M. *et al.* (2013) '5-fluorouracil-induced changes of intestinal integrity biomarkers in BALB/C mice', *Journal of Cancer Prevention*, 18(4), pp. 322–329.

Sonis, S. T. *et al.* (2004) 'Perspectives on cancer therapy-induced mucosal injury: pathogenesis, measurement, epidemiology, and consequences for patients.', *Cancer*, 100(9 Suppl), pp. 1995–2025. doi: 10.1002/cncr.20162.

Southcott, E. *et al.* (2008) 'Yoghurts containing probiotics reduce disruption of the small intestinal barrier in methotrexate-treated rats', *Digestive Diseases and Sciences*, 53(7), pp. 1837–1841. doi: 10.1007/s10620-008-0275-1.

Spence, J. R. *et al.* (2011) 'Directed differentiation of human pluripotent stem cells into intestinal tissue *in vitro*', *Nature*, 470(7332), pp. 105–109. doi: 10.1038/nature09691.

- Spencer, N. J. *et al.* (2016) 'Insights into the mechanisms underlying colonic motor patterns', *Journal of Physiology*, 594(15), pp. 1–37. doi: 10.1113/JP271919.
- Spiering, D. *et al.* (2011) 'Dynamics of the Rho-family small GTPases in actin regulation and motility', *Cell Adhesion & Migration*, 5(2), pp. 170–180. doi: 10.4161/cam.5.2.14403.
- Staquicini, F. I. *et al.* (2015) 'Receptor tyrosine kinase EphA5 is a functional molecular target in human lung cancer', *Journal of Biological Chemistry*, 290(12), pp. 7345–7359. doi: 10.1074/jbc.M114.630525.
- Stevenson, B. *et al.* (1986) 'Identification of ZO-1: a high molecular weight polypeptide associated with the tight junction (zonula occludens) in a variety of epithelia', *The Journal of Cell Biology*, 103(3), pp. 755–766.
- Strik, M. C. M. *et al.* (2004) 'Intracellular serpin SERPINB6 (PI6) is abundantly expressed by human mast cells and forms complexes with β -tryptase monomers', *Blood*, 103(7), pp. 2710–2717. doi: 10.1182/blood-2003-08-2981.
- Stringer, A. M. *et al.* (2007) 'Chemotherapy-induced diarrhea is associated with changes in the luminal environment in the DA rat.', *Experimental Biology and Medicine*, 232(1), pp. 96–106.
- Stringer, A. M. *et al.* (2009) 'Gastrointestinal microflora and mucins may play a critical role in the development of 5-fluorouracil-induced gastrointestinal mucositis', *Experimental Biology and Medicine*, 234(4), pp. 430–441. doi: 10.3181/0810-RM-301.
- Stringer, A. M. *et al.* (2013) 'Biomarkers of chemotherapy-induced diarrhoea: a clinical study of intestinal microbiome alterations, inflammation and circulating matrix metalloproteinases', *Supportive Care in Cancer*, 21(7), pp. 1843–1852. doi: 10.1007/s00520-013-1741-7.
- Strop, P. *et al.* (2004) 'Structure of a human A-type potassium channel interacting protein DPPX, a member of the dipeptidyl aminopeptidase family', *Journal of Molecular Biology*, 343(3), pp. 1055–1065. doi: 10.1016/j.jmb.2004.09.003.
- Sultani, M. *et al.* (2012) 'Anti-inflammatory cytokines: important immunoregulatory factors contributing to chemotherapy-induced gastrointestinal mucositis', *Chemotherapy Research and Practice*, 2012, pp. 1–11. doi: 10.1155/2012/490804.
- Sun, S. Y. (2010) 'N-acetylcysteine, reactive oxygen species and beyond', *Cancer Biology & Therapy*, 9(2), pp. 109–110. doi: 10.4161/cbt.9.2.10583.
- Sung, J. H. *et al.* (2011) 'Microscale 3-D hydrogel scaffold for biomimetic gastrointestinal (GI) tract model', *Lab Chip*, 11(3), pp. 389–392. doi: 10.1039/C0LC00273A.
- Suzuki, T. *et al.* (2011) 'Interleukin-6 (IL-6) regulates claudin-2 expression and tight junction permeability in intestinal epithelium', *The Journal of Biological Chemistry*, 286(36), pp. 31263–31271. doi: 10.1074/jbc.M111.238147.
- Takahashi, H. *et al.* (2014) 'Application of a combination of a knowledge-based algorithm and 2-stage screening to hypothesis-free genomic data on irinotecan-treated patients for identification of a candidate single nucleotide polymorphism related to an adverse effect', *PLoS ONE*, 9(8), p. e105160. doi: 10.1371/journal.pone.0105160.
- Takayanagi, S. *et al.* (2013) 'Gene regulatory network of unfolded protein response genes in

endoplasmic reticulum stress', *Cell Stress and Chaperones*, 18(1), pp. 11–23. doi: 10.1007/s12192-012-0351-5.

Takeichi, M. (1977) 'Functional correlation between cell adhesive properties and some cell surface proteins', *Journal of Cell Biology*, 75(2 Pt 1), pp. 464–474. doi: 10.1083/jcb.75.2.464.

Tamagnone, L. *et al.* (1999) 'Plexins are a large family of receptors for transmembrane, secreted, and GPI-anchored semaphorins in vertebrates', *Cell*, 99(1), pp. 71–80. doi: 10.1016/s0092-8674(00)80063-x.

Tamaki, C. *et al.* (2013) 'Potentials and limitations of nonclinical safety assessment for predicting clinical adverse drug reactions: correlation analysis of 142 approved drugs in Japan', *Journal of Toxicological Sciences*, 38(4), pp. 581–598. doi: 10.2131/jts.38.581.

Tang, W. *et al.* (2004) 'Development of a colorimetric method for functional chloride channel assay', *Journal of Biomolecular Screening*, 9(7), pp. 607–613. doi: 10.1177/1087057104266740.

Tantawy, A. A. G. *et al.* (2010) 'Methylene tetrahydrofolate reductase gene polymorphism in Egyptian children with acute lymphoblastic leukemia', *Blood Coagulation and Fibrinolysis*, 21(1), pp. 28–34. doi: 10.1097/MBC.0b013e32833135e9.

Tao, L. *et al.* (2015) 'Weichang'an and 5-fluorouracil suppresses colorectal cancer in a mouse model', *World Journal of Gastroenterology*, 21(4), pp. 1125–1139. doi: 10.3748/wjg.v21.i4.1125.

Teft, W. A. *et al.* (2015) 'OATP1B1 and tumour OATP1B3 modulate exposure, toxicity, and survival after irinotecan-based chemotherapy', *British Journal of Cancer*, 112(5), pp. 857–865. doi: 10.1038/bjc.2015.5.

Thiagarajah, J. R. *et al.* (2015) 'Secretory diarrhoea: mechanisms and emerging therapies', *Nature Reviews Gastroenterology and Hepatology*, 12(8), pp. 446–457. doi: 10.1038/nrgastro.2015.111.

Thompson, L. M. (2019) *Modelling barrier function of the villous and follicle-associated epithelium in 3D*.

Thompson, S. L. *et al.* (2008) 'Examining the link between chromosomal instability and aneuploidy in human cells', *Journal of Cell Biology*, 180(4), pp. 665–672. doi: 10.1083/jcb.200712029.

Tomita, M. *et al.* (2002) 'Clarification of the mechanism of structural change induced by reoxygenation following the induction of lipid peroxidation in Caco-2 cell monolayers', *Drug Metabolism and Pharmacokinetics*, 17(1), pp. 83–91. doi: 10.2133/dmpk.17.83.

Tong, J. *et al.* (2014) 'Y-27632 inhibits ethanol-induced increase in intestinal epithelial barrier permeability', *Molecular Medicine Reports*, 9(6), pp. 2357–2361. doi: 10.3892/mmr.2014.2060.

Touchefeu, Y. *et al.* (2014) 'Systematic review: the role of the gut microbiota in chemotherapy- or radiation-induced gastrointestinal mucositis - current evidence and potential clinical applications', *Alimentary Pharmacology and Therapeutics*, 40(5), pp. 409–421. doi: 10.1111/apt.12878.

Traweger, A. *et al.* (2002) 'The tight junction-specific protein occludin is a functional target

of the E3 ubiquitin-protein ligase Itch *', *The Journal of Biological Chemistry*, 277(12), pp. 10201–10208. doi: 10.1074/jbc.M111384200.

Trivedi, P. P. *et al.* (2013) 'Role of α -lipoic acid in dextran sulfate sodium-induced ulcerative colitis in mice: studies on inflammation, oxidative stress, DNA damage and fibrosis', *Food and Chemical Toxicology*, 59, pp. 339–355. doi: 10.1016/j.fct.2013.06.019.

Trynka, G. *et al.* (2011) 'Dense genotyping identifies and localizes multiple common and rare variant association signals in celiac disease', *Nature Genetics*, 43(12), pp. 1193–1201. doi: 10.1038/ng.998.

Ueda, T. *et al.* (2010) 'Generation of functional gut-like organ from mouse induced pluripotent stem cells', *Biochemical and Biophysical Research Communications*, 391(1), pp. 38–42. doi: 10.1016/j.bbrc.2009.10.157.

Uhlen, M. *et al.* (2015) 'Tissue-based map of the human proteome', *Science*, 347(6220), pp. 1260419–1260419. doi: 10.1126/science.1260419.

Uitdehaag, J. C. M. *et al.* (2014) 'Comparison of the cancer gene targeting and biochemical selectivities of all targeted kinase inhibitors approved for clinical use.', *PloS one*, 9(3), p. e92146. doi: 10.1371/journal.pone.0092146.

Umerez, M. *et al.* (2018) 'Involvement of miRNA polymorphisms in hepatotoxicity development in childhood acute lymphoblastic leukemia', *Pharmacogenomics*, 19(18), pp. 1403–1412. doi: 10.2217/pgs-2018-0113.

Uribe, J. *et al.* (1996) 'Epidermal growth factor inhibits Ca²⁺-dependent transport in T84 human colonic epithelial cells', *American Journal of Physiology: Cell Physiology*, 271(3), p. 84.

Uribe, J. M. *et al.* (2002) 'Interferon- γ activates EGF receptor and increases TGF- α in T84 cells: implications for chloride secretion.', *American Journal of Physiology: Gastrointestinal and Liver Physiology*, 283(4), pp. G923-31. doi: 10.1152/ajpgi.00237.2002.

Utech, M. *et al.* (2005) 'Mechanism of IFN- γ -induced endocytosis of tight junction proteins: myosin II-dependent vacuolarization of the apical plasma membrane', *Molecular Biology of the Cell*, 16(October), pp. 5040–5052. doi: 10.1091/mbc.E05.

Vaessen, S. F. C. *et al.* (2017) 'Regional expression levels of drug transporters and metabolizing enzymes along the pig and human intestinal tract and comparison with Caco-2 cells', *Drug Metabolism and Disposition*, 45(4), pp. 353–360.

Vandenbroucke, R. E. *et al.* (2014) 'Pro-inflammatory effects of matrix metalloproteinase 7 in acute inflammation', *Mucosal Immunology*, 7(3), pp. 579–588. doi: 10.1038/mi.2013.76.

Vázquez, M. *et al.* (2013) 'Intestinal transport of methylmercury and inorganic mercury in various models of Caco-2 and HT29-MTX cells.', *Toxicology*, 311(3), pp. 147–53. doi: 10.1016/j.tox.2013.06.002.


Vermeer, P. D. *et al.* (2006) 'MMP9 modulates tight junction integrity and cell viability in human airway epithelia', *The American Journal of Physiology: Lung Cellular and Molecular Physiology*, 269(5), pp. 751–762. doi: 10.1152/ajplung.90578.2008.

Vierbuchen, T. *et al.* (2010) 'Direct conversion of fibroblasts to functional neurons by defined factors', *Nature*, 463(7284), pp. 1035–1041. doi: 10.1038/nature08797.

- Wang, H. *et al.* (2015) 'Factors derived from Escherichia coli nissle 1917, grown in different growth media, enhance cell death in a model of 5-fluorouracil-induced Caco-2 intestinal epithelial cell damage', *Nutrition and Cancer*, 67(2), pp. 316–326. doi: 10.1080/01635581.2015.990570.
- Wang, L. *et al.* (2009) 'Influence of micro-well biomimetic topography on intestinal epithelial Caco-2 cell phenotype', *Biomaterials*, 30(36), pp. 6825–6834. doi: 10.1016/j.biomaterials.2009.08.046.
- Wang, X. *et al.* (2013) 'Differential effects of dosing regimen on the safety and efficacy of dasatinib: retrospective exposure-response analysis of a phase III study.', *Clinical Pharmacology: Advances and Applications*, 5, pp. 85–97. doi: 10.2147/CPAA.S42796.
- Wang, Y. *et al.* (2017) 'A microengineered collagen scaffold for generating a polarized crypt-villus architecture of human small intestinal epithelium', *Biomaterials*, 128, pp. 44–55. doi: 10.1016/j.biomaterials.2017.03.005.
- Wardill, H. R. *et al.* (2013) 'Chemotherapy-induced mucosal barrier dysfunction', *Current Opinion in Supportive and Palliative Care*, 7(2), pp. 155–161. doi: 10.1097/SPC.0b013e32835f3e8c.
- Watson, C. J. *et al.* (2001) 'Functional modeling of tight junctions in intestinal cell monolayers using polyethylene glycol oligomers', *American Journal of Physiology: Cell Physiology*, 281(2), pp. 388–397. doi: 10.1152/ajpcell.2001.281.2.C388.
- Wilcz-Villega, E. *et al.* (2014) 'Reduced E-cadherin expression is associated with abdominal pain and symptom duration in a study of alternating and diarrhea predominant IBS', *Neurogastroenterology & Motility*, 26(3), pp. 316–325. doi: 10.1111/nmo.12262.
- Winer, A. *et al.* (2018) 'Matrix metalloproteinase inhibitors in cancer therapy: turning past failures into future successes', *Molecular Cancer Therapeutics*, 17(6), pp. 1147–1155. doi: 10.1158/1535-7163.mct-17-0646.
- Wood, M. B. *et al.* (2016) 'TNF- α augments RANKL-dependent intestinal M cell differentiation in enteroid cultures', *Regulation of Cell Signaling Pathways*, 311(3), pp. 498–507. doi: 10.1152/ajpcell.00108.2016.
- Wright, E. M. *et al.* (2011) 'Biology of human sodium glucose transporters', *Physiological Reviews*, 91(2), pp. 733–794. doi: 10.1152/physrev.00055.2009.
- Wu, Y. T. *et al.* (2010) 'Dual role of 3-methyladenine in modulation of autophagy via different temporal patterns of inhibition on class I and III phosphoinositide 3-kinase', *The Journal of Biological Chemistry*, 285(14), pp. 10850–10861. doi: 10.1074/jbc.M109.080796.
- Yamada, T. *et al.* (2002) 'In vitro functional gut-like organ formation from mouse embryonic stem cells', *Stem Cells*, 20(1), pp. 41–49. doi: 10.1634/stemcells.20-1-41.
- Yang, Q. *et al.* (2018) 'Blockage of endoplasmic reticulum stress attenuates nilotinib-induced cardiotoxicity by inhibition of the Akt-GSK3 β -Nox4 signaling', *European Journal of Pharmacology*, 822(37), pp. 85–94. doi: 10.1016/j.ejphar.2018.01.011.
- Yasuda, M. *et al.* (2013) '5-HT3 receptor antagonists ameliorate 5-fluorouracil-induced intestinal mucositis by suppression of apoptosis in murine intestinal crypt cells', *British Journal of Pharmacology*, 168(6), pp. 1388–1400. doi: 10.1111/bph.12019.

- Youmba, S. B. *et al.* (2012) 'Methotrexate modulates tight junctions through NF- κ B, MEK, and JNK pathways', *Gastroenterology*, 54(4), pp. 463–470. doi: 10.1097/MPG.0b013e318247240d.
- Yu, D. *et al.* (2008) 'Stimulus-induced reorganization of tight junction structure: the role of membrane traffic', *Biochimica et Biophysica Acta: Biomembranes*, 1778(3), pp. 709–716. doi: 10.1016/j.bbamem.2007.07.027.
- Yu, J. *et al.* (2012) 'In vitro 3D human small intestinal villous model for drug permeability determination', *Biotechnology and Bioengineering*, 109(9), pp. 2173–2178. doi: 10.1002/bit.24518.
- Yu, J. *et al.* (2014) 'Three dimensional human small intestine models for ADME-Tox studies', *Drug Discovery Today*, 19(10), pp. 1587–1594. doi: 10.1016/j.drudis.2014.05.003.
- Zachos, N. C. *et al.* (2016) 'Human enteroids/colonoids and intestinal organoids functionally recapitulate normal intestinal physiology and pathophysiology', *Journal of Biological Chemistry*, 291(8), pp. 3759–3766. doi: 10.1074/jbc.R114.635995.
- Zandy, N. L. *et al.* (2007) 'Abl tyrosine kinases regulate cell-cell adhesion through Rho GTPases', *Proceedings of the National Academy of Sciences of the United States of America*, 104(45), pp. 17686–17691. doi: 10.1073/pnas.0703077104.
- Zhang, C. *et al.* (2015) 'Expressions of E-cadherin, p120ctn, β -catenin and NF- κ B in ulcerative colitis', *Journal of Huazhong University of Science and Technology*, 35(3), pp. 368–373. doi: 10.1007/s11596-015-1439-9.
- Zhang, J. *et al.* (2016) 'Protective effect of carboxymethylpachymaran on TNF- α -induced damage in Caco-2 cell monolayers', *International Journal of Biological Macromolecules*, 93(Pt A), pp. 506–511. doi: 10.1016/j.ijbiomac.2016.07.095.
- Zihni, C. *et al.* (2014) 'Signalling at tight junctions during epithelial differentiation and microbial pathogenesis', *Journal of Cell Science*, 127(16), pp. 3401–3413. doi: 10.1242/jcs.145029.
- Zihni, C. *et al.* (2016) 'Tight junctions: from simple barriers to multifunctional molecular gates', *Nature Reviews Molecular Cell Biology*, 17(9), pp. 564–580. doi: 10.1038/nrm.2016.80.
- Zufferey, R. *et al.* (1997) 'Multiply attenuated lentiviral vector achieves efficient gene delivery in vivo', *Nature Biotechnology*, 15(9), pp. 871–875. doi: 10.1038/nbt0997-871.
- Zuo, J. H. *et al.* (2011) 'Activation of EGFR promotes squamous carcinoma SCC10A cell migration and invasion via inducing EMT-like phenotype change and MMP-9-mediated degradation of E-cadherin', *Journal of Cellular Biochemistry*, 112(9), pp. 2508–2517. doi: 10.1002/jcb.23175.

APPENDICES



UNIVERSITY OF LIVERPOOL
Institute of Translational Medicine

Cell Line Authentication Facility

Academic lead: Dr Lakis Liloglou
WH Duncan Building, W. Derby Str, L7 8TX
Tel 0151 7949121 Email: T.Liloglou@liv.ac.uk

Certificate of cell line authenticity

Customer	Andrea Davies (Munir Pirmohamed)
Organisation	ITM/Pharmacology
Tested Cell line	CACO-2
Authentication method	GenePrint® 10, Promega Corporation
Database(s) used for comparison	DSMZ, ATCC
Authentication undertaken by	Pat Gerard
Date	08/08/18


	Alleles		Match
TH01	6	6	✓
D21S11	30	30	✓
D5S818	12	13	✓
D13S317	11,13	14	✓
D7S820	11	12	✓
D16S539	12	13	✓
CSF1PO	11	11	✓
AMEL	x	x	✓
vWA	16	18	✓
TPOX	9	11	✓

Comments (optional):
100% match on both DSMZ and ATCC websites.


Operator

Pat Gerard
Research Technician

Academic Lead



Dr Lakis Liloglou
Senior Lecturer



UNIVERSITY OF LIVERPOOL
Institute of Translational Medicine

Cell Line Authentication Facility

Academic lead: Dr Lakis Liloglou
WH Duncan Building, W. Derby Str, L7 8TX
Tel 0151 7949121 Email: T.Liloglou@liv.ac.uk

Result of STR matching analysis by your data. -- DSMZ Profile Database --

EV	Cell No.	Cell name	Locus names								
			D5S818	D13S317	D7S820	D16S539	vWA	TH01	AM	TPOX	CSF1PO
		Your Cell line	12,13	11,13,14	11,12	12,13	16,18	6,6	X,X	9,11	11,11
1.00038/38)	169	CACO-2	12,13	11,13,14	11,12	12,13	16,18	6,6	X,X	9,11	11,11
1.00038/38)	CRL-2102	C2BBE1 clone of Caco-2 (ATCC HTB-37)	12,13	11,13,14	11,12	12,13	16,18	6,6	X,X	9,11	11,11
1.00038/38)	HTB-37	Caco-2	12,13	11,13,14	11,12	12,13	16,18	6,6	X,X	9,11	11,11
1.00038/38)	RCB0988	CACO-2	12,13	11,13,14	11,12	12,13	16,18	6,6	X,X	9,11	11,11

ATCC

ATCC#	Designation	D5S818	D13S317	D7S820	D16S539	vWA	TH01	AMEL	TPOX	CSF1PO
100.0	HTB-37 Adenocarcinoma/ Human Caco-2/Colon	12,13	11,13,14	11,12	12,13	16,18	6	X	9,11	11
100.0	CRL-2102 Adenocarcinoma/ Human C2BBE1 clone of Caco-2/Colon	12,13	11,13,14	11,12	12,13	16,18	6	X	9,11	11

Figure A.1. Certificate of cell line authenticity for Caco-2 cells. Short tandem repeat profiling was undertaken at the Cell Line Authentication Facility, at the University of Liverpool for Caco-2 cells to verify cell line authenticity.

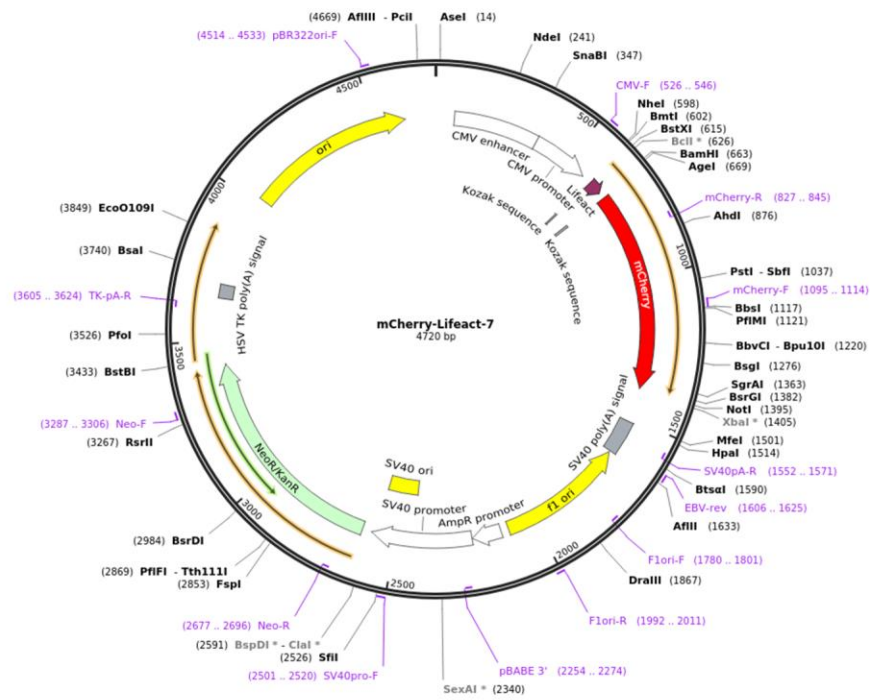
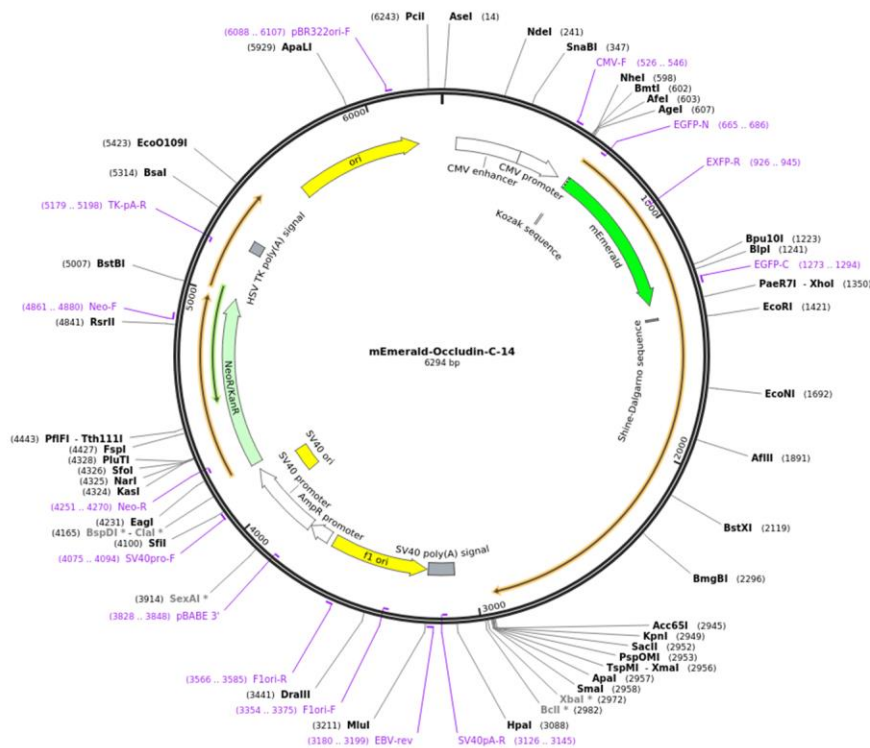
A**B**

Figure A.2. Plasmid maps of mCherry-Lifeact-7 and mEmerald Occludin-C-14. Plasmids contain sequence coding for Lifeact labelled with mCherry (A, 544911) and Occludin labelled with mEmerald (B, 54211) were purchased from Addgene. These plasmids were used to generate inserts to generate the lentiviral vector construct plasmids.

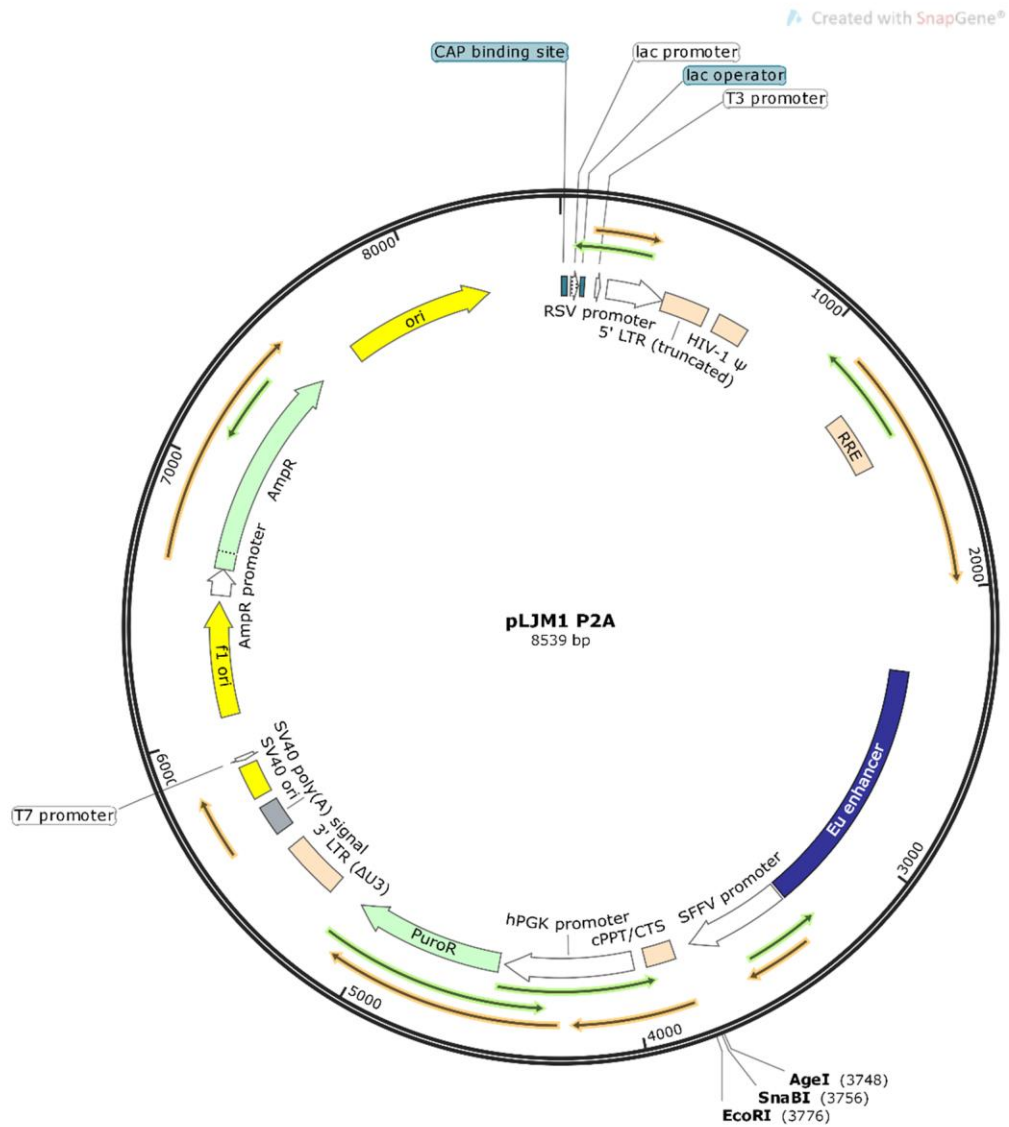


Figure A.3. Plasmid map of lentiviral transfer plasmid pLJM1 P2A. Lentiviral transfer plasmid lacking gene of interest donated by Dr Nicholas Harper. Map shows relevant restriction digest sites for generation of both pLJM1 P2A-O1 and pLJM1 P2A-L1.

pLJM1-P2A L1 sequence (cPPT Rev):

TTTTCAAGACCACTTTTCAACTACTCACTTTAGGATAAGTTTTAGGTAAAATGTGC
ATCATTATCCTGAATTATTTTCAAGTAAAGCATGTTAGTTGGTGGCATAAGAGAAAATC
AATCAGATAG|CTAGCTGCA|GTAACGCCATTTTCAAGGCATGAAAAATACCAAC
CAAGAATAGAGAAGTTCAGATCAAGGGCGGGTACATGAAAATAGCTAACGTTGGG
CCAACAGGATATCTGCGGTGAGCAGTTTCGGCCCCGGCCCGGGCCAAGAACAG
ATGGTCAACGCAGTTTCGGCCCCGGCCGAGGCCAAGAACAGATGGTCCCCAGAT
ATGGCCCAACCCTCAGCAGTTTCTTAAGACCCATCAGATGTTCCAGGCTCCCCAA
GGACCTGAAATGACCCTGCGCCTTATTTGAATTAACCAATCAGCCTGCTTCTCGCTT
CTGTTTCGCGCGCTTCTGCTTCCCAGCTCTATAAAAGAGCTCACAACCCCTCACTCG
GCGCGCCAGTCTCCGATTGACTGAGTCGCCCG|GACCGGTGCCTACGCCACC|AT
GGGCGTGGCCGACTTGATCAAGAAGTTCGAGTCCATCTCCAAGGAGGAG|GGGG
ATCCACCGGTGCGCCACC|ATGGTGAGCAAGGGCGAGGAGGATAACATGGCCATCA
TCAAGGAGTTCATGCGCTTCAAGGTGCACATGGAGGGCTCCGTGAACGGCCACGA
GTTTCGAGATCGAGGGCGAGGGCGAGGGCCGCCCTACGAGGGCACCCAGACCGC
CAAGCTGAAGGTGACCAAGGGTGGCCCCCTGCCCTTCGCCTGGGACATCCTGTCC
CCTCAGTTCATGTACGGCTCCAAGGCCTACGTGAAGCACCCCGCCGACATCCCCGA
CTACTTGAAGCTGTCCTTCCCCGAGGGCTTCAAGTGGGAGCGCGTGATGAACTTCG
AGGACGGCGGCGTGGTGACCGTGACCCAGGACTCCTCCCTGCAGGACGGCGAGT
TCATCTACAAGGTGAAGCTGCGCGGCACCAACTTCCCCTCCGACGGCCCCGTAATG
CAGAAGAAGACCATGGGCTGGGAGGCCTCCTCCGAGCGGATGTACCCGAGGAC
GGCGCCCTGAAGGGCGAGATCAAGCAGAGGCTGAAGCTGAAGGACGGCGGCCA
CTACGACGCTGAGGTCAAGACCCTACAAGGCCAAGAAGCCCGTGCAGCTGCCC
GGCGCCTACAACGTCAACATCAAGTTGGACATCACCTCCACAACGAGGACTACAC
CATCGTGGAACAGTACGAACGCGCCGAGGGCCCACTCCACCGCGGCATGGAC
GAGCTGTACAAGTAA|GAATTCTCGACCTCGAGACAAATGGCAGTATTCATCCACA
A|TTTTAAAAGA

Figure A.5. DNA sequence of mCherry-LifeAct within pLJM1 P2A-L1 plasmid. The section of the pLJM1 P2A-L1 plasmid containing mCherry-LifeAct was confirmed by Sanger sequencing using cPPT Rev primer. End of Eu enhancer (orange text), SFFV promoter (green text), LifeAct (blue text), mCherry (red text) and start of cPPT (grey text).

A

pLJM1 P2A O1 sequence (SFFV Prom For):

```
AAAAGAGCTCACAACCCCTCACTCGGCGCGCCAGTCCTCCGATTGACTGAGTCGCCCCG
|GACCGGTCGCCACCA|TGGTGAGCAAGGGCGAGGAGCTGTTACCGGGGTGGTGC
CCATCCTGGTCGAGCTGGACGGCGACGTAAACGGCCACAAGTTCAGCGTGTCCGGCG
AGGGCGAGGGCGATGCCACCTACGGCAAGCTGACCCTGAAGTTCATCTGCACCACCG
GCAAGCTGCCCCGTGCCCTGGCCCACCCTCGTGACCACCTTGACCTACGGCGTGCAGTG
CTTCGCCCCGCTACCCCGACCACATGAAGCAGCACGACTTCTTCAAGTCCGCCATGCCCG
AAGGCTACGTCCAGGAGCGCACCATCTTCTTCAAGGACGACGGCAACTACAAGACCC
GCGCCGAGGTGAAGTTCGAGGGCGACACCCTGGTGAACCGCATCGAGCTGAAGGGC
ATCGACTTCAAGGAGGACGGCAACATCCTGGGGCACAAGCTGGAGTACAACACTACAAC
AGCCACAAGGTCTATATCACCGCCGACAAGCAGAAGAACGGCATCAAGGTGAACTTCA
AGACCCGCCACAACATCGAGGACGGCAGCGTGCAGCTCGCCGACCACTACCAGCAGA
ACACCCCATCGGGCGACGGCCCCGTGCTGCTGCCCGACAACCACTACCTGAGCACCCA
GTCCAAGCTGAGCAAAGACCCCAACGAGAAGCGCGATCACATGGTCCTGCTGGAGTT
CGTGACCGCCGCGGGATCACTCTCGGCATGGACGAGCTGTACAAG|TCCGGACTCAG
ATCTCGAGGAAGCGGCGGATCTGGGTCC|GGATCATCCAGGCCTCTTGAAAGTCCACC
TCCTTACAGGCCTGATGAATTCAAACCGAATCATTATGCACCAAGCAATGACATATATGG
TGGAGAGATGCATGTTTCGACCAATGCTCTCTCAGCCAGCCTACTCTTTTTTACCCAGAAG
ATGAAATTCTCACTTCTACAAATGGACCTCTCCTCCAGGAGTGATTCCGGATCCTGTCTA
TGCTCATTATTGTGATGTGCATTGCCATCTTTGCCTGTGTGGCCTCCACGCTTGCCTGGG
ACAGAGGCTATGGAACCTCCCTTTTAGGAGGTAGTGTAGGCTACCCTTATGGAGGAAG
TGGCTTTGGTAGCTACGGAAGTGGCTATGGCTATGGCTATGGTTATGGCTATGGCTACG
GAGGCTATACAGACCCAAGAGCAGCAAAGGGCTTCATGTTGGCCATGGCTGCCTTTTG
TTTCATTGCCGCGTTGGTGATCTTTGTTACCAGTGTATAAGATCTGAAATGTCCAGAAC
AAGAAGATACTACTTAAGTGTGATAATAGTGAGTGCTATCCTGGGCATCATGGTTGTTAT
TGCCACAATTGTCTATATAATGGGA
```

Figure A.6. DNA sequence of mEmerald-occludin within pLJM1 P2A-O1 plasmid. The section of the pLJM1 P2A-O1 plasmid containing mEmerald-Occludin was confirmed by Sanger sequencing using SFFV Prom For (A) and cPPT Rev (B). End of SFFV promoter (green text), mEmerald (dark green text) and occludin (blue text). Overlap in sequencing between the two primers is shown in bold italics.

Figure A.6. continues onto next page

B

pLJM1 P2A O1 sequence (cPPT Rev):

TGTTTATTGCCACAATTGTCTATATAATGGGAGTGAACCCAACTGCTCAGTCTTCTGG
ATCTCTATATGGTTCACAAATATATGCCCTCTGCAACCAATTTTATACACCTGCAGCTACT
GGACTCTACGTGGATCAGTATTTGTATCACTACTGTGTTGTGGATCCCAGGAGGCCA
TTGCCATTGTACTGGGGTTCATGATTATTGTGGCTTTTGCTTTAATAATTTTCTTTGCTG
TGAAAACCTCGAAGAAAGATGGACAGGTATGACAAGTCCAATATTTGTGGGACAAG
GAACACATTTATGATGAGCAGCCCCCAATGTTCGAGGAGTGGGTTAAAAATGTGTCT
GCAGGCACACAGGACGTGCCTTACCCCCATCTGACTATGTGGAAAGAGTTGACAGT
CCCATGGCATACTCTTCCAATGGCAAAGTGAATGACAAGCGGTTTTATCCAGAGTCTT
CCTATAAATCCACGCCGGTTCCTGAAGTGGTTCAGGAGCTTCATTAACCTTCGCCTGT
GGATGACTTCAGGCAGCCTCGTTACAGCAGCGGTGGTAACTTTGAGACACCTTCAAA
AAGAGCACCTGCAAAGGGAAGAGCAGGAAGGTCAAAGAGAACAGAGCAAGATCA
CTATGAGACAGACTACACAACCTGGCGGCGAGTCCTGTGATGAGCTGGAGGAGGACT
GGATCAGGGAATATCCACCTATCACTTCAGATCAACAAAGACAACCTGTACAAGAGGA
ATTTTGACACTGGCCTACAGGAATACAAGAGCTTACAATCAGAACCTTGATGAGATCAA
TAAAGAACTCTCCCGTTTGGATAAAGAATTGGATGACTATAGAGAAGAAAGTGAAGA
GTACATGGCTGCTGCTGATGAATACAATAGACTGAAGCAAGTGAAGGGATCTGCAGA
TTACAAAAGTAAGAAGAATCATTGCAAGCAGTTAAAGAGCAAATTGTCACACATCAA
GAAGATGGTTGGAGACTATGATAGACAGAAAACATAG | GGTACCGCGTACGTGCAAC
AACTTCTCTCTGCTGAAACAAGCCGGAGATGTGAAGAGAATCCTGGACCCCGTTT
AAACGCCGAATTCTCGACCTCGAGACAAAT

Figure A.6. continued